RECONSTRUCTING MOLECULAR EVOLUTION BY CHANGING SUBSTRATE SPECIFICITIES WITHIN THE AMIDOHYDROLASE SUPERFAMILY OF ENZYMES

DISSERTATION ZUR ERLANGUNG DES DOKTORGRADES DER NATURWISSENSCHAFTEN (DR. RER. NAT.) DER NATURWISSENSCHAFTLICHEN FAKULTÄT III – BIOLOGIE UND VORKLINISCHE MEDIZIN – DER UNIVERSITÄT REGENSBURG

Universität Regensburg

TEXAS A&M UNIVERSITY

VORGELEGT VON

MONIKA M. MEIER AUS SCHWARZHOFEN

JUNI 2012

Promotionsgesuch eingereicht am: 20. Juni 2012

Kolloquium am: 04. Oktober 2012

Die Arbeit wurde angeleitet von: Prof. Dr. Reinhard Sterner (Universität Regensburg)
Prof. Dr. Frank M. Raushel (Texas A&M University, College Station, USA)

Prüfungsausschuss:

Vorsitzender: Prof. Dr. Reinhard Wirth

1. Prüfer: apl. Prof. Dr. Rainer Merkl
2. Prüfer: Prof. Dr. Frank M. Raushel
3. Prüfer: apl. Prof. Dr. Wolfram Gronwald

The presented work was performed from January 2009 to June 2012 in a joined project of Prof. Dr. Reinhard Sterner (Biochemistry II, Institute of Biophysics and Physical Biochemistry, University of Regensburg) and Prof. Dr. Frank M. Raushel (Department of Chemistry, Texas A&M University, College Station, USA).
From January – September 2009 and November 2010 – June 2012 the research was carried out at the University of Regensburg, and from October 2010 – October 2011 at the Texas A&M University, both under the supervision of Prof. Dr. Reinhard Sterner and Prof. Dr. Frank M. Raushel.

The work was supported by PhD fellowships of the German Academic Exchange Service (DAAD) and the *Fonds der Chemischen Industrie* to M.M.M..

DAAD
Deutscher Akademischer Austausch Dienst
German Academic Exchange Service

FCI
FONDS DER
CHEMISCHEN
INDUSTRIE

Dedicated to my parents

TABLE OF CONTENTS

TABLE OF CONTENTS I
LIST OF FIGURES VI
LIST OF TABLES IX
FORMULA INDEX XI
LIST OF ACRONYMS AND ABBREVIATIONS XII
ABSTRACT 1
ZUSAMMENFASSUNG 4
1 INTRODUCTION 7
1.1 Enzyme promiscuity 7
1.2 Organophosphate compounds and organophosphate hydrolases (OPH) 8
1.2.1 Organophosphate compounds 8
1.2.2 Organophosphate hydrolases (OPH) 10
1.3 The $(\beta\alpha)_8$-barrel-fold 11
1.4 The amidohydrolase superfamily (AHS) 13
1.5 Bacterial phosphotriesterase (PTE) and phosphotriesterase-like lactonases (PLL) 15
1.5.1 Bacterial phosphotriesterase (PTE) 15
1.5.2 Dr0930: a phosphotriesterase-like lactonase (PLL) 19
1.6 Enzyme design: Rational design versus directed evolution 21
1.6.1 Rational design 22
1.6.2 Directed evolution 22
1.7 Objectives and approach in general 23
2 MATERIALS 25
2.1 Instrumentation 25
2.2 Consumables 28
2.3 Chemicals 30
2.4 Kits 31
2.5 Enzymes 32
2.6 Bacterial strains 32
2.7 Vectors 35
2.7.1 pET vectors 35
2.7.2 pTNA vector 35
2.8 Oligodeoxynucleotides 36
2.8.1 Vector-specific amplification and sequencing primers 36
2.8.2 Amplification and mutagenic primers for *dr0930* 36
2.8.3 Amplification primers for *pte* 45
2.9 Ladders and markers 45
2.10 Buffers and solutions 45
2.10.1 Buffers and solutions for working with *E. coli* 46
2.10.2 Buffers and solutions for screening and enzyme kinetics 47
2.10.3 Buffers and solutions for working with DNA and agarose gel electrophoresis 48

2.10.4 Buffers and solutions for working with proteins 48
2.10.5 Buffers and solutions for SDS-PAGE 49
2.11 Bacterial growth media 50
2.12 Software 50

3 METHODS 52
3.1 Preparation of instrumentation and solutions 52
3.2 Microbiological methods 52
3.2.1 Cultivation and storage of *E. coli* strains 52
3.2.2 Preparation of chemically competent *E. coli* cells (Inoue *et al.*, 1990) 52
3.2.3 Transformation of chemically competent *E. coli* cells 53
3.2.4 Preparation of electro-competent *E. coli* cells (Dower *et al.*, 1988) 53
3.2.5 Preparation of DNA for electroporation 54
3.2.6 Transformation of electro-competent *E. coli* cells 54
3.2.7 Determination of transformation efficiency 54
3.2.8 *In vitro* activity screening 54
3.3 Molecular biology methods 56
3.3.1 Isolation and purification of plasmid DNA from *E. coli* 56
3.3.1.1 Isolation of plasmid DNA in analytical amounts (mini-preparation) 57
3.3.1.2 Isolation of plasmid DNA in preparative amounts (midi/maxi-preparation) 57
3.3.2 Determination of DNA concentration 57
3.3.3 Agarose gel electrophoresis 58
3.3.3.1 Isolation of DNA fragments from agarose gels 58
3.3.4 Enzymatic manipulation of dsDNA 59
3.3.4.1 Cleavage of dsDNA by restriction endonucleases 59
3.3.4.2 Ligation of DNA fragments 59
3.3.5 Amplification of DNA fragments by standard PCR (polymerase chain reaction) 60
3.3.6 Colony PCR 62
3.3.7 PCR methods for site-directed mutagenesis 62
3.3.7.1 QuikChange site-directed mutagenesis (QCM) 62
3.3.7.2 Phusion® Site-Directed Mutagenesis Kit 64
3.3.7.3 Megaprimer PCR (Sarkar & Sommer, 1990) 64
3.3.7.4 Overlap extension PCR (Ho *et al.*, 1989) 65
3.3.8 *In vitro* recombination by StEP (staggered extension process) 66
3.3.9 Transposon-mediated insertion mutagenesis (MGS™ Kit) 67
3.3.10 Construction of a gene library 69
3.3.10.1 Determination of the size of a gene library 70
3.3.11 DNA sequencing 71
3.4 Protein biochemistry methods 72
3.4.1 Gene expression and purification of recombinant protein 72
3.4.1.1 Gene expression in analytical scale 72
3.4.1.2 Gene expression and purification of recombinant proteins in preparative scale 73
3.4.2 Protein purification from the soluble cell fraction 73
3.4.2.1 Protamine sulfate and ammonium sulfate precipitation 73
3.4.2.2 Ion exchange chromatography (IEX) 74
3.4.2.3 Preparative gel filtration 77
3.4.2.4 Desalting of protein solutions 78

3.4.2.4.1 Dialysis of protein solutions 78
3.4.2.4.2 Desalting and buffer exchange by GE illustra NAP™ or PD-10 columns 78
3.4.2.4.3 Desalting via GE Sephadex G25 Desalting 78
3.4.2.5 Concentrating protein solutions 79
3.4.2.6 Storage of purified proteins 79
3.5 Analytical methods 79
3.5.1 Protein concentration determination via UV-absorption spectroscopy 79
3.5.2 SDS-polyacrylamide gel electrophoresis (SDS-PAGE) 80
3.5.3 ICP-MS measurements 81
3.5.4 Steady-state enzyme kinetics 81
3.5.4.1 Colorimetric assay for OPH activity with *p*-nitrophenol substituted OPs 81
3.5.4.2 Coupled DTNB (Ellman's Reagent) assay 82
3.5.4.3 pH-dependent colorimetric assay 82
3.5.4.4 Data analysis 83
3.5.5 Dixon plot for competitive inhibition 83
3.5.6 Determination of stereopreference 84
3.6 Protein crystallization and X-ray structure determination 85
3.6.1 Protein crystallization 85
3.6.2 Data collection 86
3.6.3 Data processing and structure determination 86
3.7 RosettaLigand Docking 87
3.7.1 Protein receptor and cofactor preparation for docking 87
3.7.2 Ligand preparation and ligand positioning 88
3.7.3 Docking calculations and analysis of docking results 88

4 RESULTS AND DISCUSSION 89
4.1 *D. radiodurans* Dr0930: a close homologue of *P. diminuta* PTE 89
4.2 Dr0930 and PTE: promiscuous and native activities 93
4.2.1 Heterologous expression in *E. coli* and purification of the recombinant wild-type Dr0930 and wild-type PTE proteins 93
4.2.2 Chemical structures of δ-nonanoic lactone and OP compounds 95
4.2.3 Steady-state kinetic characterization of wild-type Dr0930 and wild-type PTE for native and promiscuous activities 97
4.3 Laboratory evolution of wild-type Dr0930 for OPH activity 102
4.3.1 Randomization of wild-type Dr0930 by error-prone PCR (epPCR) 103
4.3.1.1 Characterization of the epPCR library 103
4.3.1.2 Verification of epPCR hits by *in vitro* activity screening with EPXN 105
4.3.1.3 Heterologous expression, purification and *in vitro* characterization of the epPCR hits 106
4.3.1.4 Metal-dependency of the OPH activity 107
4.3.1.5 Steady-state kinetic characterization of Co/Co-Dr0930_5 for the hydrolysis of OPs 1-7 108
4.3.2 *In vitro* recombination of beneficial 1st generation variants by StEP 110
4.3.2.1 Generation and characterization of a pTNA-*dr0930*-StEP library 110
4.3.2.2 *In vitro* activity screening of the pTNA-*dr0930*-StEP library 111
4.3.2.3 Heterologous expression, purification and *in vitro* characterization of hits isolated from the StEP library 113
4.3.3 Simultaneous hot spot mutagenesis (SHM) 114
4.3.3.1 Generation and characterization of a SHM library 114

4.3.3.2 *In vitro* activity screening of the pTNA-*dr0930*-SHM library using a combination of filter paper and 96-well block activity screen 116
4.3.3.3 Heterologous expression, purification and steady-state enzyme kinetic characterization of hits from the SHM library 118
4.3.3.4 Generation and characterization of consensus variants 120
4.3.4 Sequential site-directed, site-saturation and combinatorial mutagenesis 122
4.3.4.1 Combinatorial mutagenesis on template Dr0930_5 123
4.3.4.2 Site-saturation mutagenesis at position Tyr28 128
4.3.4.3 Combinatorial and insertion/deletion scanning mutagenesis on template Dr0930_81 131
4.3.4.3.1 Generation of insertion and deletion variants 131
4.3.4.3.1.1 Multiple amino acid deletion variants of βα-loop 3 131
4.3.4.3.1.2 Transposon-mediated insertion scanning mutagenesis 131
4.3.4.3.2 Site-saturation mutagenesis of Try97 on template Dr0930_81 132
4.3.4.4 Mutagenesis on template Dr0930_106 135
4.3.4.4.1 Site-saturation mutagenesis at position Phe26 135
4.3.4.4.2 Combinatorial site-directed mutagenesis on template Dr0930_106 136
4.3.5 Summary: Design of a multi-efficient OPH 140
4.4 Detailed Characterization of best engineered Dr0930 variants 141
4.4.1 Steady-state kinetic characterization for the hydrolysis of δ-nonanoic lactone (native activity) 141
4.4.2 Steady-state kinetic characterization for the hydrolysis of DEVX 143
4.4.3 Stereopreference analysis of wild-type Dr0930 and Dr0930_134 144
4.4.4 Structural analysis of engineered Dr0930 variants 149
4.4.4.1 Crystallization and X-ray structure determination of evolved Dr0930 variants 149
4.4.4.2 Analysis of beneficial mutations in engineered variants 153
4.4.5 Ligand docking studies with engineered Dr0930 variants 155
4.4.5.1 Retroperspective ligand docking 155
4.4.5.2 Docking of EPXN in the active site of Dr0930_134 157

5 FINAL DISCUSSION 161
5.1 Divergent and convergent evolution of enzymes 161
5.2 *D. radiodurans* Dr0930: a promiscuous OP hydrolyzing enzyme 162
5.3 Laboratory evolution of Dr0930 for OP hydrolysis 163
5.3.1 Design of an efficient and multi-functional OP hydrolyzing Dr0930 variant 163
5.3.2 Detailed characterization of engineered Dr0930 variants 167
5.3.3 Comparison of design achievemens to state-of-the-art designs for OPH activity 170
5.4 Implications for protein design and evolution 171
5.5 Outlook 172

6 REFERENCES 173

7 APPENDIX 185
7.1 DNA and protein sequences of wild-type Dr0930 and wild-type PTE 185
7.1.1 DNA and protein sequences of *Deinococcus radiodurans R1* Dr0930 185
7.1.2 DNA and protein sequences of *Pseudomonas diminuta* PTE 186
7.2 Structure of various substrates for PLL enzymes and PTE 187

7.3 Determination of the conversion factor ε_{577} for the pH-dependent colorimetric assay 188
7.4 Determination of the enzyme metal content by ICP-MS 189
7.5 Sequence of most active Dr0930 variants isolated from the pTNA-*dr0930*-SHM library 190
7.6 Dixon Plot for determination of K_i 191

8 ACKNOWLEDGEMENTS 192

9 EIDESSTATTLICHE ERKLÄRUNG 194

LIST OF FIGURES

Figure 1: Structures of organophosphate compounds. 8
Figure 2: Three-dimensional structure of selected OPH enzymes: PTE, MPH, OPAA, and PON1. 11
Figure 3: The $(\beta\alpha)_8$-barrel fold. 12
Figure 4: Active site region and coordination geometry of Zn^{2+}/Zn^{2+}-substituted PTE (PDB ID 1EZ2) with bound diisopropyl methylphosphonate inhibitor. 17
Figure 5: A plausible reaction mechanism of PTE for the hydrolysis of phosphotriesters, using paraoxon as an example. 18
Figure 6: Active site region and coordination geometry of the Zn^{2+}/Zn^{2+}-substituted Dr0930 (PDB ID 3FDK) with the docked high-energy intermediate of δ-nonanoic lactone hydrolysis. 20
Figure 7: A proposed reaction mechanism of Dr0930 for the hydrolysis of lactones, using δ-nonanoic lactone as an example. 21
Figure 8: DNA and protein ladders and markers. 45
Figure 9: Overview of the *in vitro* activity screening procedure. 55
Figure 10: Overview of the QuikChange site-directed mutagenesis method. 63
Figure 11: Schematic overview of the primer design for introducing point mutations (A), deletions (B), and insertions (C1+C2) applying the Phusion Site-Directed Mutagenesis Kit. 64
Figure 12: Scheme for standard megaprimer PCR. 65
Figure 13: Scheme for standard OE-PCR. 66
Figure 14: Scheme for StEP recombination. 66
Figure 15: Flowchart of insertion mutagenesis. 68
Figure 16: Structure of the 15 bp insertion (A) and translation of 15 bp insertion (B). 68
Figure 17: Structure based sequence alignment of PTE and selected PLL enzymes generated by 3D-coffee. 90
Figure 18: Structural superposition of *D. radiodurans R1* Dr0930 and *P. diminuta* PTE (A) and excerpts of the active sites of Dr0930 (B) and PTE (C). 91
Figure 19: The substrate binding pockets of Dr0930 (A) and PTE (B). 93
Figure 20: Exemplary purification overview of the recombinant wild-type Dr0930 protein. 94
Figure 21: Purification overview of the recombinant wild-type PTE protein. 95
Figure 22: Chemical structures of OP compounds (A-D) and δ-nonanoic lactone (E). 96
Figure 23: Reaction schemes including their transition states for the hydrolysis of δ-nonanoic lactone (A) and ethyl-paraoxon (B). 98
Figure 24: Saturation curves of wild-type Dr0930 (A) and wild-type PTE (B) for the hydrolysis of δ-nonanoic lactone. 98
Figure 25: Saturation curves of wild-type Dr0930 for the hydrolysis of OPs 1-7. 99
Figure 26: Saturation curves of wild-type PTE for the hydrolysis of OPs 1-7. 100
Figure 27: Catalytic efficiencies of wild-type Co/Co-Dr0930 (A) and wild-type Co/Co-PTE (B) for OPs 1-7. 101
Figure 28: *In vitro* activity screening for Dr0930 variants with improved OPH activity. 103
Figure 29: Localization of mutations identified in Dr0930_1 - Dr0930_12. 104
Figure 30: *In vitro* activity screening of the epPCR variants Dr0930_1 - Dr0930_12 using 0.5 mM EPXN. 105
Figure 31: Saturation curves of wild-type Zn/Zn-Dr0930 and Zn/Zn-Dr0930_2, Zn/Zn-Dr0930_5, Zn/Zn-Dr0930_11, and Zn/Zn-Dr0930_12 variants for the hydrolysis of EPXN. 106

Figure 32: Saturation curves of Dr0930_5 for the hydrolysis of OPs 1-7. 109
Figure 33: Catalytic efficiencies of Dr0930_5 (open bars) in comparison to wild-type Dr0930 (filled bars) (A) and deduced fold improvement of Dr0930_5 relative to wild-type Dr0930 (B). 110
Figure 34: *In vitro* activity screening of the StEP variants Dr0930_15 - Dr0930_29 using 0.5 mM EPXN. 112
Figure 35: Positions selected for simultaneous hot spot mutagenesis (SHM). 115
Figure 36: DEAE filter paper activity screen of the SHM library: identification of active colonies by digital imaging using a band pass filter. 117
Figure 37: Representative *in vitro* activity screen of a 96-well plate using 0.25 mM EPXN. 117
Figure 38: Saturation curves of Dr0930_30, Dr0930_31 and Dr0930_32 for the hydrolysis of EPXN. 119
Figure 39: *In vitro* activity screening for consensus variants Dr0930_58 - Dr0930_69 using 0.15 mM EPXN. 121
Figure 40: Selected positions for sequential site-directed and site-saturation mutagenesis. 123
Figure 41: *In vitro* activity screening of combinatorial variants Dr0930_71 - Dr0930_80 using 0.5 mM EPXN. 126
Figure 42: Saturation curves of Dr0930_73 for the hydrolysis of OPs 1-7. 127
Figure 43: *In vitro* activity screening of the 28NNS library variants Dr0930_81 - Dr0930_85 using 0.25 mM GF *p*-NP (OP 5) (A) and 0.25 mM MPXN (OP 6) (B). 129
Figure 44: Saturation curves of Dr0930_81 for the hydrolysis of OPs 1-7. 130
Figure 45: *In vitro* activity screening of the Y97NNS variants using 0.25 mM GD *p*-NP (OP 4) (A) and 0.15 mM EPXN (OP 7) (B). 133
Figure 46: Saturation curves of Co/Co-Dr0930_106 for the hydrolysis of OPs 1-7. 134
Figure 47: *In vitro* activity screening of Dr0930_129 - Dr0930_143 using 0.15 mM GB *p*-NP (OP 2) (A) and 0.2 mM GD *p*-NP (OP 4) (B). 137
Figure 48: Saturation curves of Co/Co-Dr0930_134 for the hydrolysis of OPs 1-7. 138
Figure 49: Catalytic efficiencies (k_{cat}/K_M) (A) and k_{cat} (filled bars) and K_M (open bars) values of Co/Co-Dr0930_134 for OPs 1-7. 139
Figure 50: Comparison of Dr0930_134 with wild-type Dr0930 (A) and wild-type PTE (B). 140
Figure 51: Overview on the enzyme design approach. 140
Figure 52: Saturation curves of wild-type Dr0930 and variants for the hydrolysis of δ-nonanoic lactone. 141
Figure 53: Catalytic efficiencies (A) and k_{cat} (filled bars) and K_M (open bars) parameters (B) of wild-type Co/Co-Dr0930 and Co/Co-Dr0930 variants for the hydrolysis of δ-nonanoic lactone. 142
Figure 54: Time courses for the chemical (A) and enzymatic hydrolysis (B, C, D) of approximately 50 µM racemic VR *p*-NP (OP 3). 146
Figure 55: Ratios of k_{cat}/K_M (R_P) / k_{cat}/K_M (S_P) for the hydrolysis of chiral OPs 1-5 by wild-type Dr0930 (A) and Dr0930_134 (B). 148
Figure 56: Structures of substrate analogues (DIMP, DE4MBP) and product analogues (DEP, CAC) used for co-crystallization. 150
Figure 57: Crystal of a Dr0930 variant frozen in ethylene glycol. 151
Figure 58: Structural superpositions of the engineered Dr0930_134 variant and wild-type Dr0930 (PDB ID 3FDK). 153
Figure 59: Structural superpositions of Dr0930_134 and wild-type Dr0930. 154

Figure 60: Docking poses of DIMP (A) and EPXN (B) in the crystal structure of wild-type PTE, obtained using the RosettaLigand program. 157
Figure 61: Docking poses of EPXN in the crystal structure of Dr0930_134, obtained by docking using the RosettaLigand program. 158
Figure 62: Docking poses of EPXN in the crystal structure of Dr0930_134, obtained by docking using the RosettaLigand program applying distance and angle constraints. 159
Figure 63: Structural superposition of the active sites of Dr0930_134 and PTE with the top scoring docking poses for EPXN each. 160
Figure 64: Overview of the experimental workflow. 164
Figure 65: Structures of substrates of PLL enzymes and PTE: lactones and esters (A) and OPs (B). 187
Figure 66: Determination of the conversion factor ε_{577} for the pH-dependent colorimetric assay. 188
Figure 67: Dixon plot to determine K_i for DIMP and Dr0930_134. 191

LIST OF TABLES

Table 1: Metal complexation in eight subtypes of the AHS. 14
Table 2: Properties of wild-type Dr0930 and wild-type PTE relevant for concentration determination. 80
Table 3: Composition of a 12.5% SDS-PAGE gel. 81
Table 4: PTE and selected homologues PLL enzymes. 89
Table 5: Steady-state kinetic constants of wild-type Co/Co-Dr0930 and wild-type Co/Co-PTE for the hydrolysis of δ-nonanoic lactone. 99
Table 6: Steady-state kinetic constants for wild-type Co/Co-Dr0930 and wild-type Co/Co-PTE for the hydrolysis of OPs 1-7. 101
Table 7: Dr0930 variants isolated from *in vitro* activity screening of the epPCR library. 104
Table 8: Steady-state kinetic constants of wild-type Zn/Zn-Dr0930 and variants for the hydrolysis of EPXN. 107
Table 9: Metal-dependency (Zn, Co, Mn) of the kinetic constants for wild-type Dr0930 for the hydrolysis of EPXN. 108
Table 10: Steady-state kinetic constants of Co/Co-Dr0930_5 for the hydrolysis of OPs 1-7 109
Table 11: Dr0930 variants isolated from *in vitro* activity screening of the StEP library 112
Table 12: Steady-state kinetic constants of Co/Co-Dr0930_16 and Co/Co-Dr0930_22 for the hydrolysis of EPXN. 113
Table 13: Selected positions for SHM mutagenesis and introduced set of mutations 115
Table 14: Percentage alteration of mutations at each position. 118
Table 15: Catalytic efficiencies of Dr0930 variants in comparison to wild-type Dr0930 and Dr0930_5 for the hydrolysis of OPs 1-7 119
Table 16: Consensus Variants Dr0930_58 - Dr0930_69. 121
Table 17: Steady-state kinetic parameters of Co/Co-Dr0930_70 for the hydrolysis of OPs 1-7 124
Table 18: Variants generated by combinatorial mutagenesis on template Dr0930_5 (D71N+E179D+L270M): Dr0930_71 - Dr0930_80. 125
Table 19: Steady-state kinetic constants of Co/Co-Dr0930_73 for the hydrolysis of OPs 1-7 127
Table 20: Hits isolated from Y28NNS screen on templates Dr0930_73 and Dr0930_75. 128
Table 21: Steady-state kinetic constants of Co/Co-Dr0930_81 and Co/Co-Dr0930_83 for the hydrolysis of OPs 1-7. 130
Table 22: Y97NNS variants generated on the Dr0930_81 template: Dr0930_91 - Dr0930_109. 133
Table 23: Steady-state kinetic constants of Co/Co-Dr0930_93 and Co/Co-Dr0930_106 for the hydrolysis of OPs 1-7. 135
Table 24: Variants generated by combinatorial mutagenesis on template Dr0930_106: Dr0930_129 - Dr0930_143. 136
Table 25: Steady-state kinetic parameters of Co/Co-Dr0930_134 for the hydrolysis of OPs 1-7 138
Table 26: Steady-state kinetic constants of wild-type Co/Co-Dr0930 and engineered Dr0930 variants for the hydrolysis of δ-nonanoic lactone. 142
Table 27: Steady-state kinetic constants of wild-type Co/Co-Dr0930 and engineered variants for the hydrolysis of DEVX. 144

Table 28: Summary of k_{cat}/K_M ($M^{-1}s^{-1}$) parameters deduced from the analysis of individual phases (1-3) observed upon the hydrolysis of racemic substrates by wild-type Dr0930 and Dr0930_134. 147
Table 29: Ratios of k_{cat}/K_M (R_P) / k_{cat}/K_M (S_P) for the hydrolysis of chiral OPs 1-5 by wild-type Dr0930 and Dr0930_134. 148
Table 30: Crystallization conditions for Dr0930 variants. 150
Table 31: Data collection and refinement statistics for Dr0930_81, Dr0930_106 and Dr0930_134. 152
Table 32: Metal content determined by ICP-MS. 189
Table 33: Most active variants isolated from pTNA-*dr0930*-SHM library. 190

FORMULA INDEX

Equation 1: Determination of the transformation efficiency. 54
Equation 2: Determination of DNA concentration. 58
Equation 3: Calculation of the melting temperature of oligonucleotides. 60
Equation 4: Calculation of the optimum annealing temperature of a primer in the PCR reaction. 61
Equation 5: Determination of the number of transformed cells. 70
Equation 6: Determination of the ligation efficiency. 70
Equation 7: Determination of the gene library size. 71
Equation 8: Determination of the molar extinction coefficient ε_{280}. 79
Equation 9: Determination of the specific extinction coefficient ${}^{0.1\%}A_{280}$. 79
Equation 10: Determination of the protein concentration by using the specific extinction coefficient ${}^{0.1\%}A_{280}$. 80
Equation 11: Michaelis-Menten Equation. 83
Equation 12: Velocity equation for competitive inhibition in linear form. 84
Equation 13: Single- and double-exponential fit of an exponential time course. 84
Equation 14: Determination of the catalytic efficiency of individual enantiomers 85

LIST OF ACRONYMS AND ABBREVIATIONS

Amino acids are abbreviated by the 1- or 3-letter code.

A	absorbance; adenosine
Å	Ångström (10^{-10} m)
aa	amino acid
$^{0.1\%}A_x$	specific extinction coefficient at x nm
A_{bases}	average number of nucleotide exchanges per gene
a_{bases}	number of nucleotide exchanges per analyzed gene
AChE	acetylcholinesterase
ADA	adenosine deaminase
AEX	anion exchange chromatography
AGD	acetyl glucosamine-6-phosphate deacetylase
AHS	amidohyrolase superfamily
APS	ammonium persulfate
AS	ammonium sulfate
ATP	adenosine triphosphate
bp	base pair
BChE	butyrylcholinesterase
BSA	bovine serum albumin
°C	celsius
C	cytosine
c	concentration
Cα	central C-2 carbon of amino acids
CAC	sodium cacodylate
CDA	cytosine deaminase
CWA	chemical warfare agent
DFT	density functional theory
cm	centimeter ($1 \cdot 10^{-2}$m)
C-terminal	carboxy-terminal end of a polypeptide chain
CV	column volume
CWAs	chemical warefare agents
d	pathlength [cm]
Da	dalton [g/mol]
DAA	D-amino acid deacetylase
DE4MBP	diethyl 4-methylbenzylphosphonate
DEP	diethyl phosphate
DIMP	diisopropyl methylphosphonate
DMSO	dimethyl sulfoxide
DNA	deoxyribonucleic acid
Dr0930	Dr0930 from *D. radiodurans*
dr0930	gene coding for the enzyme Dr0930

δ-NL	δ-nonanoic lactone
dNTP	deoxyribonucleotide triphosphate (N = A, C, G or T)
D. radiodurans R1	*Deinococcus radiodurans R1*
dsDNA	double stranded DNA
DFT	density functional theory
DHO	dihydroorotase
DTNB	5,5'-dithiobis-(2-nitrobenzoic acid); Ellman's reagent
DTT	dithiothreitol
E. coli	*Escherichia coli*
EC	Enzyme Commission
EDTA	ethylene diamine tetraacetic acid
ee	enantiomeric excess
*ep*PCR	error-prone PCR
EPR	electron paramagnetic resonance
EPXN	ethyl-paraoxon
eq.	equivalents of metal ion per enzyme subunit
et al.	and other authors (*et alii*)
EtBr	ethidium bromide
f	dilution factor
FACS	Fluorescence Activated Cell Sorting
G	guanosine; gene library size
g	gram
GA	tabun
GB	sarin
GD	soman
GF	cylosarin
GdmCl	guanidinium chloride
h	hour
$(His)_6$-tag	hexahistidine-tag
HYD	hydantoinase
IAD	isoaspartyl dipeptidas
IEX	ion exchange chromatography
IPTG	isopropyl-ß-D-thiogalactopyranoside
ITCHY	incremental truncation for the creation of hybrid proteins
kb	kilobase pair
k_{cat}	turnover number
k_{cat}/K_M	catalytic efficiency parameter
kDa	kilodalton ($1 \cdot 10^3$ g/mol)
K	Kelvin
K_i	dissociation constant for an enzyme-inhibitor complex
K_M	Michaelis-Menten constant, equivalent to the substrate concentration at half-maximum rate
L	ligation efficiency
l	liter
*lac*Z	gene coding for the enzyme β-galactosidase

LB	Luria-Bertani (-medium)
LD_{50}	lethal dosage value
LigI	2-pyrone-4,6-dicarboxylate lactonase
ln	natural logarithm
log	decadic logarithm
M	molar [mol/l]
m	slope; milli ($1 \cdot 10^{-3}$); mass
mA	milliampere
MCS	multiple cloning site
MeOH	methanol
mg	milligram
min	minute
ml	milliliter
mm	millimeter
mM	millimolar
MPa	megapascal
MPXN	methyl-paraoxon
MW	molecular weight
mwco	molecular weight cut off
n	nano ($1 \cdot 10^{-9}$); number of nucleotides
$n_{colonies}$; n_c	number of colonies
n_G	number of analyzed colonies
n_T	number of transformed cells
n_V	number of colonies with correct insert
ng	nanogram
nm	nanometer
NNS	degenerated codon
n_{seq}	number of sequenced genes
n_T	number of transformed cells
N-terminal	amino-terminal end of a polypeptide chain
OD_x	optical density at x nm
OE-PCR	overlap extension PCR
OPs	organophosphates
OP 1	VX *p*-NP
OP 1	GB *p*-NP
OP 3	VR *p*-NP
OP 4	GD *p*-NP
OP 5	GF *p*-NP
OP 6	methyl-paraoxon (MPXN)
OP 7	ethyl-paraoxon (EPXN)
OP 8	DEVX (Diethyl-VX)
opd	organophosphate-degradation genes
P	pellet (insoluble cell fraction)
PAGE	polyacrylamide gel electrophoresis
PCR	polymerase chain reaction

PDB	protein data bank
P. diminuta	*Pseudomonas diminuta*
pH	negative decadic logarithm of the proton concentration
PHP	phosphotriesterase homology protein
PLL	phosphotriesterase-like-lactonase
p-NP	*p*-nitrophenol
PS	protamine sulfate
PTE	phosphotriesterase from *P. diminuta*
pte	gene coding for the enzyme phosphotriesterase
QCM	QuikChange mutagenesis
QM/MM	quantum mechanical/molecular mechanical
rbs	ribosome binding site
RDP	renal dipeptidase
r.m.s.d.	root mean square deviation
rpm	revolutions per minute
RT	room temperature
RuBisCo	ribulose-1,5-bisphosphate-carboxylase
S	supernatant (soluble cell fraction); substrate concentration
s	second
SCOP	structural classification of proteins
SDS	sodium dodecyl sulfate
ssDNA	single-stranded DNA
StEP	staggered extension process
T	temperature; thymidine
T_A	annealing temperature
Taq	*Thermus aquaticus*
TBE	Tris-Borat-EDTA buffer
T_E	transformation efficiency
T_M	melting temperature of primers; temperature at which 50% of the protein is in a non-native state
TEMED	N,N,N',N'-tetramethylethylenediamine
TIM	triosephosphate isomerase
Ts	transition
Tv	transversion
U	Unit, 1U is equivalent to the amount of enzyme that converts 1 µmol substrate per minute at standard conditions
URE	urease
URI	uronate isomerase
UV	ultraviolet
V	volt
v_i	initial velocity
v_{max}	maximum velocity
V_s	volume factor
($^v/_v$)	volume percent
VIS	visible spectroscopy

W	watt
WT	wild-type
($^{w}/_{v}$)	weight per volume
Ø	diameter
Δ	difference
Δ*hisA*-Δ*hisF*	*E. coli* strain with deleted *his*A and *his*F genes
ε_x	molar extinction coefficient at x nm
λ	wavelength
µ	micro ($1 \cdot 10^{-6}$)
µF	microfarad
µg	microgram
µl	microliter
µm	micrometer
µM	micromolar
3D	three-dimensional
Ω	ohm

ABSTRACT

The analysis of the rapid molecular evolution of enzymes provides insights into the remarkable adaptability of these sophisticated macromolecules and helps to elucidate the relationship between protein sequence, structure and function.

A prominent example for rapid molecular evolution in response to changing environmental conditions is the phosphotriesterase from *Pseudomonas diminuta* (PTE), which hydrolyzes with remarkably catalytic efficiency synthetic organophosphates (OPs). Since OPs were invented only in the last century as agricultural insecticides and highly toxic chemical warfare agents, PTE is a relatively "young" enzyme. It has been postulated that it has evolved from members of the phosphotriesterase-like lactonase (PLL) family that show promiscuous organophosphate degrading activity. The goal of this thesis was to mimic this postulated evolutionary pathway from PLL to PTE in the laboratory by establishing OP hydrolysis activity on the scaffold of Dr0930, a PLL from the organism *Deinococcus radiodurans R1.* Dr0930 and PTE have a similar $(\beta\alpha)_8$-barrel fold and share crucial active site features including two catalytically essential bivalent metal ions.

In the first part of the thesis, steady-state kinetic parameters for *D. radiodurans R1* Dr0930 were determined for the hydrolysis of δ-nonanoic lactone as well as the promiscuous hydrolysis of the OP insecticides methyl-paraoxon (MPXN) and ethyl-paraoxon (EPXN) and the racemic *p*-nitrophenol (*p*-NP) analogues of OP nerve agents VX, sarin (GB), VR, soman (GD), and cyclosarin (GF). The promiscuous catalytic efficiencies for wild-type Co/Co-Dr0930 range from 2.1 $M^{-1}s^{-1}$ to 6.1×10^2 $M^{-1}s^{-1}$ and are four (GD *p*-NP) to seven (GB *p*-NP and EPXN) orders of magnitude lowered when compared to wild-type Co/Co-PTE. Mutually, promiscuous activity of wild-type PTE for the hydrolysis of δ-nonanoic lactone was found to occur with a k_{cat}/K_M of 6.8×10^1 $M^{-1}s^{-1}$.

The low promiscuous OP degrading activity of wild-type Dr0930 was increased by an iterative process comprising several steps of rational protein design and random mutagenesis in combination with *in vitro* screening for the hydrolysis of EPXN and six additional tested OP compounds. Beneficial mutations identified in the different steps were successively combined, yielding the variant Dr0930_134. Dr0930_134 contains

seven amino acid exchanges (Y28L+D71N+Y97F+E101G+E179D+V235L+P274L) and its OP hydrolysis activity for GB *p*-NP, VR *p*-NP, and GF *p*-NP is elevated by four orders of magnitude compared to wild-type Dr0930. The catalytic efficiencies achieve absolute values of up to 10^5 $M^{-1}s^{-1}$. Most remarkably, Dr0930_134 shows a k_{cat}/K_M value of 10^4 $M^{-1}s^{-1}$ for the hydrolysis of GD *p*-NP, which comes close to the catalytic efficiency of wild-type PTE for this substrate.

The engineered Dr0930 variants were characterized for their residual native lactonase activities, the stereoselectivity of OP hydrolysis, and the ability to hydrolyze P-S in addition to P-O bonds. The results showed that the substantial increase in promiscuous OP hydrolysis activity is accompanied by an equally strong decrease of the native activity, with Dr0930_134 still achieving a catalytic efficiency of 2.8×10^3 $M^{-1}s^{-1}$ for the hydrolysis of δ-nonanoic lactone. The increased OP hydrolysis activity of Dr0930_134 compared to wild-type Dr0930 comes along with an enhanced stereoselectivity for the less toxic R_P enantiomers of the chiral OP substrates. The shift in the enantiomeric preference [ratio k_{cat}/K_M (R_P) / k_{cat}/K_M (S_P)] was as high as 4.3×10^2 in the case of VR *p*-NP. The highest enantiomeric preference of 1.5×10^4-fold was observed for GB *p*-NP. The engineered Dr0930 variants were tested for their ability to hydrolyze the phosphorothiolate DEVX (Diethyl-VX), a close analogue of the nerve agent VX. In spite of their high catalytic efficiency for the hydrolysis of P-O bonds, the k_{cat}/K_M values for the hydrolysis of the P-S bond of DEVX were only 1 $M^{-1}s^{-1}$.

Structural and computational analysis was performed to identify the structural basis for the enhanced OP hydrolysis activities of the engineered Dr0930 variants. Three variants including Dr0930_134 were crystallized, and their X-ray structures were solved to a resolution of 1.8 - 2.1 Å. The variants exhibited only minor structural differences relative to wild-type Dr0930. The active site was enlarged and its hydrophobic character was increased, providing more space to accommodate the OP substrates. Moreover, additional flexibility was gained due to the elimination of a hydrogen bond between residues of the βα-loops 2 and 3. In order to identify the orientation of EPXN at the active site Dr0930_134, the substrate was docked using the RosettaLigand program. The best poses obtained were similar to the pose of EPXN when docked into the active site of *P. diminuta* PTE and confirm site-directed mutagenesis experiments that have indicated an important role of residues F26 and R228 for OP hydrolysis activity by Dr0930_134.

Taken together, the results of this thesis show that laboratory evolution can readily establish high OP hydrolysis on the scaffold of Dr0930, providing strong evidence for the postulated natural evolution of PTE from members of the PLL family.

ZUSAMMENFASSUNG

Die Analyse der schnellen molekularen Evolution von Enzymen eröffnet Einblicke in die bemerkenswerte Anpassungsfähigkeit dieser komplexen Makromoleküle und trägt somit zum Verständnis der Beziehung zwischen Proteinsequenz, Struktur und Funktion bei.

Ein bekanntes Beispiel für schnelle molekulare Evolution in Anpassung an sich schnell verändernde Umweltbedingungen ist die Phosphotriesterase aus *Pseudomonas diminuta* (PTE), welche mit einer bemerkenswerten katalytischen Effizienz synthetische Organophosphate (OP) hydrolysiert. Da diese Verbindungen erstmals im letzten Jahrhundert als landwirtschaftliche Insektizide und hochgiftige chemische Kampfstoffe synthetisiert wurden, vermutet man an, dass PTE ein evolutionär relativ "junges" Enzym ist. Es wird angenommen, dass sich die PTE aus der Familie der Phosphotriesterase-ähnlichen Lactonasen (PLL) entwickelt hat, welche promiskuitive OP hydrolytische Aktivität zeigt. Das Ziel dieser Arbeit war es, den postulierten Weg der natürlichen Evolution von PLL zu PTE im Labor nachzuvollziehen. Dazu sollte OP-Hydrolaseaktivität auf dem Proteingerüst von Dr0930, einer PLL aus dem Organismus *Deinococcus radiodurans R1*, etabliert werden. Dr0930 und PTE haben eine ähnliche $(\beta\alpha)_8$-Barrel Faltung und besitzen Gemeinsamkeiten im Bereich des aktiven Zentrums einschließlich zweier katalytisch essentieller zweiwertiger Metallionen.

Im ersten Teil dieser Arbeit wurden die enzymkinetischen Parameter von Dr0930 aus *D. radiodurans R1* für die Hydrolyse von δ-Nonalacton bestimmt. Darüber hinaus wurde die promiskuitive Hydrolyseaktivität von Dr0930 für die OP-Insektizide Methyl-Paraoxon (MPXN) und Ethyl-Paraoxon (EPXN) sowie für die racemischen *p*-Nitrophenol (*p*-NP) Analoga der OP-Nervenkampfstoffe VX, Sarin (GB), VR, Soman (GD) und Cyclosarin (GF) gemessen. Die katalytischen Effizienzen für das wildtypische Co/Co-Dr0930 Protein liegen im Bereich zwischen 2,1 $M^{-1}s^{-1}$ und 6,1 × 10^2 $M^{-1}s^{-1}$. Damit sind sie um vier (GD *p*-NP) bis sieben (GB *p*-NP und EPXN) Größenordnungen niedriger als die katalytischen Effizienzen von wildtypischem Co/Co-PTE. Umgekehrt zeigt wildtypisches PTE promiskuitive Aktivität für die Hydrolyse von δ-Nonalacton mit einem k_{cat}/K_M von 6.8 × 10^1 $M^{-1}s^{-1}$.

Die schwache promiskuitive OP-Hydrolyseaktivität von Dr0930 wurde in einem iterativen Prozess schrittweise gesteigert, wobei sowohl rationales Design als auch eine Kombination aus Zufallsmutagenese und *in vitro* Aktivitätsscreening verwendet wurden. Dabei wurde die Fähigkeit der erzeugten Mutanten zur Hydrolyse von EPXN und sechs weiterer OP-Verbindungen getestet. Die in den einzelnen Schritten identifizierten vorteilhaften Mutationen wurden in der Variante Dr0930_134 kombiniert. Diese enthält 7 Austausche (Y28L+D71N+Y97F+E101G+E179D+V235L +P274L), die im Vergleich zum wildtypischen Dr0930 zu einer Erhöhung der OP-hydrolytischen Aktivität für GB *p*-NP, VR *p*-NP und GF *p*-NP um vier Größenordnungen führen. Die Absolutwerte für die katalytischen Effizienzen erreichen Werte von bis zu 10^5 $M^{-1}s^{-1}$. Die Hydrolyse von GD *p*-NP durch Dr0930_134 erfolgt mit einem k_{cat}/K_M Wert von 10^4 $M^{-1}s^{-1}$, was im Bereich der katalytischen Effizienz von wildtypischem PTE für dieses Substrat liegt.

Die evolvierten Dr0930 Varianten wurden anschließend hinsichtlich ihrer nativen Lactonaseaktivität und bezüglich der Stereoselektivität der OP-Hydrolyse charakterisiert. Des Weiteren wurde ihre Fähigkeit überprüft, neben P-O Bindungen auch P-S Bindungen zu hydrolysieren. Die Ergebnisse zeigen, dass die beachtliche Verbesserung der promiskuitiven OP-Hydrolyseaktivität von einem vergleichbar starken Verlust der nativen Aktivität begleitet wird. Dennoch erreicht Dr0930_134 immer noch eine katalytische Effizienz von 2.8×10^3 $M^{-1}s^{-1}$ für die Hydrolyse von δ-Nonalacton. Die verbesserte OP-Hydrolyseaktivität von Dr0930_134 geht einher mit einer gesteigerten Stereoselektivität für das weniger giftige R_P-Enantiomer der chiralen OP-Substrate. Die Verschiebung der enantiomeren Präferenz [Verhältnis k_{cat}/K_M (R_P) / k_{cat}/K_M (S_P)] lag für VR *p*-NP im Bereich von 4.3×10^2. Die höchste absolute enantiomere Präferenz beträgt 1.5×10^4 und wird für GB *p*-NP beobachtet. Die evolvierten Dr0930 Varianten wurden ebenfalls hinsichtlich der Fähigkeit zur Hydrolyse von Phosphorothiolat DEVX (Diethyl-VX), einem Analogon des Nervengases VX, getestet. Trotz der effizienten Hydrolyse von P-O Bindungen, lag der k_{cat}/K_M-Wert für die Hydrolyse der P-S Bindung von DEVX bei nur etwa 1 $M^{-1}s^{-1}$.

Zur Erklärung der hohen OP-Hydrolyseaktivität der evolvierten Dr0930 Varianten wurden Strukturanalysen und Dockingstudien mit Liganden durchgeführt. Drei Dr0930 Varianten, einschließlich Dr0930_134, wurden kristallisiert und die Röntgenstrukturen wurden mit einer Auflösung von 1,8 - 2,1 Å aufgeklärt. Die Varianten zeigen nur kleine strukturelle Änderungen im Vergleich zum wildtypischen

Dr0930 Protein. Das aktive Zentrum der Varianten wurde durch die Austausche etwas vergrößert und der hydrophobe Charakter gesteigert, wodurch mehr Platz und eine günstigere Umgebung für die Bindung der OP-Substrate geschaffen wurden. Darüber hinaus wurde zusätzliche Flexibilität durch die Eliminierung einer Wasserstoffbrückenbindung zwischen Resten der $\beta\alpha$-loops 2 und 3 gewonnen. Um die Orientierung von EPXN im aktiven Zentrum von Dr0930_134 zu identifizieren, wurde das Substrat mit Hilfe des RosettaLigand Programms in das aktive Zentrum modelliert. Die besten Posen waren ähnlich zu den EPXN-Posen, die beim Docking von EPXN in das aktive Zentrum der PTE erhalten wurden. Zudem erklären die Ergebnisse die wichtige Rolle der Reste F26 und R228 für die OP-Hydrolyse, welche auf der Basis von gerichteter Mutagenese postuliert wurde.

Zusammengefasst zeigen die Ergebnisse dieser Arbeit, dass es durch Evolution im Labor möglich ist, hohe OP-Hydrolyseaktivität auf dem Gerüst von Dr0930 zu etablieren, was einen starken Hinweis auf die postulierte natürliche Evolution von PTE aus Mitgliedern der PLL Familie liefert.

1 INTRODUCTION

1.1 Enzyme promiscuity

Enzymes are exceptional catalysts that facilitate a wide variety of reactions under mild conditions, achieving high rate enhancements with excellent chemo-, regio- and stereoselectivities (Seelig & Szostak, 2007). The structural and functional diversity of enzymes has been generated by molecular evolution over billions of years (Todd *et al.*, 2001). Three mechanisms of molecular evolution have been described by which the slow step of *ab initio* gene creation can be circumvented: Horizontal gene transfer (HGT), gene duplication, and gene recombination (Jain *et al.*, 2003; Chothia *et al.*, 2003). In the past decades several examples of rapid and efficient molecular evolution of new enzymatic functions have been revealed that provide enzymes which degrade synthetic chemicals introduced to the biosystem during the last decades (Copley, 2009; Raushel & Holden, 2000; Janssen *et al.*, 2005; Shapir *et al.*, 2007), enzymes associated with drug resistance (Hall, 2004; Wang *et al.*, 2002; Weinreich *et al.*, 2006), and enzymes in plant secondary metabolism (O'Maille *et al.*, 2008; Austin *et al.*, 2008; Field & Osbourn, 2008; Khersonsky & Tawfik, 2010). It is plausible to assume that the recruitment of existing metabolic capabilities is responsible for such phenomena (Ochman *et al.*, 2000; Jain *et al.*, 2003; Chothia *et al.*, 2003).

For example, promiscuous activities (weak secondary or side activities) serve as evolutionary starting points for the divergence of new functions, and broad-specificity enzymes served as progenitors for todays specialized enzymes (Jensen, 1976). Two cases of promiscuity can be distinguished: catalytic promiscuity and substrate ambiguity (Patrick & Matsumura, 2008; O'Brien & Herschlag, 1999; Khersonsky *et al.*, 2011). For most cases, divergence of new enzyme functions is driven by substrate ambiguity, as key catalytic residues and reaction intermediates of transition states tend to be conserved throughout enzyme families and even highly diverse superfamilies (Gerlt & Babbitt, 1998). Mechanistically, promiscuity is often enabled by conformational flexibility as conformational changes enable the same enzyme to accommodate different substrates. In particular, the mobility of active site loops appears to play a key role in mediating promiscuity (Khersonsky & Tawfik, 2010; Khersonsky *et al.*, 2006). To investigate rapid, adaptive molecular evolution of

homologous enzymes in the context of promiscuous activities, organophosphate hydrolyzing enzymes are studied in this work.

1.2 Organophosphate compounds and organophosphate hydrolases (OPH)

1.2.1 Organophosphate compounds

Organophosphates (OPs) are among the most toxic compounds that have been chemically synthesized. Since the discovery of their biological activity in the 1930s, these compounds have been widely used as broad-spectrum insecticides for agricultural and domestic applications (Raushel, 2011). Moreover, OPs have been developed as chemical warfare agents (CWAs) for military use (Munro *et al.*, 1994). OPs are a large class of compounds with widely varied chemical structure. Organophosphate insecticides are primarily phosphotriesters, thiophosphotriesters, and phosphorothiolesters. OP nerve agents are chiral phosphonate compounds containing a direct P-C bond. The most noted types are the G-type (GA, GB, GD, GF) and V-type (VX, VR) nerve agents. G-type nerve agents contain either a cyanide leaving group (GA) or a fluoride leaving group (GB, GD, GF). V-type nerve agents exhibit a branched thiolate (N,N-dialkylaminoethylthiolate) leaving group, and are more toxic and persistent than G-type agents (Raushel, 2002; Bigley & Raushel, 2012; Munro *et al.*, 1994).

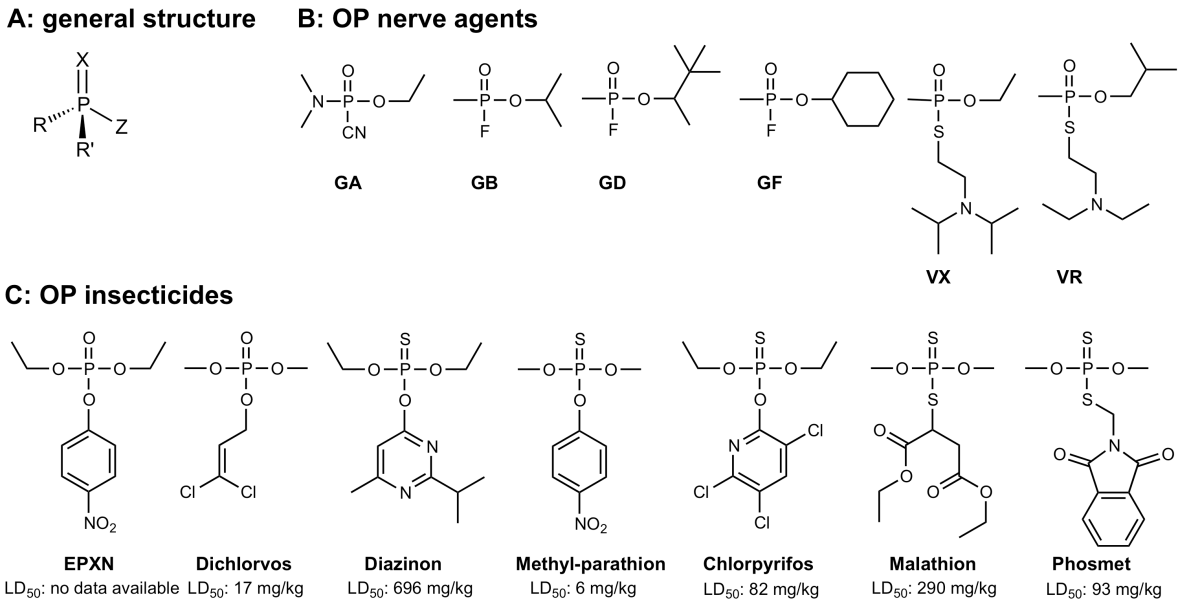

Figure 1: Structures of organophosphate compounds.

A: General structure of OP compounds. X = oxygen, sulfur; Z = halogen, aliphatic, aromatic or heterocyclic substituents; R/R' = ester linkage to an alkoxy or amino group.
B: Organophosphate nerve agents: tabun (GA, O-ethyl-(N,N-dimethyl) phosphoroamidocyanidate), sarin (GB, O-isopropyl methylphosphonofluoridate), soman (GD; O-pinacolyl methyl-phosphonofluoridate), cyclosarin (GF, O-cyclohexyl methylphosphonofluoridate), VX (O-ethyl-S-(2-diisopropyl-aminoethyl) methylphosphonothiolate) and VR (O-isobutyl-S-(2-diethylaminoethyl) methyl-phosphonothiolate).
C: Common examples for OP insecticides. Ethyl-paraoxon (EPXN) and dichlorvos are phosphotriesters. Chlorpyrifos, parathion, and diazinon are thiophosphotriester. Malathion and phosmet are phosphorotiolates. Numerous insecticides, such as malathion and phosmet, contain both a thiophosphate and thiol-ester linkage. Lethal dosage values (LD_{50}) were taken from Sigma-Aldrich MSDS (date: 1. April, 2012) and refer to oral intake in rats.

OPs are highly toxic because they rapidly inactivate the acetylcholinesterase (AChE), a key enzyme of the nervous system. AChE hydrolyzes the neurotransmitter acetylcholine at neural synapses that relays nerve pulses to mucles and other organs (Raushel, 2002). OPs react with AChE, resulting in an inactive enzyme with the nucleophilic serine residue in the active site being phosphorylated/phosphonylated. The subsequent build-up of acetylcholine blocks cholinegic nerve pulses, results in paralysis, suffocation and ultimately death (Raushel, 2011). Acute toxicity of OP nerve agents is three to four orders of magnitude greater than most of the chemically similar OP pesticides, with VX being the most potent nerve agent (Munro *et al.*, 1994). Moreover, chiral OP compounds differ greatly in their acute toxicity, with the depending on substituents and stereochemistry of the phosphorus center. The S_P isomers of GB, GD, and GF inhibit the AChE >1000-fold faster than their respective R_P isomers and can be >100-fold more toxic *in vivo* (Benschop & Dejong, 1988). Treatment with anti-cholinergic drugs is used to counteract acute OP-intoxication. Atropine, a competitive antagonist for muscarinic acetylcholine receptors, blocks the action of acetylcholine and thereby reduces the effective concentration of the neurotransmitter. It is used as an antidote, often in combination with oxime AChE reactivators such as pralidoxime. An alternative treatment is the human butyrylcholinesterase (BChE), which functions as stoichiometric catalytic scavenger for the nerve agents, as it reacts with OP in the same way as AChE (Raushel, 2011).

OP compounds are relatively easy to synthesize from readily available industrial chemicals; hence their use by international terrorist is a serious threat (Raushel, 2011; Munro *et al.*, 1994). Concerns over the health and environmental impact of OPs and their potential use for bioremediation lead to numerous efforts to identify enzymes capable of detoxifying them (Bigley & Raushel, 2010).

1.2.2 Organophosphate hydrolases (OPH)

Organophosphate hydrolyzing enzymes have been identified in archaea, bacteria and eukarya (Porzio *et al.*, 2007; Tsai *et al.*, 2010a). Common representatives of OPH enzymes are the bacterial phosphotriesterase (PTE), methyl parathion hydrolase (MPH), organophosphorus acid anhydrolase (OPAA), diisopropyl-fluorophosphatase (DFPase), and paraoxonase 1 (PON1). These enzymes are metal-dependent hydrolases that contain a hydrophobic active site. Except for DFPase and PON1, that contain – besides a structural important metal – one single catalytic metal ion, OPH enzymes contain a binuclear metal center. In any case the divalent metal(s) coordinate the substrate for catalysis and activate the phosphorus center. The mechanistic details of hydrolysis differ among OPH enzymes with both direct attack of the nucleophilic hydroxide as well as covalent catalysis being observed, as in the case of DFPase and PON1. OPH enzymes differ widely in protein sequence and three-dimensional structure. OPH adopt numerous folds: TIM-barrel fold (PTE), β-lactamase fold (MPH), pita bread fold (OPAA) and β-propeller fold (DFPase and PON1) (Bigley & Raushel, 2012; see Figure 2 for illustration). Their substrate profile for the hydrolysis of OPs varies significantly. Moreover, most OPH enzymes catalyze various other reactions, such as the hydrolysis of esters, lactones and dipeptides. Bacterial PTE is most efficient for the hydrolysis of a broad range of phosphotriesters (Dumas *et al.*, 1989), and promiscuous esterase activity has been reported (Roodveldt & Tawfik, 2005a; Afriat *et al.*, 2006). *Pseudomonas sp.* WBC-3 MPH hydrolyzes the insecticide methyl-parathion (Dong *et al.*, 2005). OPAA from *Alteromonas sp.* JD6.5, a bacterial prolidase (X-Pro), efficiently hydrolyzes G-type nerve agents (DeFrank & Cheng, 1991; Cheng *et al.*, 1997; Vyas *et al.*, 2010). *Logio vulgaris* DFPase, of which the native activity remains unclear, hydrolyzes the fluoride containing diisopropylfluorophosphat (DFP), as well as the G-type nerve agents (Hartleib & Rüterjans, 2001; Blum *et al.*, 2006). The mammalian serum PON1, a native lactonase, exhibits broad substrate specificity, hydrolyzing various γ- and δ-lactones, aryl-esters, and a broad variety of OPs (Khersonsky & Tawfik, 2005). PON1 is thought to function as a lactonase by inactivating toxic byproducts of lipid oxidation as part of the high-density lipoprotein (HDL) (Camps *et al.*, 2009).

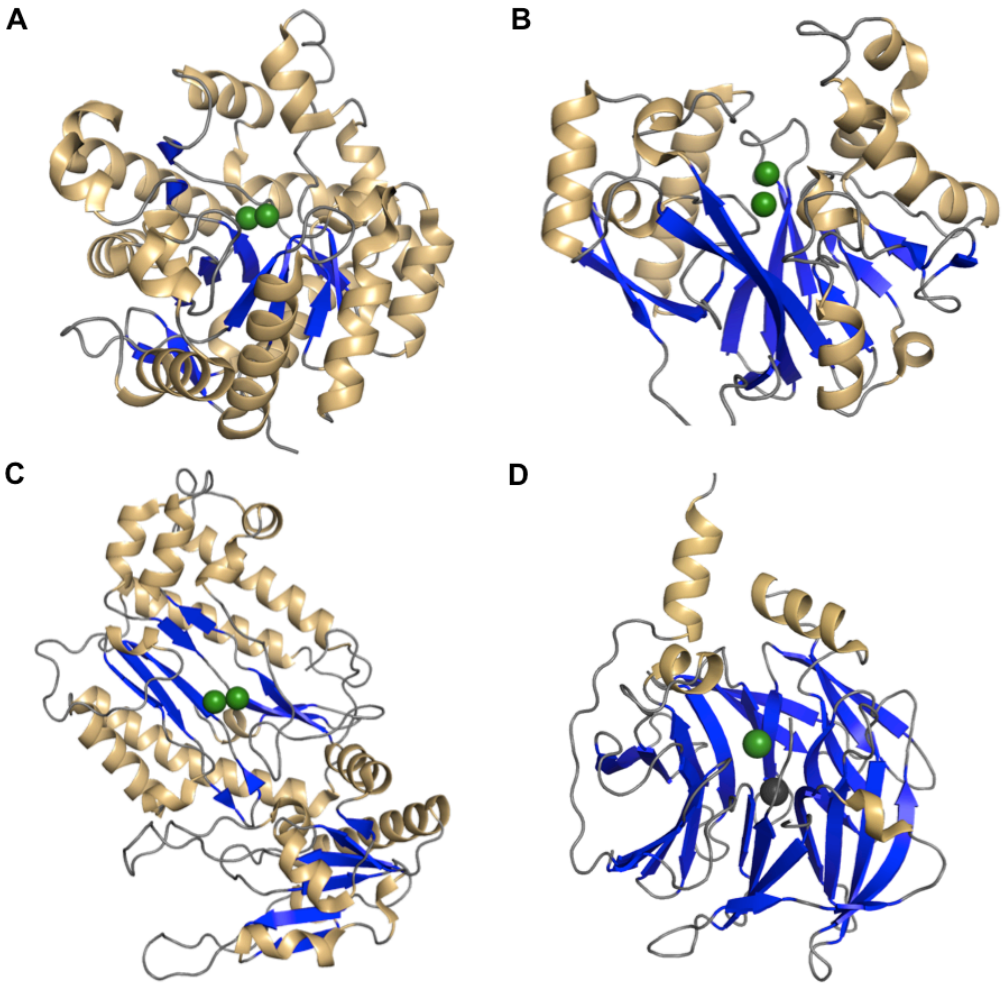

Figure 2: Three-dimensional structure of selected OPH enzymes: PTE, MPH, OPAA, and PON1. The α-helices are depicted in beige, β-strands in blue, and loops in grey. Catalytic important metal ions are depicted in green, structurally important metal ions in dark grey.
A: Bacterial phosphotriesterase (PTE) adopts a TIM-barrel fold (PDB ID 1EZ2). **B:** Methyl parathion hydrolase (MPH) adopts a αβ/βα sandwich typical of the lactamase fold (PDB ID 1P9E). **C:** Organophosphorus acid anhydrolase comprises a pita bread C-terminal domain (OPAA) (PDB ID 3L7G). **D:** Paraoxonase 1 (PON1) adopts a 6-bladed β-propeller fold containing one catalytic and one structural important calcium ion (PDB ID 1V04).

The organophosphate hydrolyzing enzyme PTE from *Pseudomonas diminuta* and enzymes homologous to PTE, adopting a $(\beta\alpha)_8$-barrel fold, are studied in this work.

1.3 The $(\beta\alpha)_8$-barrel-fold

The $(\beta\alpha)_8$-barrel structure was first found in the triosephosphate isomerase (TIM) from *Gallus gallus* (Banner *et al.*, 1975), and is therefore also known as TIM-barrel. The $(\beta\alpha)_8$-barrel fold is the most common enzyme fold: about 10% of all proteins with known three-dimensional structure contain at least one TIM-barrel domain (Sterner & Höcker, 2005). The current SCOP-database (Structural Classification of

Proteins, Version 1.75, latest update June 2009, Murzin *et al.*, 1995) lists 33 homologous superfamilies with this topology. With few notable exceptions, such as the storage proteins narbonin (Henning *et al.*, 1992, 1995) and concavalin B (Henning *et al.*, 1995), all known $(\beta\alpha)_8$-barrels are enzymes.

The canonical $(\beta\alpha)_8$-barrel contains at least 200 amino acids and is composed of eight units, each of which consists of a β-strand and an α-helix (Sterner & Höcker, 2005). Within a unit, the C-terminus of a β-strand is linked to the N-terminus of the α-helix by a βα-loop. The individual units are linked by αβ-loops, which connect the C-terminus of α-helix I with the N-terminus of β-strand I+1. The resulting βα-super-secondary structure is shown in Figure 3A. In the tertiary structure the eight β-stands form a central parallel β-sheet, which is surrounded by the eight amphipathic α-helices (Figure 3B). Their hydrophilic faces are exposed to the solvent, whereas the hydrophobic faces interact with the β-strands.

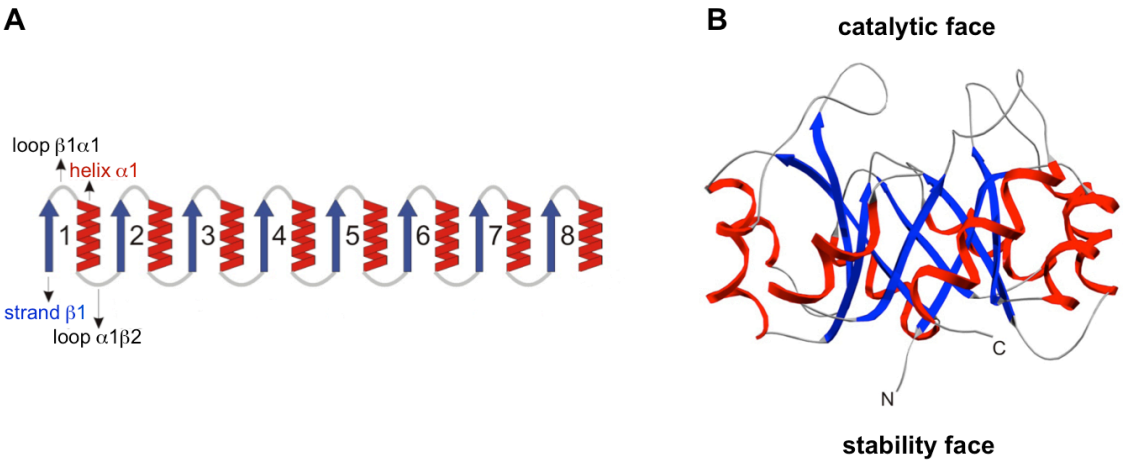

Figure 3: The $(\beta\alpha)_8$-barrel fold.
A: Topologic depiction of the right-handed βα-super-secondary structure consisting of eight (βα)-units. β-strands and α-helices are depicted in blue and red, respectively; the connecting loops are depicted in grey. **B**: Side-view of a canonical $(\beta\alpha)_8$-barrel protein, with the central eight-stranded parallel β-sheet (the barrel) surrounded by the eight α-helices. The active site is formed by residues at the C-terminal ends of the β-strands and the βα-loops (catalytic face). The remainder of the fold, including the opposite face of the barrel with the αβ-loops, is important for conformational stability (stability face). The figure was taken from Sterner & Höcker (2005).

In all known $(\beta\alpha)_8$-barrel enzymes, the active site residues are located at the C-terminal ends of the β-strands and in the βα-loops (catalytic face), while residues maintaining the stability of the fold are found in the core and on the opposite end of the barrel, which includes the αβ-loops (stability face). In general, αβ-loops are less flexible and shorter than βα-loops (Höcker *et al.*, 2001). This arrangement gives the

functional groups structural independence, making it possible to change catalytic activities without compromising stability. Therefore, $(\beta\alpha)_8$-barrels are considered to be ideal tools for the study of enzyme evolution and the design of new catalytic activities (Sterner & Höcker, 2005; Höcker, 2005).

The $(\beta\alpha)_8$-barrel proteins cover all EC-classes, except ligases; the hydrolases are the dominating class, comprising about half of the known TIM-barrels. The broad distribution indicates that the $(\beta\alpha)_8$-barrel is, together with the P-loop-containing nucleoside triphosphate hydrolase fold and the DNA/RNA-binding three-helical bundle fold, one of the most ancestral folds (Caento-Anollés *et al.*, 2007). Approximately one half of the characterized $(\beta\alpha)_8$-barrel enzymes require divalent metal ions for catalysis. A very common active site motif is the phosphate binding site, as about two-thirds of the $(\beta\alpha)_8$-barrels have substrates or cofactors with at least one phosphate group (Nagano *et al.*, 2002).

Besides TIM, whose reaction rate is diffusion controlled (Knowles, 1991), one of the best known representatives of $(\beta\alpha)_8$-barrel enzymes is OMP-decarboxylase, which accelerates its reaction by a factor of 10^{17} and is therefore the most proficient biocatalyst known (Radzicka & Wolfenden, 1995). Another important $(\beta\alpha)_8$-barrel is ribulose-1,5-bisphosphate-carboxylase (RuBisCo), which is the most abundant enzyme in the biosphere (Cooper, 2000).

1.4 The amidohydrolase superfamily (AHS)

The amidohydrolase superfamily (AHS) was identified on the basis of structural and mechanistic similarities among adenosine deaminase (ADA), phosphotriesterase (PTE), and urease (URE) (Holm & Sander, 1997). The number of documented members within this enzyme group exceeds 23,000 (Hobbs *et al.*, 2012). To date more than 30 different chemical reactions are catalyzed by known members of this superfamily, including the hydrolysis of esters and amide bonds, the deamination of nucleic acids, the hydration of double bonds, aldose/ketose isomerizations, and decarboxylations (Xiang *et al.*, 2010). AHS members have been identified in every organism sequenced to date (Nguyen *et al.*, 2008). The broad spectrum of substrates and reaction characteristics of the diverse amidohydrolase superfamily (Seibert & Raushel, 2005; Roodveldt & Tawfik, 2005b) suggests that the active site is amenable to the efficient evolution of new substrate profiles (Xiang *et al.*, 2009).

The enzymes of the mechanistically diverse AHS (Gerlt & Babbitt, 2001) adopt a distorted $(\beta\alpha)_8$-barrel fold. Almost all structurally characterized superfamily members possess a mono- or binuclear metal center within the active site. For most of the AHS, the metal center functions to activate a water molecule for the nucleophilic attack, activates the scissile bond of the substrate for bond cleavage, and stabilizes the tetrahedral or trigonal bipyramidal transition state. The two metal ions are designated as α and β. The divalent cations are predominately bridged by a carbamate functional group of a post-translationally modified lysine residue from β-strand 4, or less often by the carboxyl functional group of glutamate from β-strand 3 or 4. The α-metal is mostly buried in the structure, whereas the β-metal is more solvent exposed. In the binuclear metal centers, the hydrolytic water molecule is activated for nucleophilic attack by interaction with the α-metal ion while the carbonyl and phosphoryl groups of the substrate are polarized through Lewis acid catalysis via complexation with the β-metal ion. In the mononuclear metal centers, the substrate is activated by proton transfer from the active site, and the water is activated by metal ligation and general base catalysis (Seibert & Raushel, 2005). The amidohydrolase superfamily members have been divided into eight subtypes, according to the complexation of their metal ions (Table 1). The most common metal center is subtype I.

Table 1: Metal complexation in eight subtypes of the AHS.

		β-strands							
subtype	**metals**	**1**	**2**	**3**	**4**	**5**	**6**	**7**	**8**
I	α, β	H-X-H			K	H	H		D
II	α, β	H-X-H			E	H	H		D
III	α	H-X-H				H	h[b]		D
IV	β	h-x-h[a]		E		H	H		d[b]
V	β	h-x-h[a]	C			H	H		d[b]
VI	α, β	H-X-D		E		H	H		d[b]
VII	-	H-X-H				H			D
VIII	-	H-X-H			R	Y	H		D

Metal coordinating amino acids are abbreviated by the 1-letter code. The abbreviation X in the conserved H-X-H motif in β-strand 1 corresponds to a random amino acid residue. In the case of two metal ions, the α-metal ion is coordinated by two histidines from β-strand 1 and an aspartate from β-

strand 8, and the β-metal ion is coordinated by two histidines from β-strands 5 and 6. The bridging ligands originate from β-strands 3 or 4.
[a]: The residues are in the active site, but do not appear to be ligated directly to the divalent cations. The specific function of these residues is uncertain. [b]: These residues are not directly ligated to the divalent cations, but are hydrogen bonded to the hydrolytic water molecule.
Prominent representatives of the subtypes: subtype I: phosphotriesterase (PTE), dihydroorotase (DHO), isoaspartyl dipeptidas (IAD), urease (URE), hydantoinase (HYD); subtype II: PTE homology protein (PHP); subtype III: adenosine deaminase (ADA), cytosine deaminase (CDA); subtype IV: acetyl glucosamine-6-phosphate deacetylase (AGD); subtype V: D-amino acid deacetylase (DAA); subtype VI: renal dipeptidase (RDP); subtype VII: uronate isomerase (URI); subtype VIII: 2-pyrone-4,6-dicarboxylate lactonase (LigI).
LigI is a recently identified AHS member, where the divalent metal ion is not required for catalysis and active site residues differ from classical AHS members.
Data from Seibert & Raushel, 2005; Williams *et al.*, 2006; Hobbs *et al.*, 2012.

The homologous H-X-H motif at the end of β-strand 1, the histidine residues at the ends of β-strands 5 and 6, and an aspartate residue at the end of β-strand 8 are conserved throughout the AHS. The preservation of an unusual carbamate group in members of subtype I indicates divergent evolution from a common ancestor (Seibert & Raushel, 2005; Gerlt & Babbitt, 2001).

The atoms that directly ligate the metal ions within the different AHS members superimpose with a r.m.s.d. of only 0.2-0.6 Å. Moreover, the Cα-atoms of the eight β-strands of the amidohydrolase superfamily members superimpose well with a r.m.s.d. of 1.5 ± 0.3 Å. Despite these strong similarities the spectrum of substrates and reaction characteristics are remarkable versatile. This is mostly due to the βα-loops, in particular loop 7 and 8, which are most often involved in contacting the ligands in the active site and in determining the substrate specificity. These loops differ significantly between different AHS members in sequence, length and conformation (Seibert & Raushel, 2005; Roodveldt & Tawfik, 2005b).

1.5 Bacterial phosphotriesterase (PTE) and phosphotriesterase-like lactonases (PLL)

1.5.1 Bacterial phosphotriesterase (PTE)

The *opd* (organophosphate-degradation) genes were isolated from the soil bacteria *Pseudomonas diminuta* (PTE) (Munnecke, 1976), *Flavobacterium sp.* (PTE) (Sethunathan *et al.*, 1973), and *Agrobacterium radiobacter* (OpdA) (Horne *et al.*, 2003). The *opd* genes from *P. diminuta* and *Flavobacterium sp.* are identical in sequence and are both localized on extrachromosomal plasmids that comprise part of a transposable element (Raushel, 2002; Horne *et al.*, 2003; Siddavattam *et al.*,

2003). The *opd* gene of PTE codes for a 365 amino acid precursor containing a N-terminal signal peptide. For expression in *E. coli* the gene was processed lacking the 29 amino acid long leader peptide (Mulbry & Karns, 1989; Omburo *et al.*, 1992). PTE and OpdA share greater than 90% sequence identity and similar activity profiles (Yang *et al.*, 2003). The ability of soil bacteria to utilize OP compounds as energy and nutrient source is thought to provide significant evolutionary advantage for the affected organisms (Siddavattam *et al.*, 2003; Bigely & Raushel, 2010).

PTE hydrolyzes a wide range of synthetic organophosphate compounds, catalyzing the cleavage of P-O, P-F, and P-S bonds in a variety of insecticides and organophosphate nerve agents (Dumas *et al.*, 1989). The substrate specificity of PTE is relatively broad, and the rate of hydrolysis is very much dependent on the pK_a of the leaving group (Hong & Raushel, 1996). A natural substrate for PTE remains unknown. However, the purified enzyme exhibits a remarkably catalytic activity towards the hydrolysis of the commercial insecticide paraoxon. The kinetic constants k_{cat} and k_{cat}/K_M of the cobalt-substituted PTE for paraoxon are $4.9 \times 10^3\ s^{-1}$ and $3.8 \times 10^7\ M^{-1}s^{-1}$, respectively. The rate enhancement by this enzyme approaches 10^{12} (Dumas *et al.*, 1989; Omburo *et al.*, 1992). The high k_{cat}/K_M value for PTE-catalyzed paraoxon hydrolysis is close to the bimolecular rate constant for diffusion-controlled encounter of enzyme and substrate (10^8-$10^9\ M^{-1}s^{-1}$; Fersht, 1985). The synthesis of paraoxon was first reported in the 1950s (Schrader, 1950), suggesting that the phosphotriesterase activity has evolved in bacteria specifically to this high level of catalytic activity over the past several decades from an enzyme with a related catalytic function (Raushel & Holden, 2000). Besides the efficient hydrolysis of OPs, promiscuous esterase activity has been reported for wild-type PTE and esterase and lactonase activities for an engineered PTE variant with elevated expression level (Roodveldt & Tawfik, 2005a/b; Afriat *et al.*, 2006).

The quaternary structure of PTE is dimeric, and the protomers adopt a distorted $(\beta\alpha)_8$-barrel fold with two antiparallel β-strands at the N-terminus (Benning *et al.*, 1994). PTE belongs to subtype I of the amidohydrolase superfamily (Seibert & Raushel, 2005). The binuclear metal center at the C-terminal end of the barrel (Benning *et al.*, 1995) can be assembled in an active configuration with transition metal ions, such as Co^{2+}, Ni^{2+}, Cd^{2+}, Zn^{2+} or Mn^{2+}. The most active isozyme is the Co^{2+}-substituted PTE (Omburo *et al.*, 1992). High-resolution X-ray structures of different metal-substituted forms (Zn/Zn, Zn/Cd, Cd/Cd, and Mn/Mn) of PTE from

P. diminuta showed that the two metal ions are separated by 3.5–3.7 Å and are bridged by a post-translationally carboxylated lysine (Lys169) from β-strand 4 and a hydroxide. The α-metal is more buried and coordinated by His55 (β-strand 1), His57 (β-strand 1), and Asp301 (β-strand 8) in a trigonal bipyramidal ligation sphere. The more solvent exposed β-metal is coordinated by His201 (β-strand 5), His230 (β-strand 6) and water molecules. The observed coordination spheres are either octahedral (in the Cd^{2+}/Cd^{2+}, Mn^{2+}/Mn^{2+}, and the mixed Zn^{2+}/Cd^{2+} species) or trigonal bipyramidal (in the Zn^{2+}/Zn^{2+} species) (Benning *et al.*, 2001). The structure of the binuclear metal center in PTE is identical to the ones found in urease (Jabri *et al.*, 1995) and dihydroorotase (Thoden *et al.*, 2001). A representation of the binuclear metal center for Zn^{2+}/Zn^{2+}-substituted PTE with bound substrate analogue is depicted in Figure 4.

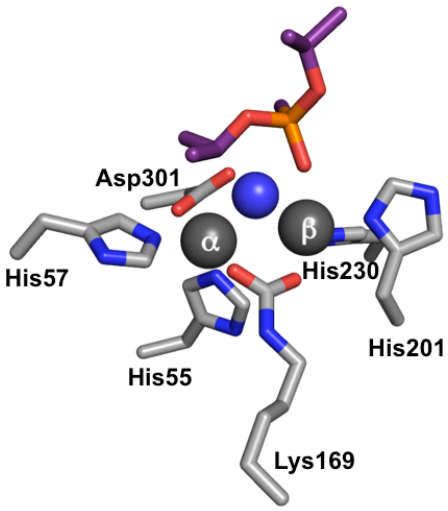

Figure 4: Active site region and coordination geometry of Zn^{2+}/Zn^{2+}-substituted PTE (PDB ID 1EZ2) with bound diisopropyl methylphosphonate inhibitor.
The α and β zinc ions are depicted as dark grey spheres, while the bridging hydroxide is depicted as dark blue sphere. The amino acid side chains are colored by element (C: grey; N: blue; O: red). The side chain of Lys169 carries a post-translational carboxylation. The substrate analog, diisopropyl methylphosphonate (DIMP), is shown in purple and colored by element (C: purple; P: orange; O: red).

Kinetic studies with enantiomeric phosphotriesters showed that wild-type PTE stereoselectively hydrolyzes chiral organophosphate triesters with a general preference for S_P-enantiomers over R_P-enantiomers by up to 90-fold with the stereochemical selectivity increasing with the difference in size between side groups (Hong & Raushel, 1999; Chen-Goodspeed *et al.*, 2001a). The same pattern has been observed for phosphonate compounds; however, due to a reversal of priority of the groups the corresponding preferred chirality is R_P (Bigley & Raushel, 2012; Tsai *et al.*, 2010a). The X-ray structure of *P. diminuta* PTE with bound substrate analogue,

diethyl 4-methylbenzylphosphonate (Vanhooke *et al.*, 1996), revealed the locations of three hydrophobic binding pockets. These pockets have been labeled as large, small, and leaving group subsites, and it has been shown that the stereospecificity of the enzyme is dictated by the size of these pockets (Chen-Goodspeed *et al.*, 2001a). Furthermore, the inherent stereoselectivity of the wild-type enzyme can be enhanced, relaxed or reversed by simultaneous alterations of the three subsites (Chen-Goodspeed *et al.*, 2001b; Tsai *et al.*, 2010a).

The reaction mechanism for the hydrolysis of phosphotriesters by PTE has been discussed controversially (Aubert *et al.*, 2004; Chen *et al.*, 2007; Wong *et al.*, 2007; Jackson *et al.*, 2008; Zhang *et al.*, 2009). Figure 5 presents a slightly modified reaction mechanism compared to the one originally proposed by Aubert *et al.* (2004), which is experimentally supported by various methods, including labeling studies (Lewis *et al.*, 1988) and various kinetic methods (Omburo *et al.*, 1992; Hong & Raushel, 1996), EPR (electron paramagnetic resonance) spectroscopy measurements (Samples *et al.*, 2007) and several X-ray structures with bound substrate analogues, a hydrolysis product, and a product analogue (Aubert *et al.*, 2004; Kim *et al.*, 2008). Furthermore, recent DFT (density functional theory) calculations by Chen *et al.* (2007) and quantum mechanical/molecular mechanical (QM/MM) simulations by Zhang *et al.* (2009) are in support of this mechanism.

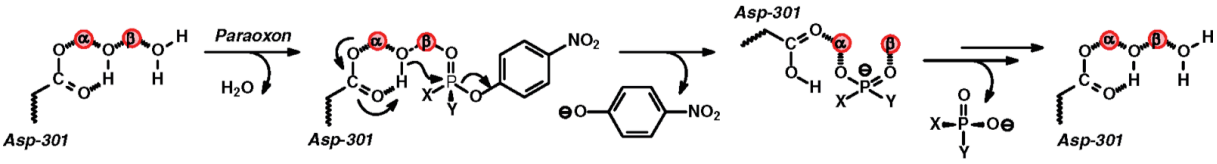

Figure 5: A plausible reaction mechanism of PTE for the hydrolysis of phosphotriesters, using paraoxon as an example.
Paraoxon binds to the β-metal ion by replacing a water molecule. The metal bridging hydroxide attacks the phosphorus center in the substrate in an S_N2-like reaction. The P-O bond breaks, *p*-nitrophenol is released, and the proton is transferred to aspartate 301. The hydrolysis product, diethyl phosphate, dissociates from the metal center (metal ions depicted in red), and the binuclear metal center is regenerated for another round of catalysis. The figure was taken from Kim *et al.* (2008).

According to this mechanism, the organophosphate substrate binds to the active site with the displacement of a water molecule from the β-metal ion. The interaction of the substrate with the β-metal ion weakens the coordination of the bridging hydroxide to the β-metal ion and facilitates the nucleophilic attack of the hydroxide in an S_N2-like reaction on the phosphorus center of the substrate. The bond to the

leaving group phenol is broken, and the single proton from the nucleophilic hydroxide is transferred to aspartate 301. The anionic diethyl phosphate is bound within the active site as a bridging ligand between the two divalent cations. The diethyl phosphate dissociates from the active site, and the binuclear metal center is subsequently recharged for another round of catalysis (Kim *et al.*, 2008).

1.5.2 Dr0930: a phosphotriesterase-like lactonase (PLL)

Genes similar to *opd* were also identified in bacteria and archaea. Representatives are from *Sulfolobus solfataricus* (SsoPox), *Sulfolobus acidocaldarius* (SacPox), *Deinococcus radiodurans* (Dr0930), *Rhodococcus erythropolis* (Ahla), *Mycobacterium tuberculosis* (PPH) and *Geobacillus kaustophilus* (GKL). These proteins are termed PLL enzymes, as they are the closest homologues to PTE, although they are only distantly related, sharing 26-35% sequence identity with *P. diminuta* PTE (Merone *et al.*, 2005; Porzio *et al.*, 2007; Afriat *et al.*, 2006). PLL's main activity is for the hydrolysis of various lactones. Most members hydrolyze quorum-sensing (QS) N-acylhomoserine (HSL) lactones, other members hydrolyze γ- and δ-lactones (Afriat *et al.*, 2006; Elias *et al.*, 2008; Elias & Tawfik, 2012). Quorum-sensing is an integral part of microbial interaction and is responsible for virulence or pathogenicity of diseases-causing bacteria (Camilli & Bassler, 2006). Importantly, most PLL members exhibit promiscuous OPH activity (Afriat *et al.*, 2006; Buchbinder *et al.*, 1998).

A close homologue of *P. diminuta* PTE with reported OPH activity is the well-characterized bacterial PLL enzyme Dr0930 from *D. radiodurans* (31% sequence identity). Dr0930 is a robust and thermostable enzyme, with reported promiscuous activity for phosphotriesters (Hawwa *et al.*, 2009b; Xiang *et al.*, 2009). Computational docking of high-energy intermediates of the KEGG database predicted potential lactones as native substrates for the enzyme. Kinetic characterization confirmed this functional assignment, showing that Dr0930 hydrolyzes γ- and δ-lactones with alkyl substitutions at the carbon adjacent to the ring oxygen. The kinetic constants k_{cat} and k_{cat}/K_M of the cobalt-substituted Dr0930 for the best substrate (known to date), δ-nonanoic lactone, are 180 s^{-1} and 1.8×10^6 $M^{-1}s^{-1}$, respectively. No activity for the hydrolysis of N-acyl derivatives of homoserine lactone was detected (Xiang *et al.*, 2009).

The quaternary structure is dimeric, and Dr0930 is a metal-dependent $(\beta\alpha)_8$-barrel enzyme belonging to the AHS. Dr0930 and PTE share high similarities in their overall fold, key sequence and active site features. Major differences are in length and conformation of the βα-loops, in particular 1, 3, 7 and 8. Dr0930 contains the additional β-metal coordinating active site residue Y97 which is conserved within the PLL family. The active site of Dr0930 is shown in Figure 6. The metal ions are complexed by conserved residues and bridged by a carboxylated lysine (Lys143) from β-strand 4 and a hydroxide ion. The α-metal is coordinated by His21 (β-strand 1), His23 (β-strand 1) and Asp264 (β-strand 8), whereas the β-metal ion is coordinated by the side chains of His176 (β-strand 5), His204 (β-strand 6), and Tyr97 (βα-loop 3) (Xiang *et al.*, 2009; Hawwa *et al.*, 2009b).

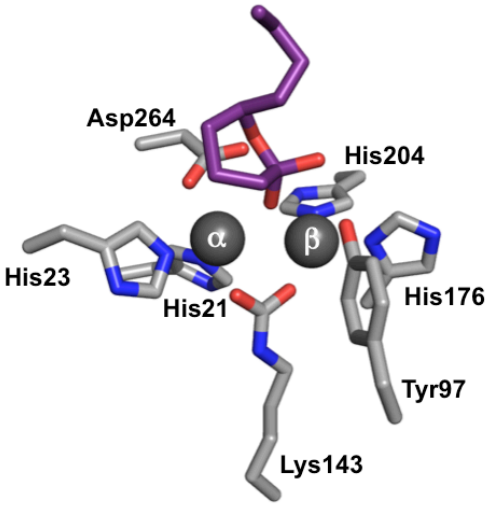

Figure 6: Active site region and coordination geometry of the Zn^{2+}/Zn^{2+}-substituted Dr0930 (PDB ID 3FDK) with the docked high-energy intermediate of δ-nonanoic lactone hydrolysis.
The α and β zinc ions are depicted as dark grey spheres. The amino acid side chains are colored by element (C: grey; N: blue; O: red). The side chain of Lys143 carries a post-translational carboxylation. The residue conserved among PLLs in the βα-loop at the C-terminal ends of the third β-strand, Y97, is shown. The PDB of the docked high-energy intermediate was kindly provided by Dr. P. Kolb, University of Marburg (from Xiang *et al.*, 2009) and is shown in purple and colored by element (C: purple; O: red).

In the catalytic mechanism proposed for Dr0930 the carbonyl oxygen of the lactone ring is polarized by interaction with the β-metal ion. In simple lactones, such as δ-nonanoic lactone, the *si* face of the lactone ring would be orientated toward the bridging hydroxide. Nucleophilic attack by the bridging hydroxide on the sp^2 carbonyl carbon of the lactone initiates the formation of a tetrahedral intermediate and the proton is transferred from the hydroxide to the active site aspartate. The intermediate would collapse with subsequent transfer of the proton to the leaving group alcohol

(Xiang *et al.*, 2009). The reaction mechanism proposed by analogy to the reaction mechanism for the OP hydrolysis of PTE is illustrated in Figure 7.

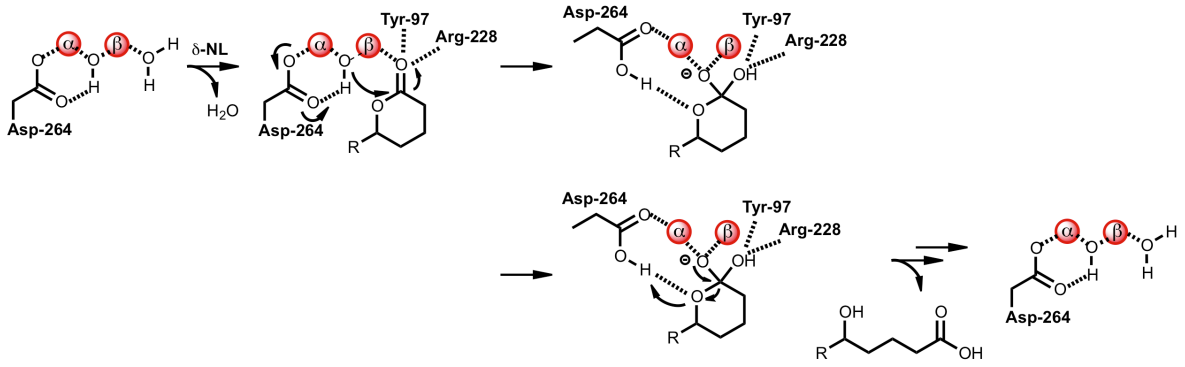

Figure 7: A proposed reaction mechanism of Dr0930 for the hydrolysis of lactones, using δ-nonanoic lactone as an example.
δ-nonanoic lactone binds to the β-metal ion by replacing a water molecule. The metal bridging hydroxide attacks the carbon center in the substrate in an S_N2-like reaction forming a tetrahedral intermediate, which is presumably stabilized by electrostatic interaction with Y97 and R228. The C-O bond breaks and the proton is transferred to aspartate 264. The proton is transferred to the leaving group alcohol and the hydrolysis product, 5-hydroxy nonanoic acid, dissociates from the metal center (metal ions depicted in red). The binuclear metal center is regenerated for another round of catalysis. R: n-butyl substituent.

PLL members exhibit promiscuous OPH activity, which is thought to be due to physical similarities between the reactive intermediate for the native lactonase reaction and the ground/intermediate state for the promiscuous OPH reaction (Elias *et al.*, 2008). The mutually identified OPH and esterase (and lactonase) activity in wild-type PTE (and an engineered PTE variant) and PLL enzymes, support that PTE, which degrades synthetic organophosphates, evolved rapidly within the last several decades from a PLL enzyme by gene duplication and diversification. The promiscuous OPH activity of the PLL enzymes potentially served as an essential starting point for its evolution (Dumas *et al.*, 1989; Raushel & Holden, 2000; Roodveldt & Tawfik, 2005a/b; Afriat *et al.*, 2006).

1.6 Enzyme design: Rational design versus directed evolution

Rational design and directed evolution are the two approaches to generate enzymes with novel functions, enhanced activity, altered substrate specificity or stereoselectivity (Arnold, 2001; Bornscheuer & Pohl, 2001; Chen, 2001; Bloom *et al.*, 2005).

1.6.1 Rational design

Using rational design, which requires a detailed knowledge of the structure and the catalytic mechanism, new enzymatic activities could be established or altered on a pre-existing protein scaffold (Woycechowsky *et al.*, 2007; Toscano *et al.*, 2007). Most challenging is the *de novo* design of enzymes with activities not found in natural biocatalysts. Besides structural information, the critical catalytic residues have to be identified, and an optimized active site has to be generated in the host protein to stabilize the geometry of the transition state. Computational design was used to establish ester hydrolysis on the thioredoxin-scaffold (Bolon & Mayo, 2001). Baker and co-workers are using the molecular modeling program Rosetta (Kuhlman & Baker, 2000; Zanghellini *et al.*, 2006) in a comprehensive approach: a library of scaffolds are tested to fit the transition state model, and a series of top ranked designs are synthesized, expressed and characterized. In this way, several novel enzymes that catalyze a variety of reactions were designed, including the non-natural retro-aldol and Kemp-elimination reactions (Jiang *et al.*, 2008; Röthlisberger *et al.*, 2008), a stereoselective intermolecular Diels-Alder cycloaddition (Siegel *et al.*, 2010), and most recently they computationally redesigned a mononuclear zinc metalloenzyme for organophosphate hydrolysis (Khare *et al.*, 2012). Although the work reported demonstrates the feasibility of computational enzyme design, the catalytic efficiencies of the generated artificial enzymes are much lower than those evolved by nature (Sterner *et al.*, 2008).

1.6.2 Directed evolution

In contrast to rational design, directed evolution does not require structural and mechanistic information to achieve significant improvements. In this approach random mutagenesis is used to create large enzyme repertoires, from which optimized variants are isolated using either selection or high-throughput (HT) screening techniques (Bloom *et al.*, 2005). Besides classical random mutagenesis by error-prone PCR (epPCR; Cadwell & Joyce, 1994), other methods such as DNA-shuffling (Stemmer, 1994), StEP (Staggered Extension Process; Zhao *et al.*, 1998) or ITCHY (Incremental Truncation for the Creation of Hybrid Proteins; Ostermeier *et al.*, 1999) have been developed and successfully applied. Using directed evolution, enzyme functions could be newly established and altered: By applying messenger

RNA display, Seelig & Szostak (2007) generated a RNA ligase enzyme with a rate enhancement of more than two-million-fold without mechanistic information. Through extensive sequence changes, including the deletion and insertion of several structural loops in the active site and subsequent directed evolution, Park *et al*. (2006) converted a member of the $\alpha\beta/\alpha\beta$ metallohydrolase superfamily (glyoxalase II) into a new family member with a different catalytic function (degradation of a β-lactam antibiotic). Sterner and co-workers established a sugar isomerization reaction on a natural and an artificial $(\beta\alpha)_8$-barrel scaffold, where the best variants showed substrate affinities and turnover numbers similar to those of wild-type enzymes catalyzing the same reaction (Claren *et al.*, 2009). Savile *et al.* (2010) used structure-based rational design and directed evolution to redesign the substrate specificity and stability of a native transaminase to replace a rhodium-based hydrogenation catalyst in the production of an antidiabetes compound sitagliptin. Recently, Tawfik and co-workers used a combination of random and targeted mutagenesis in combination with a high-throughput fluorescence-activated cell sorting (FACS) based screen to enhance the catalytic efficiency of the mammalian paraoxonase PON1 for the fluorogenic analog of S_P-cyclosarin, yielding catalytic efficiencies that approach 10^5 $M^{-1}s^{-1}$ (Gupta *et al.*, 2011).

Currently, the combination of rational design based on computational methods with the combinatorial diversity generated by directed evolution appears to be the most efficient strategy for the design of tailored enzymes (Ward, 2008; Sterner *et al.*, 2008; Toscano *et al.*, 2007). Several examples of combined approaches are described in the literature (Wang *et al.*, 2012; Khersonsky *et al.*, 2010; Khersonsky *et al.*, 2012; Khare *et al.*, 2012).

1.7 Objectives and approach in general

PTE, which degrades synthetic organophosphates, is thought to be an evolutionary young enzyme that has evolved by rapid molecular evolution from the PLL-family, whose promiscuous OPH activity might have acted as an essential starting point for its evolution. This work is based on this assumption and intends to reconstruct in the laboratory the *bona fide* natural evolutionary pathway using the robust scaffold of Dr0930 as a starting point.

Initially, the promiscuous hydrolytic activity of wild-type Dr0930 for a broad spectrum of OPs is analyzed, and mutually the ability of wild-type PTE to hydrolyze of δ-nonanoic lactone. In the central second part, an efficient OPH enzyme is generated from Dr0930 using laboratory evolution and *in vitro* activity screening. A broad spectrum of OPs, with different phosphorus chemistry, is used to design a multi-efficient OPH. Evolved variants are characterized in terms of steady-state enzyme kinetics and crystal structure analysis. The stereoselectivity is monitored and the activity for the native reaction is analyzed to relate the trade-off between native and newly evolved activity. Ligand docking studies are performed to identify the structural basis for the altered substrate preference.

The study is directed to identify the structural determinants of the substrate specificity in the PLL family versus PTE, and in a more general sense addressed to gain a comprehensive understanding of the physical and chemical parameters that relate protein structure and substrate recognition in enzyme-catalyzed reactions.

2 MATERIALS

2.1 Instrumentation

Autoclaves:	
München 25	MMM, München
VE-40	SYSTEC GmbH, Wettenberg
TOMY SS-325	CS BIO CO, Menlo Park, USA
Balances:	
MC1	SARTORIUS, Göttingen
SI-114	DENVER INSTRUMENT, Göttingen
AB204-S	METTLER TOLEDO, Columbus, USA
Cell Densitiy Meter Ultrospec 10	GE HEALTHCARE, München
Centrifuges:	
Centrifuge 5810R	EPPENDORF, Hamburg
Centrifuge 5415D	EPPENDORF, Hamburg
Centrifuge 5415R	EPPENDORF, Hamburg
Sorvall RC 2B, 5C plus	DU PONT Instruments, Bad Homburg
with SS34/GS3-Rotor	
Avanti J-26 XP	BECKMAN COULTER, Krefeld
Chromatographic devices:	
ÄKTA basic better	GE HEALTHCARE, München
ÄKTA purifier 10	GE HEALTHCARE, München
FPLC LCC-501 plus	GE HEALTHCARE, München
Used columns:	
QSepharoseFF XK 26	GE HEALTHCARE, München
Superdex 75 pg HiLoad 16/60	GE HEALTHCARE, München
Superdex 200 pg HiLoad 26/60	GE HEALTHCARE, München
Computer	
Dell Optiplex Systems	DELL Inc., Round Rock, USA
MacBook Pro	APPLE Inc., Cupertino, USA
Electroporator	
Electroporator 2510	EPPENDORF, HAMBURG

MicroPulser™ Electroporator	BIO-RAD LABORATORIES, Hercules, USA
Freezer -80 °C	MDF-U72V, SANYO, Tokyo, Japan THERMO FISCHER SCIENTIFIC, Waltham, USA
Freezer -20 °C	LIEBHERR, Nussbaumen THERMO FISCHER SCIENTIFIC, Waltham, USA
Gas burner, Gasprofi 2SCS	WLD-TEC GmbH, Göttingen
Gel electrophoresis system:	
Agarose gel electrophoresis chamber	
Agarose electrophoresis unit	HOEFER Pharmacia Biotech, USA
GeneMate Compact Gel System	BioExpress, Kaysville, USA
SDS electrophoresis chamber	
Mighty Small II	HOEFER Pharmacia Biotech, USA
Multi Gel Caster Assembling gel apparatus	GE HEALTHCARE, München
PhastSystem™ Separation Control	GE HEALTHCARE, München
Glass pipettes and glassware	SCHOTT, Mainz FISCHER SCIENTIFIC, Schwerte NOVOGLAS, Bern, Schweiz
Heating block-Thermostat HBT-2 131	HLC, Bovenden
Incubator	BINDER GmbH, Tuttlingen CURTIN MATHESON SCIENTIFIC Inc., Houston, USA
Lyophphilizer	
Lyovac GT2	LEYBOLD-HERAEUS, Hürth
Savant SpeedVac, M SVC100H	THERMO FISCHER SCIENTIFIC, Waltham, USA
Magnetic stirrer:	
MR0, MR2000	HEIDOLPH, Kehlheim
MR1, MR3001 (heatable)	HEIDOLPH, Kehlheim
PC-351	CORNING Inc, Corning, USA

Microliter pipettes	
Research 2.5, 10, 100, 200, 1000	EPPENDORF, Hamburg
Pipetman Classic™ P2, P20, P100 P200, P1000	GILSON Inc., Middleton, USA
Microplate absorbance reader	
Infinite M200 Pro	TECAN, Austria
SpectraMax-340 plate reader	MOLECULAR DEVICES, Sunnyvale, USA
Microwave	
HMT 842C	BOSCH, Nürnberg
KENMORE 565.87086	SEARS BRANDS LLC, Hoffman Estates, USA
Multichannel pipettes, electronic	
Research pro, 8-chanels, 5-100 µl, 20-300 µl, 50-1200 µl	EPPENDORF, Hamburg
EP-M8-250, 8-chanel, 25-250 µl	RAININ, San Diego, USA
Multi-Doc-It Digital Imaging System	UVP Inc., USA
PCR-cycler:	
Mastercycler personal	EPPENDORF, Hamburg
Mastercycler gradients	EPPENDORF, Hamburg
PTC-200 Thermo Cycler	MJ RESEARCH Inc., St. Buno, Canada
Peristaltic pump, Miniplus 2	GILSON Medical Electronics, France
pH-Meter	
inolab Level1	INOLAB, Weilheim
Orion Star A214	THERMO FISCHER SCIENTIFIC, Waltham, USA
Plate shaker Rocking Platform	BIOMETRA, Göttingen
Power supply unit:	
Power Pack P25	BIOMETRA, Göttingen
Power PAC300	BIO-RAD LABORATORIES, Hercules, USA
Power Supply EPS 301	GE HEALTHCARE, München

Quartz cuvettes	
101-QS (layer thickness 10 mm)	HELLMA GmbH & Co. KG, Müllheim
105-QS (layer thickness 10 mm)	HELLMA GmbH & Co. KG, Müllheim
Retainer for deep-well plates	FISCHER SCIENTIFIC, Schwerte
Shaking incubator:	
GFL 3033	GFL, Burgwedel
Certomat H	BRAUN Biotech, Melsungen
Certomat BS-1	BRAUN Biotech, Melsungen
Series 125, sticky pad	NEW BRUNSWICK SCIENTIFIC, Enfield, USA
Milli-Q Water Purification Systems	
Milli-Q Advantage A10 Water Purification System	MILLIPORE, Eschborn
PCS Sybron Barnstead	THERMO FISCHER SCIENTIFIC, Waltham, USA
Ultrasonic system, Sonifier	
Branson Sonifier 250 D	HEINEMANN, Schwäbisch Gmünd
Branson Sonifier 102C(CE)	EMERSON ELECTRIC Co, St. Louis, USA
UV-light table	
Reprostar	CAMAG Chemie Erzeugnisse, Berlin
UV Transilluminator, Spectroline	SPECTRONICS Co., Lincoln, USA
UV-Vis spectral photometer	
Cary 100 Bio	VARIAN, Darmstadt
V650	JASCO GmbH, Groß-Umstadt
UV-Vis Biophotometer	EPPENDORF, Hamburg
Vakuum pump ME 2C	VACUUMBRAND, Wertheim
Vortex Genie 2	SCIENTIFIC IND., Bohemia, USA

2.2 Consumables

Centrifugal Filter Device	
Amicon Ultra-15 (mwco: 10 kDa)	Millipore, Bedford, USA
Deep-well plates, 96 well/2000 µl	EPPENDORF, Hamburg
	CORNING Inc., Corning, USA

Desalting columns	
Micro Bio-Spin P-30 columns	BIO-RAD LABORATORIES, Hercules, USA
NAP-25™ columns	GE HEALTHCARE, München
PD-10 desalting columns	GE HEALTHCARE, München
Dialysis tubing	
Visking, 27/32, 14 kDa	ROTH GmbH &Co, Karlsruhe
Spectra/Por, 10 kDa	SPECTRUM LABORATORIES Inc, Rancho Dominguez, USA
Disposable syringes, Omnifix® 60 ml	BRAUN Biotech, Melsungen
Electroporation cuvettes, 2 mm	PEQLAB, Erlangen
Filter paper	WHATMAN, Maidstone, England
Standard cellulose filter, grade 1	
DEAE cellulose filter, grade DE81	
Latex-gloves Sempermed	SEMPERIT Technical Products GmbH, Vienna, Austria
Membrane filter ME24 Ø47 mm; 0.2 µm	SCHLEICHER&SCHUELL, Dassel
Microtiter plates, 96 well/200 µl, flat bottom	
Vis, 96 well, flat bottom	GREINER, Nürtingen THERMO FISCHER SCIENTIFIC, Waltham, USA
Vis, 96 well, sterile, with lid	SARSTEDT, Nümbrecht
UV-Vis, 96 well, flat bottom	BD, Franklin Lakes, USA
Nitrile gloves	VWR, Leuven, Belgium
Nitrocellulose filter (Ø13 mm; Cat#: VSWP01300)	MILLIPORE, Eschborn
Parafilm „M“ Laboratory Film	PECHINEY, Plastic Packaging, Menasha, USA
Pasteur pipettes	HIRSCHMANN, Ebermannstadt
PCR-tubes 0.2 ml	PEQLAB, Erlangen
Petri dish 150/25 and 94/16	GREINER bio-one, Nürtingen
Petri dish, square 245×245×18, BioDish XL	BD, Franklin Lakes, USA
PhastGel™ consumables	GE HEALTHCARE, München
PhastGel™ Homogeneous-12.5	

PhastGel™ Buffer Strips, SDS	
Pipette tips	
10 µl, 200 µl, 1000 µl	SARSTEDT, Nümbrecht
RAININ 10 µl, 20 µl, 250 µl, 1000 µl	METTLER TOLEDO, Columbus, USA
Plastic cuvettes	
½ microcuvettes, UV-transparent	SARSTEDT, Nümbrecht
1ml cuvettes	SARSTEDT, Nümbrecht
Plastic tubes:	
15 ml, 50 ml	SARSTEDT, Nümbrecht
Falcon, 15 ml and 50 ml	BD, Franklin Lakes, USA
Reaction vessels 1.5 ml and 2 ml	ROTH, Karlsruhe
	EPPENDORF, Hamburg
Reaction vessel with screw-cap, 2 ml	SARSTEDT, Nümbrecht
Sealing tape, gas-permeable, 96 well	Brand, Wertheim
	QIAGEN, Hilden
Sepharose Fast Flow bulk media	GE HEALTHCARE, München
DEAE and Q Sepharose	
Syringe filter, pore size 0.2 µm/0.45 µm	RENNER GmbH, Daunstadt
	VWR, Leuven, Belgium

2.3 Chemicals

All chemicals used were graded p.a. and purchased from the companies listed below or synthesized by Dr. Chengfu Xu (research group of Prof. Dr. F. M. Raushel, Texas A&M University, College Station, USA).

ALFA AESAR	Karlsruhe
APPLICHEM GmbH	Darmstadt
BIO101 Inc.	Carlsbad, USA
BIO-RAD LABORATORIES	Hercules, USA
BIOZYM	Hess. Oldendorf
BODE CHEMIE	Hamburg
BOEHRINGER MANNHEIM	Mannheim
CARL ROTH GMBH & Co. KG	Karlsruhe
DIFCO	Dreieich

FLUKA	Neu-Ulm
GE HEALTHCARE	München
GERBU Biotechnik GmbH	Gailberg
GIBCO/BRL	Eggestein
MERCK	Darmstadt
MP BIOCHEMICALS	Illkirch, France
NATIONAL DIAGNOSTICS	Simerville, USA
OXOID	Wesel
RIEDEL-DE HAEN	Seelze
ROCHE DIAGNOSTICS	Mannheim
ROTH	Karlsruhe
SERVA	Heidelberg
SIGMA-ALDRICH	Deisenhofen
VWR	Leuven, Belgium

2.4 Kits

ABI PRISM® BigDye™ Terminator Cycle Sequencing Ready Reaction Kit	LIFE TECHNOLOGIES, Carlsbad, USA
Classic II Suite	QIAGEN, Hilden
Crystal Screen I+II	HAMPTON RESEACH, Aliso Viejo, USA
GeneJET™ Plasmid Miniprep Kit	MBI FERMENTAS, St.-Leon-Rot
GeneJET™ Gel Extraction Kit	MBI FERMENTAS, St.-Leon-Rot
JBScreen Classic 1+4+5+8+9	JENA BIOSCIENCE, Jena
Mutation Generation System™ Kit	FISHER SCIENTIFIC, Schwerte
Nucleobond® PC100/500 DNA-Extraction Kit	MACHEREY-NAGEL, Düren
Nucleospin® Extract II	MACHEREY-NAGEL, Düren
PEG/ION Screen 1+2	HAMPTON RESEACH, Aliso Viejo, USA
PEG RX I+II	HAMPTON RESEACH, Aliso Viejo, USA
Phusion® Site-Directed Mutagenesis Kit	FISHER SCIENTIFIC, Schwerte
QIAGEN Plasmid Maxi Kit/Midi Kit	QIAGEN, Hilden
QIAprep® Spin Miniprep Kit	QIAGEN, Hilden

QIAquick PCR Purification	QIAGEN, Hilden
Quick Ligation™ Kit	NEW ENGLAND BIOLABS, Frankfurt a. M.
Wizard I+II	EMERALD BIOSYSTEMS, Bainbridge Island, USA

2.5 Enzymes

Alkaline phosphatase (CIP)	NEW ENGLAND BIOLABS, Frankfurt a. M.
GoTaq DNA polymerase	PROMEGA, Mannheim
HyperMu™ MuA Transposase	EPICENTRE, Madison, USA
Pfu DNA polymerase	PEGLAB, Erlangen
	STRATAGENE, La Jolla, USA
Phusion® (Hot Start) High-Fidelity DNA polymerase	NEW ENGLAND BIOLABS, Frankfurt a. M.
Restriction endonucleases	NEW ENGLAND BIOLABS, Frankfurt a. M.
T4-DNA ligase	MBI FERMENTAS, St.-Leon-Rot
	NEW ENGLAND BIOLABS, Frankfurt a. M.
	ROCHE DIAGNOSTICS, Mannheim

2.6 Bacterial strains

***E. coli* 5α** (NEW ENGLAND BIOLABS, Frankfurt a. M.)

*fhu*A2 Δ*(arg*F-*lac*Z*)*U169 *pho*A *gln*V*44* Φ*80* Δ*(lac*Z*)*M15 *gyr*A96 *rec*A1 *rel*A1 *end*A1 *thi-1 hsd*R17

The *E. coli* 5α strain is an *E. coli* DH5α derivative. Due to the deletion of the *fhu*A2 gene, the ferric hydroxamate uptake receptor is lacking on the cell surface, which prevents the binding of the bacteriophage T1 to this receptor and consecutive infection of the cells. Consequently *E. coli* 5α cells are T1-phage resistant. The *E. coli* 5α is a recombination-deficient strain as the *rec*A function is deleted, which is associated with a slower cell growth.

***E. coli* Turbo** (NEW ENGLAND BIOLABS, Frankfurt a. M.)

F′ *proA*$^{+}$*B*$^{+}$ *lacI*^{q} *Δ(lacZ)M15/fhuA2 Δ(lac-proAB) glnV gal R(zgb-210::Tn10)* Tet^{s} *endA1 thi-1 Δ(hsdS-mcrB)5*

E. coli Turbo cells are like *E. coli* 5α cells T1-phage resistant. As the recA function of the strain is intact, *E. coli* Turbo cells grow faster than the *rec*A^{-} strain *E. coli* 5α. *E. coli* Turbo cells form visible colonies after 8 h incubation at 37 °C.

***E. coli* XL1 Blue MRF'** (STRATAGENE, La Jolla, USA)

Δ(*mcr*A)*183* Δ(*mcr*CB-*hsd*SMR-*mrr*)*173 end*A1 *sup*E44 *thi-1 rec*A1 *gyr*A96 *rel*A1 *lac* [F´ *pro*AB *lac*I^{q}ZΔM15 Tn*10* (Tet^{r})]

In XL1 Blue MRF' cells all restriction endonucleases known in *E. coli* K12 are inactived at genome level.

***E. coli* BL21(DE3)** (Studier & Moffat, 1986)

*hsd*S *gal* [λcl *ts*857 *cnd*1 *hsd*R17 *rac*A1 *end*A1 *gyr*A96 *thi*1 *rel*A1]

E. coli BL21(DE3) cells carry a gene for T7 RNA polymerase on their chromosome, which is used for gene expression in pET systems.

***E. coli* BL21-CodonPlus(DE3)** (STRATAGENE, La Jolla, USA)

B F^{-} *ompT hsdS*($r_B^- m_B^-$) *dcm*$^{+}$ Tet^{r} *gal* λ(DE3) *end*A Hte

- RP-strain: [*arg*U *pro*L Cam^{r}]
- RIL-strain: [*arg*U *ile*Y *leu*W Cam^{r}]
- RIPL-strain: [*arg*U *pro*L Cam^{r}] [*arg*U *ile*Y *leu*W Strep/Spec^{r}]

BL21-CodonPlus (DE3) strains are engineered to contain extra copies of genes that encode the tRNAs that most frequently limit translation of heterologous proteins in *E. coli.* By supplying *E. coli* rare codons expression is enhanced where translation would otherwise be limited by the codon usage of *E. coli*. BL21-CodonPlus(DE3) RP cells contain a pACYC-based plasmid containing extra copies of the *arg*U and *pro*L tRNA genes. The RP expression strain therefore enables the efficient expression of genes that contain the *E. coli* rare arginine codons AGA and AGG and the proline codon CCC. BL21-CodonPlus(DE3) RIL cells contain a pACYC-based plasmid containing extra copies of the *arg*U, *ile*Y and *leu*W tRNA genes. The RIL expression strain therefore enables the efficient expression of genes that contain the *E. coli* rare arginine codons AGA and AGG, the isoleucine codon AUA, and leucine codon CUA. BL21-CodonPlus(DE3) RIPL cells contain a pACYC-based plasmid containing extra

copies of the *arg*U and *pro*L tRNA genes, and a pACYC-compatible plasmid pSC101 containing extra copies of the *arg*U, *ile*Y und *leu*W tRNA genes. The RIPL expression strain therefore enables the efficient expression of genes that contain the *E. coli* rare codons mentioned for both the RP and RIL strains. The pACYC-plasmid additionally contains a gene for the chloramphenicol acetyltransferase that confers chloramphenicol resistance. The pSC101-plasmid additively confers streptomycin and spectinomycin resistence.

***E. coli* BL21(DE3) Rosetta 2** (MERCK, Darmstadt)

B F^- *ompT hsdS*$_B$(r_B^- m_B^-) *gal dcm* (DE3) pRARE2 *(*Cam^r)

E. coli BL21(DE3) Rosetta 2 cells contain on a pACYC-based plasmid termed pRARE2, genes for the tRNAS *arg*U, *arg*W, *arg*X, *gly*T, *ile*X, *leu*W, *met*T, *pro*L, *thr*T, *thr*U and *tyr*U. The expression strain therfore enables the efficient expression of genes that contain the *E. coli* rare codons AGA, AGG and CGG for arginine, GGA for glycin, AUA for isoleucine, CUA for leucine, ACC and ACA for threonine, TAC for tyrosin and CCC for proline. The plasmid additively confers chloramphenicol resistance.

***E. coli* T7 Express Rosetta** (research group of Prof. Dr. R. Sterner)

*fhu*A2 *lac*Z::T7*gene*1 *lon omp*T *gal sul*A11 *dcm* R(*zgb*-210::*Tn*10--*Tet*^{S}) *end*A1 Δ(*mcr*C-*mrr*)114::IS10 R(*mcr*-73::*miniTn*10--*Tet*^{S})2) [*arg*U *arg*W *gly*T *ile*X*, leu*W *met*T *pro*L *thr*T *thr*U *tyr*U Cam^r]

This expression strain was constructed in the research group of Prof. R. Sterner. Originating from *E. coli* T7 expression cells (NEW ENGLAND BIOLABS, Frankfurt am Main), the strain contains an additional pRARE plasmid from *E. coli* Rosetta(DE3)pLysS (Merck, Darmstadt), which enables the expression of genes with rare codons in a T1-phage resistant *E. coli* strain. Besides the tetracycline resistance, the cells exhibit, due to the pRARE plasmid, accessory chloramphenicol resistance.

***E. coli* BW25113** (Datsenko & Wanner, 2000)

Δ*(ara*D-*ara*B*)567* Δ*lac*Z*4787*(::rrnB-3) *lac*Ip-4000($lacI^Q$) λ$^-$ *rph-1* Δ*(rha*D-*rha*B*)568 hsd*R514

A Δ*his*A-Δ*his*F strain was generated based on the *E. coli* BW25113 strain and kindly provided by Dr. J. Claren (Claren, 2008).

2.7 Vectors

2.7.1 pET vectors

Genes inserted into the multiple clonig site (MCS) of pET vectors (MERCK, plasmid for expression by T7 RNA Polymerase) are transcribed by the RNA-polymerase of the phage T7 (Studier *et al.,* 1990). The expression of genes takes place in special *E. coli* strains, which carry a chromosomal copy of the T7 RNA polymerase. The expression of the T7 RNA polymerase gene proceeds under the control of the *lac*UV5 promotor operator and is induced by the addition of isopropyl-β-D-thiogalactopyranoside (IPTG). The gene for the *lac*-repressor (*lacI*), which is required for suppression of gene expression in the absence of induction, is located on the plasmid and is constitutively expressed.

pET20b(+)

The pET20b(+) vector encodes an N-terminal *pelB* signal sequence for periplasmic localization, plus an optional C-terminal $(His)_6$-tag sequence. The vector confers ampicillin resistance.

pET24a(+)

The pET24a(+) vector encodes an optional C-terminal $(His)_6$-tag sequence and confers kanamycin resistance.

pET30a(+)

The pET30a(+) vector encodes an N-terminal $(His)_6$-tag followed by a thrombin restriction site. Consequently, the hexahistidin-tag can be proteolytically cleaved off from the target protein by incubation with thrombin. Furthermore, the vector encodes an optional C-terminal $(His)_6$-tag and confers kanamycin resistance.

2.7.2 pTNA vector

The pTNA-vector is a variant form of the pDS56/RBSII-vector (Bujard *et al*., 1987; Stüber *et al*., 1990). The T5 promotor and the lac operator sequence have been replaced by the (-30)–(-10)-region of the tryptophanase operon promoter (p_{TNA}) of *E. coli*, which leads to weak constitutive expression (Merz *et al*., 2000). In general, the gene is inserted between the *Sph*I- und *Hin*dIII-restriction sites. The pTNA vector

contains a gene mediating ampicillin resistance. The vector was kindly provided by Prof. Dr. Charles Yanofsky (Stanford University, USA).

2.8 Oligodeoxynucleotides

Oligonucleotides were obtained from METABION (Martinsried) or Integrated DNA Technologies, Inc. (Coralville, USA). The restriction sites in terminal amplification primers are underlined. Bases in mutagenic primers that differ from wild-type bases are printed in bold. (Partially) degenerated condons are printed in bold and italic.

2.8.1 Vector-specific amplification and sequencing primers

5'T7Promotor
5'- TAA TAC GAC TCA CTA TAG GG -3'

3'T7Terminator
5'- GCT AGT TAT TGC TCA GCG G -3'

5'CyRI
5'- TCA CGA GGC CCT TTC GTC TT -3'

3'CyPstI
5'- TCG CCA AGC TAG CTT GGA TTC T -3'

5'pTNA-*Sph*I
5'- ATT CAT TAA AGA GGA GAA ATT AAG CAT GC -3'

3'pTNA-*Hin*dIII
5'- AGG AGT CCA AGC TCA GCT AAT TAA GCT TTT A -3'

5'pTNA-F-MCS
5'- GAA AGC AAT TTT CGT ACT GTA AGG TTG -3'

3'pTNA-B-MCS
5'- CCA GAT GGA GTT CTG AGG TCA TTA CTG -3'

2.8.2 Amplification and mutagenic primers for *dr0930*

Partially degenerated codons (coding mutations) used are listed in the following: ***DKY*** (C, F, G, I, S, V), ***GYG*** (A, V), ***AYY*** (I, T), ***MWS*** (H, I, K, L, M, N, Q), ***GBS*** (A, G, V), ***MTG*** (L, M), ***WGC*** (C, S), ***RAH*** (D, E, K, N), ***KCG*** (A, S), ***GAW*** (D, E), ***HRY*** (C, H, N, R, S, Y), ***MTK*** and ***MKK*** (L, I, M), ***GYG*** (A, V).

The **NNS** codon is coding for all 20 amino acids and one stop codon (TAG). The stop codons TGA and TAA are excluded.

5'*dr0930-Sph*I-T2Q
5'- TAT GCA TG**C** **AG**G CAC AGA CGG TGA CGG GCG C -3'

3'*dr0930-Hin*dIII
5'- ATA AAG CTT TTA CCC GAA CAG CCG GGC CGG GTT -3'

5'*dr0930-Nde*I
5'- AGC CAT ATG ACG GCA CAG ACG GTG ACG GGC GC -3'

5'*dr0930-Nde*I-T2Q
5'- AAT CAT ATG **CAG** GCA CAG ACG GTG ACG GGC GC -3'

5'*dr0930-Nde*I-T2Q+A3T
5'- AAT CAT ATG **CAG ACA** CAG ACG GTG ACG GGC GC -3'

3'*dr0930-EcoR*I
5'- TGT GAA TTC TTA CCC GAA CAG CCG GGC CGG GTT -3'

3'*dr0930-Xho*I
5'- TGT CTC GAG TTA CCC GAA CAG CCG GGC CGG GTT -3'

3'*dr0930-Not*I
5'- ATT GCG GCC GCT TAC CCG AAC AGC CGG GCC GGG TT -3'

5'*dr0930*-D71N
5'- ACC CCC AAC **AAC** TGC GGA CGC AAC CCG GC -3'

3'*dr0930*-D71N
5'- GCC GGG TTG CGT CCG CA**G** **TT**G TTG GGG GT -3'

5'*dr0930*-F26G
5'- CCC CAC GAA CAC GTG ATT **GGC** GGC TAC CCC GG -3'

3'*dr0930*-F26G
5'- CCG GGG TAG CC**G** **CC**A ATC ACG TGT TCG TGG GG -3'

5'*dr0930*-F26DKY+Y28GYG
5'- CCC CAC GAA CAC GTG ATT ***DKY*** GGC ***GYG*** CCC GGC TAC GCG GGC GAC -3'

3'*dr0930*-F26DKY+Y28GYG
5'- GTC GCC CGC GTA GCC GGG ***CRC*** GCC ***RMH*** AAT CAC GTG TTC GTG GGG -3'

5'*dr0930*-F26DKY+Y28AYY
5'- CCC CAC GAA CAC GTG ATT ***DKY*** GGC ***AYY*** CCC GGC TAC GCG GGC GAC -3'

3'*dr0930*-F26DKY+Y28AYY
5'- GTC GCC CGC GTA GCC GGG ***RRT*** GCC ***RMH*** AAT CAC GTG TTC GTG GGG -3'

5'*dr0930*-D71MWS+C72
5'- GTG GTG GAC GCC ACC CCC AAC ***MWS*** TGC GGA CGC AAC CCG GCC TTC -3'

3'*dr0930*-D71MWS+C72
5'- GAA GGC CGG GTT GCG TCC GCA ***SWK*** GTT GGG GGT GGC GTC CAC CAC -3'

5'*dr0930*-D71MWS+C72I
5'- GTG GTG GAC GCC ACC CCC AAC ***MWS*** **ATT** GGA CGC AAC CCG GCC TTC -3'

3'*dr0930*-D71MWS+C72I
5'- GAA GGC CGG GTT GCG TCC **AAT** ***SWK*** GTT GGG GGT GGC GTC CAC CAC -3'

5'*dr0930*-D71GBS+C72
5'- GTG GTG GAC GCC ACC CCC AAC ***GBS*** TGC GGA CGC AAC CCG GCC TTC -3'

3'*dr0930*-D71GBS+C72
5'- GAA GGC CGG GTT GCG TCC GCA ***SVC*** GTT GGG GGT GGC GTC CAC CAC -3'

5'*dr0930*-D71GBS+C72I
5'- GTG GTG GAC GCC ACC CCC AAC **GBS ATT** GGA CGC AAC CCG GCC TTC -3'

3'*dr0930*-D71GBS+C72I
5'- GAA GGC CGG GTT GCG TCC **AAT** ***SVC*** GTT GGG GGT GGC GTC CAC CAC -3'

5'*dr0930*-E101GBS
5'- GGC TTT TAT TAC GAG GGC ***GBS*** GGC GCC ACG ACC TAC TTC AAG -3'

3'*dr0930*-E101GBS
5'- CTT GAA GTA GGT CGT GGC GCC ***SVC*** GCC CTC GTA ATA AAA GCC -3'

5'*dr0930*-E101MTG
5'- GGC TTT TAT TAC GAG GGC ***MTG*** GGC GCC ACG ACC TAC TTC AAG -3'

3'*dr0930*-E101MTG
5'- CTT GAA GTA GGT CGT GGC GCC ***CAK*** GCC CTC GTA ATA AAA GCC -3'

5'*dr0930*-E101WGC
5'- GGC TTT TAT TAC GAG GGC ***WGC*** GGC GCC ACG ACC TAC TTC AAG -3'

3'*dr0930*-E101WGC
5'- CTT GAA GTA GGT CGT GGC GCC ***GCW*** GCC CTC GTA ATA AAA GCC -3'

5'*dr0930*-E101RAH
5'- GGC TTT TAT TAC GAG GGC ***RAH*** GGC GCC ACG ACC TAC TTC AAG -3'

3'*dr0930*-E101RAH
5'- CTT GAA GTA GGT CGT GGC GCC ***DTY*** GCC CTC GTA ATA AAA GCC -3'

5'*dr0930*-Q178MWS+E179GAW
5'- GTG CCG ATC ATC ACC CAC ACT ***MWS GAW*** GGC CAG CAG GGA CCG CAG -3'

3'*dr0930*-Q178MWS+E179GAW
5'- CTG CGG TCC CTG CTG GCC ***WTC SWK*** AGT GTG GGT GAT GAT CGG CAC -3'

5'*dr0930*-Q178KCG+E179GAW
5'- GTG CCG ATC ATC ACC CAC ACT ***KCG GAW*** GGC CAG CAG GGA CCG CAG -3'

3'*dr0930*-Q178KCG+E179GAW
5'- CTG CGG TCC CTG CTG GCC ***WTC CGM*** AGT GTG GGT GAT GAT CGG CAC -3'

5'*dr0930*-R228HRY+V235MTK
5'- ATC GCC TTT GAC ***HRY*** ATC GGC TTG CAG GGC ATG ***MTK*** GGC ACC CCC -3'

3'*dr0930*-R228HRY+V235MTK
5'- GGG GGT GCC ***MAK*** CAT GCC CTG CAA GCC GAT ***RYD*** GTC AAA GGC GAT -3'

5'*dr0930*-L270GYG
5'- GAC AGC ATC TGG CAC TGG ***GYG*** GGA CGC CCG CCG GCC ATC -3'

3'*dr0930*-L270GYG
5'- GAT GGC CGG CGG GCG TCC ***CRC*** CCA GTG CCA GAT GCT GTC -3'

5'*dr0930*-L270MKK
5'- GAC AGC ATC TGG CAC TGG ***MKK*** GGA CGC CCG CCG GCC ATC -3'

3'*dr0930*-L270MKK
5'- GAT GGC CGG CGG GCG TCC ***MMK*** CCA GTG CCA GAT GCT GTC -3'

5'*dr0930*-F26C-Y28I
5'- CCC CAC GAA CAC GTG ATT **TGC** GGC **ATT** CCC GGC TAC GCG GGC GAC -3'

3'*dr0930*-F26C-Y28I
5'- GTC GCC CGC GTA GCC GGG **AAT** GCC **GCA** AAT CAC GTG TTC GTG GGG -3'

5'*dr0930*-F26V-Y28I
5'- CCC CAC GAA CAC GTG ATT **GTG** GGC **ATT** CCC GGC TAC GCG GGC GAC -3'

3'*dr0930*-F26V-Y28I
5'- GTC GCC CGC GTA GCC GGG **AAT** GCC **CAC** AAT CAC GTG TTC GTG GGG -3'

5'*dr0930*-D71N-C72
5'- GTG GTG GAC GCC ACC CCC AAC **AAC** TGC GGA CGC AAC CCG GCC TTC -3'

3'*dr0930*-D71N-C72
5'- GAA GGC CGG GTT GCG TCC GCA **GTT** GTT GGG GGT GGC GTC CAC CAC -3'

5'*dr0930*-D71G-C72
5'- GTG GTG GAC GCC ACC CCC AAC **GGC** TGC GGA CGC AAC CCG GCC TTC -3'

3'*dr0930*-D71G-C72
5'- GAA GGC CGG GTT GCG TCC GCA **GCC** GTT GGG GGT GGC GTC CAC CAC -3'

5'*dr0930*-E101G
5'- GGC TTT TAT TAC GAG GGC **GGC** GGC GCC ACG ACC TAC TTC AAG -3'

3'*dr0930*-E101G
5'- CTT GAA GTA GGT CGT GGC GCC **GCC** GCC CTC GTA ATA AAA GCC -3'

5'*dr0930*-E101S
5'- GGC TTT TAT TAC GAG GGC **AGC** GGC GCC ACG ACC TAC TTC AAG -3'

3'*dr0930*-E101S
5'- CTT GAA GTA GGT CGT GGC GCC **GCT** GCC CTC GTA ATA AAA GCC -3'

5'*dr0930*-E101N
5'- GGC TTT TAT TAC GAG GGC **AAC** GGC GCC ACG ACC TAC TTC AAG -3'

3'*dr0930*-E101N
5'- CTT GAA GTA GGT CGT GGC GCC **GTT** GCC CTC GTA ATA AAA GCC -3'

5'*dr0930*-Q178S-E179
5'- GTG CCG ATC ATC ACC CAC ACT **AGC** GAA GGC CAG CAG GGA CCG CAG -3'

3'*dr0930*-Q178S-E179
5'- CTG CGG TCC CTG CTG GCC TTC **GCT** AGT GTG GGT GAT GAT CGG CAC -3'

5'*dr0930*-Q178S-E179D
5'- GTG CCG ATC ATC ACC CAC ACT **AGC GAT** GGC CAG CAG GGA CCG CAG -3'

3'*dr0930*-Q178S-E179D
5'- CTG CGG TCC CTG CTG GCC **ATC GCT** AGT GTG GGT GAT GAT CGG CAC -3'

5'*dr0930*-V235I
5'- ATC GCC TTT GAC CGC ATC GGC TTG CAG GGC ATG **ATT** GGC ACC CCC -3'

3'*dr0930*-V235I
5'- GGG GGT GCC **AAT** CAT GCC CTG CAA GCC GAT GCG GTC AAA GGC GAT -3'

5'*dr0930*-L270
5'- GAC AGC ATC TGG CAC TGG CTG GGA CGC CCG CCG GCC ATC -3'

3'*dr0930*-L270
5'- GAT GGC CGG CGG GCG TCC CAG CCA GTG CCA GAT GCT GTC -3'

5'*dr0930*-D71G
5'- GTG GAC GCC ACC CCC AAC **GGC** TGC GGA CGC AAC CCG GCC -3'

3'*dr0930*-D71G
5'- GGC CGG GTT GCG TCC GCA **GCC** GTT GGG GGT GGC GTC CAC -3'

5'*dr0930*-E101G
5'- GGC TTT TAT TAC GAG GGC **GGG** GGC GCC ACG ACC TAC TTC -3'

3'*dr0930*-E101G
5'- GAA GTA GGT CGT GGC GCC **CCC** GCC CTC GTA ATA AAA GCC -3'

5'*dr0930*-V235L
5'- GGC TTG CAG GGC ATG **CTG** GGC ACC CCC ACC GAC GCC -3'

3'*dr0930*-V235L
5'- GGC GTC GGT GGG GGT GCC **CAG** CAT GCC CTG CAA GCC -3'

5'*dr0930*-M234I
5'- ATC GGC TTG CAG GGC **ATT** GTG GGC ACC CCC ACC GAC -3'

3'*dr0930*-M234I
5'- GTC GGT GGG GGT GCC CAC **AAT** GCC CTG CAA GCC GAT -3'

5'*dr0930*-Y28NNS
5'- CCC CAC GAA CAC GTG ATT TTC GGC ***NNS*** CCC GGC TAC GCG GGC GAC -3'

3'*dr0930*-Y28NNS
5'- GTC GCC CGC GTA GCC GGG ***SNN*** GCC GAA AAT CAC GTG TTC GTG GGG -3'

5'*dr0930*_Δ101
5'- GGC GCC ACG ACC TAC TTC AAG TTC CGC -3'

3'*dr0930*_Δ99+100+101
5'- GTA ATA AAA GCC GGT CGC GCA CAG AAT -3'

3'*dr0930*_Δ100+101
5'- CTC GTA ATA AAA GCC GGT CGC GCA CAG -3'

3'*dr0930*_Δ101
5'- GCC CTC GTA ATA AAA GCC GGT CGC GCA -3'

5'*dr0930*-V235L+Δ*Sph*I
5'- GGC TTG CAG GG**G** ATG **CTG** GGC ACC CCC AC -3'

3'*dr0930*-V235L+Δ*Sph*I
5'- GTG GGG GTG CC**C AG**C AT**C** CCC TGC AAG CC -3'

5'*dr0930*-Y97NNS+E101G
5'- TGC GCG ACC GGC TTT **NNS** TAC GAG GGC **GGC** GGC GC -3'

3'*dr0930*-Y97NNS+E101G
5'- GCG CC**G CC**G CCC TCG TA**S NN**A AAG CCG GTC GCG CA -3'

5'*dr0930*-Y97Q+E101G
5'- CAG ATT CTG TGC GCG ACC GGC TTT **CAG** TAC GAG GGC **GGC** GGC GCC ACG AC -3'

3'*dr0930*-Y97Q+E101G
5'- GTC GTG GCG CC**G CC**G CCC TCG TA**C TG**A AAG CCG GTC GCG CAC AGA ATC TG -3'

5'*dr0930*-Y97W+E101G
5'- CAG ATT CTG TGC GCG ACC GGC TTT **TGG** TAC GAG GGC **GGC** GGC GCC ACG AC -3'

3'*dr0930*-Y97W+E101G
5'- GTC GTG GCG CC**G CC**G CCC TCG TA**C CA**A AAG CCG GTC GCG CAC AGA ATC TG -3'

5'*dr0930*-Y97C+E101G
5'- CAG ATT CTG TGC GCG ACC GGC TTT **TGC** TAC GAG GGC **GGC** GGC GCC ACG AC -3'

3'*dr0930*-Y97C+E101G
5'- GTC GTG GCG CC**G CC**G CCC TCG TA**G CA**A AAG CCG GTC GCG CAC AGA ATC TG -3'

5'*dr0930*-F26Y+Y28L
5'- CAC GAA CAC GTG ATT **TAT** GGC **CTG** CCC GGC TAC -3'

3'*dr0930*-F26Y+Y28L
5'- GTA GCC GGG **CAG** GCC **ATA** AAT CAC GTG TTC GTG -3'

5'*dr0930*-F26C+Y28L
5'- CAC GAA CAC GTG ATT **TGC** GGC **CTG** CCC GGC TAC -3'

3'*dr0930*-F26C+Y28L
5'- GTA GCC GGG **CAG** GCC **GCA** AAT CAC GTG TTC GTG -3'

5'*dr0930*-F26W+Y28L
5'- CAC GAA CAC GTG ATT **TGG** GGC **CTG** CCC GGC TAC -3'

3' *dr0930*-F26W+Y28L
5'- GTA GCC GGG **CAG** GCC **CCA** AAT CAC GTG TTC GTG -3'

5'*dr0930*-F26L+Y28L
5'- CAC GAA CAC GTG ATT **CTG** GGC **CTG** CCC GGC TAC -3'

3'*dr0930*-F26L+Y28L
5'- GTA GCC GGG **CAG** GCC **CAG** AAT CAC GTG TTC GTG -3'

5'*dr0930*-F26H+Y28L
5'- CAC GAA CAC GTG ATT **CAT** GGC **CTG** CCC GGC TAC -3'

3'*dr0930*-F26H+Y28L
5'- GTA GCC GGG **CAG** GCC **ATG** AAT CAC GTG TTC GTG -3'

5'*dr0930*-F26Q+Y28L
5'- CAC GAA CAC GTG ATT **CAG** GGC **CTG** CCC GGC TAC -3'

3'*dr0930*-F26Q+Y28L
5'- GTA GCC GGG **CAG** GCC **CTG** AAT CAC GTG TTC GTG -3'

5'*dr0930*-F26R+Y28L
5'- CAC GAA CAC GTG ATT **CGT** GGC **CTG** CCC GGC TAC -3'

3'*dr0930*-F26R+Y28L
5'- GTA GCC GGG **CAG** GCC **ACG** AAT CAC GTG TTC GTG -3'

5'*dr0930*-F26I+Y28L
5'- CAC GAA CAC GTG ATT **ATT** GGC **CTG** CCC GGC TAC -3'

3'*dr0930*-F26I+Y28L
5'- GTA GCC GGG **CAG** GCC **AAT** AAT CAC GTG TTC GTG -3'

5'*dr0930*-F26M+Y28L
5'- CAC GAA CAC GTG ATT **ATG** GGC **CTG** CCC GGC TAC -3'

3'*dr0930*-F26M+Y28L
5'- GTA GCC GGG **CAG** GCC **CAT** AAT CAC GTG TTC GTG -3'

5'*dr0930*-F26T+Y28L
5'- CAC GAA CAC GTG ATT **ACC** GGC **CTG** CCC GGC TAC -3'

3' *dr0930*-F26T+Y28L
5'- GTA GCC GGG **CAG** GCC **GGT** AAT CAC GTG TTC GTG -3'

5'*dr0930*-F26N+Y28L
5'- CAC GAA CAC GTG ATT **AAC** GGC **CTG** CCC GGC TAC -3'

3'*dr0930*-F26N+Y28L
5'- GTA GCC GGG **CAG** GCC **GTT** AAT CAC GTG TTC GTG -3'

5'*dr0930*-F26K+Y28L
5'- CAC GAA CAC GTG ATT **AAA** GGC **CTG** CCC GGC TAC -3'

3'*dr0930*-F26K+Y28L
5'- GTA GCC GGG **CAG** GCC **TTT** AAT CAC GTG TTC GTG -3'

5'*dr0930*-F26S+Y28L
5'- CAC GAA CAC GTG ATT **AGC** GGC **CTG** CCC GGC TAC -3'

3'*dr0930*-F26S+Y28L
5'- GTA GCC GGG **CAG** GCC **GCT** AAT CAC GTG TTC GTG -3'

5'*dr0930*-F26V+Y28L
5'- CAC GAA CAC GTG ATT **GTG** GGC **CTG** CCC GGC TAC -3'

3'*dr0930*-F26V+Y28L
5'- GTA GCC GGG **CAG** GCC **CAC** AAT CAC GTG TTC GTG -3'

5'*dr0930*-F26A+Y28L
5'- CAC GAA CAC GTG ATT **GCG** GGC **CTG** CCC GGC TAC -3'

3'*dr0930*-F26A+Y28L
5'- GTA GCC GGG **CAG** GCC **CGC** AAT CAC GTG TTC GTG -3'

5'*dr0930*-F26D+Y28L
5'- CAC GAA CAC GTG ATT **GAT** GGC **CTG** CCC GGC TAC -3'

3'*dr0930*-F26D+Y28L
5'- GTA GCC GGG **CAG** GCC **ATC** AAT CAC GTG TTC GTG -3'

5'*dr0930*-F26E+Y28L
5'- CAC GAA CAC GTG ATT **GAA** GGC **CTG** CCC GGC TAC -3'

3'*dr0930*-F26E+Y28L
5'- GTA GCC GGG **CAG** GCC **TTC** AAT CAC GTG TTC GTG -3'

5'*dr0930*-F26G+Y28L
5'- CAC GAA CAC GTG ATT **GGC** GGC **CTG** CCC GGC TAC -3'

3'*dr0930*-F26G+Y28L
5'- GTA GCC GGG **CAG** GCC **GCC** AAT CAC GTG TTC GTG -3'

5'*dr0930*-F26P+Y28L
5'- CCC CAC GAA CAC GTG ATT **CCG** GGC **CTG** CCC GGC TAC GCG -3'

3'*dr0930*-F26P+Y28L
5'- CGC GTA GCC GGG **CAG** GCC **CGG** AAT CAC GTG TTC GTG GGG -3'

5'*dr0930*-G38R
5'- GGC GAC GTG ACG CTC **CGT** CCA TTC GAC CAC GCG -3'

3 *dr0930*-G38R
5'- CGC GTG GTC GAA TGG **ACG** GAG CGT CAC GTC GCC -3'

5'*dr0930*-L270M+P274L
5'- TGG **ATG** GGA CGC CCG **CTG** GCC ATC CCC GAA GCC -3'

3'*dr0930*-L270M+P274L
5'- GGC TTC GGG GAT GGC **CAG** CGG GCG TCC **CAT** CCA -3'

5'*dr0930*-L270+P274L
5'- TGG CTG GGA CGC CCG **CTG** GCC ATC CCC GAA GCC -3'

3'*dr0930*-L270+P274L
5'- GGC TTC GGG GAT GGC **CAG** CGG GCG TCC CAG CCA -3'

5'*dr0930*-E101G+T105S
5'- GGC **GGC** GGC GCC ACG **AGC** TAC TTC AAG TTC CGC -3'

3'*dr0930*-E101G+T105S
5'- GCG GAA CTT GAA GTA **GCT** CGT GGC GCC **GCC** GCC -3'

5'*dr0930*-L270M+R272C
5'- TGG CAC TGG **ATG** GGA **TGC** CCG CCG GCC ATC CCC -3'

3 *dr0930*-L270M+R272C
5'- GGG GAT GGC CGG CGG **GCA** TCC **CAT** CCA GTG CCA -3'

5'*dr0930*-L270+R272C
5'- TGG CAC TGG CTG GGA **TGC** CCG CCG GCC ATC CCC -3'

3'*dr0930*-L270+R272C
5'- GGG GAT GGC CGG CGG **GCA** TCC CAG CCA GTG CCA -3'

5'*dr0930*-L270+P274L (OE-PCR)
5'- ATC TGG CAC TGG CTG GGA CGC CCG **CTG** GCC ATC CCC GAA -3'

3'*dr0930*-L270+P274L (OE-PCR)
5'- TTC GGG GAT GGC **CAG** CGG GCG TCC CAG CCA GTG CCA GAT -3'

2.8.3 Amplification primers for *pte*

5'*pte-Sph*I-S2Q

5’- ATT GCA TGC AAA TCG GGA CCG GTG ACC GTA TCA ACA C -3’

3'*pte-Hin*dIII

5’- TAT AAG CTT TCA GGA AGC ACG CAG GGT CGG GGA CAG GAA -3’

2.9 Ladders and markers

In order to determine the size of DNA fragments in agarose gels the GeneRuler™ 1 kb Plus DNA Ladder (MBI FERMENTAS, St. Leon-Rot) was commonly used (Figure 8A). Alternatively, the EZ Load™ 100 bp/500 bp Molecular Ruler (Bio-Rad, Hercules, USA) was applied.

In order to determine the size of proteins for SDS-PAGE the Unstained Protein Molecular Weight Marker (MBI FERMENTAS, St. Leon-Rot) was commonly used (Figure 8B). Alternatively, the Prestained SDS-PAGE Standards, low range (Bio-Rad, Hercules, USA) or the Prestained Protein Marker, broad range (7-175 kDa) (NEW ENGLAND BIOLABS, Frankfurt a. M.) were applied.

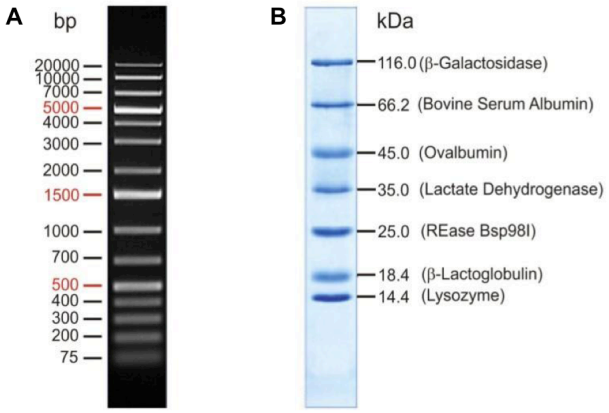

Figure 8: DNA and protein ladders and markers.
A: GeneRuler™ 1 kb Plus DNA Ladder (MBI FERMENTAS). **B:** Unstained Protein Molecular Weight Marker (MBI FERMENTAS) for SDS-PAGE (12.5 %).

2.10 Buffers and solutions

Unless otherwise specified, the buffers used were filter-sterilized and stored at room temperature. For all preparations Milli-Q grade water (MILLIPORE) or double distilled water (ddH_20) was used.

2.10.1 Buffers and solutions for working with *E. coli*

Antibiotics

Dissolved and filter-sterilized antibiotics for long-term storage were stored at -20 °C.

Ampicillin (1000×)	150 mg/ml ampicillin (Na-salt) dissolved in water and filter-sterilized
Chloramphenicol (1000×)	30 mg/ml chloramphenicol dissolved in 100 % EtOH and filter-sterilized
Kanamycin (1000×)	75 mg/ml kanamycin dissolved in water and filter-sterilized
Tetracycline (1000×)	12.5 mg/ml tetracycline dissolved in 100 % EtOH and filter-sterilized
$CoCl_2$	1 M $CoCl_2$ dissolved in water, filter-sterilized, and stored at RT
Glucose	20% ($^{w}/_{v}$) glucose dissolved in water, filter-sterilized, and stored at RT
Glycerol (87 %)	
IPTG stock solution	0.5 M IPTG dissolved in water, filter-sterilized, and stored at -20 °C
KCl	1 M KCl dissolved in water, filter-sterilized, and stored at RT
$MgCl_2$	1 M $MgCl_2$ dissolved in water, filter-sterilized, and stored at RT
$MgSO_4$	1 M $MgSO_4$ dissolved in water, filter-sterilized, and stored at RT
$MnCl_2$	1 M $MnCl_2$ dissolved in water, filter-sterilized, and stored at RT
10 × TB-Phosphate	2.31 g KH_2PO_4 (acid, 0.17 M) and 12.54 g K_2HPO_4 (base, 0.72 M) dissolved in water (total volume of 100 ml); autoclaved and stored at RT
TFB I-buffer	100 mM KCl, 50 mM $MnCl_2$, 30 mM KAc, 10 mM $CaCl_2$, 15% glycerol; stock solutions for the single components were stored at 4 °C. A volume of 100 ml TFBI-buffer was prepared prior to use.

TFB II-buffer	100 mM Tris/HCl, pH 7.0, 10 mM KCl, 75 mM $CaCl_2$, 15% glycerol; stock solutions for the single components were stored at 4 °C. A volume of 100 ml TFBII-buffer was prepared prior to use.
$ZnCl_2$	1 M $ZnCl_2$ dissolved in water, filter-sterilized, and stored at RT

2.10.2 Buffers and solutions for screening and enzyme kinetics

Acetic acid	1 mM acetic acid prepared by diluting glacial acetic acid with water and stored at RT
BICINE	25 mM BICINE pH 8.3; pH adjusted using NaOH; filter-sterilized and stored at RT
BugBuster Lysis buffer (1×)	1 × BugBuster (Novagen) in 50 mM HEPES, pH 8.5, 100 µM $CoCl_2$; prepared prior to use and stored at 4 °C
CHES (pH 9.0) stock solution	0.5 M CHES pH 9.0; pH adjusted using KOH; filter-sterilized and stored at RT
m-cresol purple	*m*-cresol purple dissolved in 100% DMSO and stored at RT
δ-nonanoic lactone	δ-nonanoic lactone dissolved in 100% DMSO and stored at -20 °C
Freeze-down solution	65% glycerol, 20 mM Tris-HCl pH 5.6, 100 mM $MgSO_4$; autoclaved and stored at RT
HEPES (pH 8.5) stock solution	1 M HEPES pH 8.5; pH adjusted using NaOH; filter-sterilized, and stored at 4 °C
OP substrate stock solution	*p*-nitrophenyl substituted OP compounds were dissolved in water to maximum solubility (<10 mM), or dissolved in 20% MeOH in case of GD *p*-NP and GF *p*-NP (OPs 4 and 5). Due to spontaneous substrate hydrolysis the precise concentration of non-hydrolyzed substrate was determined by titration with 10 M KOH using Lambert-Beer's law (ε_{400} = 17000 $M^{-1}cm^{-1}$). Aliquots were stored at -80 °C.

DEVX substrate stock	DEVX was dissolved in 20% MeOH to maximum solubility (<10 mM). The concentration was determined enzymatically using wild-type PTE at 50 mM HEPES pH 8.0, 0.3 mM DTNB, 100 µM $CoCl_2$ (ε_{412} = 14150 $M^{-1}cm^{-1}$).

2.10.3 Buffers and solutions for working with DNA and agarose gel electrophoresis

PCR dNTP solution (2 mM)	A solution of dNTP's (2 mM of each A, C, G, and T) was prepared and stored at -20 °C.
Agarose (1%)	5 g agarose dissolved in 500 ml 0.5 × TBE, boiled and stored at 60 °C
Ethidium bromide stock solution	10 mg/ml ethidium bromide (EtBr)
Sucrose color marker	60% ($^{w}/_{v}$) sucrose, 0.1% ($^{w}/_{v}$) bromphenol blue, 0.1% ($^{w}/_{v}$) xylencyanole FF dissolved in 0.5 × TBE;
TBE (5×)	445 mM boric acid, 12.5 mM EDTA, 445 mM Tris (resulting pH-value: 8.15)

2.10.4 Buffers and solutions for working with proteins

Wild-type Dr0930 and Dr0930 variants

Buffer for AEX chromatography	
Binding buffer	20 mM HEPES, pH 7.5, 100 µM $CoCl_2$
Elution buffer	20 mM HEPES, pH 7.5, 100 µM $CoCl_2$, 2 M NaCl
Buffer for preparative gel filtration	20 mM HEPES, pH 7.5, 100 µM $CoCl_2$, 300 mM NaCl; filter-sterilized and degassed
Dialysis- and storage buffer	20 mM HEPES, pH 7.5, 100 µM $CoCl_2$
HEPES (pH 7.5) stock solution	1 M HEPES (pH 7.5); pH adjusted using NaOH; filter-sterilized and stored at 4 °C
Resuspension buffer for expression in analytical and preparative scale	20 mM HEPES, pH 7.5, 100 µM $CoCl_2$

Wild-type PTE

Buffer for AEX chromatography	
Binding buffer	50 mM HEPES, pH 8.5, 100 µM $CoCl_2$
Elution buffer	50 mM HEPES, pH 8.5, 100 µM $CoCl_2$, 2 M NaCl
Buffer for preparative gel filtration	50 mM HEPES, pH 8.5, 100 µM $CoCl_2$, 300 mM NaCl; filter-sterilized, and degassed
Dialysis- and storage buffer	50 mM HEPES, pH 8.5, 100 µM $CoCl_2$
HEPES (pH 8.5) stock solution	1 M HEPES (pH 8.5); pH adjusted using NaOH; filter-sterilized and stored at 4 °C
Resuspension buffer for expression in analytical and preparative scale	50 mM HEPES, pH 8.5, 100 µM $CoCl_2$

2.10.5 Buffers and solutions for SDS-PAGE

Ammonium persulfate (APS) stock solution (10%)	10% ($^{w}/_{v}$) APS solution; filter-sterilized, and stored at -20 °C
Coomassie staining solution	0.2% ($^{w}/_{v}$) Coomassie Brilliant Blue G-250 and R-250, 50% ($^{v}/_{v}$) ethanol, 10% ($^{v}/_{v}$) glacial acetic acid; filtered and stored at RT; protected from light
Protogel™	30% ($^{v}/_{v}$) acrylamide, 0.8% ($^{v}/_{v}$) bis-acrylamide; stored at 4 °C
Buffer for SDS-PAGE resolving gel	0.4% ($^{w}/_{v}$) SDS, 1.5 M Tris-HCl, pH 8.8
Buffer for SDS-PAGE stacking gel	0.4% ($^{w}/_{v}$) SDS, 0.5 M Tris/HCl, pH 6.8
SDS-PAGE electrophoresis buffer	0.1% ($^{w}/_{v}$) SDS, 0.025 M Tris, 0.2 M glycine (resulting pH-value: 8.5)
SDS-PAGE sample buffer (5×)	5% ($^{w}/_{v}$) SDS, 25% ($^{w}/_{v}$) glycerol, 12.5% ($^{v}/_{v}$) β-mercaptoethanol, 0.025% ($^{w}/_{v}$) bromphenol blue, 1.25 M Tris/HCl, pH 6.8

2.11 Bacterial growth media

For sterilization the medium was autoclaved for 20 min at 121 °C and 2 bar. For selective media, the corresponding antibiotics were added after cooling down of the medium to 60 °C in terms of a filter-sterilized, 1000-fold concentrated stock solution.

Luria-Bertani (LB) medium	0.5% ($^{w}/_{v}$) yeast extract, 1.0% ($^{w}/_{v}$) NaCl, 1.0% ($^{w}/_{v}$) tryptone
LB agar	LB medium plus 1.5% ($^{w}/_{v}$) Bacto-Agar
SOB medium (Sambrook *et al*., 1989)	0.5% ($^{w}/_{v}$) yeast extract, 0.05% ($^{w}/_{v}$) NaCl, 2.0% ($^{w}/_{v}$) tryptone. Following autoclaving, 10 mM $MgSO_4$, 10 mM $MgCl_2$ and 2.5 mM KCl (each filter-sterilized) were added prior to use.
SOC medium	SOB medium was supplemented with 20 mM glucose (filter-sterilized) following autoclavation.
SOC agar	SOC medium plus 1.5% ($^{w}/_{v}$) Bacto-Agar
Super Broth	3.2% ($^{w}/_{v}$) tryptone, 2% ($^{w}/_{v}$) yeast extract, 0.5% ($^{w}/_{v}$) NaCl, 0.5% ($^{v}/_{v}$) 1 N NaOH
TB medium	12 g tryptone, 24 g yeast extract, 4 ml glycerol (87%); dissolved in a total volume of 900 ml water, and autoclaved; 100 ml sterile 10 × TB-Phosphate was added prior to use.

2.12 Software

Local applications

ÄKTA Unicorn Version 5.01 (318)	© GE HEALTHCARE
Bioedit Sequence Alignment Editor V.7.0.5.3	© IBIS BIOSCIENCES, Tom Hall
Cary Eclipse Version 1.1 (175)	© VARIAN Australia Pty. Ltd. 2002
Cary Win UV Version 3.0 (182)	© VARIAN Australia Pty. Ltd. 2002
CCP4 suite	Collaborative Computational Project, Number 4, 1994; Potterton *et al.*, 2004

CNS	Brunger *et al.*, 1998
Corel Draw X5	© 2003 COREL Corp.
CS ChemBioDraw Ultra, version 12.02.1092	© 1986-2010 CambridgeSoft
Endnote Version X4	© 2000 WINTERTREE Software Inc.
HKL2000 package	Otwinowski & Minor, 1997
Jalview 2.6.1	Waterhouse *et al.*, 2009
Magellan V4.0 and V7.1	© 2003 TECAN Austria
MS Office 2007(Win)/2011(Mac)	© 2010 Microsoft Corporation
Phaser version 2.1	McCoy *et al.*, 2007
PHENIX	Adams *et al.*, 2002
PyMOL™ 0.99rc6	© 2006 DELANO SCIENTIFIC LCC.
Refmac5	Murshudov *et al.*, 1997
Sequoia	Bruns *et al.*, 1999
Sequencher 4.10.1, Demo version	© Gene codes Corporation (Ann Arbor, USA)
SigmaPlot 11.0 and 12.0	© 2004/2006 SPSS Inc.
Coot and WinCoot (version 0.6.2)	Emsley & Cowtan, 2004 Emsley *et al.*, 2010
XDS	Kabsch, 1993, 2010
XtalView package	McRee, 1999

Server-assisted applications

DaliLite	http://www.ebi.ac.uk./DaliLite
T-COFFEE/Expresso	Notredame *et al.* (2000), Armougom *et al.* (2006); http://www.tcoffee.org
MolProbity	Davis *et al*., 2007; http://www.molprobity.biochem.duke.edu

3 METHODS

3.1 Preparation of instrumentation and solutions

All thermostable solutions and media were autoclaved for 20 min at 121 °C and 2 bar prior to use. Glassware and heat-stable expendable items, such as pipette tips, were also autoclaved and subsequently dried at 50 °C in a compartment drier. Additionally, glassware was incubated at 200 °C for 4 h for sterilization. Heat-labile solutions were prepared in stock solutions and filtered, either via a membrane filter with a pore size of 0.2 µm by use of a vacuum pump, or by using a syringe filter with a pore size of 0.2 µm or 0.45 µm. Solutions intended for use in chromatographic systems were degassed if required for at least 30 min in a desiccator.

3.2 Microbiological methods

3.2.1 Cultivation and storage of *E. coli* strains

All *E. coli* strains used were cultivated at 37 °C while shaking at 140 rpm (1 liter cultures) or 220 rpm (5, 50 and 250 ml cultures), respectively. For cultivation LB-medium was used, unless otherwise stated. For plasmid-harboring strains the medium was supplemented with the corresponding antibiotics (150 µg/ml ampicillin, 30 µg/ml chloramphenicol, 75 µg/ml kanamycin, 12.5 µg/ml tetracycline) using a filter-sterilized, thousand fold concentrated stock solution. To obtain single colonies, the cell suspension was plated on agar plates containing the adequate antibiotics, and incubated overnight at 37 °C. For temporary storage the plates or suspensions were sealed and stored at 4 °C. For long-term storage, glycerol cultures were made and stored at -80 °C. For this purpose an aliquot of an overnight culture was mixed in a 1:1 ratio with 87% glycerol, and stored in a sterile screw cap reaction vessel.

3.2.2 Preparation of chemically competent *E. coli* cells (Inoue *et al.*, 1990)

For preparation of chemically competent *E. coli* cells, 500 ml SOB medium was inoculated with the respective overnight culture to an OD_{600} of 0.1, and cultured at 37 °C and 220 rpm until an OD_{600} of 0.6 was reached. The culture was incubated on

ice for 15 min, transferred into 50 ml tubes, and cells were harvested by centrifugation (EPPENDORF Centrifuge 5810R, 4000 rpm, 10 min, 4 °C). The cell pellet was resuspended in 100 ml ice-cold TFB I buffer, centrifuged a second time under the same conditions as stated above. The resulting pellet was resuspended in 10 ml ice-cold TFB II-buffer. Immediately after resuspension, 100 µl aliquots of the cell suspension were transferred to Eppendorf reaction vessels on ice and stored at -80 °C.

3.2.3 Transformation of chemically competent *E. coli* cells

For transformation of chemically competent cells a 100 µl aliquot was thawed on ice, and about 100 ng plasmid DNA (maximum volume: 20 µl) was added. Following incubation on ice for 5 min, cells were heat-shocked for 45 s at 42 °C, and incubated again on ice for 5 min. A volume of 900 µl LB-medium was added, and cells were incubated for 1 h at 37 °C in a shaker at 220 rpm to develop antibiotic resistance. Finally, adequate dilutions of the cell suspension were plated on LB agar plates containing the appropriate antibiotics for selection.

3.2.4 Preparation of electro-competent *E. coli* cells (Dower *et al.*, 1988)

For preparation of electro-competent *E. coli* cells, 50 ml or 200 ml SOB-medium were inoculated with the respective overnight culture to an OD_{600} of 0.1, and incubated at 37 °C and 220 rpm until an OD_{600} of 0.6 was reached. The culture was incubated on ice for 30 min, transferred to 50 ml tubes, and cells were harvested by centrifugation (EPPENDORF Centrifuge 5810R, 4000 rpm, 10 min, 4 °C). The pellet was resuspended in 50 ml ice-cold, sterile water and incubated on ice for another 15 min. Following centrifugation the pellet was resuspended in 20 ml ice-cold, sterile water and incubated again on ice for 15 min. The cells were pelleted by centrifugation and resuspended in 10 ml ice-cold, sterile water. After the last incubation and centrifugation step the supernatant was discarded, and the cells were incubated on ice. The cell pellet was resuspended in a minimum of 1 ml sterile water, and 100 µl aliquots were transferred to Eppendorf reaction vessels. Aliquots of electro-competent cells were directly used for transformation or stored at -80 °C in 10% glycerol.

3.2.5 Preparation of DNA for electroporation

For electroporation the salt content of the DNA solution should be as low as possible, to avoid a short-circuit during the electric pulse. Therefore, the DNA which is generally dissolved in a saline buffer (e.g. ligation mixture) has to be dialyzed prior to transformation. For this purpose 10-20 µl of the DNA solution was placed for at least 1 h onto a nitrocellulose filter (MILLIPORE), which was then put onto the surface of MILLIPORE-water in a small petri dish.

3.2.6 Transformation of electro-competent *E. coli* cells

For electroporation a maximum of 20 µl salt-free DNA-solution was added to 100 µl electro-competent cells. After 5 min incubation on ice the transformation mixture was transferred into a pre-cooled electroporation cuvette (gap length 2 mm). Following the electrical pulse (2500 V, 25 µF, 200 Ω) in the electroporator (time constant between 4.0 and 6.0 ms in case of successful electroporation) the cell suspension was immediately supplemented with 1.5 ml SOC medium, and incubated for 1 h at 37 °C in a shaker. Aliquots were plated on selective agar plates, and incubated overnight at 37 °C.

3.2.7 Determination of transformation efficiency

For determination of the transformation efficiency (T_E) one aliquot of competent cells was transformed with 100 ng plasmid DNA, as described above (3.2.3 & 3.2.6). The cells were plated on selective agar using various dilutions (undiluted, 1:10, 1:100, 1:1000 etc.). The transformation efficiency was calculated as follows:

$$\mathbf{T_E} = \frac{\mathbf{n_{colonies} \cdot f}}{\mathbf{m_{DNA}}}$$

Equation 1: Determination of the transformation efficiency.

T_E transformation efficiency (colonies per µg DNA)
$n_{colonies}$ number of colonies
f dilution factor
m_{DNA} applied DNA amount [µg]

3.2.8 *In vitro* activity screening

In vitro activity screening is a fast and reliable method used to assay enzyme activities of lysed colony replicates on filter paper (filter paper activity pre-screen) or

in crude extracts (96-well block activity screen). Upon incubation with substrate, OP hydrolysis is detected as a colorimetric signal, which is based on the release of the product *p*-nitrophenol under basic conditions at 400 nm. An overview of the *in vitro* activity screening process is illustrated in Figure 9.

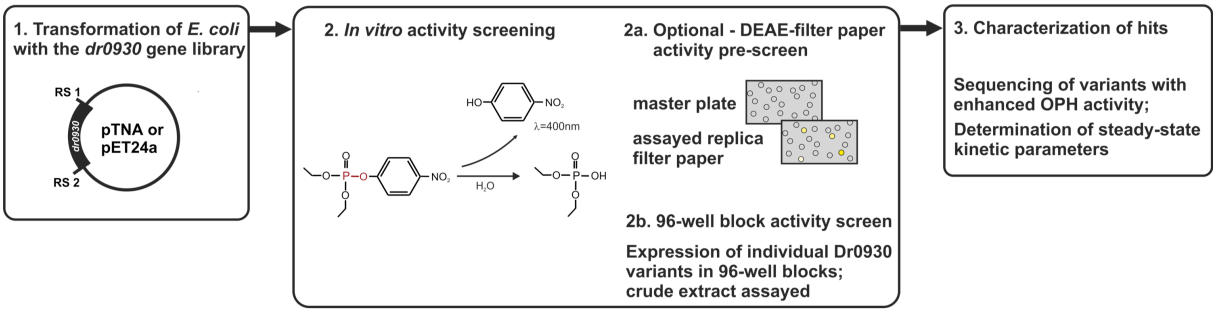

Figure 9: Overview of the *in vitro* activity screening procedure.
Filter paper based and 96-well block activity screening.

In vitro activity screening was used to compare activities of Dr0930 variants and to screen the pTNA-*dr0930* and pET24a-*dr0930* gene libraries for variants with increased OPH activity. The 96-well block activity screen enabled to analyze several hundred colonies per day.

If not state otherwise, chemically competent *E. coli* BL21-CodonPlus(DE3) cells were transformed with the pTNA-*dr0930* gene library, incubated for 1 h at 37 °C, plated on LB agar plates containing the appropriate antibiotics, and incubated overnight.

In case the DEAE-filter paper activity pre-screen was performed to discriminate active and inactive colonies, cells were plated on large square LB agar plates (245 × 245 × 18, BioDish XL, BD). Colony replicates were generated on Whatman DEAE cellulose filter paper (grade DE81) and the master plate was incubated for additional 6 h at 37 °C. DEAE-filter paper limited the diffusion of *p*-nitrophenol due to electrostatic interaction of the product with the diethylaminoethyl (DEAE) tertiary amine functional group of the anion exchange cellulose. Colony replicates on the DEAE-filter paper were lysed by incubation with a second Whatman filter paper (standard Whatman cellulose filter, Grade 1) soaked with 1 x BugBuster® protein extraction reagent (MERCK) in 50 mM HEPES pH 8.5, 100 µM $CoCl_2$ and incubated for 15 min. The activity was assayed by subsequent incubating of the replicate filter paper with Whatman filter paper soaked with 0.5 mM ethyl-paraoxon in 50 mM CHES pH 9.0. Active colonies turned yellow upon substrate hydrolysis and were identified

visually or by digital imaging (using a band pass filter of 406.5-8.1 nm). Positive colonies were picked from the master plate after overnight incubation and restreaked to obtain single colonies for subsequent 96-well block activity screening.

Single colonies were used to inoculate 96-deep-well blocks (EPPENDORF, deep-well blocks 96/2000) containing 0.75 ml Super Broth medium supplemented with the appropriate antibiotics and 0.5-1.0 mM $CoCl_2$, unless otherwise stated. The deep-well blocks were covered with a gas-permeable, self-adhesive sealing tape (QIAGEN, air-pore sheets) and incubated overnight at 37 °C, upon shaking at 240 rpm. Each 96-deep-well block contained a set of controls in triplicates, unless otherwise stated. If applicable, an aliquot of the master plate overnight culture was mixed with 65% (v/v) glycerol, 20 mM Tris-HCl pH 5.6, 100 mM MgSO4 in a 1:1 ratio and stored at -80 °C. The cells were lysed by incubation with 1 x BugBuster in 50 mM HEPES pH 8.5, 100 µM $CoCl_2$ and incubated for 30 minutes at RT. To this end, the 1 x BugBuster solution was either directly added to the 96-deep-well block cultures or to an aliquot that was transferred to a new microtiter plate. Subsequently, an aliquot of the crude lysate was used to assay activities for OP substrates 1-7 (*p*-NP analogues of VX, GB, VR, GD, and GF; MPXN and EPXN; 4.2.2) in 50 mM CHES pH 9.0 using a new microtiter plate. Depending on the OP compound and the stringency of the screen, substrate concentrations of 0.15-0.5 mM were used. If applicable, the crude lysate was diluted in a 1:5 or 1:10 ratio in 50 mM HEPES pH 8.5, 100 µM $CoCl_2$ prior to use. For substrates 4 (GD *p*-NP) and 5 (GF *p*-NP) a final concentration of 10% methanol was added to the assay set-up. The release of *p*-nitrophenol was spectrophotometrically monitored in constant time intervals at 400 nm and 30 °C, using an absorbance plate reader (TECAN, Infinite M200 Pro or MOLECULAR DEVICES, SpectraMax-340 plate reader). Plasmids of the most active colonies were extracted and analyzed by sequencing. In combination with the DEAE filter paper activity pre-screen, the method enables for high-throughput analysis of several thousand colonies per day.

3.3 Molecular biology methods

3.3.1 Isolation and purification of plasmid DNA from *E. coli*

Purification of plasmid DNA was performed according to the principle of alkaline cell lysis (Le Gouill *et al.*, 1994). Bacterial cell cultures were lysed by adding SDS

and sodium hydroxide. The suspension was subsequently neutralized by addition of ammonium acetate; proteins and genomic DNA precipitated, whereas circular plasmid DNA remained in solution.

3.3.1.1 Isolation of plasmid DNA in analytical amounts (mini-preparation)

For analytical isolation and purification of plasmid DNA from *E. coli* mini preparation kits from either FERMENTAS (GeneJET™ Plasmid Miniprep Kit) or QIAGEN (QIAprep® Spin Miniprep Kit) were used. For this purpose 5 ml from overnight cell cultures were harvested by centrifugation (EPPENDORF 5415D, 13200 rpm, 1 min, RT). The isolation of plasmid DNA was performed according to the protocol supplied by the manufacturer. For elution of plasmid DNA from the silica column a volume of 50 µl of sterile water was used. The recovered plasmid DNA was stored at -20 °C.

3.3.1.2 Isolation of plasmid DNA in preparative amounts (midi/maxi-preparation)

For isolation of plasmid DNA for preparative applications midi/maxi preparation kits from either MACHERY-NAGEL (Nucleobond® PC 100/500 DNA-Extraction Kits) or QIAGEN (QIAGEN Plasmid Midi/Maxi Kits) were used.

For midi-preparation 50 ml of an *E. coli* overnight culture was harvested by centrifugation (EPPENDORF 5810R, 4000 rpm, 10 min, 4 °C). The subsequent isolation was performed according to the protocol supplied by the manufacturer. The plasmid DNA was eluted using 50 µl of sterile water and stored at -20 °C.

Maxi-preparation was applied to extract plasmids from gene libraries. To this end, transformants grown on large plates (Ø 14.5 cm) were scraped off using a sterile spatula and liquid LB medium. The resulting cell suspension was centrifuged (EPPENDORF 5810R, 4000 rpm, 10 min, 4 °C) and the plasmid mixture was isolated according to the protocol supplied by the manufacturer. For each maxi-preparation a maximum of 5 g cell pellet was used.

3.3.2 Determination of DNA concentration

The DNA concentration was spectroscopically determined at a wavelength of 260 nm. According to Lambert-Beer's law an OD_{260} value of 1 (with

$^{0.1\%}A_{260}$ = 20 $cm^2\ mg^{-1}$ and a pathlength of 1 cm) corresponds to a DNA concentration of 50 µg/ml dsDNA (35 µg/ml RNA and 33 µg/ml ssDNA, respectively). Thus, the DNA concentration can be calculated as follows:

$$\mathbf{c_{dsDNA}} = \frac{\mathbf{A_{260} \cdot 50 \cdot f}}{\mathbf{1000}}$$

Equation 2: Determination of DNA concentration.
c_{dsDNA} concentration of double stranded DNA [µg/µl]
A_{260} absorbance at 260 nm
f dilution factor

A pure DNA solution should not show measurable absorption above 300 nm, and its OD_{260}/OD_{280} quotient should be at least 1.8.

3.3.3 Agarose gel electrophoresis

DNA fragments were separated by agarose gel electrophoresis according to their length. By adding ethidium bromide, a DNA intercalating fluorescent dye, the bands in the gel become visible under UV-light (Sharp *et al*., 1973). For preparation of agarose gels 1% (w/v) agarose was dissolved in 0.5% TBE buffer by boiling it up in the microwave. Following cooling down to 50-60 °C, 0.2 µl of an ethidium bromide stock solution (10 mg/ml) was added per ml agarose. The solution was then cast into the gel chamber, and a comb was inserted. Following solidification, the gel was covered with 0.5% TBE buffer, and the comb was removed. The DNA samples were supplemented with DNA loading dye if required and pipetted into the gel pockets. The electrophoresis was performed using a voltage of 190 V for about 20 min. The negatively charged DNA migrates to the anode, whereby DNA fragments are retarded to a different extent by the agarose matrix due to differences in size. The fragments were detected under UV-light (λ = 302 nm) and documented using the Imager Multi-Doc-It Digital Imaging system if applicable. To estimate the size of the fragments, a volume of 5 µl of the GeneRuler™ 1 kb Plus DNA Ladder (Fermentas) or EZ Load™ 500bp/100bp Molecular Ruler (Bio-Rad) was applied to a separate pocket of the gel.

3.3.3.1 Isolation of DNA fragments from agarose gels

The corresponding fragments were excised from the agarose gel under UV-light (λ = 302 nm) with a scalpel and transferred to a reaction vessel. DNA was extracted

using gel extraction kits from MACHERY-NAGEL (Nucleospin®II-Kit), FERMENTAS (GeneJET™ Gel Extraction Kit) or QIAGEN (QIAquick Gel Extraction Kit) according to the protocol supplied by the manufacturer. The isolated DNA was eluted in 30 µl sterile water and stored at -20 °C.

3.3.4 Enzymatic manipulation of dsDNA

3.3.4.1 Cleavage of dsDNA by restriction endonucleases

For specific cleavage of dsDNA type II restriction endonucleases were applied (Sambrook *et al.*, 1989, Wilson & Murray, 1991), which bind to a palindromic recognition sequence (restriction site). These restriction enzymes generate single stranded overhangs (sticky ends), which contain 3'-hydroxyl and 5'-phosphate ends. For analytical cleavage a maximum of 1 µg DNA was incubated at 37 °C in the appropriate buffer with 20 U of each restriction enzyme for about 2 h in a volume of 50 µl. For preparative cleavage, with the objective of subsequent ligation, 2 µg or the entire amount of PCR product and 2 µg of vector DNA were digested with 20 U of each restriction enzyme in a volume of 50 µl at 37 °C for 2 h. The volume of added restriction endonuclease in the reaction mixture should not exceed 10% of the total volume, as the activity of enzymes is influenced by glycerol, a component of the enzyme storage solution. The fragments were analyzed by agarose gel electrophoresis (3.3.3) and purified for subsequent ligation (3.3.3.1).

3.3.4.2 Ligation of DNA fragments

For ligation, digested vector and insert were mixed at an estimated molar ratio of 1:3 and ligated in a total volume of 20 µl with 1 U T4 DNA ligase (FERMENTAS or NEB) in the buffer supplied by the manufacturer, either overnight in a thermal cycler at 16 °C or for 1 h at RT. In order to increase the transformation efficiency, the T4 DNA ligase was heat inactivated by incubation at 65 °C for 10 min. Alternatively, the Quick Ligation™ Kit (NEW ENGLAND BIOLABS) was used, which allows for ligation within 5 minutes at RT. The procedure was performed according to the protocol supplied by the manufacturer. Subsequently, competent *E. coli* cells were chemically (3.2.3) transformed with the ligation mixture.

For ligation of gene libraries the digested vector and the randomized insert were also mixed in an estimated molar ratio of 1:3 and ligated in the buffer supplied by the

manufacturer with 1 U T4 DNA ligase (Roche). Incubation was performed overnight at 16 °C in a thermal cycler in a total volume of 20 µl. Subsequently, the T4 DNA ligase was heat inactivated by incubation at 65 °C for 10 min and dialyzed. Subsequently, competent *E. coli* cells were transformed by electroporation (3.2.5 & 3.2.6).

3.3.5 Amplification of DNA fragments by standard PCR (polymerase chain reaction)

The polymerase chain reaction (PCR; Mullis & Faloona, 1987; Saiki *et al*., 1988) is used to amplify a specific DNA fragment *in vitro*. This is achieved by cyclic repetition of the denaturation of the double-stranded DNA, followed by the hybridization (annealing) of primers (synthetic oligonucleotides that flank the DNA sequence of interest) and enzymatic DNA synthesis (extension). The DNA fragment is exponentially amplified. The reaction was performed in a total volume of 50 µl in a thermal cycler (lid temperature 110 °C). The standard reaction mixture contained 5-100 ng of template DNA, 2.5 U GoTaq® DNA polymerase, 5× Green GoTaq® reaction buffer [contains 7.5 mM $MgCl_2$ (final concentration: 1.5 mM $MgCl_2$) and loading buffer], 0.2 mM dNTP mix, and 1 µM of each primer. The standard PCR program was as follows:

step	temperature [°C]	duration
1. Initialization step	95	3 min
2. Denaturation	95	45 s
3. Annealing	T_A	45 s
4. Extension	72	1 min/kb
5. Finale elongation	72	10 min
6. Final hold	16	∞

Steps 2 to 4 were repeated 30 times.

The optimum annealing temperature T_A of the primers was calculated according to the following equation (Chester & Marshak, 1993), which takes the GC-content and the length of the primers into account:

$$\mathbf{T_M = 69,3 + 0,41 \cdot (\%GC) - \frac{650}{n}}$$

Equation 3: Calculation of the melting temperature of oligonucleotides.

T_M melting temperature of primers [°C]
%GC GC-content of primers [%]
n number of nucleotides in the primer

$$\mathbf{T_A = \left(\frac{T_{M1} + T_{M2}}{2}\right) - 3°C}$$

Equation 4: Calculation of the optimum annealing temperature of a primer in the PCR reaction.

T_A annealing temperature [°C]
T_{M1} & T_{M2} melting temperatures of the primers [°C]

The optimum annealing temperature was also experimentally determined using a thermal cycler with gradient function (EPPENDORF Mastercycler ep). To this end, different PCRs with annealing temperatures between 50 °C and 70 °C were set up in parallel, and the yields of the amplification products were determined.

If applicable, the specificity and yield of the amplification product was increased by applying nested PCR. To this end, two successive PCRs were carried out using two sets of primers. The PCR product from the first amplification step served as template for the second amplification using nested primers that bind within the PCR product and result in a shorter DNA fragment.

For high fidelity amplification of DNA fragments Phusion® High-Fidelity DNA polymerase was used, which – in contrast to Taq polymerase – possesses 3'→5' proofreading activity. The reaction was performed in a total volume of 50 µl containing 10 ng of template DNA, 1 U Phusion® High-Fidelity DNA polymerase, 5 × Phusion® HF reaction buffer [contains 7.5 mM $MgCl_2$ (final concentration: 1.5 mM $MgCl_2$)], 3 % (v/v) DMSO (optional; added for GC-rich templates), 0.2 mM dNTP mix, and 1 µM of each primer. The standard PCR program for Phusion® High-Fidelity DNA polymerase was as follows:

step	temperature [°C]	duration
1. Initialization step	98	30 s
2. Denaturation	98	10 s
3. Annealing	T_A	20 s
4. Extension	72	15 s/kb
5. Finale elongation	72	10 min
6. Final hold	16	∞

Steps 2 to 4 were repeated 30 times.

Best amplification results were achieved with an annealing temperature of 65 °C.

3.3.6 Colony PCR

To verify the success of cloning, an insert screening was performed by colony PCR. Transformants grown on selective LB agar were added to the PCR mixture by picking a single colony with a pipette tip and transferring small quantities of cells to the reaction mixture. The cells were subsequently disrupted in the initial denaturation step at 95 °C, and the released DNA was used as template in the following amplification cycles. If not stated otherwise, vector-specific amplification primers were used. The standard reaction mixture included 1 U GoTaq® DNA polymerase, 5 × Green GoTaq® reaction buffer, 0.2 mM dNTP-mix, 1 µM of each primer, and water to a final volume of 20 µl. The amplification was performed according to the standard protocol described in 3.3.5.

3.3.7 PCR methods for site-directed mutagenesis

3.3.7.1 QuikChange site-directed mutagenesis (QCM)

The QuikChange site-directed mutagenesis method allows for the efficient introduction of point mutations, insertions and deletions in any type of dsDNA plasmids. It is performed using Pfu DNA polymerase, which replicates both plasmid strains with high fidelity due to its 3'→5' proofreading activity.

The technique originally developed by STRATAGENE (La Jolla, USA) was modified according to a protocol published by Wang & Malcolm (1999) using a two-stage mutagenesis protocol. For introduction of point mutations complementary mutagenic primers with up to 35 bases in length and 12-15 bases of template complementary sequence on both sides of the mismatch were used. Pfu DNA polymerase extends and incorporates mutagenic primers during temperature cycling and generates a mutated plasmid containing staggered nicks. To avoid unproductive primer dimer formation, two separate primer extension reactions were performed initially. In the second step both primer extension reactions are combined and linearly amplified. Methylated DNA template is digested by treatment of the product with *Dpn*I. *E. coli* cells are transformed with the nicked vector DNA carrying the desired mutations, and the nicks are sealed by the DNA repair apparatus of the cells. See Figure 10 for illustration.

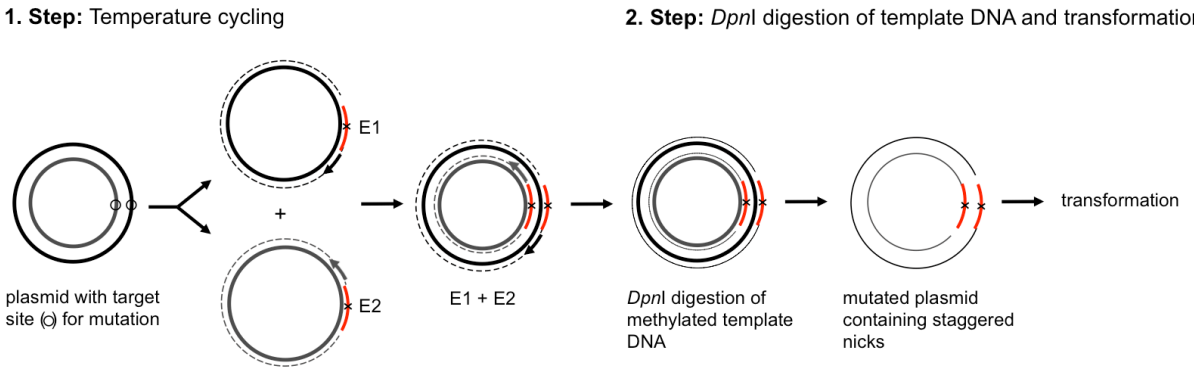

Figure 10: Overview of the QuikChange site-directed mutagenesis method.
In the first step the mutated plasmids containing staggered nicks are generated in two parallel primer extension reactions (E1 and E2). The reactions E1 and E2 are combined and amplified. In the second step, the DNA template is digested by treatment with *Dpn*I, and *E. coli* cells are transformed with the nicked vector DNA containing the desired mutations. The figure was adapted from the QuikChange™ Site-Directed Mutagenesis Kit manual (STRATAGENE).

The two separate primer extension reactions (E1 and E2) were performed each in a total volume of 50 µl containing 50 ng of template plasmid comprising the gene of interest, 2.5 U Pfu DNA polymerase, 10× Pfu DNA polymerase reaction buffer [contains 20 mM $MgCl_2$ (final concentration: 2 mM $MgCl_2$)], 0.2 mM dNTP mix, and 1.6 µM of either the 5' or 3' primer. The standard primer extension program using Pfu DNA polymerase was as follows:

step	temperature [°C]	duration
1. Initialization step	95	3 min
2. Denaturation	95	45 s
3. Annealing	T_A	1 min
4. Extension	72	2 min/kb
5. Finale elongation	72	10 min
6. Final hold	16	∞

Steps 2 to 4 were repeated 4 times.
Best results were achieved with an annealing temperature of 55 °C.

Subsequently, 25 µl of each primer extension reaction (E1 and E2) were mixed, supplemented with additional 2.5 U Pfu DNA polymerase and subjected to 18 cycles of QCM as described above. The methylated template DNA was digested by directly adding 20 U *Dpn*I to 25 µl of the QCM reaction mix and incubated at 37 °C for 1.5 h. Then, chemically competent *E. coli* Turbo cells were transformed using 10 µl of *Dpn*I-digested QCM mix.

3.3.7.2 Phusion® Site-Directed Mutagenesis Kit

For multiple amino acid insertions and deletions in plasmid DNA site-directed mutagenesis was performed using the Phusion® Site-Directed Mutagenesis Kit (FISHER SCIENTIFIC), according to the protocol supplied by the manufacturer. The complementary mutagenic primers required 5' phosphorylation. Details for the primer design are shown in Figure 11.

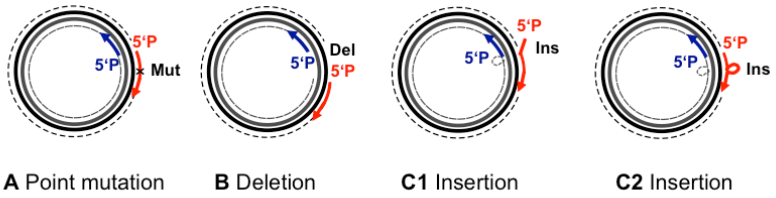

Figure 11: Schematic overview of the primer design for introducing point mutations (A), deletions (B), and insertions (C1+C2) applying the Phusion Site-Directed Mutagenesis Kit.
5' P: 5' phosphorylation. The figure was adapted from the Phusion® Site-Directed Mutagenesis Kit manual.

Amplification of the target plasmid with two 5' phosphorylated primers and Phusion® Hot Start II DNA polymerase was performed essentially as described in 3.3.5. The PCR product was circularized with Quick T4 DNA Ligase in a 5 min reaction (3.3.4.2) and chemically competent *E. coli* Turbo cells were transformed using 10 µl of the reaction mix.

3.3.7.3 Megaprimer PCR (Sarkar & Sommer, 1990)

The megaprimer PCR method is a site-directed mutagenesis method that is conducted in two sequential PCR reactions. In a first PCR the megaprimer was generated, by amplifying a DNA fragment using a gene flanking primer and the mutagenic primer. The gel-purified megaprimer (3.3.3 & 3.3.3.1) was used, together with a gene flanking primer of the opposite site of the gene, to obtain the full-length gene in a second PCR.

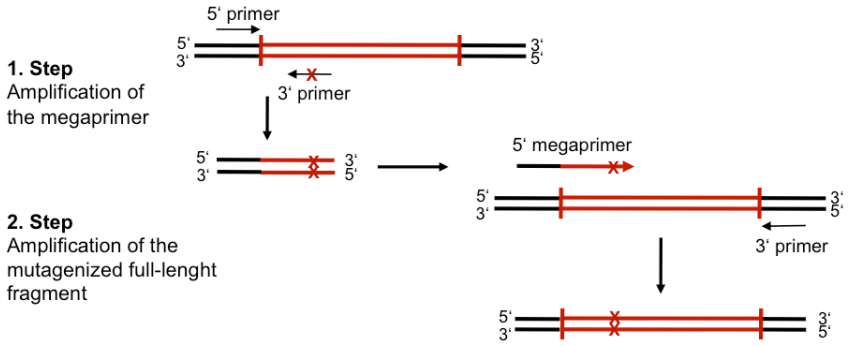

Figure 12: Scheme for standard megaprimer PCR.
Site-directed mutations were introduced in the first step by mutagenic primer, complementary to the target DNA.

Both PCRs were performed according to the previously described method (3.3.5). The optimum annealing temperature was experimentally determined, if required. In general, this method was applied, when the mutated nucleotide was located within the first or last 100 bases of a gene.

3.3.7.4 Overlap extension PCR (Ho *et al.*, 1989)

Site-directed mutagenesis by overlap extension PCR (OE-PCR) uses two complementary mutagenic primers with a length of 25-35 bp that are complementary to the target DNA and comprise the nucleotide changes in the central region of their sequences. The first two separate PCRs generated two overlapping fragments carrying the desired mutation, using a set of mutagenic primer and flanking primer each. These mutagenic fragments were subsequently purified by preparative gel electrophoresis (3.3.3 & 3.3.3.1). The gel-purified fragments were used as templates in combination with the flanking primers to amplify the entire gene. The amplification was carried out according to the standard protocol described in 3.3.5. For an illustrating scheme see Figure 13.

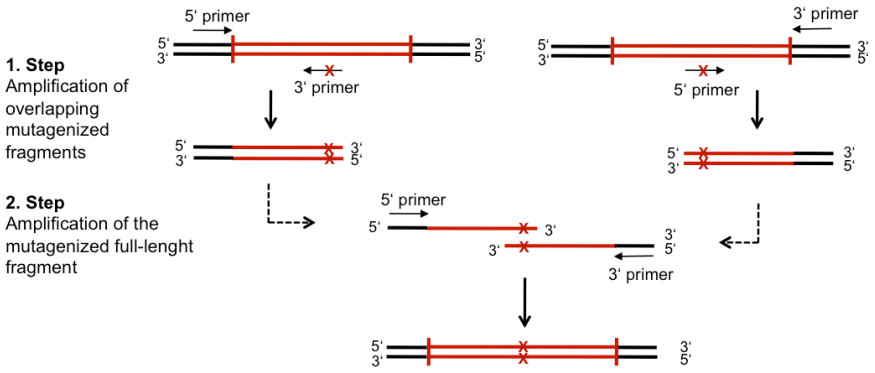

Figure 13: Scheme for standard OE-PCR.
In the first step the 5' and 3' fragments are amplified in two separate PCRs with a gene flanking primer and a mutagenic primer using the target DNA as template. In the second step the fragments served as template and the mutagenized full length construct is amplified using the flanking primers.

3.3.8 *In vitro* recombination by StEP (staggered extension process)

In vitro recombination by staggered extension process (Zhao *et al.*, 1998) is an efficient method for the recombination of homologous template sequences. Template sequences are primed followed by repeated cycles of denaturation and extremely abbreviated annealing/polymerase-catalyzed extension. Partially extended fragments hybridize randomly on templates harboring different mutations and extend further. This is repeated until full-length sequences are formed. At each round of annealing, template switching results in crossovers in regions of sequence homology, yielding polynucleotides contain sequence information from different parental sequences. The recombination diversity can be controlled by altering time and temperature of the annealing/extension steps. See Figure 14 for illustration.

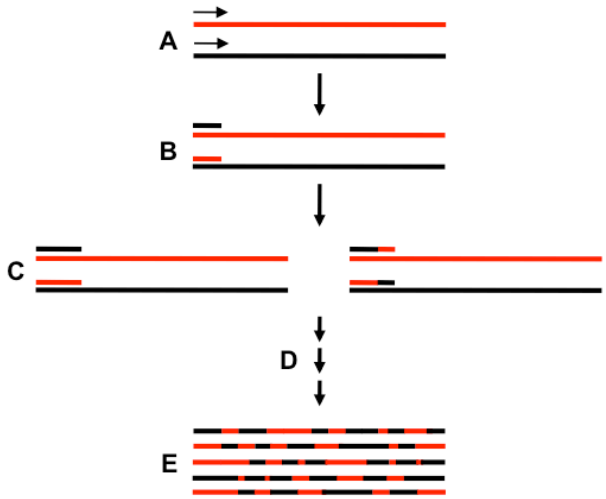

Figure 14: Scheme for StEP recombination.

A: Denatured templates genes are primed with one defined primer. **B:** Short fragments are produced by brief polymerase-catalyzed extension. **C:** In a subsequent cycle of StEP, fragments randomly prime the templates (template switching) and extend further. **D+E:** The process is repeated until full-length gens are produced. The figure was adapted from Zhao *et al.* (1998).

The technique was applied to rapidly recombine beneficial mutations from positive first-generation variants while deleterious mutations are removed due to backcrossing with the wild-type sequence.

The reaction was performed in a total volume of 50 µl containing 10 ng of each template DNA, 2.5 U GoTag® DNA polymerase, 5× Green GoTaq® reaction reaction buffer [contains 7.5 mM $MgCl_2$ (final concentration: 1.5 mM $MgCl_2$) and loading buffer], 0.2 mM dNTP mix, and 0.15 µM of each primer. The PCR program was as follows:

step	**temperature [°C]**	**duration**
1. Initialization step	95	5 min
2. Denaturation	94	30 s
3. Annealing/Extension	T_A	3 s
4. Final hold	4	∞

Steps 2 to 3 were repeated 130 times.

The optimum annealing temperature was experimentally determined applying a gradient of 40-55°C (EPPENDORF Mastercycler ep). Subsequently, nested PCR was performed as described in 3.3.5 in order to increase the yield of the amplification product.

3.3.9 Transposon-mediated insertion mutagenesis (MGS™ Kit)

The Mutation Generation System™ Kit (MGS™ Kit, FISHER SCIENTIFIC) has been designed for rapid and efficient construction of linker scanning libraries for functional analysis of proteins and regulatory DNA regions. The system employs the highly efficient transposition machinery of the bacteriophage Mu to insert an artificial transposon, designated as Entranceposon, randomly into any target plasmid. MuA Transposase catalyzes the *in vitro* transposition reaction. The inserted clones generated in the transposition reaction are digested with the *Not*I restriction endonuclease to remove the body of the Entranceposon, and subsequent self-ligation results in a 15 bp insertion in the target DNA. See Figure 15 for illustration.

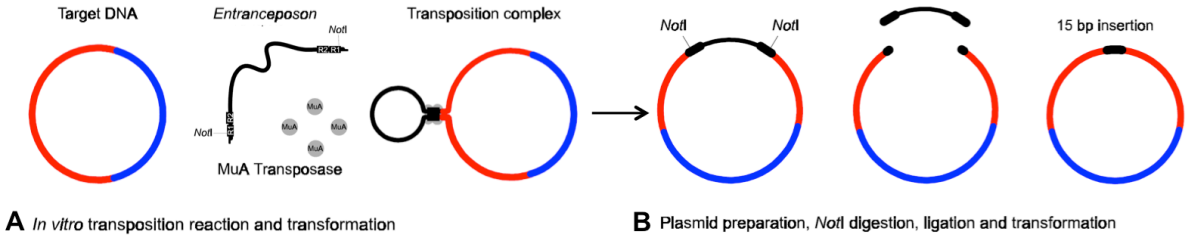

Figure 15: Flowchart of insertion mutagenesis.
A: *In vitro* transposition reaction/transposon insertion reaction, transformation and selection of transposon insertion clones, and plasmid preparation. The insert containing the Entranceposon is subcloned into a fresh vector. **B:** Plasmid preparation. *Not*I digestion, ligation, and transformation. The Figure was adapted from the MGS™ Kit manual.

In case the transposition occurs in the coding region of the target gene, the 15 bp insertion is translated into five extra in-frame amino acids (Figure 16).

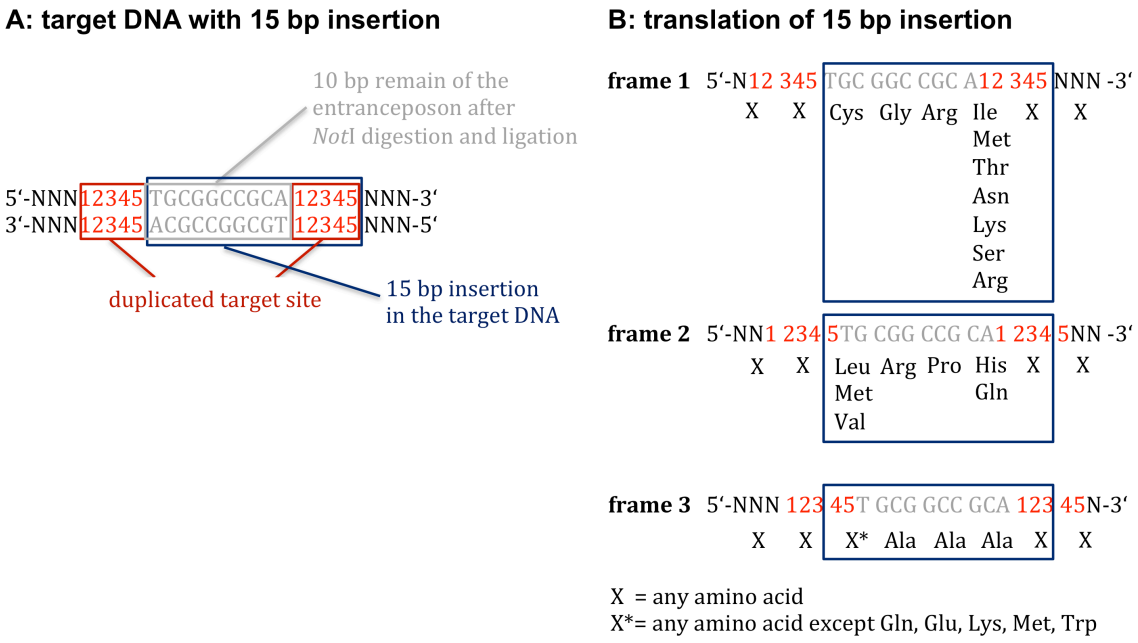

Figure 16: Structure of the 15 bp insertion (A) and translation of 15 bp insertion (B).
A: 15bp insertion into target DNA results in duplicated target sites. **B:** In-frame translation. The Figure was adapted from the MGS™ Kit manual.

The transposon insertion reaction using HyperMu MuA transposase (EPICENTRE; 50× more active than regular MuA transposase) and M1-Cam^R Entranceposon (supplied with MGS™ Kit; 1254 bp) was performed in a total volume of 20 µl containing a minimum of 150 ng of template plasmid, 100 ng M1-Cam^R Entranceposon, 1 U HypeMu MuA transposase (EPICENTRE), 10× HyperMu reaction buffer. The reaction mix was incubated at 30 °C for 4 h using a thermal

cycler. The HyperMu MuA transposase was inactivated by adding HyperMu 10x STOP solution (containing 1% SDS) and heat inactivation at 75 °C for 10 min. Chemically competent *E. coli* Turbo cells were transformed with the reaction mix and plated on LB agar plates containing the plasmid and Entranceposon selection marker (10 µg/ml CHLOR for M1-Cam^R). Transformants from plates were scraped, pooled, and plasmid DNA was prepared using QIAGEN Midi prep kit (3.3.1.2). As the transposon insertion occurs also in the vector backbone, the insert containing the entranceposon was subcloned into a fresh vector (3.3.4.1 and 3.3.4.2), and plasmid DNA was prepared. Subsequently, the body of the entranceposon was removed by *Not*I digestion and the fragment was gel-purified (3.3.3 & 3.3.3.1). Subsequently, *Not*I-digested fragments were re-ligated using the Quick Ligation™ Kit. To favour self-ligation of the *Not*I-digested fragments the DNA concentration in the ligation set up was diluted to 1-5 ng/µl. Chemically competent *E. coli* Turbo cells were transformed with the reaction mix and plated on LB agar plates containing the plasmid selection marker. Transformants from plates were scraped, pooled and plasmid DNA was prepared using QIAGEN Midi prep kit (3.3.1.2). To map the insertion site of randomly chosen transposon insertion clones colony-PCR (3.3.6) was performed using *Not*I mini-primers provided with the kit (forward and reverse transposon specific primers) and vector-specific flanking primers. Alternatively, insertion sites can be mapped by *Not*I restriction endonuclease digestion of the plasmid preparation. 10 randomly chosen transposon insertion clones were subjected to sequencing to determine the exact position of the insert and the inserted amino acid sequence.

3.3.10 Construction of a gene library

The gene, from which a library was generated, was subjected to simultaneous mutagenesis of selected positions (SHM) (3.3.7.3 and 3.3.7.4), StEP recombination (3.3.8) or transposon-mediated insertion mutagenesis (3.3.9). The reaction product and 2 µg target vector were cleaved with the corresponding restriction endonucleases and purified by agarose gel electrophoresis (3.3.3 & 3.3.3.1). The DNA was eluted in 50 °C warm, sterile water to obtain optimum yield. The ligation (3.3.4.2) was performed in 6-9 parallel reactions à 20 µl overnight at 16 °C. Freshly prepared electro-competent Δ*hisA*-Δ*hisF* or NEB Turbo cells (100 µl) were transformed with 5 µl dialyzed ligation mixture each (3.2.5 & 3.2.6), i.e. 15-30

transformations were carried out per gene library. The cell suspension was supplemented with 1.5 ml SOC medium per transformation assay, pooled in 50 ml falcon vessels, and incubated for 1 h at 37 °C and 220 rpm. Subsequently, the cells were harvested by centrifugation (EPPENDORF Centrifuge 5810R, 4000 rpm, 10 min, 25 °C) and resuspended in 8 ml SOC medium. The cell suspension was then plated in aliquots à 200 µl on 40 large SOC selective agar plates (Ø 14.5 cm). For determination of the gene library size, 100 µl of different dilutions were streaked out on small selective SOC agar plates (Ø 8.5 cm) (see 3.3.10.1).

The transformants grown on large SOC plates were scraped off using a sterile spatula and liquid LB media. The resulting cell suspension was pooled and centrifuged (EPPENDORF Centrifuge 5810R, 4000 rpm, 15 min, 4 °C). The cell pellet was weighted, and the plasmid gene library was isolated by maxi-preparation (3.3.1.2).

3.3.10.1 Determination of the size of a gene library

To determine the size of a gene library (number of independent clones with correct insert length), 100 µl of transformed cells were diluted 10^{-1} to 10^{-8}-fold, and plated on small SOC agar plates containing the adequate antibiotics. Following overnight incubation at 37 °C colonies were counted, and the number of transformed cells was determined according to Equation 5:

$$\mathbf{n_T = n_C \cdot f \cdot V_s}$$

Equation 5: Determination of the number of transformed cells.

n_T	number of transformed cells
n_C	number of colonies on the agar plate
f	plating dilution factor
V_s	volume dilution factor (total volume of plated cell suspension, divided by 100 µl)

Subsequently the ligation efficiency ($0 \leq L \leq 1$) was determined by performing colony PCR with at least 20 selected colonies (3.3.6) using Equation 6.

$$\mathbf{L = \frac{n_V}{n_G}}$$

Equation 6: Determination of the ligation efficiency.

L	ligation efficiency
n_V	number of colonies with correct insert
n_G	number of analyzed colonies (usually 20)

The size of the gene library (G) was determined with Equation 7 by multiplying the number of transformed cells (n_T) by the ligation efficiency (L):

$$\mathbf{G = n_T \cdot L}$$

Equation 7: Determination of the gene library size.

In order to determine the quality of a gene library usually 10 randomly selected clones were analyzed by sequencing.

3.3.11 DNA sequencing

All Dr0930 and PTE gene constructs generated and used in this work were entirely sequenced to exclude inadvertent mutations. The determination of nucleotide sequences was performed either by the company Geneart (part of Life Technologies, Regensburg) or at the Gene Technologies Laboratory at the Texas A&M University (College Station, USA). DNA was sequenced according to the dideoxy-chain termination method (Sanger *et al.*, 1977). In this technique 2', 3'-dideoxynucleotides stained with different fluorescence labels are used in addition to the 2'-deoxynucleotides in a thermal cycle sequencing reaction (Sears *et al*., 1992; Slatko, 1994). The reaction products are 3'-labelled single-stranded termination fragments, which were separated by gel electrophoresis. Subsequently, the nucleotide sequence was analyzed.

Samples for sequencing orders at Genart contained 100-300 ng DNA and 1.25 µM of sequencing primer in a total volume of 8 µl. Genart performed the sequencing reaction, and analyzed the data using an ABI PRISM® 3700 DNA Analyzer (APPLIED BIOSYSTEMS).

Alternatively, templates were sequenced with an ABI PRISM® BigDye™ Terminator Cycle Sequencing Ready Reaction Kit (PERKIN ELMER APPLIED BIOSYSTEMS) and analyzed by the Gene Technologies Laboratory using an ABI PRISM® 3100 Genetic Analyzer (APPLIED BIOSYSTEMS). To this end, the sequencing reaction was performed in a total volume of 6 µl in a thermal cycler. The standard reaction mixture contained 2 µl BigDye™ Terminator Ready Reaction Mix (contains 5× reaction buffer, dNTPs, ddNTPs, AmpliTaq DNA Polymerase FS), 400-600 ng plasmid DNA, and 3 µM of sequencing primer, according to the protocol

supplied by the manufacturer. The PCR program for cycle sequencing was as follows:

step	temperature [°C]	duration
1. Initialization step	96	2 min
2. Denaturation	96	30 s
3. Annealing	T_A	15 s
4. Extension	60	4 min
5. Final hold	4	∞

Steps 2 to 4 were repeated 30 times.
Best results were achieved with an annealing temperature of 55 °C.

Extension products were purified and excess dye-terminators were removed using Micro Bio-Spin P-30 spin columns (BIO-RAD) according to the protocol supplied by the manufacturer. Samples were dryed using a SpeedVac device, and submitted to the Gene Technologies Laboratory for evaluation.

The sequences were received in ABI-formate and analyzed using the software Sequencher.

3.4 Protein biochemistry methods

3.4.1 Gene expression and purification of recombinant protein

3.4.1.1 Gene expression in analytical scale

To test, whether cloned genes are overexpressed and in order to analyze whether the recombinant proteins were produced in soluble form, expression was performed in analytical scale in triplicates (“test expression”).

To this end, 5 ml LB medium were supplemented with the appropriate antibiotics, inoculated with an overnight culture of a single colony to an OD_{600} of 0.1, and incubated at 37 °C and 220 rpm. At an OD_{600} value of 0.4–0.6, the cultures were supplemented with 1.0 mM $CoCl_2$, if not stated otherwise, and induced by adding IPTG to a final concentration of 0.5 mM. Following incubation at 37 °C (wild-type Dr0930 and Dr0930 variants) or 30 °C (wild-type PTE) for 4 h, the cell suspension was centrifuged (EPPENDORF Centrifuge 5415R, 8000 rpm, 5 min, 4 °C). The pellet was resuspended in 100 µl of 20 mM HEPES, pH 7.5, 100 µM $CoCl_2$ (wild-type Dr0930 and Dr0930 variants) or 50 mM HEPES, pH 8.5, 100 µM $CoCl_2$ (wild-type

PTE). The cells were disrupted by sonication (amplitude 20%, 20 s) or by addition of 100 µl PopCulture® reagent (1×; ready to use reagent; MERCK) followed by incubation at RT for 40 minutes. Following centrifugation (EPPENDORF Centrifuge 5415R, 13200 rpm, 10 min, 4 °C) the supernatant (containing soluble protein) was taken off, and the pellet (containing insoluble protein) was resuspended in an equal volume of the appropriate resuspension buffer. Aliquots of the supernatant (S) and the resuspended pellet (P) were supplemented with SDS sample buffer (5×), and incubated for 5 min at 95 °C. Subsequently, a volume of 5-10 µl of both S and P was analyzed by SDS-PAGE.

3.4.1.2 Gene expression and purification of recombinant proteins in preparative scale

For purification of proteins in preparative scale, 1 l LB (wild-type Dr0930 and Dr0930 variants) or TB (wild-type PTE) medium was supplemented with the corresponding antibiotics and 0.5 mM $CoCl_2$ or 1.0 mM $CoCl_2$, respectively. The medium was inoculated with a freshly prepared overnight *E. coli* culture from a single colony to an OD_{600} value of 0.1. The suspension was incubated at 37 °C and 140 rpm. At an OD_{600} value of 0.4-0.6, for wild-type Dr0930 and variants the suspension was supplemented with additional 0.5 mM $CoCl_2$. The suspension was induced with 0.5 mM IPTG and incubated overnight at 37 °C (wild-type Dr0930 and Dr0930 variants) or 30 °C (wild-type PTE), respectively. The cells were harvested by centrifugation (Sorvall RC5B plus, GS3 Rotor, 4000 rpm, 10 min, 4 °C), and the pellet was resuspended in 30 ml of 20 mM HEPES, pH 7.5, 100 µM $CoCl_2$ (wild-type Dr0930 and Dr0930 variants) or 50 mM HEPES, pH 8.5, 100 µM $CoCl_2$ (wild-type PTE), respectively. Cells were disrupted by sonication on ice (amplitude 70%, 4 min, interval: 15 s pulse and 15 s pause). The suspension was centrifuged (Sorvall RC5B plus, SS34 Rotor, 13000 rpm, 30 min, 4 °C) and the supernatant (S) was further processed.

3.4.2 Protein purification from the soluble cell fraction

3.4.2.1 Protamine sulfate and ammonium sulfate precipitation

Protamine sulfate and ammonium sulfate precipitation are efficient methods used for initial sample concentration and cleanup (GE HEALTHCARE, Strategies for

Protein Purification, Handbook). Protamine sulfate, a small cationic protein that binds and precipitates nucleic acids, is used to remove DNA impurities from protein samples. During ammonium sulfate precipitation, proteins will begin to salt out as increased salt concentrations enhance hydrophobic interactions between proteins. Different proteins are precipitated at different salt concentrations, consequently differences in hydrophobicity result in a fractionated precipitation. Proper selection of ammonium sulfate concentration allows for the removal of protein impurities from the crude extract.

A 1% (w/v) protamine sulfate solution was prepared by dissolving 0.2 g protamine sulfate in 20 ml resuspension buffer (20 mM HEPES, pH 7.5, 100 µM $CoCl_2$ or 50 mM HEPES, pH 8.5, 100 µM $CoCl_2$) by incubation at 40-50 °C. Prior to use the solution was cooled down. The following steps were carried out in the cold room at 4 °C: 1% (w/v) protamine sulfate solution was added dropwise to the supernatant on ice, while stirring vigorously, and the suspension was incubated for another 20 min on ice. The suspension was centrifuged (Sorvall RC5B plus, SS34 Rotor, 13000 rpm, 30 min, 4 °C), and the supernatant (S) was subjected to ammonium sulfate precipitation. For this purpose, $(NH_4)_2SO_4$ was added to a final concentration of 45% saturated solution, portion-wise as crystalline $(NH_4)_2SO_4$ salt using a spatula, while stirring vigorously on ice. The amount of $(NH_4)_2SO_4$ was calculated using the weblink provided by EnCor Biotechnology Inc (Gainesville, USA; www.encorbio.com/protocols/AM-SO4.htm). The suspension was centrifuged (Sorvall RC5B plus, SS34 Rotor, 13000 rpm, 30 min, 4 °C), and the pellet, containing the protein of interest, was resuspended in 15 ml of 20 mM HEPES, pH 7.5, 100 µM $CoCl_2$ or 50 mM HEPES, pH 8.5, 100 µM $CoCl_2$. Both fractions were further analyzed by SDS-PAGE (3.5.2) and absorption spectroscopy. Subsequently, $(NH_4)_2SO_4$ was removed by dialysis (3.4.2.4.1).

3.4.2.2 Ion exchange chromatography (IEX)

Ion exchange chromatography is based on the competition of charged molecules (proteins and salt ions) for interaction with immobilized ion exchange groups of opposite charge. In the first stage, charged molecules adsorb reversibly to the immobilized support material. Subsequently, bound molecules are eluted by a gradient of steadily increasing ionic strength, or alternatively a pH-gradient. The charge of the protein is mainly dependent on the amino acids with charged side

chains. In the acidic or neutral pH-range the amino groups, mainly those of Lys, Arg and His, are protonated and the protein exposes cationic behavior, whereas in a neutral or basic pH-range, the carboxyl groups of Asp and Glu residues are negatively charged and consequently the protein is anionic. The total charge of proteins is mainly dependent on the amino acid composition and the pH-value of the surrounding buffer. Ion exchange chromatography can be subdivided into cation exchange chromatography, in which positively charged ions bind to a negatively charged resin, and anion exchange chromatography, where negatively charged ions bind to a positively charged resin.

Wild-type Dr0930 and Dr0930 variants were purified using a XK26 column packed with Q Sepharose Fast Flow ion exchange media (GE HEALTHCARE, CV: 40 ml) or another anion exchange column (Resource Q 6 ml; MonoQ 5/50 GL). Wild-type PTE was purified using a simple gravity flow column (SIGMA ALDRICH) packed with DEAE Fast Flow ion exchange material (GE HEALTHCARE, CV: 20 ml).

The purification with the Q Sepharose Fast Flow column was performed using the chromatography system ÄKTA™ Purifier 10 (GE HEALTHCARE) as follows:

Flow rate:	5 ml/min
Equilibration:	1 CV binding buffer[a]
Sample volume:	15-30 ml protein solution in binding buffer[a]
Wash:	2 CV binding buffer[a]
Elution:	8 CV 1st gradient (0–0.5 M NaCl in binding buffer[a]), 1 CV 2nd gradient (0.5–2 M NaCl in binding buffer[a]); 4 ml fractions were collected.
Column purification:	5 CV elution buffer[b]
Reequilibration:	3 CV binding buffer[a]
Purging and storage:	5 CV H_2O; 3 CV 20% ethanol

[a]: binding buffer: 20 mM HEPES, pH 7.5, 100 µM $CoCl_2$
[b]: elution buffer: 20 mM HEPES, pH 7.5, 100 µM $CoCl_2$, 2 M NaCl

The purification with the Resource Q 6 ml column was performed using the chromatography system ÄKTA™ Purifier 10 (GE HEALTHCARE) as follows:

Flow rate:	5 ml/min
Equilibration:	2 CV binding buffer[a]
Sample volume:	35 ml protein solution in binding buffer[a]
Wash:	6 CV binding buffer[a]
Elution:	20 CV gradient (0–1.5 M NaCl in binding buffer[a]); 3 ml fractions were collected.
Column purification:	5 CV elution buffer[b]
Reequilibration:	5 CV binding buffer[a]
Purging and storage:	5 CV H_2O; 3 CV 20% ethanol

[a]: binding buffer: 20 mM HEPES, pH 7.5
[b]: elution buffer: 20 mM HEPES, pH 7.5, 2 M NaCl

The purification with the MonoQ 5/50 GL column was performed using the chromatography system ÄKTA™ Purifier 10 (GE HEALTHCARE) as follows:

Flow rate:	2 ml/min
Equilibration:	2 CV binding buffer[a]
Sample volume:	20 ml protein solution in binding buffer[a]
Wash:	10 CV binding buffer[a]
Elution:	30 CV gradient (0–0.5 M NaCl in binding buffer[a]); 0.5 ml fractions were collected.
Column purification:	5 CV elution buffer[b]
Reequilibration:	5 CV binding buffer[a]
Purging and storage:	5 CV H_2O; 3 CV 20% ethanol

[a]: binding buffer: 20 mM HEPES, pH 7.5
[b]: elution buffer: 20 mM HEPES, pH 7.5, 2 M NaCl

The elution of protein was monitored by detecting the absorbance at 260, 280 and 550 nm (inherent absorption of wild-type Dr0930 and Dr0930 variants). Further analysis of the eluted fractions was done using SDS-PAGE (3.5.2). Pure fractions were pooled and dialyzed against 5 l of 20 mM HEPES, pH 7.5, 100 µM $CoCl_2$ (3.4.2.4.1).

The purification of wild-type PTE by the DEAE Sepharose Fast Flow column was performed manually using a gravity flow column and an isocratic gradient in a simple and fast bind-wash-elute procedure: impurity proteins bind to the column whereas wild-type PTE elutes (reverse-purification). The procedure is described as follows:

Equilibration:	2 CV binding buffer[a]
Sample volume:	25 ml protein solution in binding buffer[a]
Elution:	2 CV binding buffer[a]; 1 ml fractions were collected.
Column purification:	5 CV elution buffer[b]
Reequilibration:	5 CV binding buffer[a]
Purging and storage:	5 CV H_2O; 3 CV 20% ethanol

[a]: binding buffer: 50 mM HEPES, pH 8.5, 100 µM $CoCl_2$
[b]: elution buffer: 50 mM HEPES, pH 8.5, 100 µM $CoCl_2$, 2 M NaCl

The eluted fractions were analyzed using SDS-PAGE (3.5.2). Pure fractions were pooled and dialyzed against 5 l of 50 mM HEPES, pH 8.5, 100 µM $CoCl_2$ (3.4.2.4.1).

3.4.2.3 Preparative gel filtration

Gel filtration is a chromatographic technique, which is based upon the principle of a reverse molecular sieve (size exclusion chromatography). When the mobile phase passes through the porous support material at a constant flow rate, small molecules are able to diffuse into the pores, while larger molecules are excluded. As a consequence, small molecules are retarded with respect to larger molecules, which cause proteins to be fractionated according to their size.

In this work preparative gel filtration was performed with the ÄKTA purifier 10 (GE HEALTHCARE) at RT or the FPLC LCC-501 device (GE HEALTHCARE) in the cold room at 4 °C, using a Hi Load 26/60 Superdex 200 Prep Grade (GE HEALTHCARE, CV: 320 ml) or Hi Load 16/60 Superdex 75 Prep Grade column (GE HEALTHCARE, CV: 120 ml). These columns consist of highly cross-linked porous agarose beads (mean particle size: 34 µm; different pore size) to which dextran has been covalently bound. The maximum volume of loaded protein was about 5-10 ml. For this reason the sample had to be concentrated (3.4.2.5) before it was loaded onto the column using a superloop. The column was equilibrated with 20 mM HEPES, pH 7.5, 100 µM $CoCl_2$, 300 mM NaCl (wild-type Dr0930 and Dr0930 variants) or 50 mM HEPES, pH 8.5, 100 µM $CoCl_2$, 300 mM NaCl (wild-type PTE). Proteins were eluted with 1.2 CV of the same buffer at a flow rate of 1 ml/min (back pressure: max. 0.3 MPa). The run was recorded using a manual plotter, which measured the absorbance at 280 nm. The fraction collector was started at the beginning of the elution, and fractions of 4 ml volume were collected. The fractions were further analyzed by SDS-PAGE (3.5.2).

3.4.2.4 Desalting of protein solutions

3.4.2.4.1 Dialysis of protein solutions

To exchange the buffer of a protein solution or to remove salt, a dialysis was performed overnight against an at least 100-fold volume excess of buffer at 4 °C in the cold room. A dialysis tubing (Visking or Spectra/Por) with a molecular cut-off of 14 kDa (or 10 kDa) was used, which retains the protein while low molecular substances can pass through the membrane. For enzyme kinetic measurements the purified Dr0930 variants were dialyzed once against 5 l of 20 mM HEPES, pH 7.5, 100 µM $CoCl_2$ (wild-type Dr0930 and Dr0930 variants) or 50 mM HEPES, pH 8.5, 100 µM $CoCl_2$ (wild-type PTE).

3.4.2.4.2 Desalting and buffer exchange by GE illustra NAP™ or PD-10 columns

If applicable, protein solutions were desalted or buffers were exchanged in-between chromatography runs, prior to ICP-MS measurements or prior to the pH-dependent colorimetric assay using the GE illustra NAP™ (prepacked with Sephadex™ G-25 DNA Grade) or PD-10 columns according to the protocols supplied by the manufacturer.

3.4.2.4.3 Desalting via GE Sephadex G25 Desalting

If the Dr0930 variants were purified by two successive anionic exchange chromatography steps (3.4.2.2), the protein solution was desalted after the first purification step using the GE Sephadex G25 Desalting column. Desalting was performed with the chromatography system ÄKTA™ Purifier 10 (GE HEALTHCARE) as follows:

Flowrate:	10 ml/min
Equilibration:	0.1 CV
Sample volume:	max. 20 ml protein solution in buffer[a], containing up to 1.5 mM NaCl
Isocratic elution:	2 CV binding buffer[a]; 5 ml fractions were collected.
Storage:	binding buffer[a]

[a]: binding buffer: 20 mM HEPES, pH 7.5

3.4.2.5 Concentrating protein solutions

Protein solutions were concentrated using Amicon® centrifugal filter devices (Amicon Ultra-15; molecular cut-off: 10 kDa) by a semi-permeable membrane according to the instructions of the manufacturer (Eppendorf Centrifuge 5810R, 4000 rpm, 4 °C).

3.4.2.6 Storage of purified proteins

Purified and concentrated proteins were frozen in liquid nitrogen either dropwise or as aliquots in reaction vessels and stored at -80 °C.

3.5 Analytical methods

3.5.1 Protein concentration determination via UV-absorption spectroscopy

The aromatic amino acids tryptophan, tyrosin and phenylalanine as well as disulfide bonds (cystine) absorb UV-light in a wavelength interval between 250 and 300 nm. The molar extinction coefficient at 280 nm (ε_{280}) can be determined from the amino acid composition (Pace *et al.*, 1995) (Equation 8).

$$\boldsymbol{\varepsilon_{280} = \sum \mathrm{Trp} \cdot 5500 + \sum \mathrm{Tyr} \cdot 1490 + \sum \mathrm{Cystine} \cdot 125}$$

Equation 8: Determination of the molar extinction coefficient ε_{280}.
ε_{280} molar extinction coefficient at 280 nm [$M^{-1}cm^{-1}$]

The specific extinction coefficient ($^{0.1\%}A_{280}$) can be calculated according to Equation 9 taking the molecular weight into account.

$$^{0.1\%}\boldsymbol{A_{280}} = \frac{\boldsymbol{\varepsilon_{280}}}{\mathbf{MW}}$$

Equation 9: Determination of the specific extinction coefficient $^{0.1\%}A_{280}$.
$^{0.1\%}A_{280}$ specific extinction coefficient at 280 nm [cm^2/mg]
MW molecular weight of the protein [g/mol]

Using Lambert-Beer's law, the protein concentration can be determined by measuring the absorbance at 280 nm (Equation 10):

$$\mathbf{A_{280}} = {}^{0.1\%}\mathbf{A_{280}} \cdot \mathbf{c} \cdot \mathbf{d}$$

$$\mathbf{c} = \frac{\mathbf{A_{280}}}{{}^{0.1\%}\mathbf{A_{280}} \cdot \mathbf{d}}$$

Equation 10: Determination of the protein concentration by using the specific extinction coefficient $^{0.1\%}A_{280}$.
A_{280} absorbance at 280 nm
c concentration [mg/ml]
d pathlength [cm]
$^{0.1\%}A_{280}$ specific extinction coefficient at 280 nm [cm^2/mg]

Absorbance spectra between 220 and 350 nm were recorded. The absorbance maximum should be at 278 nm and the A_{280}/A_{250} ratio should be at least 1.8 for a pure protein solution. No absorbance above 300 nm should be detectable to exclude any distortion of the results caused by light scattering resulting from aggregation. Table 2 shows the molar extinction coefficients, molecular weights, and specific extinction coefficients of the wild-type proteins used in this work. For protein variants the respective coefficients were recalculated.

Table 2: Properties of wild-type Dr0930 and wild-type PTE relevant for concentration determination.
Number of tryptophan and tyrosine residues, molar extinction coefficients, molecular weight (MW) and specific extinction coefficients of investigated wild-type proteins.

protein	Σ Trp + Tyr	ε_{280} [$M^{-1}cm^{-1}$]	MW [g/mol]	$^{0.1\%}A_{280}$ [cm/mg]
wild-type PTE	4 × Trp + 5 × Tyr	29450	36420	0.81
wild-type Dr0930	3 × Trp + 9 × Tyr	29910	34728	0.86

3.5.2 SDS-polyacrylamide gel electrophoresis (SDS-PAGE)

Proteins are denatured by the detergent sodium dodecyl sulfate (SDS) and negatively charged in proportion to their molecular weights. SDS binds to the protein in a ratio of approximately one molecule SDS per 1.4 amino acid residues. The net charge of proteins can be neglected compared to the negative charge of the protein complexed with SDS, which yields an approximately uniform mass to charge ratio. As a consequence, electrophoretic mobility depends only on the sieve effect of the gel: the migration speed is inversely proportional to the logarithm of mass (Laemmli 1970). Table 3 shows the composition of the 12.5% SDS gels used in this work.

Table 3: Composition of a 12.5% SDS-PAGE gel.
Amount specification applies to 13 gels.

	resolving gel (12.5%)	stacking gel (6%)
resolving/stacking gel buffer	19.5 ml	7.38 ml
acrylamide-SL (30%)	26.2 ml	5.9 ml
H_2O	31.58 ml	15.95 ml
TEMED	0.089 ml	0.029 ml
APS (10%)	0.195 ml	0.089 ml

Samples were supplemented 1:4 with 5× SDS-PAGE sample buffer and incubated for 5 min at 95 °C. Gel pockets were loaded with 5-20 µl of sample, and gels were run at 50 mA and 300 V for about 30 min. Subsequently gels were stained with SDS-PAGE staining solution, whereby the detection limit of the Coomassie Brilliant Blue dye G-250 is between 200-500 ng protein/mm^2. Gels were swayed for 10 min in the staining solution and excess dye was removed by repeatedly boiling in water (microwave 900 W).

Alternatively, ready-to use PhastGel™ Homogeneous-12.5 gels with PhastGel™ Buffer Strips, SDS (GE HEALTHCARE) were used in a PhastSystem™ Separation Control (GE HEALTHCARE) according to the protocols supplied by the manufacturer.

3.5.3 ICP-MS measurements

ICP-MS measurements were performed by Dr. Siddhesh Kamat and Swapnil Ghodge (group of Prof. Dr. F. M. Raushel), using the PerkinElmer DRC II ICP-MS device (software: Eland, PerkinElmer). For this purpose protein buffer was exchanged to metal-free buffer using GE illustra NAP™-25 or PD-10 columns. If applicable, protein and buffer samples were lyophilized for the shipment.

3.5.4 Steady-state enzyme kinetics

3.5.4.1 Colorimetric assay for OPH activity with *p*-nitrophenol substituted OPs

The OPH activity for *p*-nitrophenyl substituted OPs (compounds 1-7, 4.2.2) was measured in a colorimetric assay (Dumas *et al.*, 1989). The activity was followed by observing the release of the product *p*-nitrophenol under basic conditions at 400 nm

(ε_{400} = 17000 M^{-1} cm^{-1}) and 30 °C. Reactions were performed in 50 mM CHES, pH 9.0, 100 µM $CoCl_2$ and various concentrations of substrate (Omburo *et al.*, 1992). For OP compounds 4 and 5 the assay was supplemented with 12% MeOH, due to limited solubility of the substrates. Measurements were performed with a Cary 100 Bio (VARIAN) or V650 (JASCO) spectrophotometer (total volume = 1 ml) or a SpectraMax-340 plate reader (MOLECULAR DEVICES, total volume = 250 µl), using plastic cuvettes and VIS 96-well plates, respectively. The reaction was started by adding the enzyme. Background of free *p*-nitrophenol, associated with absorbance at 400 nm, as well as limited solubility of substrates restricted the maximum substrate concentration applicable. The concentration of OP compounds 1-7 was determined by titration with KOH prior to steady-state enzyme kinetics (2.10.2).

3.5.4.2 Coupled DTNB (Ellman's Reagent) assay

The OPH activity for the hydrolysis of phosphorothiolates (OP compound 8, 4.2.2) was measured in a coupled colorimetric assay (adapted from Yang *et al.*, 2003). Cleavage of the phosphorothiolate bond was followed by inclusion of DTNB (Ellman's reagent, 5,5'-dithiobis-(2-nitrobenzoic acid)), which reacts with the free thiol released as product. The disulfide bond of DTNB is cleaved yielding 2-nitro-5-thiobenzoate (NTB^-), which ionizes to NTB^{2-} dianion (yellow color) under basic conditions. The reaction is followed at 412 nm (ε_{412} = 14150 M^{-1} cm^{-1}) and 30 °C. Reactions were performed in 50 mM HEPES pH 8.0, 0.3 mM DTNB, 100 µM $CoCl_2$, 12% MeOH, and various concentrations of substrate. The concentration of OP compound 8 was determined enzymatically using wild-type PTE (2.10.2).

3.5.4.3 pH-dependent colorimetric assay

The hydrolysis of δ-nonanoic lactone (δ-NL; 4.2.2) was monitored using a pH-sensitive colorimetric assay (Chapman & Wong, 2002; Khersonsky & Tawfik, 2005). Proton release from carboxylic acid formation was followed using the pH-indicator *m*-cresol purple. The reactions were performed in 2.5 mM BICINE (initial pH: 8.3), 0.1 mM $CoCl_2$, 1.4% DMSO, 0.1 mM *m*-cresol purple, 0.2 M NaCl and various concentrations of substrate (0-2 mM). The change in absorbance at 577 nm was monitored at 30 °C.

The proteins Dr0930 and PTE were stored in 20 mM HEPES pH 7.5, 100 µM $CoCl_2$ or 50 mM HEPES pH 8.5, 100 µM $CoCl_2$, respectively. Prior to use, the buffer was exchanged to 10 mM bicine pH 8.3, 100 µM $CoCl_2$ using a NAP-25 desalting column. The assay mixture was pre-incubated for 10 min at 30 °C to obtain a constant baseline, and the reaction was started by adding the enzyme. The conversion factor was determined by *in-situ* calibration with acetic acid (change of absorbance A_{577} per change in proton concentration, $\varepsilon_{577} = 1.17 \times 10^3\ M^{-1}cm^{-1}$). A slight background rate was observed in the absence of any enzyme, presumably due to acidification of the reaction assay by atmospheric CO_2 (Khersonsky & Tawfik, 2005). The background rate was independent of the substrate concentration, and subtracted from the initial rates.

3.5.4.4 Data analysis

Steady-state kinetic parameters were determined by fitting the experimental data of the saturation curves to the Michaelis-Menten equation (Equation 11), using the computer program SigmaPlot.

$$\mathbf{v} = \frac{\mathbf{v_{max}} \cdot [\mathbf{S}]}{\mathbf{K_M} + [\mathbf{S}]}$$

Equation 11: Michaelis-Menten Equation.
v: initial velocity
v_{max}: maximum velocity
S: substrate concentration
K_M: Michaelis constant

The catalytic rates (v) were corrected for background rate of spontaneous hydrolysis in the absence of enzyme. If the substrate concentration required to saturate an enzyme variant was higher than the maximal solubility of the substrate, V_{max}/K_M was determined by a linear regression of the initial part of the saturation curve.

3.5.5 Dixon plot for competitive inhibition

The Dixon plot is used to determine the type of enzyme inhibition and the dissociation constant (K_i) for an enzyme-inhibitor complex (Segel, 1993). The velocity equation for competitive inhibition can be converted to a linear form in which the varied ligand is [I] (Equation 12).

$$\frac{\mathbf{1}}{\mathbf{v}} = \frac{\mathbf{K_M}}{\mathbf{v_{max}} \cdot [\mathbf{S}] \cdot \mathbf{K_i}} [\mathbf{I}] + \frac{\mathbf{1}}{\mathbf{v_{max}}} \left(\mathbf{1} + \frac{\mathbf{K_M}}{[\mathbf{S}]}\right)$$

Equation 12: Velocity equation for competitive inhibition in linear form.
v: initial velocity
v_{max}: maximum velocity
S: substrate concentration
K_M: Michaelis constant
K_i: dissociation constant

The effect on velocity (v) is determined over a range of inhibitor concentrations [I]. A plot of 1/v versus [I] at a constant unsaturating concentration of [S] (here: [S] = K_M) yields a straight line with a positive slope. If the inhibition is known to be competitive, K_i can be determined from the slope of a linear fit of the data points according to Equation 12. The type of enzyme inhibition is confirmed to be competitive, when the linear graph intersects with the y-achses (1/v) at $1/v_{max}$ and the x-achses ([I]) at $-K_i$.

3.5.6 Determination of stereopreference

The enzymatic hydrolysis of racemic OP compounds was monitored as a function of time. The change of A_{400} over time is an exponential time courses. Depending on the compound and enzyme variant used, one or two phases can be observed and fit by a single- or double exponential fit according to Equation 13.

$$\mathbf{A}(t) = \mathbf{y_0} + \mathbf{a}\left(\mathbf{1} - e^{-k_1 t}\right)$$

$$\mathbf{A}(t) = \mathbf{y_0} + \mathbf{a}\left(\mathbf{1} - e^{-k_1 t}\right) + \mathbf{b}\left(\mathbf{1} - e^{-k_2 t}\right)$$

Equation 13: Single- and double-exponential fit of an exponential time course.
A(t): absorption at time t
y_0: off-set (in absorbance)
a, b: magnitudes of exponential phases
k_1, k_2: observed rate constants
t time

If a double-exponential fit did not converge due to limited data points, either the observed rate constant of the second phase, k_2, or the magnitude of the second exponential phase, b, were constrained. The substrate concentration was kept below the K_M value; hence, the time course follows pseudo-first order kinetics and the associated rate constants are directly proportional to the amount of enzyme added (Cleland, 1970; Nowlan *et al.*, 2006). The catalytic efficiency, k_{cat}/K_M, was estimated from the exponential components according to Equation 14.

$$\frac{k_{cat}}{K_M} = \frac{k_x}{[E]}$$

Equation 14: Determination of the catalytic efficiency of individual enantiomers.
k_x: observed rate constant
[E]: enzyme concentration

To identify the configuration of the non-hydrolyzed isomer in solution after the reaction has approached an end point at approximately half amplitude, wild-type PTE or engineered PTE variants, with previous reported stereopreference for 4-acetylphenol leaving group analogues of OPs 1-5 (Tsai *et al.*, 2010a), were added to the reaction mixture, inducing the (exclusive) hydrolysis of the residual isomer.

3.6 Protein crystallization and X-ray structure determination

Data collection and X-ray structure determination was performed in collaboration with Nicholas Fox (group of Prof. Dr. David Barondeau, Texas A&M University, College Station, USA) and Dr. Chitra Rajendran (group of Prof. Dr. Christine Ziegler, University of Regensburg).

3.6.1 Protein crystallization

Protein crystallization was performed by sitting- and hanging drop vapor diffusion methods (McPherson, 1982). To explore various conditions, initial crystal screening was performed using commercially available crystallization kits containing 96 unique conditions. The crystallization kits used in this work are listed as follows: Crystal Screen I+II (Hampton Research), PEG/ION Screen 1+2 (Hampton Research), PEG RX I+II (Hampton Research), and Wizard I+II (Emerald BioSystems) were used for Dr0930_81. Crystall screens Classic II Suite (Qiagen) and JBScreen Classic 1, 4, 5, 8, 9 (Jena Bioscience) were used for Dr0930_106 and Dr0930_134. Initial crystal screening was either performed manually or using an automatic robotic system: Phoenix Liquid Handling System (96-syringe, ARI-Art Robins Instrumentation, sitting-drop method; 1 µl protein mix + 1 µl reservoir solution, 55 µl reservoir volume; T = 22 °C). In any case, crystallization conditions were manually refined applying a one or two variable (precipitant concentration, additive, pH, protein concentration) grid screen. For all set-ups, the protein solution was supplemented with 1.0 mM $CoCl_2$. In order to obtain a structure with bound ligand, co-crystallization set-ups with

substrate and product analogues, soaking experiments with higher amounts of ligand, and streak- and macro-seeding experiments were performed. For co-crystallization experiments inhibitors were added in the following amount to the protein solution: 3% (v/v) diisopropyl methylphosphonate (DIMP; 165 mM), 1% (v/v) diethyl 4-methylbenzylphosphonate (DE4MBP; 41 mM; limited solubility), 100 mM diethyl phosphate (DEP), 100 mM sodium cacodylate (CAC). To increase the solubility of the inhibitors, organic solvents such as DMSO and methanol were added to some of the set-ups. Set-up volumes in a typical manual performed hanging drop co-crystallization experiment, were as follows: 2 µl of protein (approximately 12.8 - 13.5 mg/ml, supplemented with 1.0 mM $CoCl_2$ and inhibitor) and 2 µl of precipitating agent were mixed and placed on a siliconized coverslip, and equilibrated over 500 µl of the precipitating agent (T = 20 °C). The Crystals of the Dr0930 variants were diamond shaped, purple in color and obtained under various conditions within a few days to weeks.

3.6.2 Data collection

Single crystals were transferred to a cryo protectant solution and flash frozen in liquid nitrogen. Diffraction data was collected at Stanford Synchrotron Radiation Lightsource (SSRL; at Stanford University, Menlo Park, USA) by remote data collection on beamline 7-1 or measurements were performed on-site at the Swiss Light Source (SLS; at Paul Scherrer Institute, Villigen, Switzerland) at beamline PXII at 295 K and 100 K, recording single 0.1 or 0.5 degree images on a CCD (ADSC QUANTUM 315r) or PILATUS detector, respectively.

3.6.3 Data processing and structure determination

The data sets for Dr0930_81 were indexed, integrated and scaled with the HKL2000 package (Otwinowski & Minor, 1997), and phases were determined by molecular replacement with Phaser version 2.1 (McCoy *et al.*, 2007). For Dr0930_106 and Dr0930_134, data processing was done using XDS (Kabsch, 1993), and the data quality assessment was performed using phenix.xtriage (Adams *et al.*, 2002). Molecular replacement was performed with MOLREP within the CCP4i suite (Potterton *et al.*, 2004). In all cases the structure of wild-type Dr0930 (PDB ID 3FDK) was used as search model and initial refinement of the structures was performed

using Refmac5 (Murshudov *et al.*, 1997) of the CCP4 suite (Collaborative Computational Project, Number 4, 1994).

For Dr0930_81 difference electron density and omit maps were manually fit with the XtalView package (McRee, 1999), and further refinement was done with CNS (Brunger *et al.*, 1998). All structures were superimposed with Sequoia (Bruns *et al.*, 1999). For Dr0930_106 and Dr0930_134, the model was further improved in several refinement rounds using the automated restrained refinement within the program PHENIX (Adams *et al.*, 2002) and interactive modeling with Coot (Emsley & Cowtan, 2004). The final models were analyzed using the program MolProbity (Davis *et al.*, 2007).

3.7 RosettaLigand Docking

Ligand docking was performed by Christoph Malisi (group of Dr. Birte Höcker, MPI Tübingen) using the RosettaLigand program as implemented in the Rosetta software suite version 3.3 (Davis & Baker, 2009; http://www.rosettacommons.org/manuals/archive/rosetta3.3_user_guide/d4/d47/ligand_dock.html). The program parameters applied were based on the parameters used in Khare *et al.* (2012). The RosettaLigand application tries to identify conformations and relative orientations of a receptor-ligand complex that minimizes the Rosetta energy score function, employing a stochastic search algorithm. Many conformations are created, of which only the best scoring ones are used for further analysis. The program was used in this work to dock DIMP and EPXN ligands into the active site of wild-type PTE and Dr0930_134.

3.7.1 Protein receptor and cofactor preparation for docking

The protein receptor structures (PTE: PDB ID 1EZ2; Dr0930_134) and cofactors were reformatted for ligand docking experiments. Hydrogen atoms were added in the protein receptor structures using Chimera (Pettersen *et al.*, 2004). A residue parameter file was created for the carboxylated Lysine (KCX 143) as described in the Rosetta documentation. The identity of the active site cobalt atoms for the Dr0930 variant were changed to zinc and distance constraints were calculated for the side chain atoms coordinating these metals in order to maintain the native coordination geometry. A penalty energy term was applied, if these atoms deviate more than 0.2 Å from the measured distances. Rosetta's receptor minimization protocol was used to

create ten minimized structures for each receptor protein. The resulting repacked structure with the lowest energy was used for docking calculations.

3.7.2 Ligand preparation and ligand positioning

Ligand conformers were created with the software omega2, and charges were added by molcharge (Hawkins *et al.*, 2010). Ligand parameter files were created as described in the Rosetta documentation.

The selection of starting positions for the ligands is decribed in the following: For the PTE protein receptor, a random conformation of DIMP, excluding the native one the ligand assumes in the crystal structure, was chosen as starting position to avoid biasing of the docking algorithm toward the known binding mode. The starting positions of EPXN were determined by roughly positioning an arbitrary ligand conformer in the binding pocket of PTE. For Dr0930_134, the ligand conformer was superimposed with the phosphorus atom of DIMP in the PTE structure 1EZ2, and then the complex was superimposed onto the Dr0930 structure.

For some Dr0930_134 docking runs, geometric constraints, derived from the 1EZ2 structure, were put on the phosphoryl oxygen and the phosphorus atoms of the ligand to enrich results containing the desired catalytic geometry. The distance between the phosphoryl oxygen and the interacting β-zinc ion was constrained to 2.5 ± 0.4 Å and the angle formed by zinc, phosphoryl oxygen and phosphorus atom was set to 140° ± 30°.

3.7.3 Docking calculations and analysis of docking results

For each receptor-ligand pair, 5000 receptor-ligand conformations were created with the RosettaLigand application. For analysis, the top 5% docking results by Rosetta's total energy score were ranked according to their predicted binding energies. The top 10 or 20 ranked binders were then used for analysis. The described ranking scheme is suggested by the RosettaLigand documentation to identify good binders among low energy and therefore plausible complex structures.

4 RESULTS AND DISCUSSION

4.1 *D. radiodurans* Dr0930: a close homologue of *P. diminuta* PTE

Dr0930 from *D. radiodurans R1* belongs to the family of phosphotriesterase-like lactonases (PLL). PLL enzymes are the closest homologues to PTE, although they share only 26-35% sequence identity with the bacterial phosphotriesterase *P. diminuta* PTE (Merone *et al.*, 2005; Porzio *et al.*, 2007; Afriat *et al.*, 2006). The native enzymatic activity of PLL enzymes is for the hydrolysis of 5- and 6-membered lactones that vary in type and position of the substitution on the lactone ring (C-O bond cleaved). Furthermore, PLL enzymes share a low promiscuous OPH activity for ethyl-paraoxon (P-O bond cleaved).

Mutually, promiscuous esterase activity (2-naphthyl acetate) has been reported for wild-type PTE and esterase and lactonase activities (e.g. 2-naphthyl acetate, dihydrocoumarine, 5-thiobutyl-γ-butyrolactone) for an engineered PTE variant with elevated expression level. However, no activity has yet been reported for δ-nonanoic lactone, the most proficient substrate of Dr0930 (Roodveldt & Tawfik, 2005a/b; Afriat *et al.*, 2006).

Table 4 summarizes annotated and characterized PLL enzymes and lists the corresponding native and promiscuous substrates.

Table 4: PTE and selected homologues PLL enzymes.

	seq. identity	annotated substrates	promiscuous substrates
P. diminuta PTE	-	various OPs	2-naphthyl acetate
D. radiodurans Dr0930	31%	γ-/δ-lactone	EPXN, MPXN
G. kaustophilus GKL	28%	γ-/δ-lactone	EPXN, HSL
S. solfataricus SsoPox	31%	TBBL	MPXN, EPXN, diazinon, chlorpyrifos, coumaphos, parathion
R. erythropolis AhlA	28%	TBBL, HSL, γ-/δ-lactone	EPXN
M. tuberculosis PPH	34%	γ-/δ-lactone, TBBL, HSL	EPXN

Seq. identity: sequence identity relative to *P. diminuta* PTE. OP: organophosphate. HSL: N-acyl homoserine lactone (5-membered lactone ring with N-acyl substitution at position C3). TBBL: 5-thiobutyl-γ-butyrolactone (5-membered lactone ring with thiobutyl substitution at position C5). Ethyl-paraoxon: O,O-diethyl O-(4-nitrophenyl) phosphate. γ-/δ-lactone: 5- and 6-membered lactone ring with alkyl substitution at position C5 and C6, respectively. EPXN: ethyl-paraoxon. MPXN: methyl-paraoxon.

P. diminuta PTE: *Pseudomonas diminuta* PTE (Omburo *et al.*, 1992; Dumas *et al.*, 1989; Roodveldt & Tawfik, 2005a/b). *D. radiodurans* Dr0930: *Deinococcus radiodurans R1* Dr0930 (Xiang *et al.*, 2009; Hawwa *et al.*, 2009b). *G. kaustophilus* GKL: *Geobacillus kaustophilus* GKL (Chow *et al.*, 2010). *S. solfataricus* SsoPox: *Sulfolobus solfataricus* SsoPox (Elias *et al.*, 2008; Merone *et al.*, 2008). *R. erythropolis* AhlA: *Rhodococcus erythropolis* AhlA (Afriat *et al.*, 2006). *M. tuberculosis* PPH: *Mycobacterium tuberculosis* PPH (Afriat *et al.*, 2006). The listed PLL enyzmes share 29-59% sequence identity among each other.

The structures of substrates listed in Table 4 are shown in Figure 65 in the appendix.

A structure based sequence alignment of PTE and PLL enzymes from Table 4, generated by 3D-Coffee (Expresso; www.tcoffee.org), is shown in Figure 17.

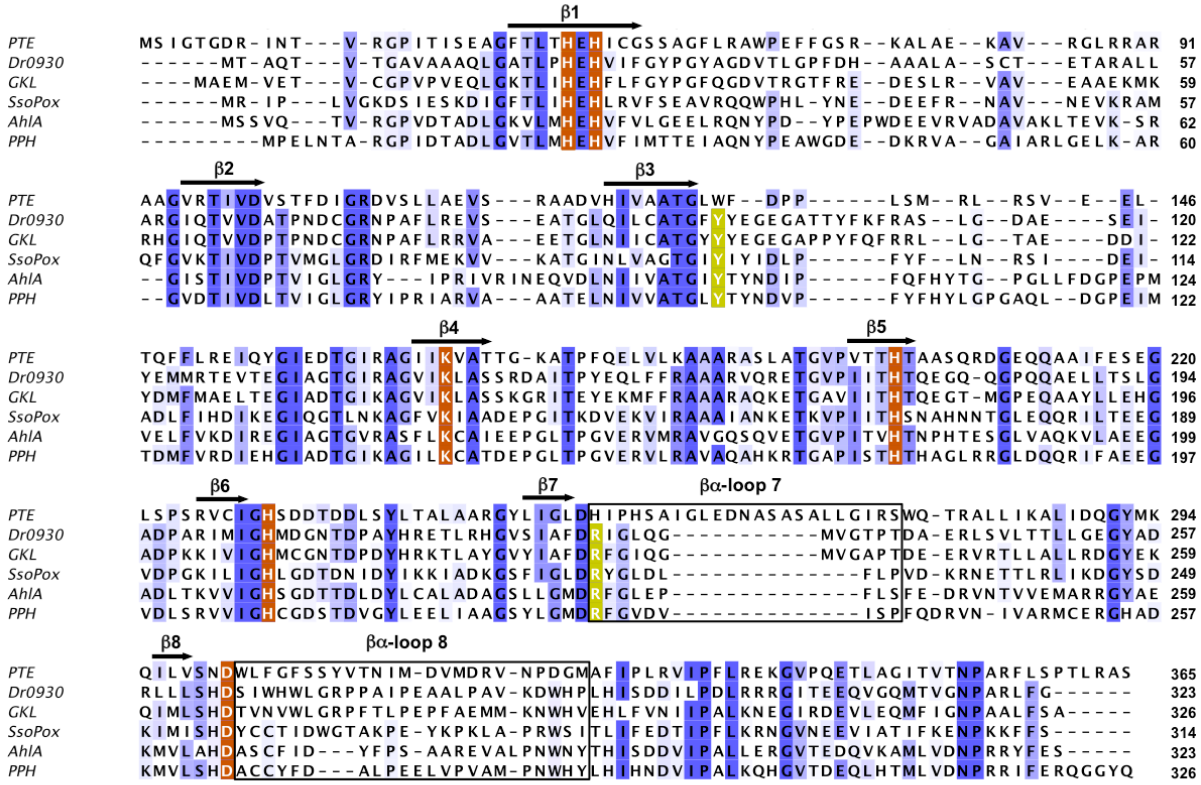

Figure 17: Structure based sequence alignment of PTE and selected PLL enzymes generated by 3D-coffee.
Sequence alignment of *P. diminuta* PTE, *D. radiodurans* Dr0930, *G. kaustophilus* GKL, *S. solfataricus* SsoPox, *R. erythropolis* AhlA, and *M. tuberculosis* PPH. Conserved residues are colored in shades of blue. Catalytic important residues for PTE and PLL enzymes are highlighted in orange. Catalytic important residues only conserved for PLL enzymes are highlighted in light green. The boxes highlight the residues corresponding to loops at the C-terminal ends of β-strands 7 and 8.

The H-E-H motif in β-strand 1, the carboxylated lysine from β-strand 4, the histidine residues at the ends of β-strands 5 and 6, and an aspartate residue at the end of β-strand 8 are conserved. Conserved active site residues of PLL enzymes are tyrosine and arginine in the βα-loops 3 and 7. These residues differ from the PTE residues (Trp131 and His254). Major structural differences are in the length and

conformation of the βα-loops (in particular loops 7 and 8). X-ray structures of ligated PLL enzymes and docking experiments, revealed that particularly residues from these loops form a hydrophobic channel accomodating the aliphatic side chain of the substituted lactones (see also Figure 19A); the lactone ring is positioned by polar (e.g. conserved Tyr and Arg, and others residues depending on enzyme and substrate) and non-polar interactions (Elias *et al.*, 2008; Chow *et al.*, 2010, Xiang *et al.*, 2009).

D. radiodurans Dr0930 is the best structurally and functionally characterized bacterial PLL enzyme. Dr0930 is a robust, thermostable (T_M = 88°C) and highly soluble protein, exhibiting promiscuous activity for the hydrolysis of the insecticides methyl- and ethyl-paraoxon (Hawwa *et al.*, 2009b; Xiang *et al.*, 2009). A partial structural superposition of *D. radiodurans R1* Dr0930 and *P. diminuta* PTE is shown in Figure 18A. The polar residues important for substrate positioning in Dr0930 and PTE are shown in Figure 18B and C.

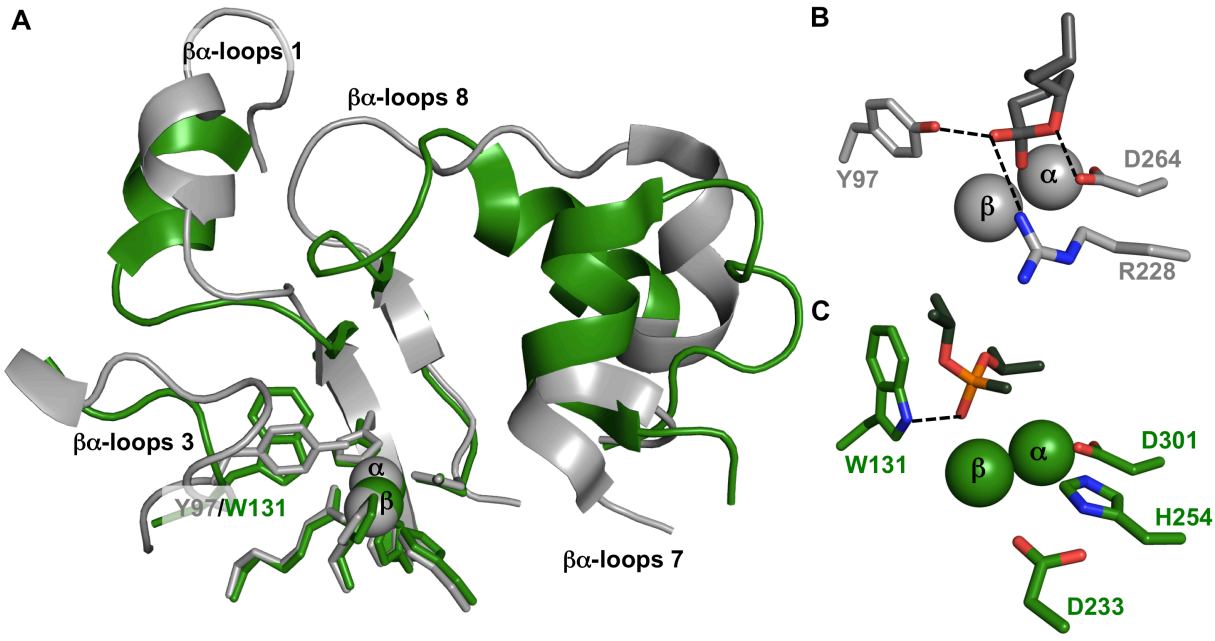

Figure 18: Structural superposition of *D. radiodurans R1* Dr0930 and *P. diminuta* PTE (A) and excerpts of the active sites of Dr0930 (B) and PTE (C).
Dr0930 (PDB ID 3FDK) and PTE (PDB ID 1EZ2) are depicted in grey and green, respectively.
A: Parts of the backbone are shown, which illustrate major structural differences in the length and conformation of the βα-loops (predominately βα-loop 1, 3, 7 and 8). The over-all backbone conformation of Dr0930 is quite similar to that of PTE (backbone r.m.s.d = 1.3 Å), in particular the central barrel (not shown) and metal coordinating residues superimpose well. Residue Y97, which is conserved within the PLL family and located in βα-loop 3 (Figure 17), aligns with W131 in PTE. The quartenary structure of PTE and Dr0930 is dimeric; the dimer is formed by interaction of βα-loop 1 and 3 (not shown).

B: Excerpt of the active site of Dr0930 with the docked tetrahedral intermediate that is formed upon the hydrolysis of δ-nonanoic lactone (depicted in dark grey). The lactone intermediate in Dr0930 is positioned by polar interactions with Y97 (2.8 Å; Y97 aligns with W131 in PTE), R228 (5.3 Å; R228 aligns with H254 in PTE) and D264 (2.3 Å; D264 aligns with D301 in PTE). The side chain of the R228 residue is shifted by approximately 3 Å in the docked structure relative to the conformation observed in the crystal structure to accommodate the ligand (native conformation is not shown).

C: Excerpt of the active site of PTE, complexed with the substrate analogue DIMP (diisopropyl methylphosphonate; depicted in dark green). PTE exhibits only one hydrogen bond (3.2 Å) between N^{E1} of Trp131 and the phosphoryl oxygen of DIMP. Together with D301 and D233, H254 is involved in proton shuttling in PTE. The equivalent residues in Dr0930 to D301 and H254 are D264 and R228. At the equivalent position of D233 in Dr0930 is a glycine (G207; not shown).

The substrate binding pockets for Dr0930 and PTE are shown in Figure 19A and B, respectively.

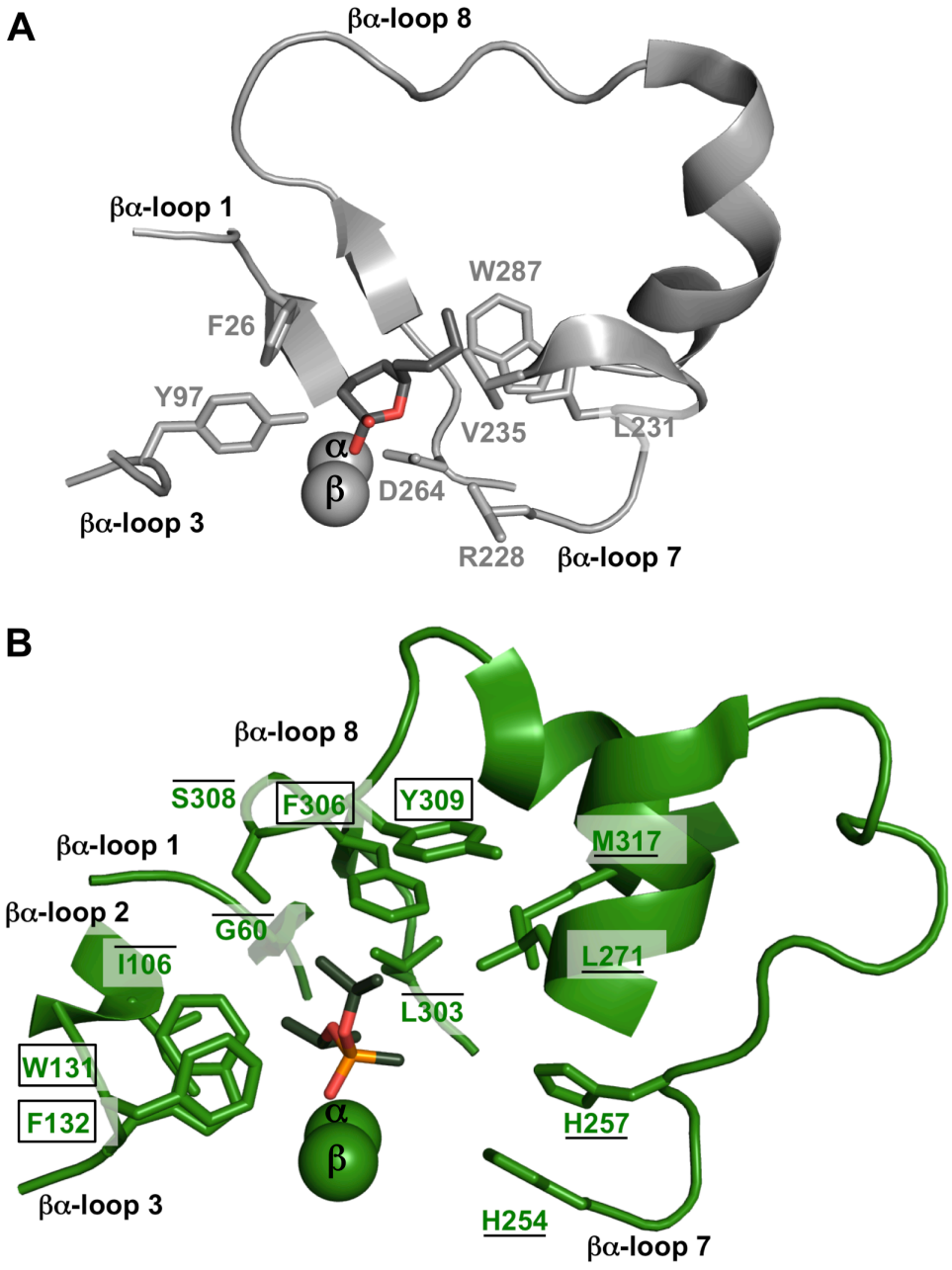

Figure 19: The substrate binding pockets of Dr0930 (A) and PTE (B) (same view as in Figure 18A).
Dr0930 (PDB ID 3FDK) and PTE (PDB ID 1EZ2) are depicted in grey and green, respectively. For Dr0930 the docked tetrahedral intermediate that is formed upon the hydrolysis of δ-nonanoic lactone is shown and depicted in dark grey. For PTE the co-crystallized substrate analogue DIMP (diisopropyl methylphosphonate) is shown and depicted in dark green.
A: The substrate binding pocket of Dr0930 is formed by βα-loops 1, 3, 7 and 8. The lactone intermediate is positioned by polar interactions with Y97, R228 and D264 and non-polar interactions with mainly F26, L231, V235, and W287. The βα-loops 7 and 8 form a hydrophobic channel that accommodates the aliphatic side chain of the substitued lactone.
B: The substrate binding pocket of PTE is formed by βα-loops 1, 2, 3, 7 and 8. Except for the electrostatic interaction between Trp131 and the phosphoryl oxygen of the DIMP ligand, PTE exhibits a hydrophobic substrate binding pocket. The substrate binding pocket is subdivided in three subsites. The small subsite is occupied by the O-isopropyl substituent of DIMP and formed by βα-loops 1, 2, and 8 (G60, I106, L303, and S308; overlined). The large subsite is occupied by the methyl substituent of DIMP and formed by βα-loops 7 and 8 (H254, H257, L271, and M317; underlined). The leaving group subsite is occupied by the O-isopropyl substituent of DIMP and formed by βα-loops 3 and 8 (W131, F132, F306, Y309; boxed).

The hydrolytic activity of PLL enzymes towards various lactone derivatives has been characterized extensively. However, except for SsoPox, the promiscuous OPH activity of PLL enzymes has only been investigated for methyl- and ethyl-paraoxon so far (Afriat *et al.*, 2006; Chow *et al.*, 2009; Chow *et al.*, 2010; Elias *et al.*, 2008; Hawwa *et al.*, 2009b; Merone *et al.*, 2008; Xiang *et al.*, 2009). However, the hitherto determined kinetic parameters for the hydrolysis of ethyl-paraoxon by PLL enzymes are not comparable as assay conditions vary significantly (Merone *et al.*, 2008; Afriat *et al.*, 2006; Chow *et al*., 2010; Hawwa *et al.*, 2009a/b; Xiang *et al.*, 2009).

To explore the substrate scope, wild-type Dr0930 was characterized here for its promiscuous activity using a broad spectrum of OPs. Mutually, wild-type PTE was analyzed for its ability to hydrolyze δ-nonanoic lactone.

4.2 Dr0930 and PTE: promiscuous and native activities

4.2.1 Heterologous expression in *E. coli* and purification of the recombinant wild-type Dr0930 and wild-type PTE proteins

Chemically competent *E. coli* BL21(DE3) Rosetta 2 and *E. coli* BL21(DE3) cells were transformed with the pET30a-*dr0930* and pET20b-*pte* constructs, and single colonies were used to inoculate 2 l LB and 8 l TB medium, respectively. The medium was supplemented with 0.5 mM $CoCl_2$ and 1.0 mM $CoCl_2$ each. Following induction of gene expression with 0.5 mM IPTG and addition of extra 0.5 mM $CoCl_2$ for the Dr0930 expression cultures, the cell suspension was incubated overnight at 37 °C and 30 °C, respectively (3.4.1.2). The cells were resuspended in 20 mM HEPES,

pH 7.5, 100 µM $CoCl_2$ and 50 mM HEPES, pH 8.5, 100 µM $CoCl_2$, respectively. Cells were disrupted by sonication. The recombinant proteins were purified from the soluble fraction of the cell extract by protamine sulfate and ammonium sulfate precipitation (3.4.2.1) and, either anion exchange chromatography (3.4.2.2) or a combination of anion exchange chromatography and gel filtration chromatography (3.4.2.3). Combined pure protein fractions were dialyzed overnight against 5 l of 20 mM HEPES, pH 7.5, 100 µM $CoCl_2$ and 50 mM HEPES, pH 8.5, 100 µM $CoCl_2$, respectively.

Typical elution profiles and SDS-gels of the purification steps of wild-type Dr0930 and wild-type PTE are shown in Figure 20 and Figure 21.

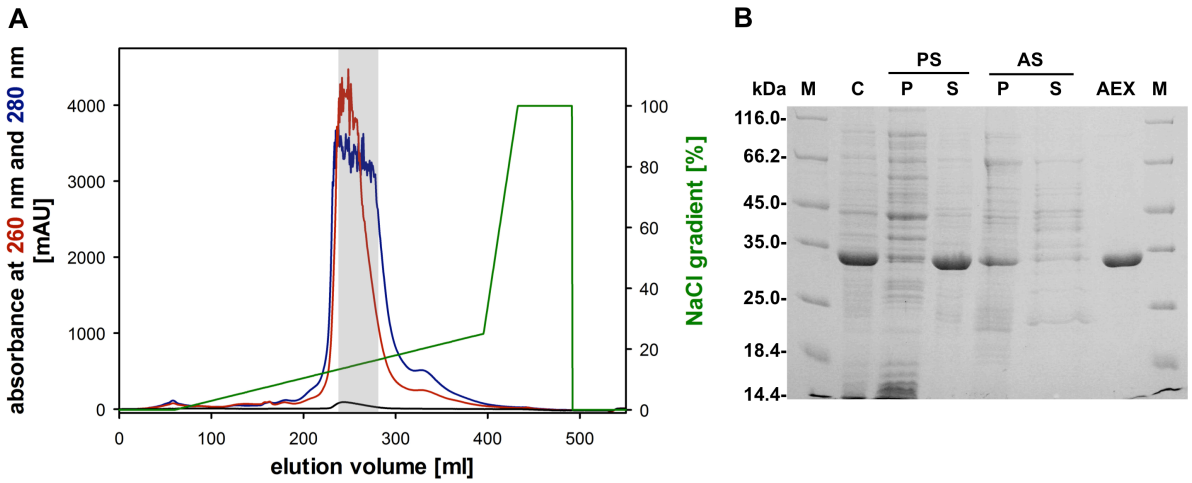

Figure 20: Exemplary purification overview of the recombinant wild-type Dr0930 protein.
A: Elution profile of the purification step via anion exchange chromatography (Q Sepharose Fast flow), monitored by measuring the absorbance at 260 nm (red) and 280 nm (blue). The elution was performed with a gradient of 0-2 M NaCl (green). The absorbance at 550 nm, which corresponds to the absorbance maximum of wild-type Dr0930 in the VIS-spectrum, is shown in black. The combined fractions are shaded in grey.
B: SDS-PAGE (12.5% polyacrylamide) of the elution fractions of protamine sulfate precipitation (PS), ammonium sufate precipitation (AS; 45%), and anion exchange chromatography (AEX: combined and dialyzed fractions after QSepharoseFF purification step). P: pellet (insoluble fraction); S: supernatant (soluble fraction); M: protein ladder and marker (LMW); C: crude extract (soluble fraction of the cell extract) providing the starting point for purification.

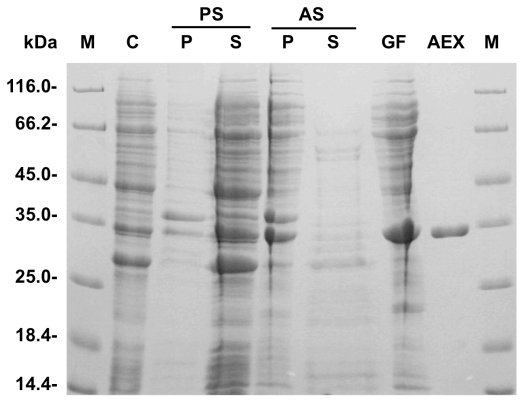

Figure 21: Purification overview of the recombinant wild-type PTE protein.
SDS-PAGE (12.5% polyacrylamide) of the elution fractions of protamine sulfate (PS) and ammonium sulfate precipitation (AS; 45%), gel filtration (GF), and anion exchange chromatography (AEX). P: pellet (insoluble fraction); S: supernatant (soluble fraction); M: protein ladder and marker (LMW); C: crude extract (soluble fraction of the cell extract) providing the starting point for purification. The resuspended pellet of the ammonium sulfate precipitation was further purified by preparative gel filtration (Hi Load 16/60 Superdex 75 Prep Grade). Combined, dialyzed and concentrated fractions were purified by anion exchange chromatography using a DEAE column.

For wild-type Dr0930 and Dr0930 variants, as well as wild-type PTE, a purification grade of more than 95% was achieved as judged by SDS-PAGE. Wild-type Dr0930 yielded approximately 50 mg protein/liter culture. The protein yield for wild-type PTE of 4.7 mg protein/liter culture was significantly lower.

The metal content was analyzed by ICP-MS measurements (3.5.3), and yielded 0.6-1.2 equivalent Co and 0-0.12 equivalent Zn, and up to 0.23 equivalent Fe for wild-type Co/Co-Dr0930. Wild-type Co/Co-PTE contained 1.22 equivalent Co and 0.12 equivalent Zn. Purified wild-type Co/Co-Dr0930 was found to contain a mixture of Co, Zn and Fe when expressed in medium supplemented with $CoCl_2$. Fe^{2+} is easily oxidized to Fe^{3+}, which might lead to diminished enzymatic activity. Therefore, 0.1 mM iron chelator 2,2' bipyridal was added to the expression culture of wild-type Dr0930 to reduce the iron content, however without success. At high concentrations wild-type Co/Co-Dr0930 and Dr0930 variants were intensively purple colored (absorption maximum at 550 nm), presumably due to a charge transfer complex between active site residue Y97 and incorporated iron within the binuclear metal center (Xiang *et al.*, 2009).

4.2.2 Chemical structures of δ-nonanoic lactone and OP compounds

Figure 22 shows the chemical structures of OP compounds (Figure 22A-D) and δ-nonanoic lactone (Figure 22E). Compounds in Figure 22B-E were used in this study.

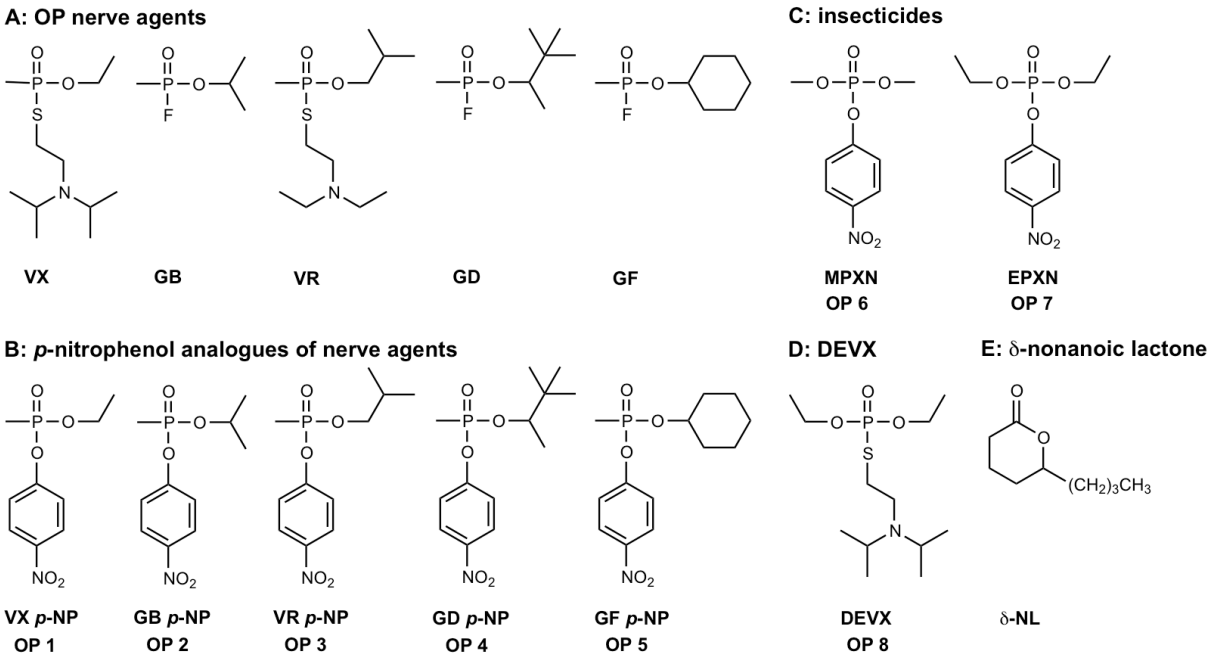

Figure 22: Chemical structures of OP compounds (A-D) and δ-nonanoic lactone (E).
A: Organophosphate nerve agents: VX, GB (sarin), VR, GD (soman), GF (cyclosarin). **B:** *p*-nitrophenol analogues of nerve agents, abbreviated by numbers: OPs 1-5. **C:** Commercially available insecticides, methyl-paraoxon (MPXN, OP 6) and ethyl-paraoxon (EPXN, OP 7). **D:** Diethyl-VX (DEVX; O, O-diethyl-S-(2-diisopropylaminoethyl) phosphorothiolate, OP 8), a close analogue of VX. **E:** δ-nonanoic lactone (δ-NL). Bonds cleaved upon hydrolysis: P-S/P-F (A), P-O (B, C), P-S (D), C-O (E).

The OP compounds used in this study can be devided in three groups regarding their phosphorus chemistry: methylphosphonates (Figure 22A and B), phosphortriesters (Figure 22C), and phosphorothiolates (Figure 22D). Methylphosphonates, exhibit a direct P-C bond. Due to the extremely high toxicity of the original nerve agents *p*-nitrophenol analogues of G- and V-type OP nerve agents were used here. Likewise, the *p*-nitrophenol leaving group allows for colorimetric signal detection upon OP hydrolysis. The methylphosphonates are distinguished by various substituents at the phosphorus center with the size of the substituent increasing for OP compounds 1 to 5: O-ethyl (VX, OP 1), O-isopropyl (GB, OP 2), O-isobutyl (VR, OP 3), O-pinacolyl (GD, OP 4), O-cyclohexyl (GF, OP 5). The phosphonate compounds 1-5 are chiral (exhibit two enantiomers, termed R_P and S_P), due to a chiral P-center. Soman exhibits four stereoisomers due to an additional chiral C-center within the pinacolyl substituent: the isomers are termed R_PR_C, R_PS_C, S_PS_C, and S_PR_C. The methylphosphonates used in this study were used as racemates. Phosphotriesters exhibit three O-linked groups at the P-center. The commerically available insecticides, methyl-paraoxon (MPXN, OP 6) and ethyl-paraoxon (EPXN, OP 7), used in this study are achiral. In phosphorothiolates the ester oxygen is

replaced by sulfur. DEVX (OP 8) differs from VX by substitution of the methyl substituent at the P-center by O-ethyl.

The δ-nonanoic lactone (δ-NL; Figure 22E), used in this study to determine the lactonase activity, is a cyclic ester with an alkyl substitution (n-butyl) at the carbon adjacent to the ring oxygen.

4.2.3 Steady-state kinetic characterization of wild-type Dr0930 and wild-type PTE for native and promiscuous activities

Dr0930 efficiently hydrolyzes γ- and δ-lactones with alkyl substitutions at the carbon adjacent to the ring oxygen. Moreover, promiscuous OPH activity of wild-type Dr0930 for the hydrolysis of the phosphotriesters methyl- and ethyl-paraoxon has been described (Xiang *et al.*, 2009; Hawwa *et al.*, 2009b). Wild-type PTE exhibits broad substrate specificity for the hydrolysis of OPs. Moreover, Tawfik and co-workers reported promiscuous esterase activity for wild-type PTE towards 2-naphthyl acetate (k_{cat}/K_M of 2.5×10^2 $M^{-1}s^{-1}$) and esterase and lactonase activities an engineered PTE variant with elevated expression level (Roodveldt & Tawfik, 2005a/b; Afriat *et al.*, 2006).

Here, the native and promiscuous activities of wild-type Dr0930 and wild-type PTE were analyzed and both enzymes were kinetically characterized for the hydrolysis of OP compounds 1-7 and δ-nonanoic lactone (Figure 22).

The reaction schemes and transition states for the hydrolysis of δ-nonanoic lactone and ethyl-paraoxon are exemplarily shown in Figure 23. A C-O bond versus a P-O bond is cleaved and reactions proceed via a tetrahedral versus a pentavalent oxyanionic intermediate. The promiscuous OPH activity of PLL enzymes is thought to be due to physical similarities between the reactive intermediate for the native lactonase reaction and the ground/intermediate state for the promiscuous OPH reaction (Elias *et al.*, 2008; Ben-David *et al.*, 2012).

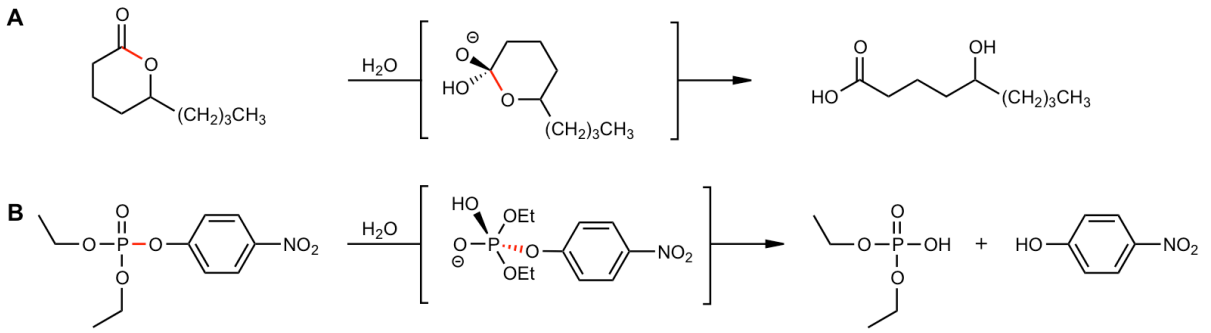

Figure 23: Reaction schemes including their transition states for the hydrolysis of δ-nonanoic lactone (A) and ethyl-paraoxon (B).
A: δ-nonanoic lactone is hydrolyzed to 5-hydroxy nonanoic acid and proton release resulting from carboxylic acid formation was followed using the pH-indicator *m*-cresol purple. The cleaved C-O bond is highlighted in red. The hydrolysis of proceeds via a sp^3 transition state (tetrahedral intermediate). **B:** Ethyl-paraoxon is hydrolyzed to diethyl phosphate, and the released *p*-nitrophenol causes a yellow color change. The cleaved P-O bond is highlighted in red. The hydrolysis of ethyl-paraoxon proceeds via a pentavalent transition state.

Wild-type Dr0930 and wild-type PTE were characterized for the hydrolysis of δ-nonanoic lactone (δ-NL) using a pH-sensitive colorimetric assay (3.5.4.3). The saturation curves deduced from the initial velocity measurements in presence of different substrate concentrations are shown in Figure 24.

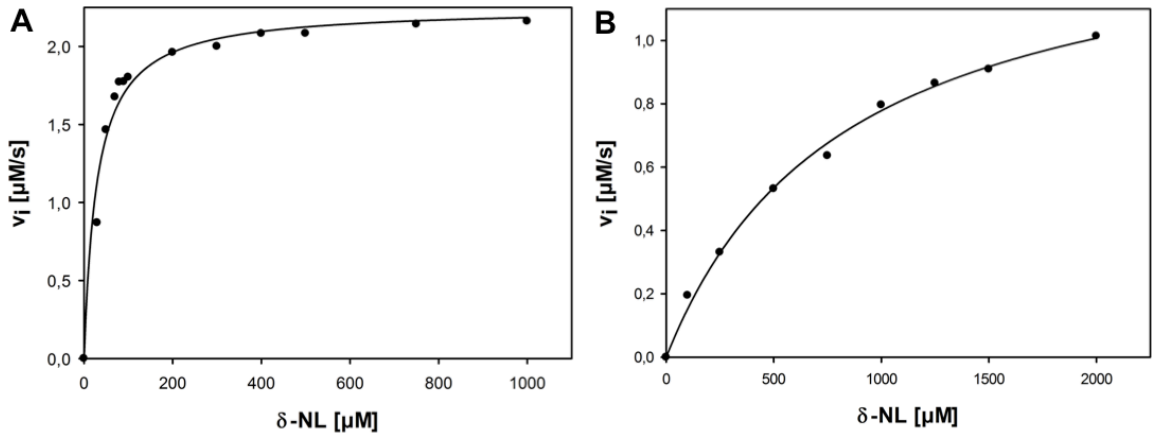

Figure 24: Saturation curves of wild-type Dr0930 (A) and wild-type PTE (B) for the hydrolysis of δ-nonanoic lactone.
The reactions were performed in 2.5 mM BICINE (initial pH: 8.3), 0.1 mM $CoCl_2$, 1.4% DMSO, 0.1 mM *m*-cresol purple, 0.2 M NaCl and variable concentration of δ-nonanoic lactone (0-2mM). The reaction was monitored at 577 nm (ε_{577} = 1.17 × 10^3 $M^{-1}cm^{-1}$) and 30 °C. Prior to use, the protein buffer was exchanged to 10 mM bicine, pH 8.3, 100 µM $CoCl_2$ using a NAP-25 desalting column. Reactions with wild-type PTE (B) were performed with 25 µM enzyme concentration. Wild-type Dr0930 was diluted in 10 mM bicine pH 8.3, 100 µM $CoCl_2$, 1 mg/ml BSA prior to use. BSA has no influence on the activity (data not shown). Reactions with wild-type Dr0930 (A) were performed with 10 nM enzyme concentration. The initial velocity v_i is plotted versus the concentration of substrate. The solid line shows the result of the hyperbolic fit of the data points (SigmaPlot).

The steady-state kinetic parameters, turnover number (k_{cat}), Michaelis constant (K_M), and the catalytic efficiency (k_{cat}/K_M), determined from the fit of the saturation curves to the Michealis-Menten equation (Equation 11) are summarized in Table 5.

Table 5: Steady-state kinetic constants of wild-type Co/Co-Dr0930 and wild-type Co/Co-PTE for the hydrolysis of δ-nonanoic lactone.

	wild-type Co/Co-Dr0930			wild-type Co/Co-PTE		
	k_{cat} [s^{-1}]	K_M [mM]	k_{cat}/K_M [$M^{-1}s^{-1}$]	k_{cat} [s^{-1}]	K_M [mM]	k_{cat}/K_M [$M^{-1}s^{-1}$]
δ-NL	2.2×10^2	0.028	7.9×10^6	5.7×10^{-2}	0.84	6.8×10^1

Kinetic parameters of wild-type Dr0930 for the hydrolysis of δ-nonanoic lactone are in accordance with literature values. Xiang *et al.* (2009) reported $k_{cat} = 1.8 \times 10^2$ s^{-1}, $K_M = 0.09$ mM, $k_{cat}/K_M = 1.8 \times 10^6$ $M^{-1}s^{-1}$ measured at essentially identical conditons in the absence of 0.1 mM $CoCl_2$ in the reaction assay.

The cobalt-substituted Dr0930 hydrolyzes δ-nonanoic lactone with a catalytic efficiency of 7.9×10^6 $M^{-1}s^{-1}$. The lactonase activity of wild-type Co/Co-PTE for δ-nonanoic lactone yielded a 10^5-fold lower catalytic efficiency of 6.8×10^1 $M^{-1}s^{-1}$.

Wild-type Dr0930 and wild-type PTE were characterized for the hydrolysis of various OPs: methylphosphonates (OPs 1-5) and phosphotriesters (OPs 6+7) using a colorimetric assay for *p*-nitrophenol substituted OPs performed at 400 nm (3.5.4.1). Saturation curves of wild-type Dr0930 and wild-type PTE for OPs 1-7 are shown in Figure 25 and Figure 26, respectively.

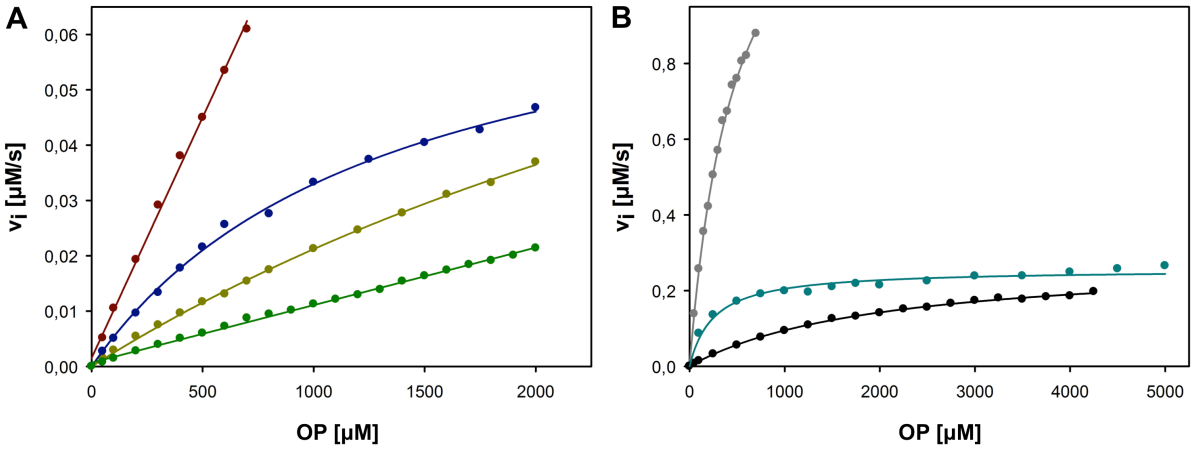

Figure 25: Saturation curves of wild-type Dr0930 for the hydrolysis of OPs 1-7.
A: Saturation curves for OPs 2-5. OP 2 (●), OP 3 (●), OP 4 (●), OP 5 (●). **B:** Saturation curves for OPs 1, 6 and 7. OP 1 (●), OP 6 (●), OP 7 (●).
The reactions were performed in 50 mM CHES, pH 9.0, 100 µM $CoCl_2$ and variable concentration of OPs. For OP compounds 4 and 5 the reaction assay was supplemented with 12% MeOH. The reaction was monitored at 400 nm ($\varepsilon_{400} = 1.7 \times 10^4$ $M^{-1}cm^{-1}$) and 30 °C. Reactions were performed using 5 µM wild-type Dr0930. The initial velocity v_i is plotted versus the concentration of substrate. The solid line shows the result of the hyperbolic or linear fit of the data points (SigmaPlot).

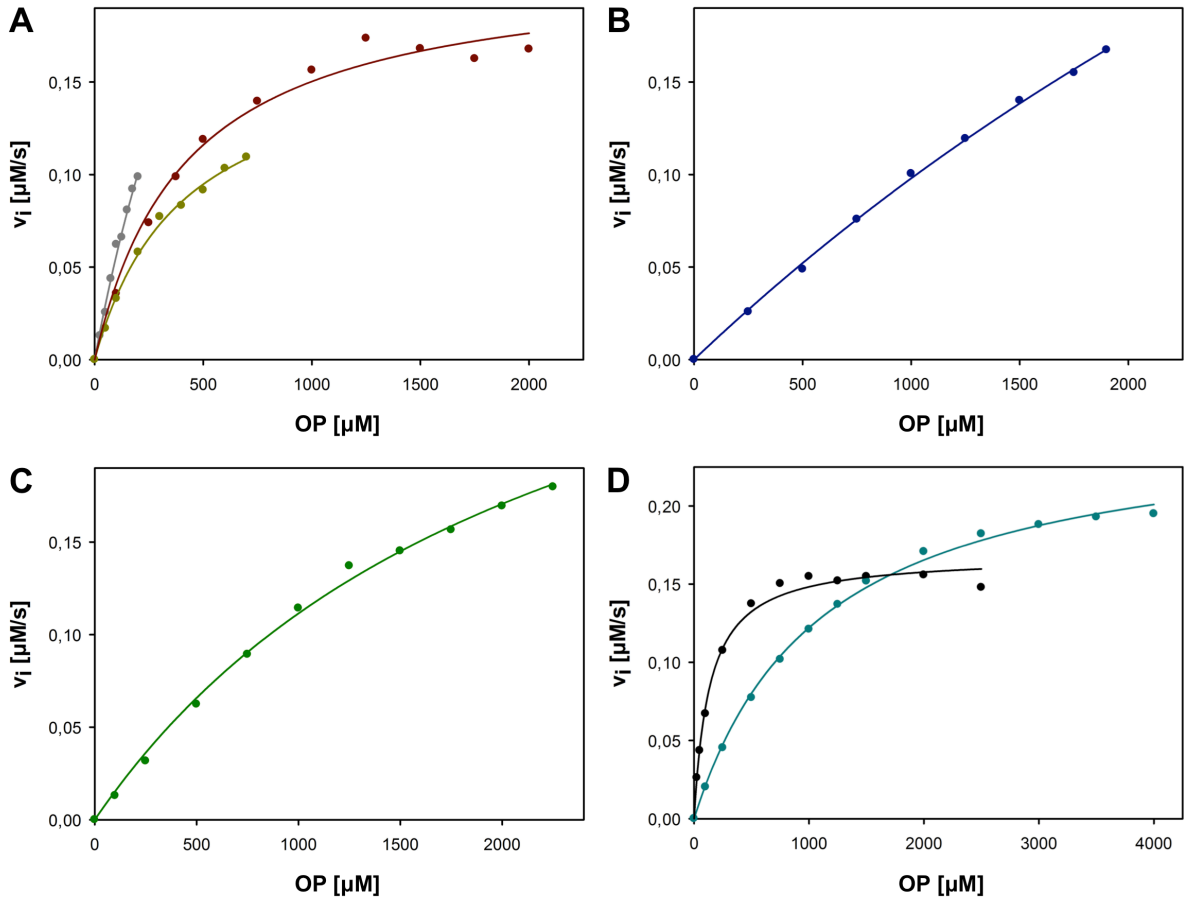

Figure 26: Saturation curves of wild-type PTE for the hydrolysis of OPs 1-7.
Saturation curves of wild-type PTE for the hydrolysis of OP 1 (●), OP 2 (●), OP 3 (●) (A), OP 4 (●) (B), OP 5 (●) (C), OP 6 (●) and OP 7 (●) (D).
The reactions were performed in 50 mM CHES, pH 9.0, 100 µM $CoCl_2$ and variable concentration of OPs. For OP compounds 4 and 5 the reaction assay was supplemented with 12% MeOH. The reaction was monitored at 400 nm (ε_{400} = 1.7 × 10^4 $M^{-1}cm^{-1}$) and 30 °C. Reactions were performed with varied concentrations of wild-type PTE: 50 pM (A), 10 nM (B), 0.25 nM (C), and 10 pM (D) enzyme concentration. The enzyme was diluted in 50 mM HEPES, pH 8.5, 100 µM $CoCl_2$ buffer supplemented with 1 mg/ml BSA in order to stabilize the protein at low concentrations. BSA has no influence on the activity (data not shown). The initial velocity v_i is plotted versus the concentration of substrate. The solid line shows the result of the hyperbolic fit of the data points (SigmaPlot).

Steady-state kinetic parameters deduced from the saturation curves are summarized in Table 6.

Table 6: Steady-state kinetic constants for wild-type Co/Co-Dr0930 and wild-type Co/Co-PTE for the hydrolysis of OPs 1-7.

	wild-type Co/Co-Dr0930			wild-type Co/Co-PTE		
	k_{cat} [s^{-1}]	K_M [mM]	k_{cat}/K_M [$M^{-1}s^{-1}$]	k_{cat} [s^{-1}]	K_M [mM]	k_{cat}/K_M [$M^{-1}s^{-1}$]
1: VX *p*-NP	3.0×10^{-1}	0.49	6.1×10^{2}	9.6×10^{3}	0.75	1.28×10^{7}
2: GB *p*-NP	-	-	9.8×10^{0a}	4.3×10^{3}	0.42	1.0×10^{7}
3: VR *p*-NP	2.6×10^{-2}	5.1	5.1×10^{0}	3.4×10^{3}	0.40	8.5×10^{6}
4: GD *p*-NP	1.2×10^{-2}	2.6	6.8×10^{0a}	8.8×10^{1}	7.7	1.15×10^{4a}
5: GF *p*-NP	-	-	2.1×10^{0}	1.5×10^{3}	2.26	6.6×10^{5}
6: MPXN	5.0×10^{-2}	0.25	2.0×10^{2}	2.6×10^{4}	1.10	2.4×10^{7}
7: EPXN	5.7×10^{-2}	2.0	2.9×10^{1}	1.7×10^{4}	0.14	1.2×10^{8}

[a]: average of two independent measurements. -: k_{cat}/K_M was determined from non-saturating concentrations by a linear fit of the initial part of the saturation curve, as the substrate concentration required to saturate an enzyme variant was higher than the maximal solubility of the substrate. Compounds 1-5 were applied as racemates.
Literature values are available for OP compounds 2, 4, 6 and 7 (Li *et al.*, 2001; Omburo *et al.*, 1992; Chen-Goodspeed *et al.*, 2001a/b). The determined kinetic parameters for OPH of wild-type PTE are in good agreement with published values. Literature values published for GD *p*-NP (Li *et al.*, 2001) differ slightly from values determined here in duplicates. The published parameters determined at 25 °C in 50 mM CHES, pH 9.0, 10% MeOH are as follows: k_{cat} = 44 s^{-1}, K_M = 1.1 mM, $k_{cat}/K_M = 4.0 \times 10^4$ $M^{-1}s^{-1}$.

The bar diagram in Figure 27 illustrates the range of catalytic efficiencies of wild-type Dr0930 and wild-type PTE for OP compounds 1-7.

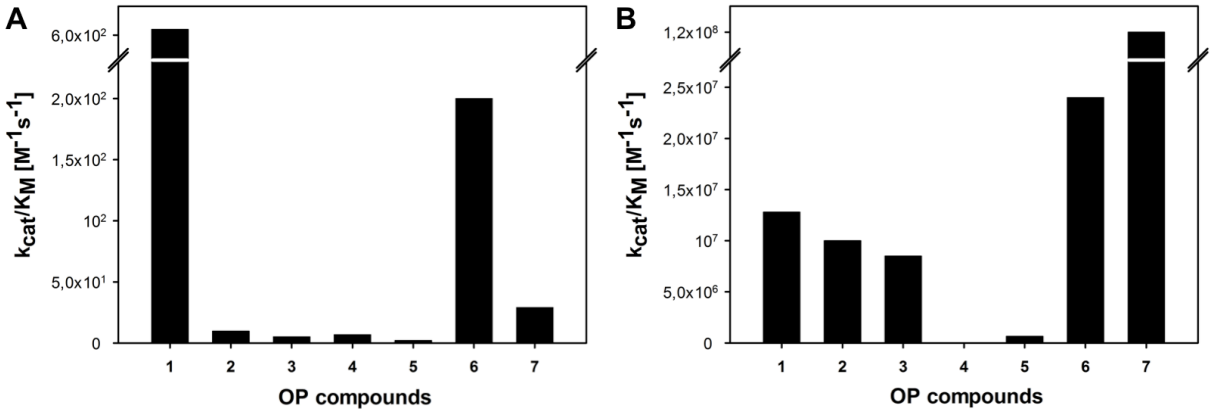

Figure 27: Catalytic efficiencies of wild-type Co/Co-Dr0930 (A) and wild-type Co/Co-PTE (B) for OPs 1-7.

Wild-type Dr0930 exhibits overall low promiscuous activity for the hydrolysis of phosphotriesters and methylphosphonates, with best activities for the hydrolysis of OPs with small substituents at the P-center (OPs 1+6). The K_M values are in the mM

range. The catalytic efficiency of wild-type Dr0930 is four (OP 4) to seven (OPs 2+7) orders of magnitude lower when compared to wild-type PTE.

Wild-type PTE exhibits a broad range of activity for the hydrolysis of OPs 1-7. PTE most efficiently hydrolyzes phosphotriesters (OPs 6+7) and methylphosphonates with small substituents at the P-center (OPs 1-3), exhibiting extremely high k_{cat} values, but also relative high K_M values. The remarkably high catalytic efficiency for EPXN (OP 7) approaches the diffusion controlled limit (Dumas *et al.*, 1989). The OPs 4 and 5, comprising bulky substituents at the P-center, are hydrolyzed at significantly lower rates.

In summary, the efficiencies of the promiscuous and native activities differ, for both Dr0930 and PTE, by several orders of magnitude. Moreover, both enzymes exhibit high K_M and low k_{cat} values for the promiscuous substrates. This may result from improper substrate binding interaction and positioning relative to the catalytic machinery (Khersonsky & Tawfik, 2010).

However, the mutually identified enzymatic activities in wild-type Dr0930 and wild-type PTE further support their evolutionary relationship. As wild-type Dr0930 exhibits activity against a broad spectrum of OP compounds, it is an ideal scaffold to enhance its OPH activity using laboratory evolution and studying rapid molecular evolution in the laboratory.

4.3 Laboratory evolution of wild-type Dr0930 for OPH activity

Earlier attempts to increase the OPH activity of the promiscuous Dr0930 enzyme have been performed. The eight substrate specificity determining $\beta\alpha$-loops of PTE were transplanted to Dr0930 in order to generate a chimeric Dr0930-PTE protein with enhanced OPH activity, however without success. Moreover, a limited number of site-directed mutants were generated by rational design to mimick the hydrophobic substrate binding pocket of wild-type PTE in Dr0930 (Xiang *et al.*, 2009). The rational design aimed to enlarge the small substrate binding pocket of Dr0930 (F26G and C72I), and to implement the residues important for proton shuttling in PTE in Dr0930 (R228H and G207D). The best rationally designed variant Dr0930-F26G+C72I yielded only a 10-fold improvement in catalytic efficiency for EPXN. The kinetic constants k_{cat}, K_M and k_{cat}/K_M of the zinc-substituted Dr0930-F26G+C72I for EPXN are 1.9×10^{-2} s^{-1}, 2.7 mM and 7.7×10^{0} M^{-1} s^{-1} (Xiang *et al.*, 2009).

As the results of the rational design approach were limited, a random-based approach was used in order to further increase the OPH activity of wild-type Dr0930. The design applied several rounds of mutagenesis in an iterative process. The individual steps of laboratory evolution are described in the following.

First experiments were performed with $ZnCl_2$ until the strong positive effect of $CoCl_2$ on the catalytic activity was identified. The metal contents for the Dr0930 variants are summarized in the appendix. Variants generated in the course of laboratory evolution are termed Dr0930_# using consecutive numbers.

4.3.1 Randomization of wild-type Dr0930 by error-prone PCR (epPCR)

4.3.1.1 Characterization of the epPCR library

At the start of the work, the generation and characterization of the epPCR library was completed. The results are briefly described in the following.

A plasmid-based gene library (pTNA-*dr0930*-epPCR), containing 2.7×10^7 independent clones, was generated by error-prone PCR (Meier, 2008). The library (Ts/Tv ratio of 1.9) contained 6 nucleotide exchanges/gene, which corresponds to 2-5 aa exchanges/protein. About 2.0×10^3 clones were assayed for the hydrolysis of EPXN using an *in vitro* activity screening. The experimental approach is illustrated in Figure 28.

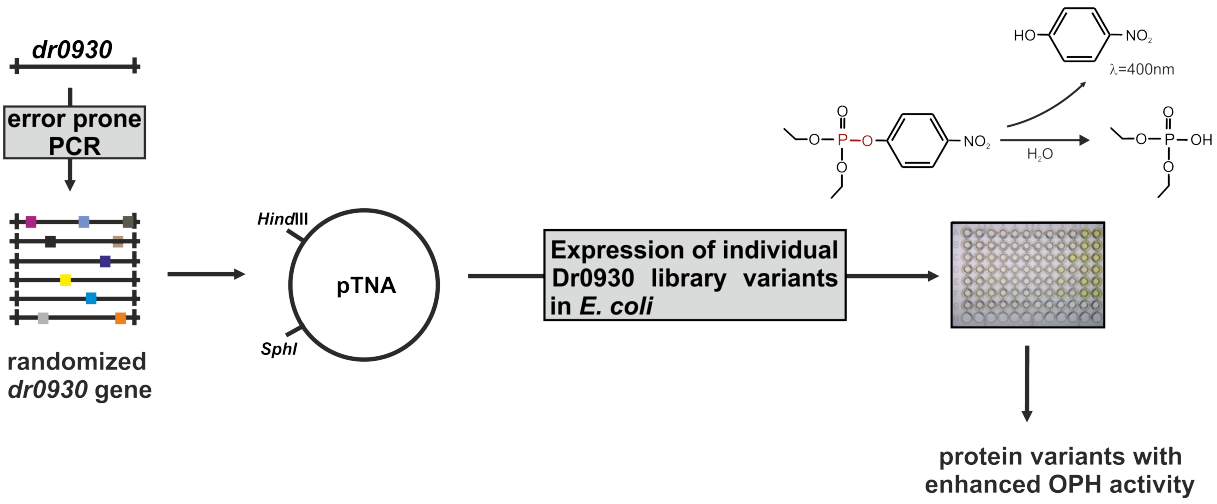

Figure 28: *In vitro* activity screening for Dr0930 variants with improved OPH activity.
A plasmid-based gene library was generated by epPCR on the wild-type Dr0930 scaffold. *E. coli* cells were transformed with the library, individual colonies were grown in 96-well blocks, and the enzymatic activity of the crude extract was assayed.

The plasmids of the best clones were isolated and their *dr0930* inserts were sequenced to identify the incorporated mutations. The 12 most promising variants are listed in Table 7.

Table 7: Dr0930 variants isolated from *in vitro* activity screening of the epPCR library.

Dr0930_#: mutations	
1: G30D+V235M+G316V	**7:** Y28C+L57Q+F107Y+E122D
2: V35E+A103V	**8:** N208I
3: G38V+E51A	**9:** L157Q+D299G
4: P39L+D71N+A163V	**10:** A103T+A280T
5: D71N+E179D+L270M	**11:** A3T+G38R+T105S+P274L
6: S48R+A145V+R148H	**12:** R272C

Dr0930 variants contain the T2Q mutation, as the *dr0930* gene library was constructed in the pTNA vector using a *Sph*I restriction site at the 5'-end. For further details see Meier (2008).

Most mutations are localized in the βα-loops in the active site (Figure 29). Most noteworthy is the exchange D71N, on the basis of its proximity to the active site and its dual occurance in the variants Dr0930_4 and Dr0930_5.

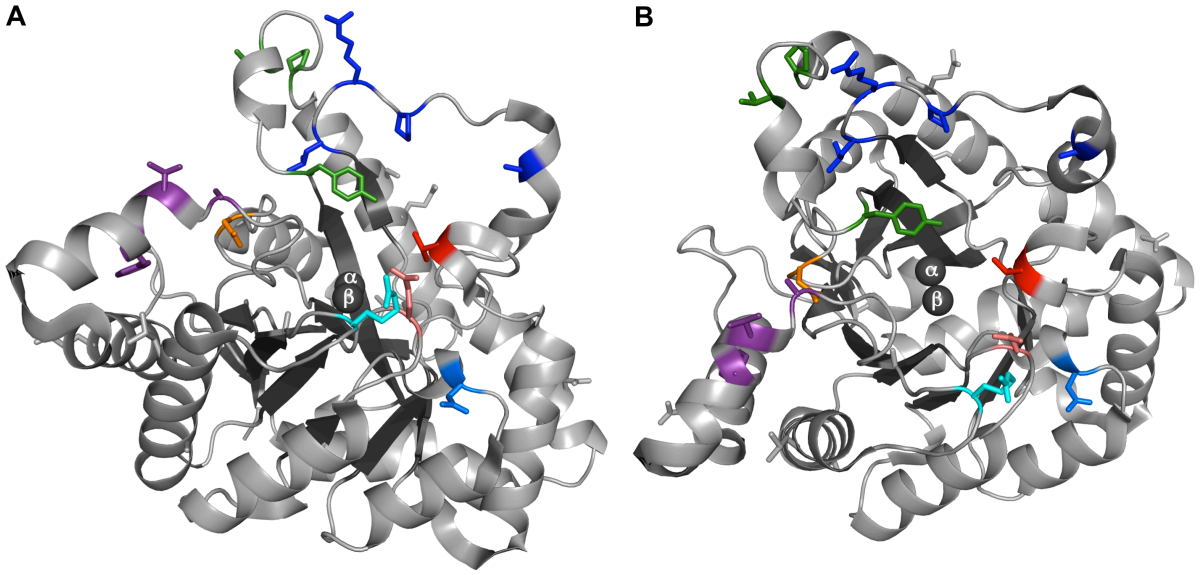

Figure 29: Localization of mutations identified in Dr0930_1 - Dr0930_12.
Side view (A) and top view (B). Most mutations were localized in the βα-loops. The mutations in the βα-loops are colored by loop number: 1 (green), 2 (orange), 3 (purple), 4 (cyan), 5 (light pink), 6 (light blue), 7 (red), and 8 (dark blue). The β-sheets and α and β zinc ions are depicted in dark grey.

4.3.1.2 Verification of epPCR hits by *in vitro* activity screening with EPXN

Due to the low activity and consecutive weak signal in the *in vitro* activity screen, the isolated hits were re-screened to verify and priorize the hits for subsequent *in vitro* characterization by steady-state enzyme kinetics. In order to analyze the effect of the single mutation D71N, the construct Dr0930-D71N (Dr0930_13) was generated by OE-PCR (3.3.7.4) on the template pTNA-*dr0930*-T2Q using the mutagenic primers 5'- and 3'-*dr0930*-D71N and the terminal gene primers 5'-*dr0930*-*Sph*I-T2Q and 3'-*dr0930*-*Hin*dIII.

The Dr0930_1 - Dr0930_12 variants were analyzed by *in vitro* activity screening (3.2.8). To this end, *E. coli* T7 Express Rosetta cells transformed with the pTNA constructs were grown in 96-well blocks, containing 1.5 ml SuperBroth medium supplemented with 1.0 mM $ZnCl_2$. The cells were lysed by incubation with 1 x BugBuster in 50 mM HEPES pH 8.5, and the activity of the crude lysate was assayed using 0.5 mM EPXN. Figure 30 shows the result of the re-screen.

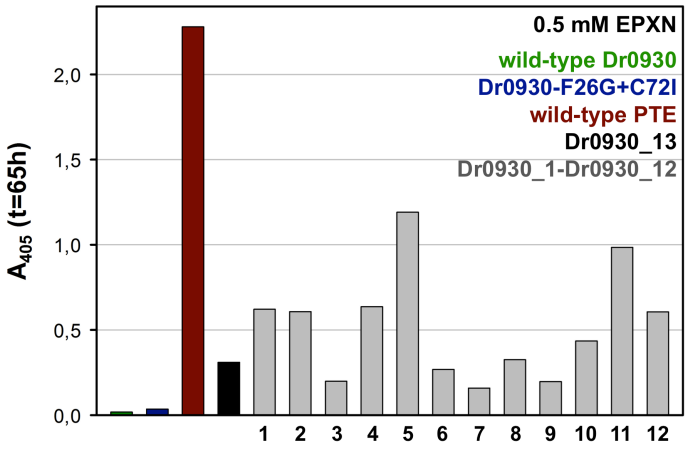

Figure 30: *In vitro* activity screening of the epPCR variants Dr0930_1 - Dr0930_12 using 0.5 mM EPXN.
The activity of the crude lysate was assayed in 50 mM CHES pH 9.0, and 0.5 mM EPXN at 405 nm and 30 °C. The average values of triplicate measurements are shown. The signal of spontaneous background hydrolysis was subtracted from all values (empty pTNA vector was used as negative control). Wild-type Dr0930, the rational designed variant Dr0930-F26G+C72I, Dr0930_13 (Dr0930-D71N) and wild-type PTE (positive control) were used as controls. The reaction of wild-type PTE completed within the deadtime of the experiment.

The positive effect of the single mutation D71N on the catalytic activity is significant. The best hits, Dr0930_2, Dr0930_5, Dr0930_11, and Dr0930_12, were selected for *in vitro* characterization in order to quantify the effect of the identified mutations by steady-state enzyme kinetics.

4.3.1.3 Heterologous expression, purification and *in vitro* characterization of the epPCR hits

The inserts of *dr0930_2*, *dr0930_5*, *dr0930_11*, and *dr0930_12* were subcloned in pET24a expression plasmid using *Nde*I and *Not*I restriction sites. To this end, the inserts were amplified by standard PCR (3.3.5) using the terminal gene primers 5'*dr0930-Nde*I-T2Q (or 5'*dr0930-Nde*I-T2Q+A3T) and 3'*dr0930-Not*I. The full-length fragments were digested with *Nde*I and *Not*I restriction enzymes, and ligated with equally digested pET24a.

E. coli T7 Express Rosetta cells were transformed with the pET24a-*dr0930* constructs, and a single colony was used to inoculate 2 l LB medium, supplemented with 1.0 mM $ZnCl_2$. Following induction of gene expression with 0.5 mM IPTG, the cell suspension was incubated overnight at 37 °C. The cells were harvested, resuspended in 20 mM HEPES, pH 7.5, disrupted by sonication, and centrifuged. The recombinant proteins were purified from the soluble fraction by combinations of anion exchange chromatography using QSepharoseFF and MonoQ columns (3.4.1.2 & 3.4.2.2). Combined protein fractions were dialyzed overnight against 5 l of 20 mM HEPES, pH 7.5. The Dr0930 variants were characterized for the hydrolysis of EPXN, in 50 mM CHES pH 9.0 at 400 nm and 30 °C (3.5.4.1). Saturation curves in comparison to wild-type Dr0930 are shown in Figure 31.

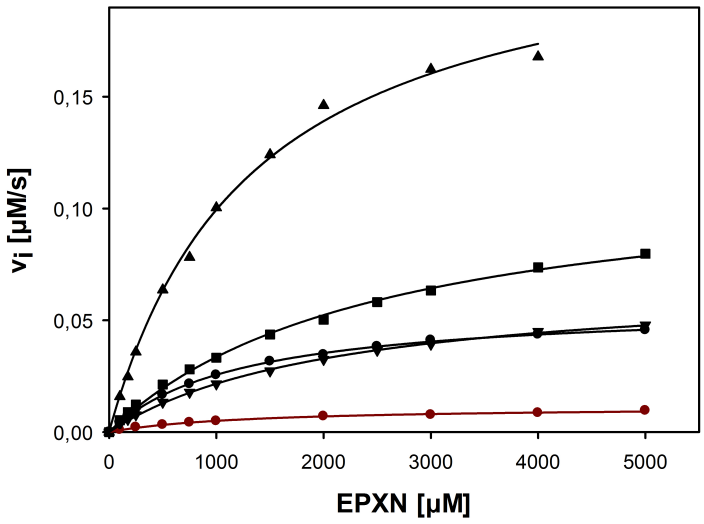

Figure 31: Saturation curves of wild-type Zn/Zn-Dr0930 and Zn/Zn-Dr0930_2, Zn/Zn-Dr0930_5, Zn/Zn-Dr0930_11, and Zn/Zn-Dr0930_12 variants for the hydrolysis of EPXN.
Dr0930 wild-type (●), Dr0930_2 (■), Dr0930_5 (▲), Dr0930_11 (●), Dr0930_12 (▼). The reactions were performed in 50 mM CHES, pH 9.0 and a variable concentration of EPXN (0-5 mM). The reaction was monitored at 400 nm (ε_{400} = 1.7 × 10^4 $M^{-1}cm^{-1}$) and 30 °C. Reactions were performed using 10 µM enzyme concentration. The initial velocity v_i is plotted versus the concentration of substrate. The solid line shows the result of the hyperbolic or linear fit of the data points (SigmaPlot).

The steady-state kinetic parameters, turnover number (k_{cat}), Michaelis constant (K_M), and the catalytic efficiency (k_{cat}/K_M), determined from the fit of the saturation curve to the Michealis-Menten equation (Equation 11) are summarized in Table 8.

Table 8: Steady-state kinetic constants of wild-type Zn/Zn-Dr0930 and variants for the hydrolysis of EPXN.

		EPXN		
		k_{cat} [s^{-1}]	K_M [mM]	k_{cat}/K_M [$M^{-1}s^{-1}$]
Zn/Zn-Dr0930_2	V35E+A103V	1.2×10^{-2}	2.5	4.8×10^{0}
Zn/Zn-Dr0930_5	D71N+E179D+L270M	2.3×10^{-2}	1.3	1.8×10^{1}
Zn/Zn-Dr0930_11	A3T+G38R+T105S+P274L	5.7×10^{-3}	1.2	4.8×10^{0}
Zn/Zn-Dr0930_12	R272C	6.8×10^{-3}	2.2	3.1×10^{0}
wild-type Zn/Zn-Dr0930[a]		1.2×10^{-3}	1.4	8.3×10^{-1}

Dr0930 variants contain the T2Q mutation. [a]: data taken from Xiang *et al.* (2009).

The four characterized Dr0930 variants exhibited a 4-22 fold improvement in catalytic efficiency, with the best variant being Dr0930_5.

In an attempt to further increase the OPH activity of Dr0930_5, the beneficial mutation F26G of the rationally designed variant Dr0930-F26G+C72I (Xiang *et al.*, 2009) was added onto the Dr0930_5 construct. The pET24a-*dr0930*-F26G+D71N+E179D+L270M (Dr0930_14) construct was generated by OE-PCR (3.3.7.4) on the template pET24a-*dr0930_5* using the mutagenic primers 5'(3')*dr0930*-F26G and the terminal gene primers 5'*dr0930-Nde*I and 3'*dr0930-Not*I. The variant was heterologously expressed and purified as described in 4.3.1.3. Steady-state enzyme kinetic characterization of Zn/Zn-Dr0930_14 gave a reduced catalytic efficiency of 6.5×10^{0} $M^{-1}s^{-1}$ (data not shown), confirming no additive effect of the beneficial mutations.

4.3.1.4 Metal-dependency of the OPH activity

The metal dependency of wild-type Dr0930 for the hydrolysis of EPXN was investigated. Zn, Co and Mn were tested as active site metals. In order to allow for the incorporation of these metals upon protein production, the expression medium was supplemented with 1.0 mM of either $ZnCl_2$, $CoCl_2$ or $MnCl_2$. The kinetic parameters for the purified recombinant proteins are summarized in Table 9.

Table 9: Metal-dependency (Zn, Co, Mn) of the kinetic constants for wild-type Dr0930 for the hydrolysis of EPXN.

	EPXN		
	k_{cat} [s^{-1}]	K_M [mM]	k_{cat}/K_M [$M^{-1}s^{-1}$]
wild-type Zn/Zn-Dr0930[a]	1.2×10^{-3}	1.4	8.3×10^{-1}
wild-type Mn/Mn-Dr0930[b]	1.0×10^{-2}	6.8	1.5×10^{0}
wild-type Co/Co-Dr0930[b]	5.7×10^{-2}	2.0	2.9×10^{1}

[a]: data taken from Xiang *et al.* (2009). The reactions were performed at 400 nm ($\varepsilon_{400} = 1.7 \times 10^4$ $M^{-1}cm^{-1}$) and 30 °C in 50 mM CHES, pH 9.0 [b]: The reactions were performed at 400 nm and 30 °C in 50 mM CHES, pH 9.0, 100 µM $CoCl_2$ and $MnCl_2$, respectively.

Wild-type Dr0930 exhibits a strong metal dependency for the hydrolysis of EPXN with approximately 35-fold (20-fold) preference in catalytic efficiency for Co over Zn (Mn). Xiang *et al.* (2009) investigated the metal-dependency of wild-type Dr0930 for the hydrolysis of δ-nonanoic lactone. The catalytic efficiencies for Mn and Co-substituted enzymes were found to be similar, with the Co/Co- or Mn/Mn-substituted enzymes being slightly more active than the Zn-substituted enzyme (4-fold). The OPH activity of Co-, Mn-, and Zn-substituted wild-type PTE was found to be overall similar (Omburo *et al.*, 1992). All subsequent experiments were performed with $CoCl_2$.

4.3.1.5 Steady-state kinetic characterization of Co/Co-Dr0930_5 for the hydrolysis of OPs 1-7

The variant Dr0930_5 was isolated by *in vitro* activity screening with EPXN. In order to quantify the effect of the identified mutations on the impact of OPH in general, the cobalt-substituted variant was characterized for the hydrolysis of OPs 1-7.

Dr0930_5 was heterologously expressed as described in medium supplemented with 1.0 mM $CoCl_2$ (3.4.1.2). The protein was purified by protamine sulfate and ammonium sulfate precipitation, and anion exchange chromatography using a QSepharoseFF column (3.4.2.1 & 3.4.2.2). The saturation curves of purified Dr0930_5 for OPs 1-7 are shown in Figure 32.

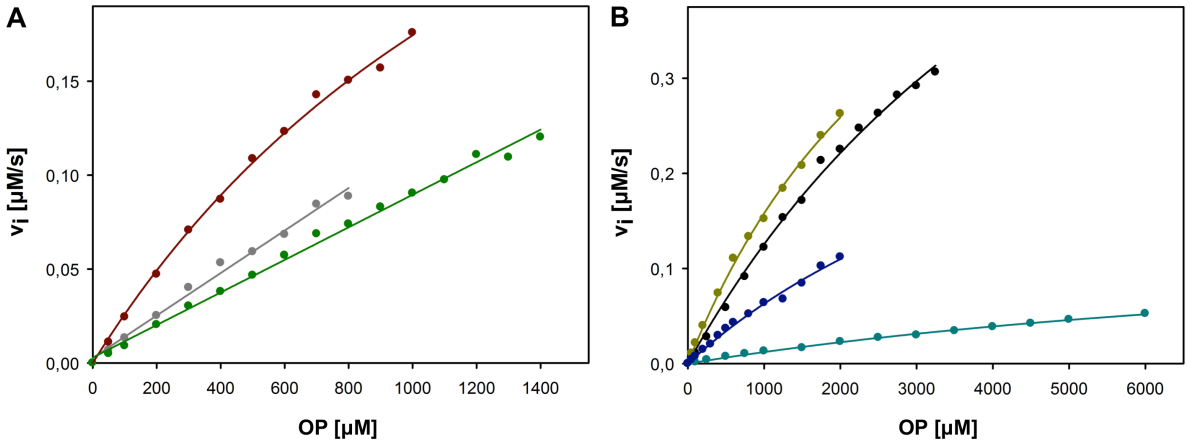

Figure 32: Saturation curves of Dr0930_5 for the hydrolysis of OPs 1-7.
A: Saturation curves for OP 1 (●), 2 (●) and 5 (●). **B:** Saturation curves for OP 3 (●), 4 (●), 6 (●) and 7 (●).
The reactions were performed in 50 mM CHES, pH 9.0, 100 µM $CoCl_2$ and variable concentration of OPs. For OP compounds 4 and 5 the reaction assay was supplemented with 12% MeOH. The reaction was monitored at 400 nm (ε_{400} = 1.7 × 10^4 $M^{-1}cm^{-1}$) and 30 °C. Reactions were performed with 0.2 µM Dr0930_5. The initial velocity v_i is plotted versus the concentration of substrate. The solid line shows the result of the hyperbolic or linear fit of the data points (SigmaPlot). Dr0930_5: Dr0930-T2Q+D71N+E179D+L270M.

The steady-state kinetic parameters determined from the fit of the saturation curve are summarized in Table 10.

Table 10: Steady-state kinetic constants of Co/Co-Dr0930_5 for the hydrolysis of OPs 1-7.

	Co/Co-Dr0930_5		
	k_{cat} [s^{-1}]	K_M [mM]	k_{cat}/K_M [$M^{-1}s^{-1}$]
1: VX *p*-NP	-	-	5.0 × 10^2
2: GB *p*-NP	2.4 × 10^0	1.74	1.38 × 10^3
3: VR *p*-NP	3.6 × 10^0	3.54	1.0 × 10^3
4: GD *p*-NP	2.1 × 10^0	5.83	3.7 × 10^2
5: GF *p*-NP	-	-	4.4 × 10^2
6: MPXN	7.5 × 10^{-1}	11.4	6.6 × 10^1
7: EPXN	4.7 × 10^0	6.5	7.2 × 10^2

–: k_{cat}/K_M was determined from non-saturating concentrations by a fit of the initial part of the saturation curve. Compounds 1-5 were applied as racemates. Dr0930_5: Dr0930-T2Q+D71N+E179D+L270M.

Figure 33A illustrates the absolute values of the catalytic efficiencies of Dr0930_5 for OPs 1-7 in comparison to wild-type Dr0930. Figure 33B summarizes the fold improvement for the respective OP compounds relative to wild-type Dr0930.

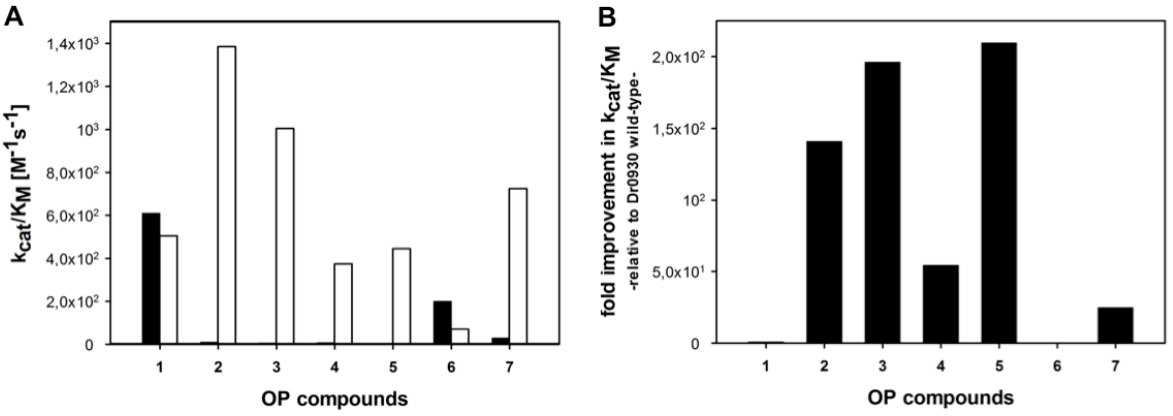

Figure 33: Catalytic efficiencies of Dr0930_5 (open bars) in comparison to wild-type Dr0930 (filled bars) (A) and deduced fold improvement of Dr0930_5 relative to wild-type Dr0930 (B). Compared to wild-type Dr0930, the catalytic efficiencies of Dr0930_5 for GB *p*-NP (OP 2), VR *p*-NP (OP 3), GD *p*-NP (OP 4), GF *p*-NP (OP 5), and EPXN (OP 7) are enhanced by up to 2.1 × 10^2 fold, at the expense of slightly reduced catalytic efficiencies for VX *p*-NP (OP 1) (0.82 fold) and MPXN (OP 6) (0.33 fold).

The highest catalytic efficiencies of Dr0930_5 are achieved for GB *p*-NP (OP 2) and VR *p*-NP (OP 3), obtaining k_{cat}/K_M values of up to 1.4 × 10^3. The improvement in catalytic efficiency is mainly due to an increased k_{cat} value. The catalytic efficiencies for VX *p*-NP (OP 1) and MPXN (OP 6) are slightly diminished compared to wild-type Dr0930. Dr0930_5 achieves a substantial fold improvement of up to two orders of magnitude for GB *p*-NP (OP 2), VR *p*-NP (OP 3) and GF *p*-NP (OP 5).

Dr0930_5 exhibits a similar metal dependency as wild-type Dr0930: the catalytic efficiency of the Co-substituted enzyme for the hydrolysis of EPXN is 40-fold higher than for the Zn-substituted enzyme (see Table 8 and Table 10).

4.3.2 *In vitro* recombination of beneficial 1st generation variants by StEP

Homologous template sequences are recombined by the StEP method (Zhao *et al.*, 1998) that allows for the efficient *in vitro* recombination of closely spaced mutations. The technique was applied to rapidly recombine beneficial mutations from the positive-first generation variants acquired in separate variants while deleterious mutations should be removed due to backcrossing with the wild-type sequence.

4.3.2.1 Generation and characterization of a pTNA-*dr0930*-StEP library

Using StEP, the Dr0930_2, Dr0930_5, Dr0930_11 and Dr0930_12 variants were recombined with the rationally designed variant Dr0930-F26G+C72I and wild-type Dr0930.

To this end, the *dr0930* inserts were amplified under StEP conditions (3.3.8), which contained the mixture of pTNA-*dr0930* templates (10 ng each), GoTaq DNA polymerase (2.5 U; Promega), 0.2 mM dNTP, 1.5 mM $MnCl_2$, and 0.15 µM plasmid primers (5'- and 3'pTNA-F-MCS). The PCR was performed at an experimentally determined optimum annealing temperature of 50 °C and 130 abbreviated amplification cycles. Subsequently, nested PCR was performed under standard conditions on the gel-purified PCR-product to amplify the yield of full-length product using the terminal gene primer 5'pTNA-*Sph*I and 3'pTNA-*Hin*dIII (3.3.5). The amplification products were purified from a 1% agarose gel and pooled (3.3.3 & 3.3.3.1). The mixture of *in vitro* recombined *dr0930* genes was then digested with *Sph*I and *Hin*dIII (3.3.4.1), and the purified reaction products were ligated into (equally digested) pTNA plasmid (3.3.4.2), yielding pTNA-*dr0930*-StEP. The dialyzed ligation reactions were used to transform electrocompetent *E. coli* Δ*his*A-Δ*his*F cells (3.2.5 & 3.2.6). In total 16 transformations were carried out. The preparation of the pTNA-*dr0930*-StEP gene library and the calculation of the library size were performed as described in 3.3.10 and 3.3.10.1.

The ligation efficiency of the StEP library was estimated to be 94% by colony PCR of 50 clones. The library contained about 7×10^7 independent variants. Assuming that all mutations are recombined in a random fashion, the theoretical library size contains 4.1×10^3 variants. Sequencing of the *dr0930* inserts of 10 randomly selected clones showed that the StEP protocol resulted in 3.8 nucleotide exchanges per gene that corresponded to 2.2 aa exchanges/protein. The high number of amplification cycles lead to the introduction of new mutations (on average 0.5 additional mutations per gene). The maximum number of tracable cross-overs was three.

4.3.2.2 *In vitro* activity screening of the pTNA-*dr0930*-StEP library

In vitro activity screening of the pTNA-*dr0930*-StEP library for the hydrolysis of EPXN was performed essentially as described (3.2.8). The colorimetric signal improved due to supplementation of the medium with 1.0 mM $CoCl_2$ instead of 1.0 mM $ZnCl_2$, and optimized expression due to the usage of *E. coli* BL21-CodonPlus(DE3) cells. Plasmids of the most active colonies were extracted and analyzed by sequencing. The 15 most significantly improved variants identified are listed in Table 11.

Table 11: Dr0930 variants isolated from *in vitro* activity screening of the StEP library.

Dr0930_#: mutations	
15: D71N+T105S+L270M	**23:** A3T+G38R+T105S+E179D+P274L
16: A3T+G38R+T105S	**24:** G38R+T105S+E179D+G194S
17: G38R+T105S+L270M	**25:** D71N+L270M
18: E101G+R272C	**26:** A3T+G38R+T105S+V141A
19: G38R+T105S	**27:** A3T+G38R+T105S+L270M
20: A3T+G38R+A43T+T105S+L270M	**28:** G38R+T105S+P274L
21: A3T+G38R+T105S+R272C	**29:** A3T+D71N+T105S+E179D+L270M
22: E101K+T105S	

Dr0930 variants contain the T2Q mutation. In addition to the shown variants, the template variant Dr0930_11 was also isolated.

The results of the *in vitro* activity screening with 0.5 mM EPXN are shown in Figure 34.

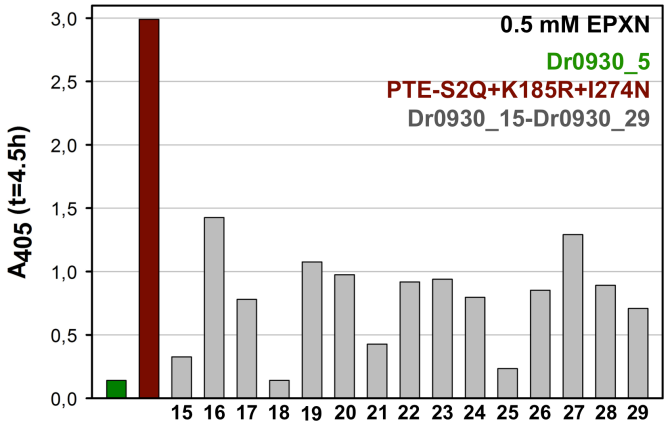

Figure 34: *In vitro* activity screening of the StEP variants Dr0930_15 - Dr0930_29 using 0.5 mM EPXN.
The activity of the crude lysate was assayed in 50 mM CHES pH 9.0, and 0.5 mM EPXN at 405 nm and 30 °C. The average values of triplicate measurements are shown. The signal of spontaneous background hydrolysis was subtracted from all values (empty pTNA vector was used as negative control). The first generation variant, Dr0930_5, and a PTE variant engineered for soluble expression (positive control; PTE-S2Q+K185R+I274N; the S2Q mutation is due to the insertion in the pTNA vector using *Sph*I restriction site at the 5'-end) were used as controls. The reaction of the latter completed within the deadtime of the experiment.

Most isolated variants contained the mutations G38R (βα-loop 1) and T105S (βα-loop 3). Two new mutations (G/K) were identified at position E101 (βα-loop 3). The best variants Dr0930_16 and Dr0930_22, which contains an exchange at the recently identified position E101 (βα-loop 3), were selected for *in vitro* characterization in order to quantify the activity improvement by steady-state enzyme kinetics.

4.3.2.3 Heterologous expression, purification and *in vitro* characterization of hits isolated from the StEP library

The *dr0930_16* and *dr0930_22* inserts were subcloned in the pET24a expression plasmid using *Nde*I and *Not*I restriction sites. The inserts were amplified using terminal gene primers 5'*dr0930-Nde*I and 5'*dr0930-Nde*I-A3T in combination with 3'*dr0930-Not*I, and the full-length fragment was digested via *Nde*I and *Not*I restrictions enzymes, and ligated with equally digested pET24a. Heterologous expression in *E. coli* T7 Express Rosetta was performed in media supplemented with 1.0 mM $CoCl_2$, and the recombinant proteins were purified by a combination of anion exchange (QSepharoseFF) and gel filtration chromatography (Superdex 200) (3.4.1.2, 3.4.2.2 & 3.4.2.3). The steady-state kinetic parameters for the hydrolysis of EPXN determined from the fit of the saturation curves of purified Dr0930_16 and Dr0930_22 (data not shown) are summarized in Table 12 in comparison to wild-type Dr0930 and Dr0930_5.

Table 12: Steady-state kinetic constants of Co/Co-Dr0930_16 and Co/Co-Dr0930_22 for the hydrolysis of EPXN.

		EPXN		
		k_{cat} [s^{-1}]	K_M [mM]	k_{cat}/K_M [$M^{-1}s^{-1}$]
Co/Co-Dr0930_16[a]	A3T+G38R+T105S	3.7×10^{-1}	0.7	5.2×10^{2}
Co/Co-Dr0930_22[a]	E101K+T105S	5.5×10^{-1}	2.2	2.5×10^{2}
wild-type Co/Co-Dr0930[b]		5.7×10^{-2}	2.0	2.9×10^{1}
Co/Co-Dr0930_5[c]	D71N+E179D+L270M	4.7×10^{0}	6.5	7.2×10^{2}

[a]:The reactions were performed at 30 °C in 50 mM CHES, pH 9.0 and monitored at 400 nm ($\varepsilon_{400} = 1.7 \times 10^4$ $M^{-1}cm^{-1}$). [b]: The reactions were performed at 30 °C in 50 mM CHES, pH 9.0, 100 µM $CoCl_2$ and monitored at 400 nm. [c]: Dr0930_5 contains an additional T2Q mutation.

Compared to the first generation variant Dr0930_5, the variants Dr0930_16 and Dr0930_22 showed improved K_M values, but also reduced k_{cat} values. The catalytic efficiencies are similar to Dr0930_5, and 18- and 9-fold increase compared to wild-type Dr0930. In the crude extract screen both variants showed higher catalytic activity than Dr0930_5, which might be due to a positive effect of the mutations on protein stability and/or solubility.

The variants Dr0930_16 and Dr0930_22 were isolated by *in vitro* activity screening with EPXN. In order to quantify the effect of the identified mutations on the impact of OPH in general, the variants were characterized for the hydrolysis of OPs

1-7. However, the variants showed only minor improvements compared to wild-type Dr0930 (data not shown).

4.3.3 Simultaneous hot spot mutagenesis (SHM)

In the following a focused library was generated by targeted randomization of selected hot spots. We aimed to optimize key-active site residues mutated earlier by our group and others (Hawwa *et al.*, 2009b) using simultaneous hot spot mutagenesis (SHM).

4.3.3.1 Generation and characterization of a SHM library

Ten prominent positions identified in our previously described experiments (4.3.1 & 4.3.2) and positions identified by Mesecar and co-workers (most important identified mutations: D71G, E101G, M234I, V235L; Hawwa *et al.*, 2009b) with a maximum distance of 13 Å between the Cα-atom of the active site residue of Dr0930 and the phosphorus atom of the superimposed DIMP inhibitor bound to PTE were selected for site-directed mutagenesis using partially degenerated codons. The main criteria for the type of mutation choosen, was the generation of a hydrophobic active site containing smaller amino acids in order to reduce the steric hindrance to accommodate the larger OP substrates (see Figure 22).

The following positions were mutated in the SHM library: F26, Y28, D71, C72, E101, Q178, E179, R228, V235, and L270. The position R228 in Dr0930 corresponds to H254 in *P. diminuta* PTE, and R254 in *A. radiobacter* OpdA. Together with the active-site aspartate, which deprotonates the pentacoordinated intermediate, this residue is important for proton shuttling. Although we knew that the mutation of the corresponding active site R223 to His in *S. solfataricus* SsoPox resulted in a large descrease in activity (Elias *et al.*, 2008) we introduced smaller and polar amino acids (Cys, Tyr, Ser, Asn, His) at position R228 in order to provide space for the accommodation of the ligand. A broad set of mutations was allowed at positions 71 and 101. Figure 35 shows the selected positions. The set of introduced mutations is given in Table 13.

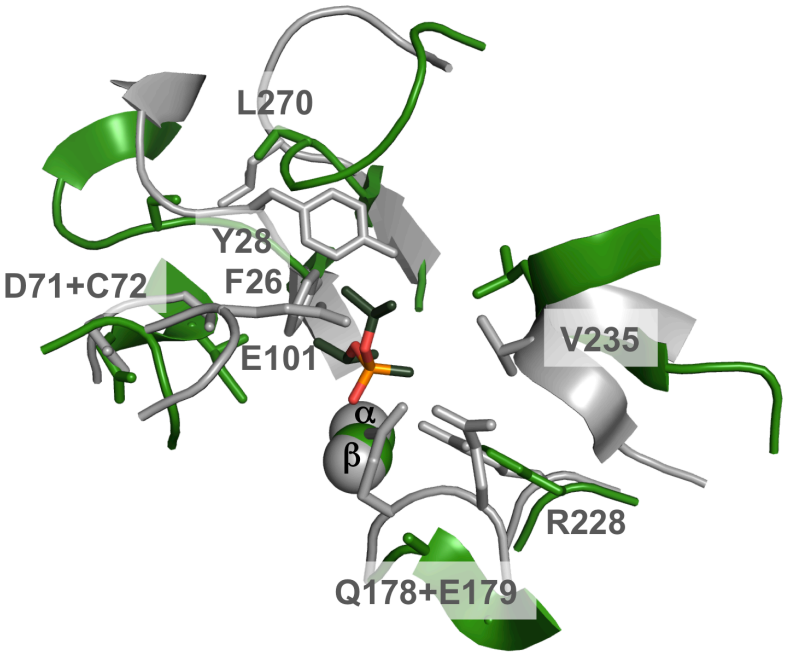

Figure 35: Positions selected for simultaneous hot spot mutagenesis (SHM; same view as in Figure 18A).
Structural superposition of wild-type Dr0930 (PDB ID 3FDK; grey) and wild-type PTE with co-crystallized DIMP ligand (PDB ID 1EZ2; depicted in green). The labeled positions F26 (βα-loop 1), Y28 (βα-loop 1), D71 (βα-loop 2), C72 (βα-loop 2), E101 (βα-loop 3), Q178 (βα-loop 5), E179 (βα-loop 5), R228 (βα-loop 7), V235 (βα-loop 7), and L270 (βα-loop 8) were selected for simultaneous hot-spot mutagenesis. The equivalent PTE residues (see Figure 17) are shown but not labeld.

Table 13: Selected positions for SHM mutagenesis and introduced set of mutations.

F26: G, V, I	**Q178:** N, A, L, M, S, R
Y28: A, V, L	**E179:** E, D
D71: N, G, Q, A, V, L, M	**R228:** C, Y, S, N, H
C72: C, I	**V235:** L, M
E101: G, A, V, L, M, C, S, N, D, K	**L270:** A, V, L, M

The positions F26, C72, and R228 have been mutated earlier in a rational design approach (Xiang *et al.*, 2009). The positions Y28, D71, E101, E179, V235, and L270 have been identified in variants isolated from the epPCR and StEP library. Except for positions Q178 and L270 all positions have also been mutated by Mesecar and co-workers (Hawwa *et al.*, 2009b).

The partially degenerated codons were selected regarding the *E. coli* codon usage. Adjacent positions with less than 6 amino acid distance were mutagenized using one primer. The theoretical library size was calculated to contain 8.6×10^7 independent variants. The mutations were introduced by sequential OE-PCR (3.3.7.4) on the pTNA-*dr0390* template. The primers used are listed in 2.8.2. In the first step the DNA fragments were amplified under standard PCR conditions (3.3.5) by using a set of neighboring primers in various combinations. The respective

amplified fragments were mixed in stoichiometric ratios, and used to amplify 5' (3') megaprimers with the gene flanking primer 5'pTNA-*Sph*I (3'pTNA-*Hin*dIII) primer in combination with the 3' (5') *dr0930*-101GBS, 3' (5') *dr0930*-101MTG, 3' (5') *dr0930*-101WGC, and 3' (5') *dr0930*-101RAH mutagenic primers in a Phusion gradient PCR (3.3.5). Amplified 5' and 3' megaprimer fragments were mixed in stoichiometric ratios, and the full-length genes were generated using the gene flanking primers 5'pTNA-*Sph*I and 3'pTNA-*Hin*dIII in a Phusion gradient PCR. Processing of the pTNA-*dr0930*-SHM library and plasmid preparation was performed essentially as described in 4.3.2.1. The ligation efficiency was estimated to be 82% by colony PCR of 50 clones. The library contained about 4×10^8 independent variants, covering the theoretical library size of 8.6×10^7. Altogether, 52 clones were analyzed by sequencing, of which 7 constructs contained a frame shift. Sequencing of the *dr0930* inserts of the 45 in-frame clones confirmed that the protocol resulted in overall very homogeneous randomization (data not shown) and the introduction of an average of additional 0.4 aa exchanges/protein.

4.3.3.2 *In vitro* activity screening of the pTNA-*dr0930*-SHM library using a combination of filter paper and 96-well block activity screen

Due to the large library size a DEAE-filter paper activity screen was used as a pretest to discriminate active and inactive colonies of the pTNA-*dr0930*-SHM library (3.2.8). To this end, *E. coli* BL21-CodonPlus(DE3) cells transformed with the pTNA-*dr0930*-SHM library were plated on large square LB agar plates. Enzyme activities of lysed colony replicates on DEAE-filter paper were assayed using 0.5 mM EPXN in 50 mM CHES pH 9.0. Active colonies turned yellow upon substrate hydrolysis and were identified visually or by digital imaging. 100,000 colonies were screened in total, of which approximately 30% were active. An exemplary plate excerpt of the DEAE filter paper screen is shown in Figure 36.

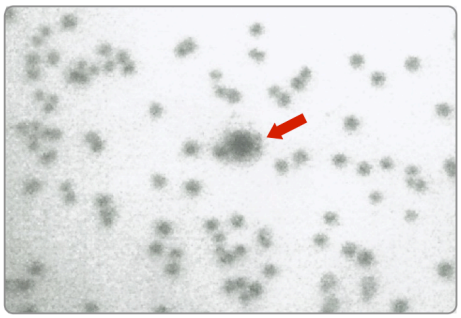

Figure 36: DEAE filter paper activity screen of the SHM library: identification of active colonies by digital imaging using a band pass filter.
E. coli BL21-CodonPlus(DE3) cells transformed with the pTNA-*dr0930*-SHM library were plated on large square LB agar plates. Colony replicates on the DEAE-filter paper were lysed by incubation with a second Whatman filter paper soaked with 1 × BugBuster in 50 mM HEPES pH 8.5, 100 µM $CoCl_2$, and incubated for 15 min. The activity was assayed by subsequent incubating of the replicate filter paper with Whatman filter paper soaked with 0.5 mM EPXN in 50 mM CHES pH 9.0. Active colonies turned yellow upon substrate hydrolysis and were identified visually or by digital imaging (using a band pass filter 406.5-8.1 nm) and further analyzed using 96-well block screening.

Isolated hits were verified by *in vitro* activity screening of the crude extracts (96-well block activity screen; 3.2.8). A representative result of the screen with 0.5 mM EPXN is shown in Figure 37.

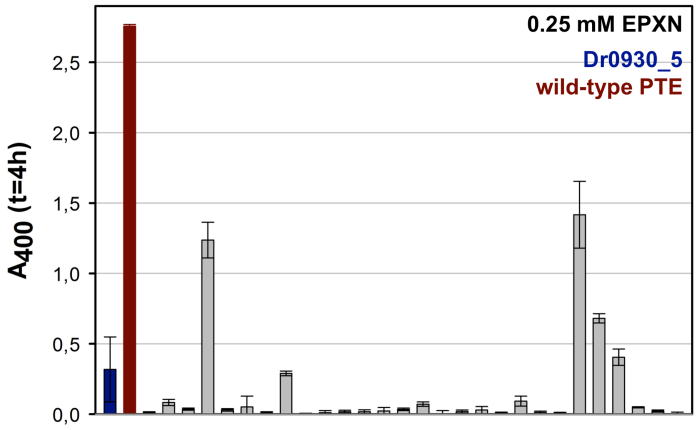

Figure 37: Representative *in vitro* activity screen of a 96-well plate using 0.25 mM EPXN.
The activity of the crude lysate was assayed in 50 mM CHES pH 9.0, and 0.25 mM EPXN at 400 nm and 30 °C. The average values of triplicate measurements with standard deviations are shown. The signal of spontaneous background hydrolysis was subtracted from all values (empty pTNA vector was used as negative control). The first generation variant, Dr0930_5, and wild-type PTE (positive control; containing the S2Q mutation) were used as controls. The reaction of the latter completed within the deadtime of the experiment. The best hit of this plate is Dr0930_31 (Dr0930-T2Q+F26C+Y28I+D71A+E101N+Q178S+E179D+V235I).

Plasmids of the 28 most active colonies (Dr0930_30 - Dr0930_57) were extracted and analyzed by sequencing. A complete list of constructs is listed in the appendix (Table 33). Table 14 summarizes the percentage alteration of mutations at each position, calculated from the 28 most active variants from the SHM library.

Table 14: Percentage alteration of mutations at each position.

position	aa/position (%)
F26	**C** (61%), **I/V** (18% each), **F** (3%)
Y28	**I** (75%), **T** (14%), **V** (7%), **A** (4%)
D71	**G** (32%), **N** (22%), **L** (18%), **M** (14%), **A/V** (7% each)
C72	**C** (68%), **I** (32%)
E101	**N/S** (18% each), **G** (13%), **M/V** (11% each), **L/C/D** (7% each), **A/K** (4% each)
Q178	**S** (71%), **Q** (25%), **T** (4%)
E179	**D** (50%), **E** (50%)
R228	**R** (100%)
V235	**I** (54%), **L** (36%), **M** (10%)
L270	**V** (43%), **L** (29%), **I** (18%), **A** (7%), **R** (3%)

Some positions exhibited a strong amino acid preference (Ile at position Y28, Cys at position 72, Ser at position Q178, Arg at position 228), whereas others showed a rather broad residue distribution (positions D71 and E101). Most noteworthy, each hit contained amino acids other than wild-type amino acids at position 28, 71, 101, and 235. Furthermore, the results indicated that R228 is essential for the activity, as it was identified in all isolated hits (see also 4.4.5.2). Deleterious mutations, such as mutations other than Arg at position 228, lead to a high percentage of inactive and weaky active clones.

The three most active variants, Dr0930_30, Dr0930_31 and Dr0930_32 were selected for *in vitro* characterization in order to quantify the activity improvement by steady-state enzyme kinetics.

4.3.3.3 Heterologous expression, purification and steady-state enzyme kinetic characterization of hits from the SHM library

The *dr0930_30*, *dr0930_31*, and *dr0930_32* inserts were subcloned in the pET24a expression plasmid using *Nde*I and *Xho*I restriction sites. To this end, the inserts were amplified using terminal gene primers 5'*dr0930-Nde*I and 3'*dr0930-Xho*I (3.3.5), the full-length fragment was digested with *Nde*I and *Xho*I restrictions enzymes, and ligated with equally digested pET24a.

Heterologous expression in *E. coli* BL21(DE3) Rosetta 2 was performed in media supplemented with 1.0 mM $CoCl_2$ (3.4.1.2), and the recombinant proteins were

purified by protamine sulfate and ammonium sulfate precipitation (3.4.2.1) and a combination of anion exchange (QSepharoseFF) and gel filtration chromatography (Superdex 200) (3.4.2.2 & 3.4.2.3). The saturation curves of purified Dr0930_30, Dr0930_31 and Dr0930_32 for EPXN are shown in Figure 38.

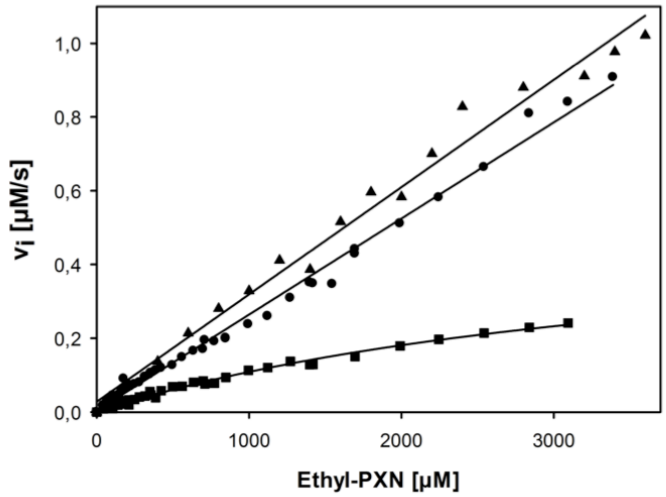

Figure 38: Saturation curves of Dr0930_30, Dr0930_31 and Dr0930_32 for the hydrolysis of EPXN.
Dr0930_30 (●), Dr0930_31 (■), Dr0930_32 (▲).
The reactions were performed in 50 mM CHES, pH 9.0, 100 µM $CoCl_2$ and variable concentration of OPs. For OP compounds 4 and 5 the reaction assay was supplemented with 12% MeOH. The reaction was monitored at 400 nm (ε_{400} = 1.7 × 10^4 $M^{-1}cm^{-1}$) and 30 °C. Reactions were performed with an enzyme concentration of 75 nM. The initial velocity v_i is ploted versus the concentration of substrate. The solid line shows the result of the hyperbolic or linear fit of the data points (SigmaPlot). Dr0930_30: F26V+Y28I+D71G+C72I+E101M+Q178S+V235L+L270I, Dr0930_31: F26C+Y28I+D71A+E101N+Q178S+E179D+V235I, Dr0930_32: F26C+Y28I+D71G+E101D+Q178S+V235L+L270V.

The steady-state kinetic parameters (k_{cat}/K_M only) determined from the fit of the saturation curves for OPs 1-7 are summarized in Table 15.

Table 15: Catalytic efficiencies of Dr0930 variants in comparison to wild-type Dr0930 and Dr0930_5 for the hydrolysis of OPs 1-7.

	Dr0930 WT	Dr0930_5	Dr0930_30	Dr0930_31	Dr0930_32
	k_{cat}/K_M [$M^{-1}s^{-1}$]	k_{cat}/K_M [$M^{-1}s^{-1}$]	k_{cat}/K_M [$M^{-1}s^{-1}$]	k_{cat}/K_M [$M^{-1}s^{-1}$]	k_{cat}/K_M [$M^{-1}s^{-1}$]
OP 1	6.1 × 10^2	5.0 × 10^2	4.0 × 10^2	3.3 × 10^2	1.2 × 10^2
OP 2	9.8 × 10^0	1.38 × 10^3	8.4 × 10^2	4.7 × 10^2	3.3 × 10^2
OP 3	5.1 × 10^0	1.0 × 10^3	6.9 × 10^2	4.5 × 10^2	2.5 × 10^2
OP 4	6.8 × 10^0	3.7 × 10^2	4.0 × 10^2	6.7 × 10^2	2.2 × 10^2
OP 5	2.1 × 10^0	4.4 × 10^2	1.3 × 10^3	5.6 × 10^2	2.3 × 10^2
OP 6	2.0 × 10^2	6.6 × 10^1	4.3 × 10^2	2.0 × 10^2	4.6 × 10^2
OP 7	2.9 × 10^1	7.2 × 10^2	3.45 × 10^3	1.8 × 10^3	3.9 × 10^3

Dr0930_30: F26V+Y28I+D71G+C72I+E101M+Q178S+V235L+L270I, Dr0930_31: F26C+Y28I+D71A+E101N+Q178S+E179D+V235I, Dr0930_32: F26C+Y28I+D71G+E101D+Q178S+V235L+L270V.

The three characterized variants exhibited up to 135-fold increased activity for EPXN compared to wild-type Dr0930 and a 2.5-5.4-fold increased activity relative to Dr0930_5. The activity for the hydrolysis of MXPN was increased by a factor of 3-7 relative to Dr0930_5.

Remarkably, most variants exhibited overall high K_M values and the catalytic efficiencies were determined from a linear fit of the data points. Moreover, although the characterized variants contain 7-8 mutations, the catalytic efficiencies for OPs 1-5 are not at all or only slightly improved compared to Dr0930_5, which carries only 3 mutations.

4.3.3.4 Generation and characterization of consensus variants

In order to further increase the OPH activity, 12 consensus variants were generated based on the frequently encountered exchanges listed in Table 14. The total number of mutations in each consensus variant was limited to six, keeping wild-type amino acids at position E179, R228, and L270. The exchanges Y28I+Q178S+V235I were fixed, whereas positions 26 (C, V), 71 (N, G) and 101 (G, S, N) were kept variable.

The megaprimer fragments were amplified from constructs listed in the appendix (Table 33) using mutagenic primers listed in 2.8.2 and the terminal gene primers 5’dr0930-*Sph*I-T2Q and 3’dr0930-*Hin*dIII. The megaprimers were combined by OE-PCR (3.3.7.4) using terminal gene primers 5’*dr0930-Sph*I-T2Q and 3’*dr0930-Hin*dIII in a Phusion gradient PCR (3.3.5). The full-length fragments were digested with *Sph*I and *Hin*dIII restriction enzymes, and ligated with equally digested pTNA vector. The generated consensus variants are listed in Table 16.

Table 16: Consensus Variants Dr0930_58 - Dr0930_69.

Dr0930_#: Y28I+Q178S+V235I	
58: +F26C+D71N+E101G	**64:** +F26V+D71N+E101G
59: +F26C+D71N+E101S	**65:** +F26V+D71N+E101S
60: +F26C+D71N+E101N	**66:** +F26V+D71N+E101N
61: +F26C+D71G+E101G	**67:** +F26V+D71G+E101G
62: +F26C+D71G+E101S	**68:** +F26V+D71G+E101S
63: +F26C+D71G+E101N	**69:** +F26V+D71G+E101N

Dr0930 variants contain the T2Q mutation.

In vitro activity screening of Dr0930_58 - Dr0930_69 was performed as described (3.2.8) using 0.15 mM EPXN as substrate. The result is illustrated in Figure 39.

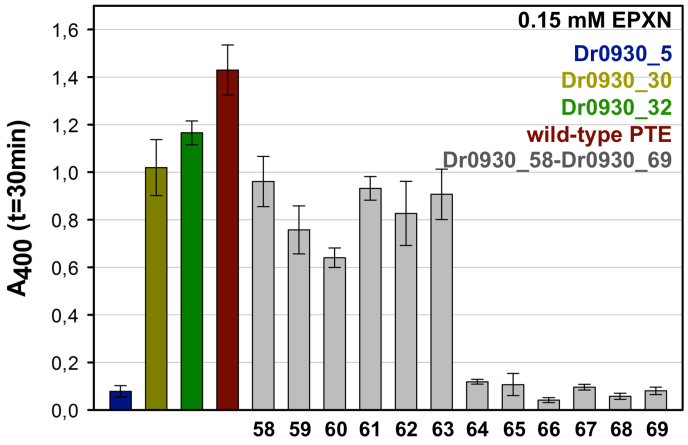

Figure 39: *In vitro* activity screening for consensus variants Dr0930_58 - Dr0930_69 using 0.15 mM EPXN.
The activity of the crude lysate was assayed in 50 mM CHES pH 9.0, and 0.15 mM EPXN at 400 nm and 30 °C. The average values of triplicate measurements with standard deviations are shown. The signal of spontaneous background hydrolysis was subtracted from all values (empty pTNA vector was used as negative control). The first generation variant, Dr0930_5, and hits isolated from the SHM library (Dr0930_30 and Dr0930_32), and wild-type PTE (positive control; containing the S2Q mutation) were used as controls. The reaction of the latter completed within the deadtime of the experiment. Dr0930_58 - Dr0930_63 contain the F26C mutation, Dr0930_64 - Dr0930_69 contain the F26V mutation. Dr0930_61: Dr0930-F26C+Y28I+D71G+E101G+Q178S+V235I.

Compared to Dr0930_30 and Dr0930_32, none of the consensus variants showed enhanced activity for the hydrolysis of EPXN. Moreover, variants containing the F26V mutation showed overall diminished activity, compared to consensus variants containing the F26C mutation.

In order to verify the result *in vitro*, the consensus variant Dr0930_61 was exemplarily selected for characterization. To this end, the construct was subcloned in the pET24a vector using *Nde*I and *Xho*I restriction sites. The inserts were amplified

using terminal gene primers 5'*dr0930-Nde*I and 3'*dr0930-Xho*I (3.3.5), and the full-length fragment was digested with *Nde*I and *Xho*I restrictions enzymes, and ligated with equally digested pET24a.

The variant was heterologously expressed, purified and steady-state kinetically characterized for the hydrolysis of EPXN as described (4.3.3.3). The kinetic constant k_{cat}/K_M of the cobalt-substituted Dr0930_61 for EPXN was determined from a linerar fit of the data and is 3.1×10^3 $M^{-1}s^{-1}$. The kinetic parameters for OP compounds 1-6 were not determined. The approach was not further pursued as no significant enhancement in activity was achieved.

As the *in vitro* screen of the SHM library was only performed with EPXN (OP 7), the improvements were limited to increased hydrolytic activity for the phosphotriesters MPXN (OP 6) and EPXN (OP 7) (see Table 15) when compared to Dr0930_5. Moreover, all isolated variants contained the wild-type amino acid a position R228 (see Table 14); mutations other than R228 lead to inactive variants. Hence, this position seems to be critical for the OPH activity.

4.3.4 Sequential site-directed, site-saturation and combinatorial mutagenesis

In the following smaller focused libraries were generated in order to reduce the screening effort. This included targeted randomization of single hot spots by site-directed or site-saturation mutagenesis in an interactive process of combinatorial mutagenesis. Key active site residues mutated earlier were re-optimized gradually. Positions were selected based on their proximity to the active site and a structure-guided approach comparing differences between Dr0930 and PTE. In contrast to the SHM approach the positions were mutated consecutively instead of simultaneously.

Moreover, *in vitro* activity screening was performed under more stringent screening conditions. As the activity increased, the signal became more sensitive and enabled the substrate concentration to be reduced to specifically screen for improvements in k_{cat}/K_M. Small library sizes (less than 1000 variants) enabled simulatenously to screen for OP compounds 1-7, instead of only EPXN (OP 7) and the design of a multi-efficient OPH.

Starting from template Dr0930_5 (Dr0930-T2Q+D71N+E179D+L270M) selected active active site positions were successively targeted. The semi-rational design approach aimed to generate a larger hydrophobic active site. Mutagenesis focused

on residues located predominately in βα-loops 1, 3, 7, and 8. The most important positions are illustrated in Figure 40.

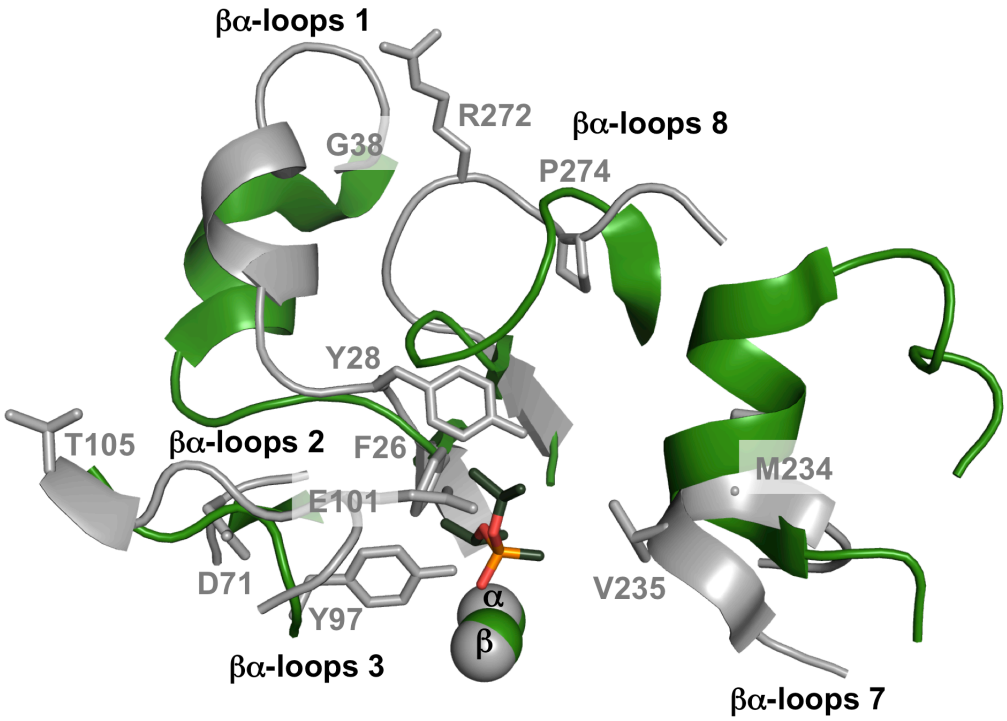

Figure 40: Selected positions for sequential site-directed and site-saturation mutagenesis (same view as in Figure 18A).
Structural superposition of wild-type Dr0930 (grey) and wild-type PTE (greeen) with co-crystallized substrate analogue DIMP (PDB ID 1EZ2). The most important positions selected for mutagenesis (F26, Y28, G38, D71, Y97, E101, T105, M234, V235, R272 and P274) are highlighted in grey. The βα-loops 1, 2, 3, 7, and 8 are shown. The positions Phe26 (βα-loop 1), Tyr28 (βα-loop 1), Phe97 (βα-loop 3), were subjected to detailed analysis using site-saturation mutagenesis. The mutations identified by Mesecar and co-workers (D71G, E101G, M234I, and V235L; Hawwa *et al.*, 2009b) and mutations identified in hits isolated from the epPCR library (G38R, T105S, R272C, P274L) were analyzed by combinatorial mutagenesis. As major structural differences between Dr0930 and PTE are in the length and conformation of βα-loops, deletion and insertion (scanning) mutagenesis was also performed.

4.3.4.1 Combinatorial mutagenesis on template Dr0930_5

Mesecar and co-workers discovered Dr0930 variants with enhanced activity for MPXN and EPXN (Hawwa *et al.*, 2009b). By site-saturation mutagenesis of active site residues they obtained two variants, Dr0930-D71G+E101G+V235L and Dr0930-D71G+E101G+M234I, with catalytic efficiencies for EPXN of 7.7×10^2 $M^{-1}s^{-1}$ and 2.1×10^2 $M^{-1}s^{-1}$, respectively. These variants contained mutations at positions previously identified by our group: Dr0930_4 and Dr0930_5 contain the mutation D71N, Dr0930_1 the mutation V235M, and Dr0930_18 and Dr0930_22 contain the mutations E101G and E101K, respectively.

The kinetic constants of wild-type Dr0930 reported in Hawwa *et al.* (k_{cat}/K_M for EPXN and MPXN: 1.4×10^0 $M^{-1}s^{-1}$ and 5.8×10^{-1} $M^{-1}s^{-1}$) vary considerably from the values determined here; apparently Mesecar and co-workers did not add metal to the growth medium; they only incubated the enzyme with $CoSO_4$ prior to steady-state enzyme kinetics.

For comparative analysis, their best variant Dr0930-D71G+E101G+V235L (Dr0930_70) was *in vitro* characterized for the hydrolysis of OPs 1-7 under the same conditions used here. The pET24a-*dr0930_70* construct was generated on the *dr0930* template. Initially four megaprimers were generated by standard PCR (3.3.5) using the following combinations of primers: 5'T7P and 3'*dr0930*-D71G, 5'*dr0930*-D71G and 3'*dr0930*-E101G, 5'*dr0930*-E101G and 3'*dr0930*-V235L, 5'*dr0930*-V235L and 3'T7T. In a second step the four megaprimer fragments were assembled by Phusion gradient PCR (3.3.5) using gene flanking primers 5'T7P and 3'T7T for amplification. The full-length fragment was digested with *Nde*I and *Xho*I restriction enzymes and ligated with equally digested pET24a. Heterologous expression in *E. coli* BL21(DE3) Rosetta 2 was performed in media supplemented with 1.0 mM $CoCl_2$ (3.4.1.2), and the recombinant protein was purified by protamine and ammonium sulfate precipitation and a combination of anion exchange (QSepharoseFF) and gel filtration chromatography (Superdex 200) (3.4.2.1 & 3.4.2.2 & 3.4.2.3). The steady-state kinetic parameters of the purified protein determined from the fit of the saturation curves with OPs 1-7 (data not shown) are summarized in Table 17.

Table 17: Steady-state kinetic parameters of Co/Co-Dr0930_70 for the hydrolysis of OPs 1-7.

	Co/Co-Dr0930_70		
	k_{cat} [s^{-1}]	K_M [mM]	k_{cat}/K_M [$M^{-1}s^{-1}$]
1: VX *p*-NP	-	-	5.6×10^2
2: GB *p*-NP	-	-	1.0×10^3
3: VR *p*-NP	-	-	9.8×10^2
4: GD *p*-NP	-	-	3.1×10^2
5: GF *p*-NP	-	-	3.2×10^2
6: MPXN	4.5×10^0	9.0	5.0×10^2
7: EPXN	4.4×10^0	2.3	1.9×10^3

The reactions were performed in 50 mM CHES, pH 9.0, 100 µM $CoCl_2$ and variable concentration of OPs. For OP compounds 4 and 5 the reaction assay was supplemented with 12% MeOH. The

reaction was monitored at 400 nm (ε_{400} = 1.7 × 10^4 $M^{-1}cm^{-1}$) and 30 °C. -: k_{cat}/K_M was determined from non-saturating concentrations by a fit of the initial part of the saturation curve. Compounds 1-5 were applied as racemates. Dr0930_70: Dr0930-D71G+E101G+V235L.

The catalytic efficiencies obtained here were somewhat elevated compared to those published in Hawwa *et al.* (2009b). However, as the kinetic constants for wild-type Co/Co-Dr0930 determined here are much higher than those published, the variant achieves only a 65-fold improvement in k_{cat}/K_M for EPXN compared to the published 560-fold improvement. When compared to Dr0930_5, Dr0930_70 achieves higher catalytic efficiencies for EPXN (2.6 fold) and MPXN (7.6 fold); the catalytic efficiencies for OPs 1-5 are similar to Dr0930_5 (see Table 10 and Table 17).

In order to further increase the OPH activity of Dr0930_5, the mutations D71G, E101G, M234I, and V235L, were added in various combinations. The variants were generated by sequential OE-PCR on the template pET24a-*dr0930_5* using gene flanking primers 5'T7P and 3'T7T in various combinations with the mutagenic primers 5'(3')*dr0930*-D71G, 5'(3')*dr0930*-E101G, 5'(3')*dr0930*-M234I and 5'(3')*dr0930*-V235L. In a second step the megaprimer fragments were assembled by Phusion gradient PCR (3.3.5) using terminal gene primers 5'*dr0930-Nde*I and 3'*dr0930-Xho*I as nested primers for amplification. The full-length fragment was digested with *Nde*I and *Xho*I restriction enzymes and ligated with equally digested pET24a. The generated variants are listed in Table 18.

Table 18: Variants generated by combinatorial mutagenesis on template Dr0930_5 (D71N+E179D+L270M): Dr0930_71 - Dr0930_80.

Dr0930_#: E179D+L270M	
71: +D71N+E101G	**76:** +D71G+E101G
72: +D71N+V235L	**77:** +D71G+V235L
73: +D71N+E101G+V235L	**78:** +D71G+E101G+V235L
74: +D71N+M234I	**79:** +D71G+M234I
75: +D71N+E101G+M234I	**80:** +D71G+E101G+M234I

The variants were characterized by *in vitro* activity screening (3.2.8). To this end, *E. coli* BL21(DE3) Rosetta 2 cells transformed with the constructs were grown in media supplemented with 0.5 mM $CoCl_2$, lysed, and assayed using 0.5 mM EPXN. The results are shown in Figure 41.

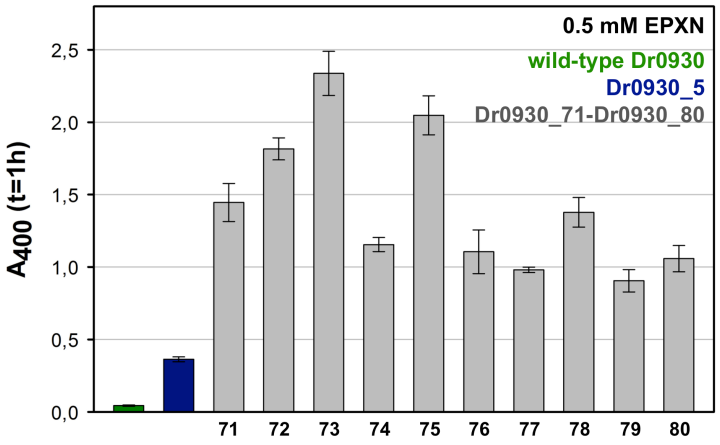

Figure 41: *In vitro* activity screening of combinatorial variants Dr0930_71 - Dr0930_80 using 0.5 mM EPXN.
The activity of the crude lysate was assayed in 50 mM CHES pH 9.0, and 0.5 mM EPXN at 400 nm and 30 °C. The average values of triplicate measurements with standard deviations are shown. The signal of spontaneous background hydrolysis was subtracted from all values (empty pTNA vector was used as negative control). Wild-type Dr0930 and the Dr0930_5 template were used as controls. Dr0930_71 - Dr0930_75 contain the D71N mutation, Dr0930_76 - Dr0930_80 contain the D71G mutation. Dr0930_73: Dr0930-D71N+E101G+E179D+V235L+L270M.

All variants show significantly enhanced activity compared to Dr0930_5. Overall the Dr0930_71 - Dr0930_75 variants, containing the D71N mutation, were more active than variants containing D71G mutation (Dr0930_76 - Dr0930_80). The best variant Dr093_73 was selected for steady-state enzyme kinetic characterization. The variant was heterologously expressed and purified as decribed (4.2.1), and characterized for the hydrolysis of OPs 1-7. The saturation curves are shown in Figure 42.

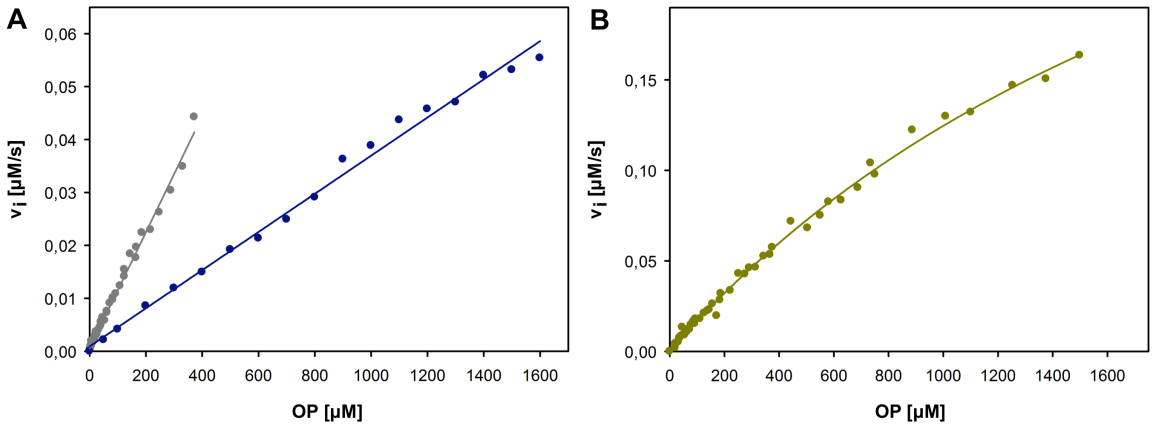

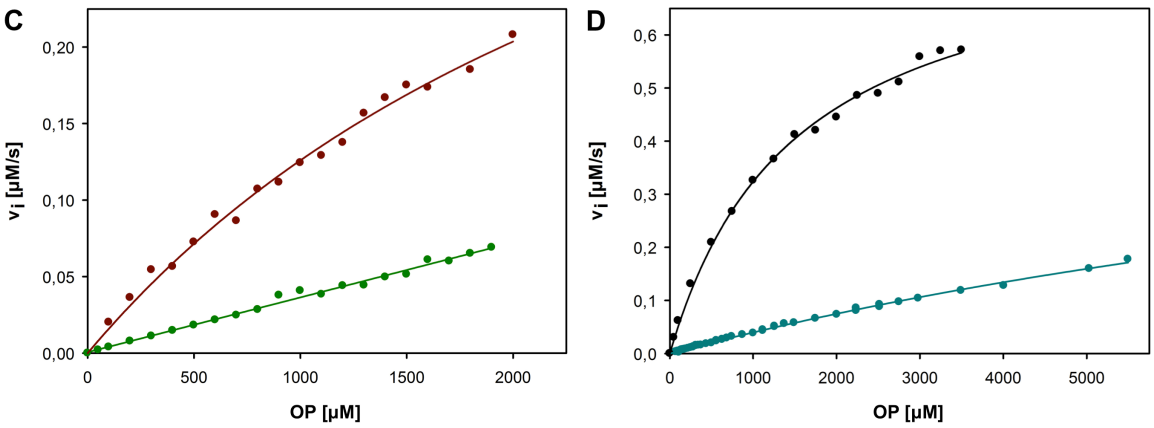

Figure 42: Saturation curves of Dr0930_73 for the hydrolysis of OPs 1-7.
Saturation curves for OP 1 (●) + 4 (●) (A), OP 3 (●) (B), OP 2 (●) +5 (●) (C), OP 6 (●) + 7 (●) (D). The reactions were performed in 50 mM CHES, pH 9.0, 100 µM $CoCl_2$ and variable concentration of OPs. For OP compounds 4 and 5 the reaction assay was supplemented with 12% MeOH. The reaction was monitored at 400 nm (ε_{400} = 1.7 × 10^4 $M^{-1}cm^{-1}$) and 30 °C. Reactions were performed at 150 nM enzyme concentration. The initial velocity v_i is plotted versus the concentration of substrate. The solid line shows the result of the hyperbolic or linear fit of the data points (SigmaPlot). Dr0930_73: Dr0930-D71N+E101G+E179D+ V235L+L270M.

The steady-state kinetic parameters determined from the fit of the saturation curves are summarized in Table 19.

Table 19: Steady-state kinetic constants of Co/Co-Dr0930_73 for the hydrolysis of OPs 1-7.

	Co/Co-Dr0930_73		
	k_{cat} [s^{-1}]	K_M [mM]	k_{cat}/K_M [$M^{-1}s^{-1}$]
1: VX *p*-NP	-	-	6.7 × 10^2
2: GB *p*-NP	3.6 × 10^0	3.2	1.1 × 10^{3a}
3: VR *p*-NP	3.0 × 10^0	2.6	1.2 × 10^3
4: GD *p*-NP	-	-	2.4 × 10^2
5: GF *p*-NP	-	-	2.4 × 10^2
6: MPXN	4.4 × 10^0	15.4	2.8 × 10^2
7: EPXN	5.4 × 10^0	1.5	3.6 × 10^3

-: k_{cat}/K_M was determined from non-saturating concentrations by a fit of the initial part of the saturation curve. [a]: data reproduced with same enzyme preparation; average value of three measurements given. Compounds 1-5 were applied as racemates. Dr0930_73: Dr0930-D71N+E101G+E179D+ V235L+L270M.

Compared to Dr0930_5, Dr0930_73 exhibits a 4-5 fold improvement in k_{cat}/K_M for EPXN and MPXN. The catalytic efficiencies for OPs 1-5 are not improved and similar to parameters obtained for the Dr0930_5 template (see Table 10).

4.3.4.2 Site-saturation mutagenesis at position Tyr28

Site-saturation mutagenesis at position Tyr28 was performed due to its proximity to the active site (Figure 40). The Y28NNS site-saturation mutagenesis was performed on two different templates: Dr0930_73 (D71N+E101G+E179D+V235L+ L270M) and Dr0930_75 (D71N+E101G+E179D+M234I+L270M).

In most cases, *in vitro* activity screening with EPXN resulted in improvement in OPH activity for only phosphotriester compounds (see Table 15 and 4.3.2.3). To ensure, that the design resulted in a simultaneous increase of the catalytic efficiencies towards all substrates, the smaller and targeted libraries were screened with all 7 OP compounds.

Plasmid-based gene libraries, pET24a-*dr0930_73*-Y28NNS and pET24a(+)-*dr0930_75*-Y28NNS, on the templates pTNA-*dr0930_73* and pTNA-*dr0930_75* were generated by Phusion PCR (3.3.5) using the mutagenic primers 5'(3')*dr0930*-Y28NNS in combination with the terminal gene primers 5'*dr0930-Nde*I and 3'*dr0930-Xho*I. The full-length fragments were digested with *Nde*I and *Xho*I, and inserted in equally digested pET24a vector. BL21(DE3) Rosetta 2 cells were directly transformed with the ligated library. *In vitro* activity screening with 8-fold library coverage was performed as described (3.2.8). Single colonies were grown in 96-well blocks, containing 0.75 ml SuperBroth medium supplemented with 0.5 mM $CoCl_2$. Cells were lysed, and the activity of the crude lysate was assayed simultaneously for the hydrolysis of OPs 1-7. The best 70 hits were re-screened with 0.25 mM substrate in 50 mM CHES pH 9.0. The most proficient clones with increased activity for all OPs were isolated and analyzed by sequencing. The constructs are listed in Table 20.

Table 20: Hits isolated from Y28NNS screen on templates Dr0930_73 and Dr0930_75.

Dr0930_#: D71N+E101G+E179D+L270M	
81: +V235L+Y28L	**83:** +M234I+Y28L
82: +V235L+Y28W	**84:** +M234I+Y28I
	85: +M234I+Y28M

The hits Dr0930_81 and Dr0930_82 were isolated from the pTNA-*dr0930_73*-Y28NNS library. The hits Dr0930_83, Dr0930_84 and Dr0930_85 were isolated from the pTNA-*dr0930_75*-Y28NNS library.

Results of the *in vitro* activity screening with GF *p*-NP (OP 5) and MPXN (OP 6) are exemplarily shown in Figure 43.

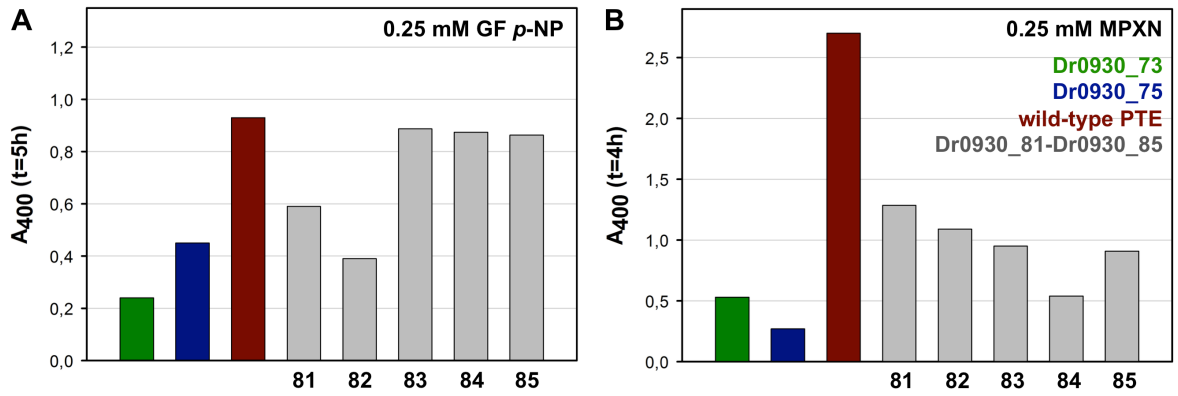

Figure 43: *In vitro* activity screening of the 28NNS library variants Dr0930_81 - Dr0930_85 using 0.25 mM GF *p*-NP (OP 5) (A) and 0.25 mM MPXN (OP 6) (B).
The activity of the lysed crude extract was assayed in 50 mM CHES pH 9.0, and 0.25 mM substrate at 400 nm and 30 °C. The A_{400} values of the controls were measured in triplicates, single values are given for Dr0930_81 - Dr0930_85. The signal of spontaneous background hydrolysis was subtracted from all values (empty pTNA vector was used as negative control). Dr0930_73, Dr0930_75 and wild-type PTE were used as controls.

From the Y28NNS libraries, hits containing a hydrophobic amino acid (Leu, Ile, Met and Trp mutation) at position 28 were isolated. Dr0930_83 - Dr0930_85, (containing M234I and Y28L/I/M mutations), appeared to be more active in the crude extract screening for methylphosphonates GF *p*-NP (OP 5) and GD *p*-NP (OP 4; data not shown) than Dr0930_81 and Dr0930_82 (containing V235L+Y28L/W). On the other hand, Dr0930_81 appeared to be slightly more active for MPXN (OP 6) than Dr0930_83.

Dr0930_81 and Dr0930_83, both containing a Leu at position 28, were selected for steady-state kinetic characterization. Both variants were heterologously expressed in media supplemented with 1.0 mM $CoCl_2$, purified by protamine sulfate and ammonium sulfate precipitation in combination with anion exchange chromatrography (4.2.1). Steady-state kinetic characterization was performed as described (3.5.4.1). The saturation curves of Dr0930_81 for the hydrolysis of OPs 1-7 are shown in Figure 44.

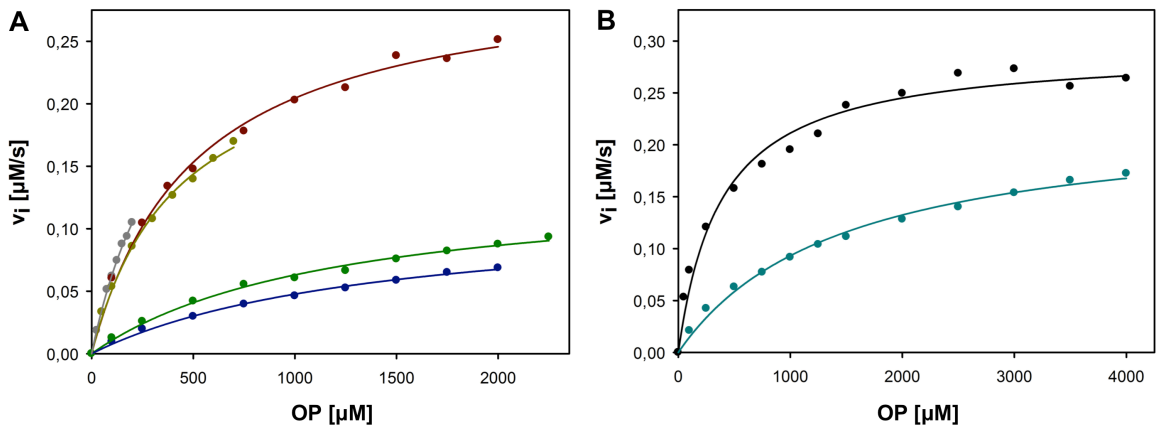

Figure 44: Saturation curves of Dr0930_81 for the hydrolysis of OPs 1-7.
Saturation curves for OP 1 (●), 2 (●), 3 (●), 4 (●) and 5 (●) (A), and OP 6 (●) + 7 (●) (B). The reactions were performed in 50 mM CHES, pH 9.0, 100 µM $CoCl_2$ and variable concentration of OPs. For OP compounds 4 and 5 the reaction assay was supplemented with 12% MeOH. The reaction was monitored at 400 nm (ε_{400} = 1.7 × 10^4 $M^{-1}cm^{-1}$) and 30 °C. Reactions were performed at 100 nM enzyme concentration. The initial velocity v_i is plotted versus the concentration of substrate. The solid line shows the result of the hyperbolic or linear fit of the data points (SigmaPlot). Dr0930_81: Dr0930-Y28L+D71N+E101G+ E179D+V235L+L270M.

The steady-state kinetic parameters determined from the fit of the saturation curves are summarized in Table 21.

Table 21: Steady-state kinetic constants of Co/Co-Dr0930_81 and Co/Co-Dr0930_83 for the hydrolysis of OPs 1-7.

	Co/Co-Dr0930_81			Co/Co-Dr0930_83		
	k_{cat} [s^{-1}]	K_M [mM]	k_{cat}/K_M [$M^{-1}s^{-1}$]	k_{cat} [s^{-1}]	K_M [mM]	k_{cat}/K_M [$M^{-1}s^{-1}$]
1: VX *p*-NP	3.1 × 10^0	0.39	7.9 × 10^3	-	-	1.3 × 10^3
2: GB *p*-NP	3.1 × 10^0	0.5	6.2 × 10^3	3.1 × 10^0	1.23	2.5 × 10^3
3: VR *p*-NP	2.6 × 10^0	0.42	6.2 × 10^3	-	-	1.5 × 10^3
4: GD *p*-NP	1.15 × 10^0	1.42	8.1 × 10^2	-	-	5.6 × 10^2
5: GF *p*-NP	1.4 × 10^0	1.2	1.17 × 10^3	-	-	1.2 × 10^3
6: MPXN	2.3 × 10^0	1.46	1.58 × 10^3	3.0 × 10^0	12.1	2.5 × 10^2
7: EPXN	2.9 × 10^0	0.38	7.6 × 10^3	7.1 × 10^0	3.1	2.3 × 10^3

-: k_{cat}/K_M was determined from non-saturating concentrations by a fit of the initial part of the saturation curve. Compounds 1-5 were applied as racemates. Dr0930_81: Dr0930-Y28L+D71N+E101G+ E179D+V235L+L270M. Dr0930_83: Dr0930-Y28L+D71N+E101G+E179D+M234I+L270M.

Relative to the Dr0930_73 template (Table 19), Dr0930_81 obtained improved catalytic efficiencies for all 7 OPs, exhibiting up to 12-fold higher catalytic efficiencies relative to the template Dr0930_73, and absolute k_{cat}/K_M values of 10^3 $M^{-1}s^{-1}$. Compared to wild-type Dr0930, Dr0930_81 obtains a fold improvement of up to

1.2×10^3, with the highest improvement being obtained for VR *p*-NP (OP 3). Dr0930_81 (containing V235L) was used as template for the next round of mutagenesis as it exhibits slightly higher k_{cat}/K_M values for OPs 1-4 and OPs 6+7 (up to 6-fold), and overall lower K_M values than Dr0930_83 (containing M234I).

4.3.4.3 Combinatorial and insertion/deletion scanning mutagenesis on template Dr0930_81

4.3.4.3.1 Generation of insertion and deletion variants

PTE and Dr0930 differ in the length and conformation of βα-loops, in particular βα-loops 1, 3, 7, and 8. The βα-loop 7 of PTE is 11 amino acids longer than the βα-loop 7 in Dr0930, and contains an extra helix; βα-loops 3 and 8 of Dr0930 and PTE adopt different conformations. In order to adjust Dr0930 to the PTE structure, variants containing multiple amino acid deletions in βα-loop 3 and a five amino acid insertion library were generated on the Dr0930_81 template.

4.3.4.3.1.1 Multiple amino acid deletion variants of βα-loop 3

Hawwa *et al.* (2009b) discovered Dr0930 variants that contained in addition to the mutation Y97L, amino acid deletions in βα-loop 3 (deletion of G100 and E101). The variants exhibited enhanced catalytic efficiency for the hydrolysis of MPXN (OP 6) and EPXN (OP 7) of approximately 20-fold. Here, the deletion variants Dr0930_86, Dr0930_87, and Dr0930_88 were generated, where the amino acids at positions 99-101, 100+101, and 101 were deleted. The variants were generated on the template pTNA-*dr0930_81* using the Phusing® Site-Directed Mutagenesis Kit according to the protocol supplied by the manufacturer (3.3.7.2) and the primer 5'*dr0930*_Δincl101 in combination with 3'*dr0930*_Δ99+100+101, 3'*dr0930*_Δ100+101, 3'*dr0930*_Δ101. The variants were analyzed by *in vitro* activity screening with OPs 1-7 (3.2.8), and exhibited slightly diminished activity (data not shown). The variants Dr0930_86 - Dr0930_88 were not further characterized.

4.3.4.3.1.2 Transposon-mediated insertion scanning mutagenesis

A 5 in-frame amino acid insertion library was generated on the template Dr0930_81 using a commercially available transposon-mediated insertion scanning

mutagenesis kit (MGS^{TM} Kit). The library (theoretical library size of 10^3 individual variants) was generated in the pTNA vector using *Sph*I and *Hin*dIII restriction sites according to the protocol supplied by the manufacturer (3.3.9). Sequencing of the *dr0930* inserts of 10 clones showed that 9 clones contained the 15 bp insertion. The insertions were homogeneously distributed (data not shown). Approximately 700 clones were analyzed by *in vitro* activity screening using GB *p*-NP (OP 2), GD *p*-NP (OP 4) and EPXN (OP 7) (3.2.8). Two variants with similar activity for GB *p*-NP and GD *p*-NP, but with diminished activity for EPXN, were isolated (data not shown). Both variants contained the insertion of an alanine stretch in βα-loop 7: Dr0930_89 (GAAAQ insertion following Q232) and Dr0930_90 (GAAAL insertion at following V235). The result of the experiment confirmed the potential of insertion scanning mutagenesis, and indicates that the βα-loop 7 might be important for substrate specificity. Dr0930_81 tolerated 5 amino acid insertions without inactivation. Due to time constraints randomization of the inserts in the βα-loop 7 was not performed.

4.3.4.3.2 Site-saturation mutagenesis of Tyr97 on template Dr0930_81

Site-saturation mutagenesis at position Tyr97 was performed due to the proximity of the residue to the active site (Figure 40). Tyr97 is conserved within the PLL enzymes (Figure 17); at the equivalent position in *P. diminuta* PTE is a Trp (Trp131). In order to obtain Dr0930 variants with enhanced OPH activity, Y97 has been mutagenized earlier in *D. radiodurans* Dr0930 (Xiang *et al*., 2009; Hawwa *et al.*, 2009b) and *S. solfataricus* SsoPox (Elias *et al.*, 2008). In order to quantify the effect of all 19 single mutations in a systematic manner, and to make a detailed analysis, the variants were generated individually.

The constructs were generated by OE-PCR (3.3.7.4) on the template *dr0930_81* using the mutagenic NNS primers 5'(3')*dr0930*-Y97NNS-E101G or the single mutagenic primers 5'(3')*dr0930*-Y97Q, 5'(3')*dr0930*-Y97W and 5'(3')*dr0930*-Y97C in combination with the 5'(3')*dr0930*-V235L+Δ*Sph*I primers (simultaneously deleted the internal *Sph*I restriction site) and terminal gene primers 5'*dr0930-Sph*I and 3'*dr0930-Hin*dIII. The full-length fragments were digested with *Sph*I and *Hin*dIII restriction enzymes and ligated with equally digested pTNA. The inserts of the 19 individual constructs were verified by sequencing. The generated variants are listed in Table 22.

Table 22: Y97NNS variants generated on the Dr0930_81 template: Dr0930_91 - Dr0930_109.

Dr0930_#: Y28L+D71N+E101G+E179D+V235L+L270M			
91: +Y97M	**96:** +Y97P	**101:** +Y97R	**106:** +Y97F
92: +Y97V	**97:** +Y97H	**102:** +Y97N	**107:** +Y97C
93: +Y97I	**98:** +Y97S	**103:** +Y97G	**108:** +Y97Q
94: +Y97D	**99:** +Y97A	**104:** +Y97T	**109:** +Y97W
95: +Y97L	**100:** +Y97E	**105:** +Y97K	

Dr0930 variants contain the T2Q mutation.

E. coli BL21-CodonPlus(DE3) cells transformed with the pTNA-*dr0930_91* - pTNA-*dr0930_109* constructs were grown in media supplemented with 1.0 mM $CoCl_2$. The crude extract was screened for the hydrolysis of OPs 1-7 (0.15 mM for OPs 1-3 and OPs 6+7; 0.25 mM for OPs 4+5). *In vitro* activity screening results for OPs 4 and 7 are exemplarily shown in Figure 45.

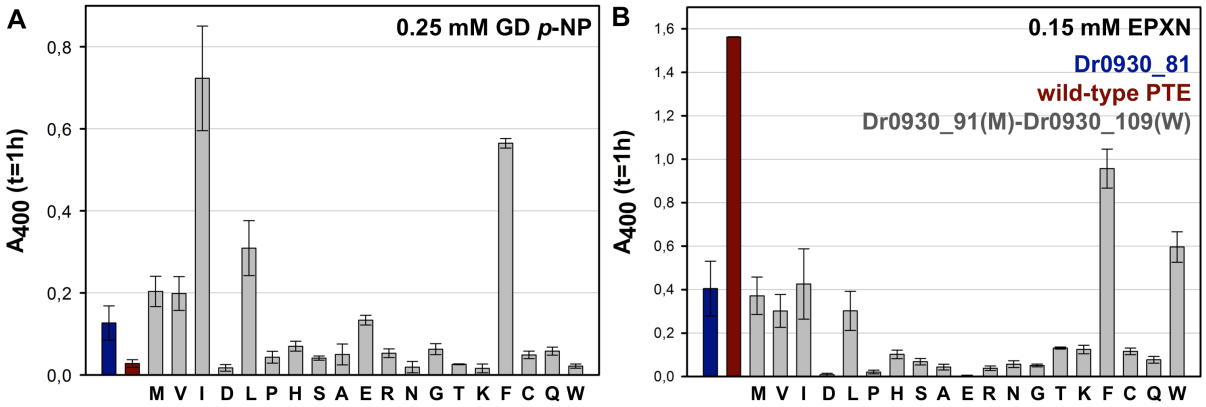

Figure 45: *In vitro* activity screening of the Y97NNS variants using 0.25 mM GD *p*-NP (OP 4) (A) and 0.15 mM EPXN (OP 7) (B).
The activity of the lysed crude extract was assayed in 50 mM CHES pH 9.0, and 0.25/0.15 mM substrate at 400 nm and 30 °C. The A_{400} values were measured in triplicates, the standard deviation is given. The signal of spontaneous background hydrolysis was subtracted from all values (empty pTNA vector was used as negative control). Dr0930_81 (template; Dr0930-Y28L+D71N+E101G+E179D+V235L+L270M) and wild-type PTE (positive control) were used as controls. Although, wild-type PTE exhibits a higher catalytic efficiency for GD *p*-NP than Dr0930_81 (see Table 6 and Table 21), in the crude extract screen it showed lower activity relative to Dr0930_81 due to a lower expression level.

Dr0930 variants containing hydrophobic amino acids (Ile, Leu, Phe, Trp) at position 97 showed increased activity for the hydrolysis of OPs. Dr0930_93 (Y97I) and Dr0930_106 (Y97F) exhibited significantly increased activity for the hydrolysis of GD *p*-NP (OP 4; Figure 45A) and GF *p*-NP (OP 5; data not shown). Dr0930_106 and Dr0930_109 (Y97W) were the most active variants for EPXN (OP 6; Figure 45B) and

MPXN (OP 6; data not shown). However, the improvements of the variant Dr0930_109 (Y97W) were only significant for the hydrolysis of MPXN and EPXN.

Dr0930_93 and Dr0930_106, showing increased activity for all seven OPs, were subjected to *in vitro* characterization in order to quantify the effect of the identified mutations by steady-state enzyme kinetics. The constructs *dr0930_93* and *dr0930_106* were subcloned into the pET24a expression vector. The inserts were amplified by Phusion PCR (3.3.5) using the terminal amplification primers 5'*dr0930-Nde*I and 3'*dr0930-Xho*I. The full-length fragments were digested with *Nde*I and *Xho*I restriction enzymes, ligated with equally digested pET24a vector.

Dr0930_93 (Y97I) and Dr0930_106 (Y97F) were heterologously expressed in media supplemented with 1.0 mM $CoCl_2$, and purified as described (4.2.1). The saturation curves of Dr0930_106 for OPs 1-7 are shown in Figure 46.

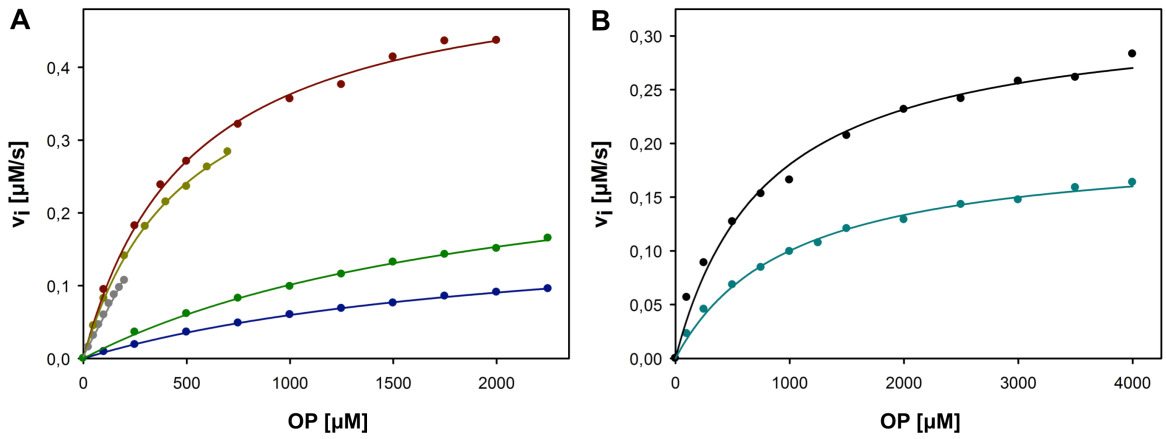

Figure 46: Saturation curves of Co/Co-Dr0930_106 for the hydrolysis of OPs 1-7.
Saturation curves for OP 1 (●), 2 (●), 3 (●), 4 (●) and 5 (●) (A), and OP 6 (●) + 7 (●) (B). The reactions were performed in 50 mM CHES, pH 9.0, 100 µM $CoCl_2$ and variable concentration of OPs. For OP compounds 4 and 5 the reaction assay was supplemented with 12% MeOH. The reaction was monitored at 400 nm (ε_{400} = 1.7 × 10^4 $M^{-1}cm^{-1}$) and 30 °C. Reactions were performed at 25 nM enzyme concentration. The initial velocity v_i is plotted versus the concentration of substrate. The solid line shows the result of the hyperbolic or linear fit of the data points (SigmaPlot). Dr0930_106: Dr0930-Y28L+D71N+Y97F+E101G+E179D+V235L+L270M.

The steady-state kinetic parameters determined from the fit of the saturation curves are summarized in Table 23.

Table 23: Steady-state kinetic constants of Co/Co-Dr0930_93 and Co/Co-Dr0930_106 for the hydrolysis of OPs 1-7.

	Co/Co-Dr0930_93			Co/Co-Dr0930_106		
	k_{cat} [s^{-1}]	K_M [mM]	k_{cat}/K_M [$M^{-1}s^{-1}$]	k_{cat} [s^{-1}]	K_M [mM]	k_{cat}/K_M [$M^{-1}s^{-1}$]
1: VX *p*-NP	-	-	1.2×10^4	-	-	2.2×10^4
2: GB *p*-NP	3.73×10^1	1.5	2.5×10^4	2.19×10^1	0.51	4.3×10^4
3: VR *p*-NP	1.47×10^1	0.39	3.8×10^4	1.9×10^1	0.48	4.0×10^4
4: GD *p*-NP	1.63×10^1	3.8	4.3×10^3	7.51×10^0	2.15	3.5×10^3
5: GF *p*-NP	2.96×10^1	4.9	6.0×10^3	1.27×10^1	2.13	6.0×10^3
6: MPXN	n.a.	n.a.	n.a.	8.0×10^0	1.0	8.0×10^3
7: EPXN	9.2×10^0	1.5	6.1×10^3	1.3×10^1	0.8	1.6×10^4

-: k_{cat}/K_M was determined from non-saturating concentrations by a fit of the initial part of the saturation curve. n.a.: not analyzed. Compounds 1-5 were applied as racemates. Dr0930_93: Dr0930-Y28L+D71N+Y97I+E101G+E179D+V235L+L270M. Dr0930_106: Dr0930-Y28L+D71N+Y97F+E101G+E179D+V235L+L270M.

The catalytic efficiencies of Dr0930_93 and Dr0930_106 are overall very similar. The absolute values of k_{cat}/K_M of approach 10^4 $M^{-1}s^{-1}$. Compared to Dr0930_106, Dr0930_93 exhibits approximately two fold higher k_{cat} values for GD *p*-NP (OP 4) and GF *p*-NP (OP 5), but also slightly higher K_M values. Dr0930_106 was used as template for further combinatorial mutagenesis due to its lower K_M value. When compared to the template Dr0930_81, Dr0930_106 obtains a 2-7-fold improvement in k_{cat}/K_M. Relative to wild-type Dr0930, Dr0930_106 obtains highest fold improvements for GB *p*-NP (OP 2) (4.4×10^3) and VR *p*-NP (OP 3) (7.8×10^3).

4.3.4.4 Mutagenesis on template Dr0930_106

4.3.4.4.1 Site-saturation mutagenesis at position Phe26

Site-saturation mutagenesis at position Phe26 was performed due to the proximity of the residue to the active site (Figure 40). The corresponding residue in PTE, G60, is crucial for the OPH activity (Chen-Goodspeed *et al.*, 2001a/b). Although, the position was mutagenized earlier (Xiang *et al.*, 2009; Hawwa *et al.*, 2009b), the position was subjected to detailed characterization in order to quantify the effect of the single mutations. The 19 variants (Dr0930_110 - Dr0930_128) were generated by QuikChange mutagenesis (3.3.7.1) on the template pTNA-*dr0930_106* using single primers listed in 2.8.2. *In vitro* activity screening with 0.15 mM OPs 1-7 was performed as described (3.2.8). All 19 variants were essentially inactive for OPs

1-6, and showed significantly diminished activity for OP 7 (data not shown). Thus, residue F26 seems to be critical for substrate positioning (see also 4.4.5.2).

4.3.4.4.2 Combinatorial site-directed mutagenesis on template Dr0930_106

Beneficial mutations identified in the first-generation variants Dr0930_11 and Dr0930_12 isolated from the epPCR library (Figure 30; Table 8) were added in various combinations onto the best variant Dr0930_106. The mutations are localized in βα-loops 1, 3 and 8: G38R (βα-loop 1), T105S (βα-loop 3), P274L (βα-loop 8), R272C (βα-loop 8) (Figure 40). Likewise, combinatorial variants were generated with Met or Leu (wild-type amino acid) at position 270 (βα-loop 8) to analyze the effect of the more distant mutation.

Constructs containing single or double mutations were generated by (consecutive) QuikChange mutagenesis (3.3.7.1) on the template pTNA-*dr0930_106* using primers listed in 2.8.2. Constructs containing three or four mutations were generated by QuikChange mutagenesis (3.3.7.1) or OE-PCR (3.3.7.4) using the constructs generated earlier. The primers used are listed in 2.8.2, 5'*dr0930-Sph*I-T2Q and 3'*dr0930-Hin*dIII were used as terminal gene primers. Genes were inserted in the pTNA vector using *Sph*I and *Hin*dIII restriction sites. The generated variants are listed in Table 24.

Table 24: Variants generated by combinatorial mutagenesis on template Dr0930_106: Dr0930_129 - Dr0930_143.

Dr0930_#: Y28L+D71N+Y97F+E101G+E179D+V235L+L270M	
129: +G38R	**137:** +G38R+P274L
130: +T105S	**138:** +G38R+M270L+P274L
131: +R272C	**139:** +G38R+T105S+R272C
132: +P274L	**140:** +G38R+T105S+P274L
133: +M270L+R272C	**141:** +G38R+M270L+R272C
134: +M270L+P274L	**142:** +G38R+T105S+M270L+R272C
135: +G38R+T105S	**143:** +G38R+T105S+M270L+P274L
136: +G38R+R272C	

Dr0930 variants contain the T2Q mutation.

E. coli BL21-CodonPlus(DE3) cells transformed with the pTNA-*dr0930_129* - pTNA-*dr0930_143* constructs were grown in media supplemented with 1.0 mM $CoCl_2$. The lysed and diluted crude extract was screened for the hydrolysis of OPs 1-7 (0.15 mM for OPs 1-3 and OPs 6+7; 0.2 mM for OPs 4+5). *In vitro* activity screening results for GB *p*-NP (OP 2) and GD *p*-NP (OP 4) are exemplarily shown in Figure 47.

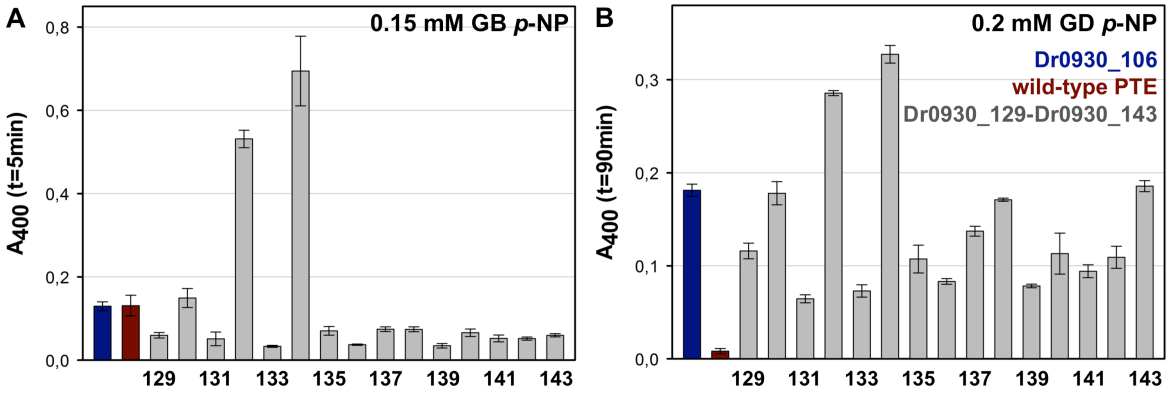

Figure 47: *In vitro* activity screening of Dr0930_129 - Dr0930_143 using 0.15 mM GB *p*-NP (OP 2) (A) and 0.2 mM GD *p*-NP (OP 4) (B).
The activity of the crude lysate was assayed in 50 mM CHES pH 9.0, and 0.15/0.2 mM substrate at 400 nm and 30 °C. The A_{400} values were measured in triplicates and the standard deviation is given. The signal of spontaneous background hydrolysis was subtracted from all values (empty pTNA vector was used as negative control). Dr0930_106 (template; Dr0930-Y28L+D71N+Y97F+E101G+E179D+V235L+L270M) and wild-type PTE (positive control) were used as controls. Although wild-type PTE exhibits a higher catalytic efficiency for GB *p*-NP than Dr0930_106 (Table 6; Table 23), in the crude extract screen it showed lower activity relative to Dr0930_106 due to a lower expression level. Due to the high activity, the lysed crude extract was diluted in 50 mM HEPES pH 8.5, 100 µM $CoCl_2$ prior to the screen.

The best variants Dr0930_132 and Dr0930_134 contain the P274L mutation and differ at position 270 (Met versus wild-type Leu). The other mutations (G38R, T105S, and R272C) had no beneficial effect on the activity. The Dr0930_132 and Dr0930_134 variants showed comparable solubility (data not shown); hence Dr0930_134 was selected for *in vitro* characterization as it shows slightly higher activity and contains one less mutation.

The construct *dr0930_134* was subcloned in the pET24a expression plasmid. The insert was amplified using terminal gene primers 5'*dr0930-Nde*I and 3'd*r0930-Xho*I. The full-length fragment was digested with *Nde*I and *Xho*I restriction enzymes, and ligated with equally digested pET24a. The variant was heterologously expressed and purified as described (4.2.1). Saturation curves from steady-state kinetic characterization of Co/Co-Dr0930_134 with OPs 1-7 are shown in Figure 48.

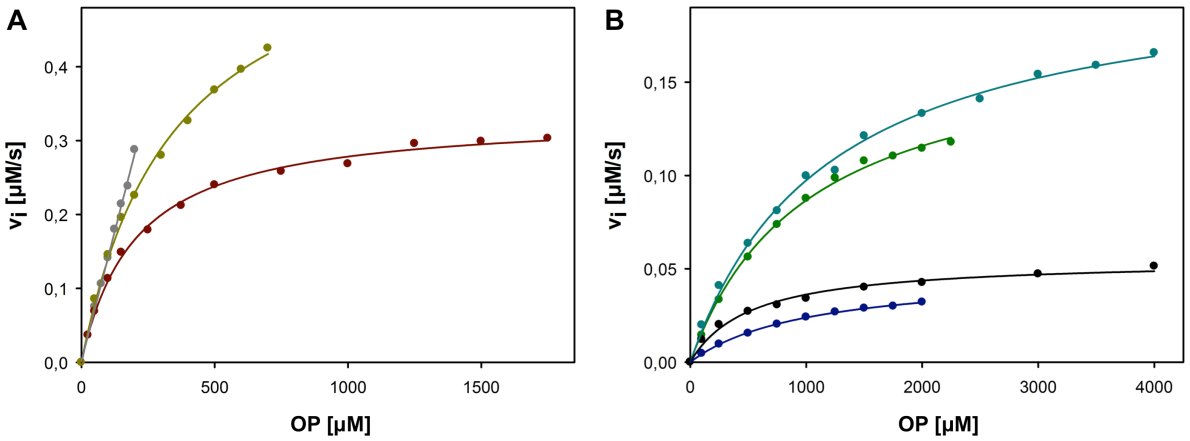

Figure 48: Saturation curves of Co/Co-Dr0930_134 for the hydrolysis of OPs 1-7.
Saturation curves for OP 1 (●), 2 (●), 3 (●) (**A**), and 4 (●), 5 (●), 6 (●), 7 (●) (**B**).
The reactions were performed in 50 mM CHES, pH 9.0, 100 µM $CoCl_2$ and variable concentration of OPs. For OP compounds 4 and 5 the reaction assay was supplemented with 12% MeOH. The reaction was monitored at 400 nm (ε_{400} = 1.7 × 10^4 $M^{-1}cm^{-1}$) and 30 °C. The saturation curves were determined in triplicates; exemplary curves are shown. Dr0930_136 was diluted in 20 mM HEPES pH 7.5, 100 µM $CoCl_2$ buffer supplemented with 1 mg/ml BSA in order to stabilize the protein at high dilutions. BSA has no influence on activity (data not shown). Reactions were performed with 5 nM enzyme concentration. The initial velocity v_i is plotted versus the concentration of substrate. The solid line shows the result of the hyperbolic or linear fit of the data points (SigmaPlot). Dr0930_134: Dr0930-Y28L+D71N+Y97F+E101G+E179D+V235L+P274L.

The steady-state kinetic parameters determined from the fit of the saturation curves are summarized in Table 25.

Table 25: Steady-state kinetic parameters of Co/Co-Dr0930_134 for the hydrolysis of OPs 1-7.

	Co/Co-Dr0930_134[a]		
	k_{cat} [s^{-1}]	K_M [mM]	k_{cat}/K_M [$M^{-1}s^{-1}$]
1: VX *p*-NP	-	-	2.5 ± 0.7 × 10^5
2: GB *p*-NP	6.8 ± 0.3 × 10^1	0.19 ± 0.01	3.6 ± 0.2 × 10^5
3: VR *p*-NP	1.27 ± 0.04 × 10^2	0.36 ± 0.02	3.5 ± 0.2 × 10^5
4: GD *p*-NP	9.4 ± 0.3 × 10^0	1.03 ± 0.08	9.2 ± 0.6 × 10^3
5: GF *p*-NP	4.0 ± 0.4 × 10^1	1.1 ± 0.1	3.5 ± 0.1 × 10^4
6: MPXN	4.2 ± 0.4 × 10^1	1.26 ± 0.07	3.4 ± 0.4 × 10^4
7: EPXN	1.1 ± 0.1 × 10^1	0.53 ± 0.08	2.0 ± 0.1 × 10^4

[a]: The kinetic constants were determined in three independent measurements. The standard deviation is given. -: k_{cat}/K_M was determined from non-saturating concentrations by a fit of the initial part of the saturation curve. Compounds 1-5 were applied as racemates. Dr0930_134: Dr0930-Y28L+D71N+Y97F+E101G+E179D+V235L+P274L.

Figure 49A illustrates the catalytic efficiencies of Dr0930_134 for OPs 1-7, Figure 49B provides the individual values of k_{cat} and K_M.

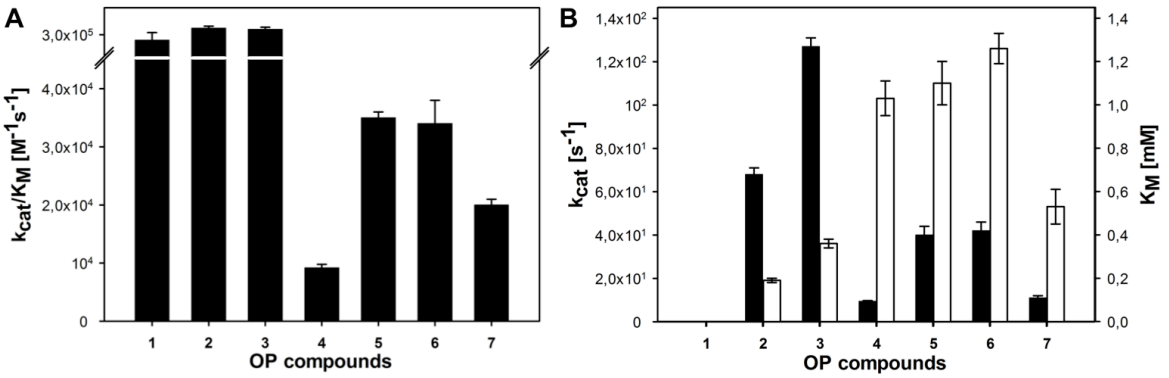

Figure 49: Catalytic efficiencies (k_{cat}/K_M) (A) and k_{cat} (filled bars) and K_M (open bars) values of Co/Co-Dr0930_134 for OPs 1-7.
The kinetic constants were determined in three independent measurements. The standard deviation is given. For OP 1: only k_{cat}/K_M was determined from non-saturating concentrations by a fit of the initial part of the saturation curve.

Dr0930_134 is most efficient for the hydrolysis of methylphosphonates with a small substituent at the P-center (OPs 1-3), achieving high catalytic efficiencies of 10^5 $M^{-1}s^{-1}$. Highest k_{cat} values were achieved for OPs 2 and 3. The K_M values within methylphosphonate compounds 2-5 increase with the size of the substituent at the P-center. Moreover, Dr0930_134 achieves a fold improvement in k_{cat}/K_M ranging from 1.3 for EPXN (OP 7) to more than one order of magnitude (11.4-fold) for VX *p*-NP (OP 1), when compared to the previous variant Dr0930_106.

Figure 50A illustrates the fold activity improvement of Dr0930_134 compared to the starting template wild-type Dr0930. The fold improvement in k_{cat}/K_M is substantial, ranging from two (VX *p*-NP (OP 1), MPXN (OP 6), EPXN (OP 7)) to four (GB *p*-NP (OP 2), VR *p*-NP (OP 3), GF *p*-NP (OP 5)) orders of magnitude. The fold improvement is mainly due to an enhancement in k_{cat}. When compared to wild-type Dr0930, the K_M values are, except for MPXN, only slightly reduced (not shown). Compared to wild-type PTE, the catalytic efficiencies of Dr0930_134, are lower by one to two orders of magnitude for methylphosphonates (OPs 1-5) and three to four orders of magnitude for phosphotriesters (MPXN and EPXN) (not shown). However, the catalytic efficiency for GD *p*-NP (OP 4) is essentially identical to that obtained by wild-type PTE (Figure 50B).

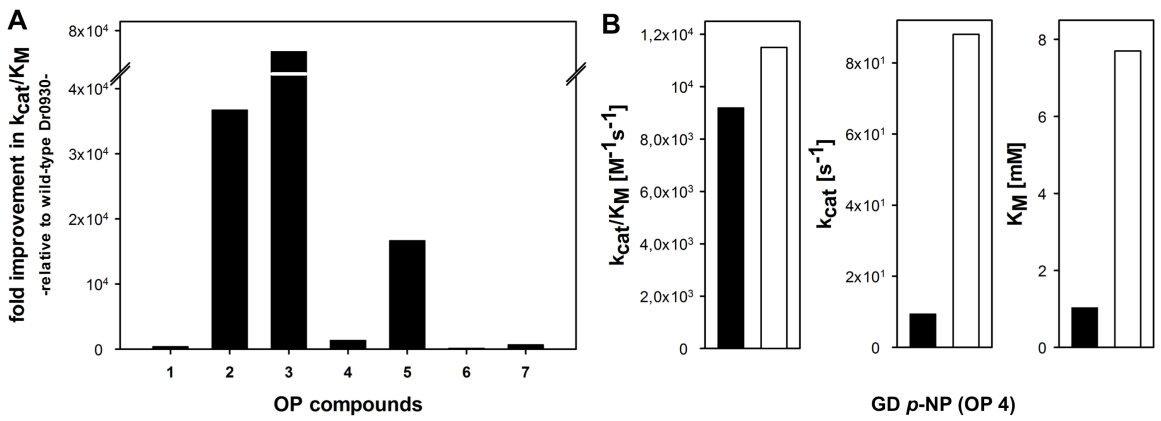

Figure 50: Comparison of Dr0930_134 with wild-type Dr0930 (A) and wild-type PTE (B).
A: Fold improvements of Dr0930_134 in k_{cat}/K_M compared to wild-type Dr0930: 4.1×10^2 (OP 1), 3.7×10^4 (OP 2), 6.9×10^4 (OP 3), 1.4×10^3 (OP 4), 1.7×10^4 (OP 5), 1.7×10^2 (OP 6), 6.9×10^2 (OP 7). **B:** Comparison of absolute values of k_{cat}/K_M, k_{cat}, and K_M of Dr0930_134 (filled bars) and wild-type PTE (open bars) for GD *p*-NP (OP 4).

The catalytic efficiency for the hydrolysis of VR *p*-NP (OP 3) by Dr0930_134 has been improved by 6.9×10^4-fold thereby reaching k_{cat}/K_M values that approach the level of natural enyzmes (see Table 25: $k_{cat}/K_M > 10^5$ $M^{-1}s^{-1}$; Bar-Even *et al.*, 2011). Moreover, the results support the notion that broad substrate specificity does not necessarily trade-off with catalytic efficiency (Goldsmith *et al.*, 2012).

4.3.5 Summary: Design of a multi-efficient OPH

Figure 51 summarizes the crucial evolved Dr0930 variants most important for in the design for a multi-efficient OPH.

Engineered Dr0930 variants				
Dr0930_5 **D71N+E179D+L270M**	**Dr0930_73** D71N+**E101G**+E179D +**V235L**+L270M	**Dr0930_81** **Y28L**+D71N+E101G +E179D+V235L+ L270M	**Dr0930_106** Y28L+D71N+**Y97F** +E101G+E179D+ V235L+L270M	**Dr0930_134** Y28L+D71N+Y97F +E101G+E179D+ V235L+**P274L**
Mutagenesis strategy				
random mutagenesis by error-prone PCR	combinatorial mutagenesis	Y28NNS site- saturation mutagenesis	Y97NNS site- saturation mutagenesis	combinatorial mutagenesis
Fold improvements in k_{cat}/K_M relative to wild-type Dr0930 (previous variant)				
up to 2.1×10^2-fold	up to 2.4×10^2-fold (up to 5-fold)	up to 1.2×10^3-fold (up to 12-fold)	up to 7.8×10^3-fold (up to 7-fold)	up to 6.9×10^4-fold (up to 11-fold)

Figure 51: Overview on the enzyme design approach.
The engineered Dr0930 variants crucial in the design for a multi-efficient OPH are summarized.

Most noteworthy, the first generation variant, Dr0930_5, yielded the highest improvement of up to 2.1×10^2-fold in k_{cat}/K_M. The fold improvements of the consecutive evolved variants were no more than one order of magnitude.

4.4 Detailed Characterization of best engineered Dr0930 variants

Next, the engineered Dr0930 variants listed in Figure 51 were kinetically characterized for the hydrolysis of δ-nonanoic lactone (native activity) and the hydrolysis of the phosphorothiolate DEVX (OP 8). Moreover, the stereopreference for OPs 1-5 of wild-type Dr0930 and the best variant Dr0930_134 were analyzed. The crystal structures of three engineered Dr0930 variants were solved, and ligand docking was performed to explain the structural basis for the enhanced OPH activity.

4.4.1 Steady-state kinetic characterization for the hydrolysis of δ-nonanoic lactone (native activity)

In order to relate the trade-off between native and engineered promiscuous activity, the Dr0930 variants, Dr0930_5, Dr0930_73, Dr0930_81, Dr0930_106, and Dr0930_134, were characterized for the hydrolysis of δ-nonanoic lactone (δ-NL) using a pH-sensitive colorimetric assay (3.5.4.3). The saturation curves are shown in Figure 52 in comparison to wild-type Dr0930.

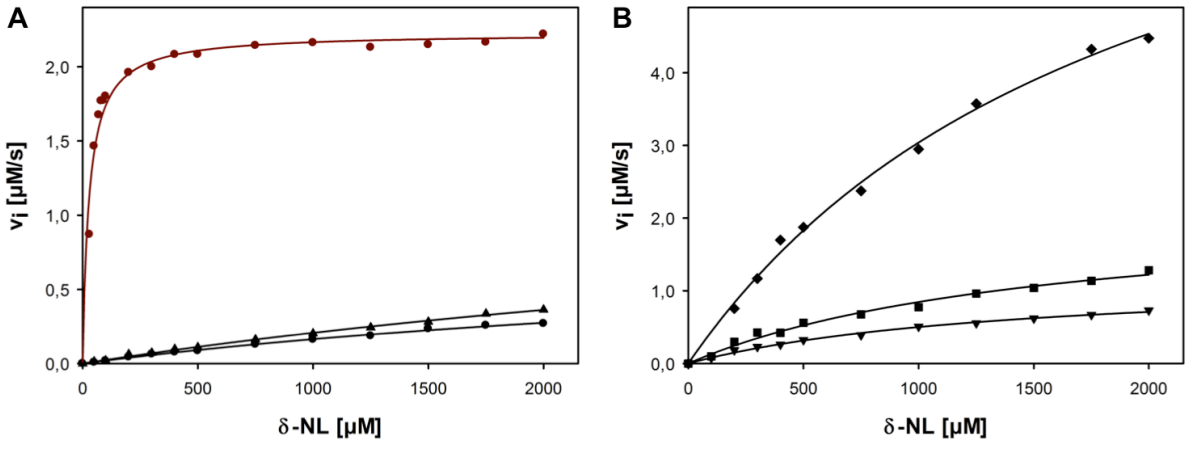

Figure 52: Saturation curves of wild-type Dr0930 and variants for the hydrolysis of δ-nonanoic lactone.
A: wild-type Dr0930 (●), Dr0930_73 (▲), Dr0930_81 (●). **B:** Dr0930_5 (◆), Dr0930_106 (▼), Dr0930_134 (■).
The reactions were performed in 2.5 mM BICINE (initial pH: 8.3), 0.1 mM $CoCl_2$, 1.4% DMSO, 0.1 mM *m*-cresol purple, 0.2 M NaCl and variable concentration of δ-nonanoic lactone (0-2 mM). The reaction was monitored at 577 nm (ε_{577} = 1.17×10^3 $M^{-1}cm^{-1}$) and 30 °C. Prior to use, the protein buffer was

exchanged to 10 mM bicine pH 8.3, 100 µM $CoCl_2$ using a NAP-25 desalting column. Wild-type Dr0930 and Dr0930 variants were diluted in 10 mM bicine pH 8.3, 100 µM $CoCl_2$, 1 mg/ml BSA. BSA has no influence on activity (data not shown). Reactions were performed at 10 nM (A) and 0.5 µM (B) enzyme concentration, respectively. The initial velocity v_i is plotted versus the concentration of substrate. The solid line shows the result of the hyperbolic fit of the data points (SigmaPlot).

The steady-state kinetic parameters determined from the fit of the saturation curve are summarized in Table 26 and Figure 53.

Table 26: Steady-state kinetic constants of wild-type Co/Co-Dr0930 and engineered Dr0930 variants for the hydrolysis of δ-nonanoic lactone.

		δ-NL		
		k_{cat} [s^{-1}]	K_M [mM]	k_{cat}/K_M [$M^{-1}s^{-1}$]
Dr0930 wild-type		2.2×10^2	0.028	7.9×10^6
Dr0930_5[a]	D71N+E179D+L270M	1.79×10^1	1.94	9.2×10^3
Dr0930_73	D71N+E101G+E179D+V235L +L270M	1.43×10^2	5.87	2.4×10^4
Dr0930_81	Y28L+D71N+E101G+E179D +V235L+L270M	8.59×10^1	4.23	2.0×10^4
Dr0930_106	Y28L+D71N+Y97F+E101G +E179D+V235L+L270M	2.4×10^0	1.42	1.7×10^3
Dr0930_134	Y28L+D71N+Y97F+E101G +E179D+V235L+P274L	4.4×10^0	1.59	2.8×10^3
PTE wild-type		5.7×10^{-2}	0.84	6.8×10^1

[a]: Dr0930_5 contains an additional T2Q mutation, which is assumed to have no effect on activity. The saturation curve of wild-type PTE for the hydrolysis of δ-nonanoic lactone is shown in Figure 24B.

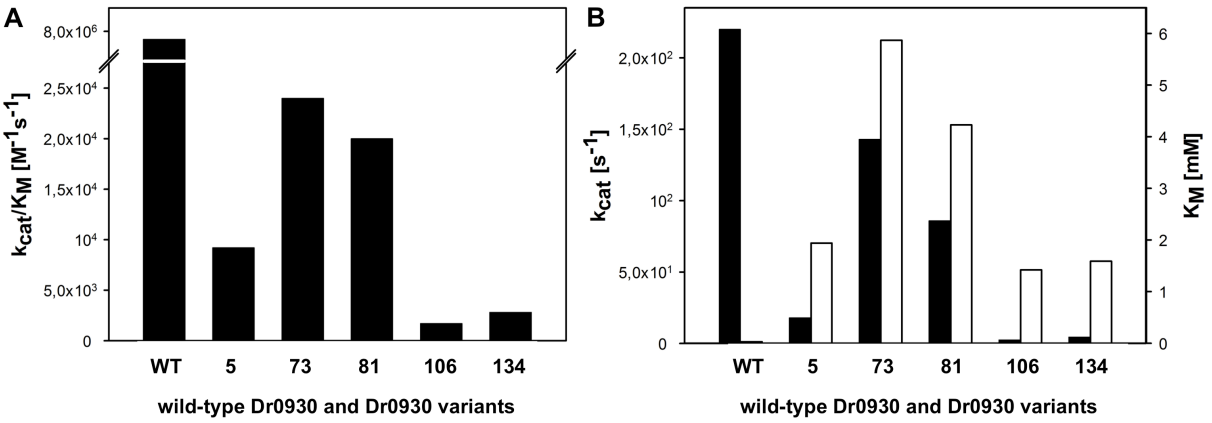

Figure 53: Catalytic efficiencies (A) and k_{cat} (filled bars) and K_M (open bars) parameters (B) of wild-type Co/Co-Dr0930 and Co/Co-Dr0930 variants for the hydrolysis of δ-nonanoic lactone.
A: The catalytic efficiencies of Dr0930_5, Dr0930_73, Dr0930_81, Dr0930_106 and Dr0930_134 compared to wild-type Dr0930 are reduced by 8.6×10^2, 3.3×10^2, 4.0×10^2, 4.7×10^3, and 2.8×10^3 -fold, respectively. **B:** The engineered variants exhibit significantly increased K_M values (in the mM range) and decreased k_{cat} values compared to wild-type Dr0930.

Compared to wild-type Dr0930, the catalytic efficiency for the hydrolysis of δ-nonanoic lactone by the best engineered variant, Dr0930_134 (fold improvement in k_{cat}/K_M for the hydrolysis of OPs 1-7 is 1.7×10^2 - 6.9×10^4), is diminished by three orders of magnitude (absolute value of catalytic efficiency of 2.8×10^3 $M^{-1}s^{-1}$), due to an approximately 50-fold increase in K_M and a 50-fold decrease in k_{cat}. Hence, the increase in promiscuous OPH activity is accompanied by an equal decrease in the original function. Despite the partial trade-off, Dr0930_134 is a truly bifunctional enzyme exhibiting broad substrate specificity. The catalytic efficiencies of lactone and OP hydrolysis are in the range of 10^3 - 10^5 $M^{-1}s^{-1}$.

Interestingly, the catalytic efficiency for δ-nonanoic lactone did not continuously decrease in the course of the design. The k_{cat}/K_M value drops by two orders of magnitude with the first variant, whereas the two subsequent variants show slightly increased activity compared to Dr0930_5. With the introduction of the Y97F mutation the activity drops by another order of magnitude. The effect of the mutation of the PLL-conserved residue Y97 to Phe on the δ-nonanoic lactone activity has been investigated earlier in Xiang *et al.* (2009): the activity for Zn/Zn-Dr0930-Y97F was lower by a factor of approximately 2.5×10^2 compared to wild-type Dr0930.

Overall, our results confirm that the engineered OPH activity can be extremely high while retaining a k_{cat}/K_M of 10^3 $M^{-1}s^{-1}$ for the native activity, the hydrolysis of δ-nonanoic lactone.

4.4.2 Steady-state kinetic characterization for the hydrolysis of DEVX

To investigate the extended substrate specificity for the phosphorothiolate bond cleavage, the activity of wild-type Dr0930 and the engineered variants was investigated for the hydrolysis of DEVX (OP 8) and the kinetic parameters were compared to those for wild-type PTE. Wild-type Dr0930 and Dr0930 variants were characterized by steady-state enzyme kinetics using a DTNB coupled assay (3.5.4.2). The kinetic parameters determined form saturation curves (data not shown) are summarized in Table 27.

Table 27: Steady-state kinetic constants of wild-type Co/Co-Dr0930 and engineered variants for the hydrolysis of DEVX.

		DEVX		
		k_{cat} [s^{-1}]	K_M [mM]	k_{cat}/K_M [$M^{-1}s^{-1}$]
Dr0930 wild-type[a]		n.d.	n.d.	n.d.
Dr0930_5[b]	D71N+E179D+L270M	7.3×10^{-3}	5.5	1.3×10^{0}
Dr0930_73	D71N+E101G+E179D+V235L +L270M	1.5×10^{-2}	7.7	1.9×10^{0}[c]
Dr0930_81	Y28L+D71N+E101G+E179D +V235L+L270M	6.5×10^{-3}	9.5	6.8×10^{-1}
Dr0930_106	Y28L+D71N+Y97F+E101G +E179D+V235L+L270M	6.7×10^{-3}	3.48	2.0×10^{0}
Dr0930_134[a]	Y28L+D71N+Y97F+E101G +E179D+V235L+P274L	n.d.	n.d.	n.d.
PTE wild-type[c]		5.6×10^{-1}	10.6	5.3×10^{1}

The reactions were performed in 50 mM HEPES pH 8.0, 0.3 mM DTNB, 100 µM $CoCl_2$, 12% MeOH and variable concentrations of DEVX (0-3.5 mM). The reaction was monitored at 412 nm ($\varepsilon_{412} = 1.415 \times 10^4\ M^{-1}cm^{-1}$) and 30 °C. n.d.: not detected. [a]: No activity was detected for wild-type Dr0930 and Dr0930_134 for the hydrolysis of DEVX up to 50 µM enzyme concentration. [b]: Dr0930_5 contains an additional T2Q mutation, which is assumed to have no effect on activity. [c]: Kinetic parameters for DEVX differ from previous measured parameters ($k_{cat} = 1\ s^{-1}$, $K_M = 0.8$ mM, $k_{cat}/K_M = 1.2 \times 10^3\ M^{-1}s^{-1}$; personal communication Dr. A. Bigley), predominantly in K_M.

The kinetic parameters for wild-type PTE with DEVX determined here differ from previously determined values by one order of magnitude in K_M (k_{cat} is essentially identical). The reason for this remains unclear. Overall, phosphorothiolates are hydrolyzed by wild-type PTE at significantly lower rates compared to OPs 1-7. The catalytic efficiencies of the engineered Dr0930 variants are low, and 1-2 fold reduced compared to wild-type PTE. Moreover, wild-type Dr0930 and the best engineered variant exhibit no measureable activity at 50 µM enzyme concentration.

Our results show that although Dr0930_134 is extremely efficient for the hydrolysis of P-O bond within VX *p*-NP, no activity for the hydrolysis of P-S bond within structurally similar DEVX is observable.

4.4.3 Stereopreference analysis of wild-type Dr0930 and Dr0930_134

The design of Dr0930 for enhanced OPH activity was performed applying racemic OPs. To assess the stereopreference and analyze potential changes during the design approach the stereoselectivity of wild-type Dr0930 and the best evolved variant, Dr090_134, were investigated for the methylphosphonates OPs 1-5.

The strategy to elucidate the stereopreference is exemplarily illustrated for VR *p*-NP (OP 3) in Figure 54 and briefly described in the following. Chemical and enzymatic hydrolysis of OP is monitored as a function of time, and the change in A_{400} over time is an exponential time course. Initially, the total concentration of VR *p*-NP ($[S]<K_M$) and the resulting amplitude corresponding to 100% hydrolysis is determined by chemical hydrolysis of VR *p*-NP using KOH (Figure 54A). The time courses for the enzymatic hydrolysis of OP 3 by wild-type Dr0930 (blue curve) and Dr0930_134 (red curve) are presented in Figure 54B. The time course of wild-type Dr0930 exhibits a double exponential curve shape. A double exponential fit of the data (Equation 13) provides the rate constants for the two enantiomers using a single concentration of enzyme. The obtained rate constants divided by the enzyme concentration yields k_{cat}/K_M. The time course for Dr0930_134 indicates, that the two enantiomers are hydrolyzed at significantly different rates, since only one-half of the total substrate is hydrolyzed within 30 min. A higher concentration of enzyme is added to hydrolyze the remaining enantiomer. Both phases are analyzed by single exponential fits. To assign the configuration of the non-hydrolyzed isomer in solution after the reaction has approximately reached an end point at half amplitude, wild-type PTE or engineered PTE variants, PTE-G60A and PTE-H254G+H257W+L303T, with assigned stereopreference (Tsai *et al.*, 2010a) were added to the reaction mixture. The rate assignment is exemplarily shown for Dr0930_134 in Figure 54C and D. An appropriate amount of Dr0930_134 is added to 50 µM VR *p*-NP, inducing the hydrolysis of one enantiomer. After one-half of the total substrate is hydrolyzed (50% amplitude), PTE-G60A (high enantiomeric preference for R_P) is added to hydrolyze the R_P enantiomer. As no change in absorbance is observed, the hydrolyzed stereoisomer has R_P configuration, indicating the fast phase of racemate hydrolysis corresponds to the R_P-isomer. As additional control PTE-H254G+H257W+L303T, with high enantiomeric preference for S_P, was added to the reaction mixture to hydrolyze the remaining S_P enantiomer resulting in fast hydrolysis. The catalytic efficiency determined for the phase of PTE-H254G+H257W+L303T in Figure 54C is equal to the catalytic efficiency determined for the first phase of PTE-H254G+H257W +L303T in Figure 54D, confirming the conformational assignment.

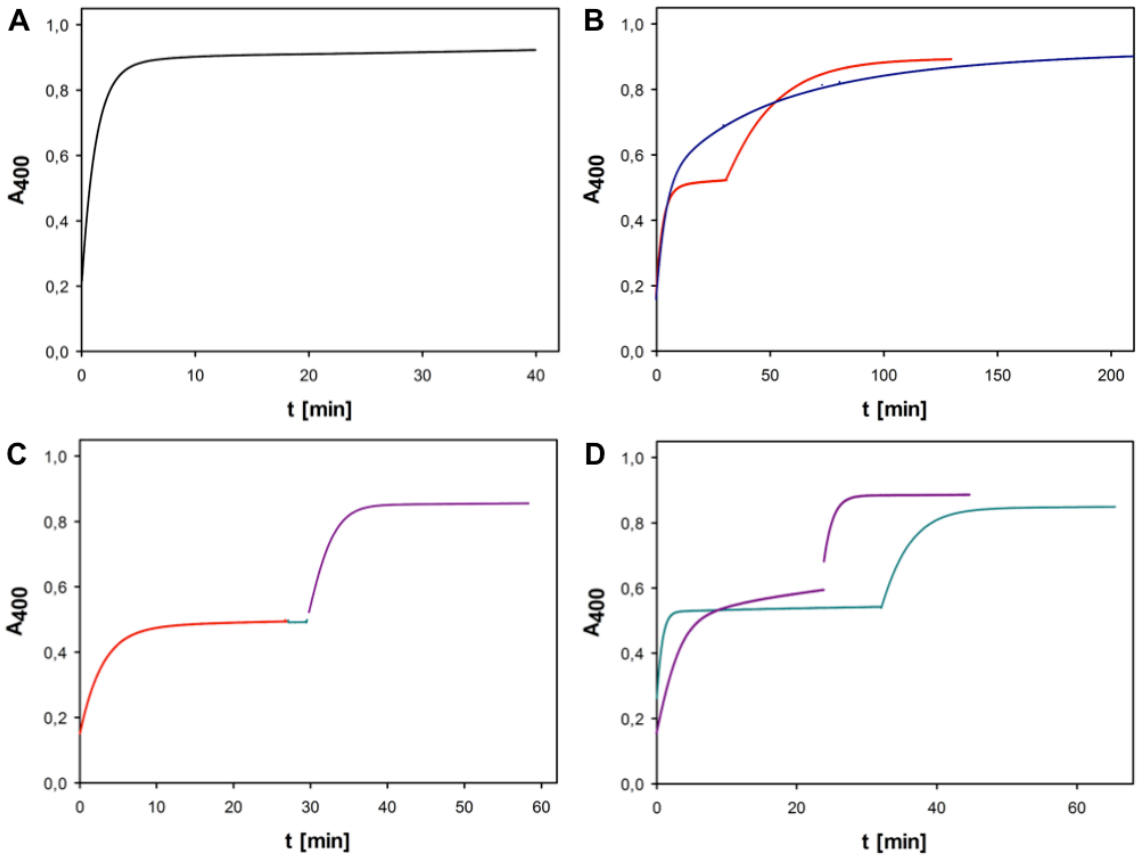

Figure 54: Time courses for the chemical (A) and enzymatic hydrolysis (B, C, D) of approximately 50 µM racemic VR *p*-NP (OP 3).
The stereopreference of wild-type Dr0930 and Dr0930_134 was assigned using previously reported stereopreferences of wild-type PTE and PTE variants for *p*-acetylphenyl substituted OPs (Tsai *et al.*, 2010a). The PTE variants, PTE-G60A and PTE-H254G+H257W+L303T, were kindly provided by Dr. A. Bigley (group of Prof. Dr. F. M. Raushel).
A: Hydrolysis of racemic VR *p*-NP by 75 mM KOH as a function of time. The total concentration of VR *p*-NP was determined by complete chemical hydrolysis.
B: Time courses for the hydrolysis of racemic VR *p*-NP using 110 µM wild-type Dr0930 (blue) and 4.9 nM Dr0930_134 (red). Dr0930_134 hydrolyzes both enantiomers at significantly different rates. After 30 minutes one half of the substrate was hydrolyzed by Dr0930_134, and 4.8 µM Dr0930_134 was added to the reaction to hydrolyze the remaining enantiomer. The hydrolysis profile data for wild-type Dr0930 fits to the sum of two exponentials. For Dr0930_134 the data of the individual phases fits to a single exponential fit each.
C: The hydrolysis of the R_P enantiomer of racemic VR *p*-NP was initiated with 4.9 nM Dr0930_134. After 27 minutes 0.65 nM PTE-G60A variant (dark cyan) was added (enantiomeric preference for R_P; ratio R_P:S_P (VR *p*-acetylphenyl) = 7600:1) and no further hydrolysis was observed. At 30 minutes 4.1 nM PTE-H254G+H257W+L303T variant (dark purple; enantiomeric preference for S_P, ratio R_P:S_P (VR *p*-acetylphenyl) = 1:120) was added to hydrolyze the remaining S_P enantiomer. The k_{cat}/K_M value determined from the fit of the time course of PTE-H254G+H257W+L303T is equal to the k_{cat}/K_M value determined for the first phase of PTE-H254G+H257W+L303T in Figure 54D.
D: Hydrolysis of racemic VR *p*-NP by 4.1 nM PTE-H254G+H257W+L303T (dark purple) and 0.65 nM PTE-G60A (dark cyan) as a function of time. At 23 and 32 minutes respectively, higher concentrations of enzyme (0.28 µM and 3 µM) were added for complete hydrolysis. The data for the first phase of PTE-G60A and both second phases is fit by a single exponential fit. The data of the first phase for H254G+H257W+L303T fits to the sum of two exponentials.

Dr0930_134 hydrolyzes R_P-VR *p*-NP with a 6.5×10^3 fold preference over S_P-VR *p*-NP. The values of k_{cat}/K_M (1) for the fast phase (R_P) are in good agreement with values determined by steady-state enzyme kinetics.

Racemic GD *p*-NP (OP 4) contains four diastereomers. In the enzymatic time courses for wild-type Dr0930 and Dr0930_134, only one or three phases, respectively, could be clearly distinguished from one another (data not shown). The conformational assignment was performed as described earlier. For wild-type Dr0930, the only phase amounted to 50% of the signal amplitude observed upon chemical hydrolysis, corresponding to the degradation of the two R_P enantiomers. For Dr0930_134 one fast phase (50% amplitude, fit by single exponential fit) and a significantly slower phase (double exponential curve shape) were obtained. The fast phase corresponds primarily to the degradation of the two R_P enantiomers, while the S_P enantiomers only began to degrade in the second phase. The S_PS_C or S_PR_C stereoisomer cannot be assigned by comparative analysis.

The values of k_{cat}/K_M (1) and (2) determined from the fit of the exponential phases for the hydrolysis of the racemic compounds are reported in Table 28.

Table 28: Summary of k_{cat}/K_M ($M^{-1}s^{-1}$) parameters deduced from the analysis of individual phases (1-3) observed upon the hydrolysis of racemic substrates by wild-type Dr0930 and Dr0930_134.

		wild-type Co/Co-Dr0930	Co/Co-Dr0930_134
1: VX *p*-NP	k_{cat}/K_M (1) [$M^{-1}s^{-1}$]	1.9×10^3	$1.1 \pm 0.1 \times 10^6$
	k_{cat}/K_M (2) [$M^{-1}s^{-1}$]	1.0×10^0	$1.3 \pm 0.4 \times 10^3$
2: GB *p*-NP	k_{cat}/K_M (1) [$M^{-1}s^{-1}$]	5.6×10^1	$9.6 \pm 0.3 \times 10^5$
	k_{cat}/K_M (2) [$M^{-1}s^{-1}$]	3.0×10^{-1}	$6.3 \pm 0.7 \times 10^1$
3: VR *p*-NP	k_{cat}/K_M (1) [$M^{-1}s^{-1}$]	3.0×10^1	$1.1 \pm 0.1 \times 10^6$
	k_{cat}/K_M (2) [$M^{-1}s^{-1}$]	2.0×10^0	$1.7 \pm 0.1 \times 10^2$
4: GD *p*-NP	k_{cat}/K_M (1) [$M^{-1}s^{-1}$]	6.2×10^0	$1.3 \pm 0.1 \times 10^4$
	k_{cat}/K_M (2) [$M^{-1}s^{-1}$]		$2.5 \pm 0.5 \times 10^0$
	k_{cat}/K_M (3) [$M^{-1}s^{-1}$]		$3.4 \pm 0.8 \times 10^{-1}$
5: GF *p*-NP	k_{cat}/K_M (1) [$M^{-1}s^{-1}$]	7.1×10^0	$8 \pm 1 \times 10^4$
	k_{cat}/K_M (2) [$M^{-1}s^{-1}$]	2.0×10^{-1}	$1.7 \pm 0.3 \times 10^1$

The reactions were performed in 50 mM CHES, pH 9.0, 100 µM $CoCl_2$ and variable concentration of OPs. For OP compounds 4 and 5 the reaction assay was supplemented with 12% MeOH. The reaction was monitored at 400 nm ($\varepsilon_{400} = 1.7 \times 10^4\ M^{-1}cm^{-1}$) and 30 °C. Wild-type Dr0930 and Dr0930_134 were diluted in 20 mM HEPES pH 7.5, 100 µM $CoCl_2$, and 1 mg/ml BSA, 20 mM HEPES pH 7.5, 100 µM $CoCl_2$, respectively. BSA has no influence on activity (data not shown). Values for Dr0930_134 were determined in triplicates; the standard deviations are given.
The enantiomeric preference was assigned by addition of wild-type PTE and variants when the hydrolysis profile had reached approximately an end point at half amplitude. The enantiomeric preference for both wild-type Dr0930 and Dr0930_134 is $R_P > S_P$ for OPs 1-3 and OP 5. The enantiomeric preference for OP 4 is $R_PR_C + R_PS_C > S_PR_C$ or S_PS_C. For wild-type Dr0930 only one phase of 50% amplitude was determined. Addition of PTE-G60A and PTE-H254G+H257W+L303T

confirmed that the phase corresponds to the hydrolysis of R_PR_C + R_PS_C. For Dr0930_134 one fast phase of 50% amplitude was determined corresponding to the hydrolysis of R_PR_C + R_PS_C. The second phase was fit by double exponential fit yielding two rate constants corresponding to rates for S_PR_C and S_PS_C. However, the rate constant cannot be assigned to either S_PR_C or S_PS_C.
The values of k_{cat}/K_M (1) for the fast phase are in good agreement with values determined by steady-state enzyme kinetics (see Table 6 and Table 25). For comparative analysis, the values determined by steady-state enzyme kinetics need to be multiplied by a factor of two as the effective substrate concentration is half, as only the hydrolysis of the R_P isomer is followed under steady-state enzyme conditions.

The enantiomeric preference of wild-type Dr0930 and Dr0930_134 is for the less toxic R_P isomers of OPs 1-5 (OP 4: R_PR_C + R_PS_C > S_PR_C or S_PS_C). The ratios of k_{cat}/K_M (R_P) / k_{cat}/K_M (S_P) are summarized in Table 29.

Table 29: Ratios of k_{cat}/K_M (R_P) / k_{cat}/K_M (S_P) for the hydrolysis of chiral OPs 1-5 by wild-type Dr0930 and Dr0930_134.

	R_P/S_P for **1**	R_P/S_P for **2**	R_P/S_P for **3**	R_P/S_P for **4**[a]	R_P/S_P for **5**
wild-type Dr0930	1.9×10^3:1	1.9×10^2:1	1.5×10^1:1	n.d.	3.6×10^1:1
Dr0930_134	8.5×10^2:1	1.5×10^4:1	6.5×10^3:1	5.2×10^3:1	4.7×10^3:1

n.d.: not determined. [a]: R_P:S_P for OP 4 is equal to k_{cat}/K_M (1) / k_{cat}/K_M (2), presumably (R_PR_C + R_PS_C) / S_PR_C or S_PS_C.

The k_{cat}/K_M (R_P) / k_{cat}/K_M (S_P) ratios for wild-type Dr0930 and Dr0930_134 are illustrated comparatively in Figure 55.

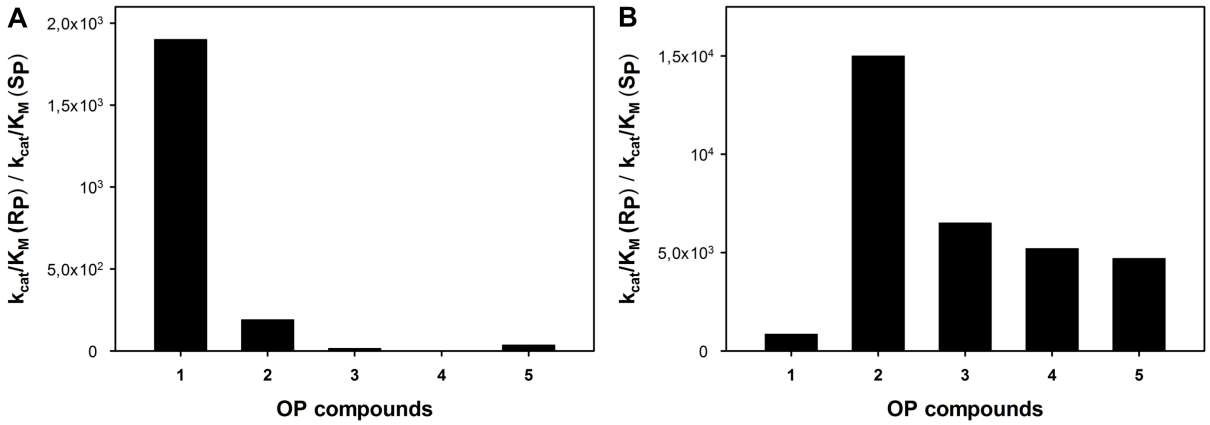

Figure 55: Ratios of k_{cat}/K_M (R_P) / k_{cat}/K_M (S_P) for the hydrolysis of chiral OPs 1-5 by wild-type Dr0930 (A) and Dr0930_134 (B).

Wild-type Dr0930 and Dr0930_134 both exhibit a stereopreference for the less toxic R_P-OPs 1-5. The sterepreference for wild-type Dr0930 is only pronounced for VX *p*-NP (OP 1) and GB *p*-NP (OP 2), the two methylphosphonate compounds with small substituents at the P-center. Dr0930_134 hydrolyzes R_P-OPs with up to

1.5×10^4-fold preference over S_P-OPs, with the highest discrimination being observed for GB *p*-NP (OP 2). Compared to wild-type Dr0930 the stereopreference of Dr0930_134 for VX *p*-NP (OP 1) is slightly diminished. The stereopreference of Dr0930_134 for the OPs 2-5 is significantly enhanced, resulting in a shift in enantiomeric preference between wild-type Dr0930 and Dr0930_134 as high as 4.3×10^2-fold for VR *p*-NP (OP 3). Altogether, the results demonstrate that the enhanced OPH activity of Dr0930_134 is associated with an enhancement in its inherent stereoselectivity for OPs 2-5.

The stereopreference of PTE is also for R_P. However, its stereopreference is less pronounced and increasing with the size of the substituent on the P-center (k_{cat}/K_M (R_P) / k_{cat}/K_M (S_P) for GF *p*-acetylphenyl is 7.6×10^2:1). Both, Dr0930 and PTE exhibit high stereopreference for R_P, indicating that the relative orientation of the OP substrates in the substrate binding pockets of PTE and Dr0930 are identical (see also Figure 63).

4.4.4 Structural analysis of engineered Dr0930 variants

4.4.4.1 Crystallization and X-ray structure determination of evolved Dr0930 variants

To elucidate the structural basis of the enhanced OPH activity of the evolved Dr0930 variants, we attempted to co-crystallize the three best Dr0930 variants, Dr0930_81, Dr0930_106 and Dr0930_134, with substrate analogues (DIMP, DE4MBP) and product analogues (DEP, CAC) of PTE. The structures of the inhibitors used are shown in Figure 56. By analogy to crystallization experiments with PTE, the ligands were assumed not to be very potent inhibitors; consequently, high amounts of compound were added to the crystal set-ups. The amounts used were identical or higher to conditions used to obtain complexed PTE structures (Benning *et al.*, 2000; Vanhooke *et al.*, 1996; Kim *et al.*, 2008). However, the concentration of substrate analogues added was limited by the solubility of the compounds, particularly for DE4MP.

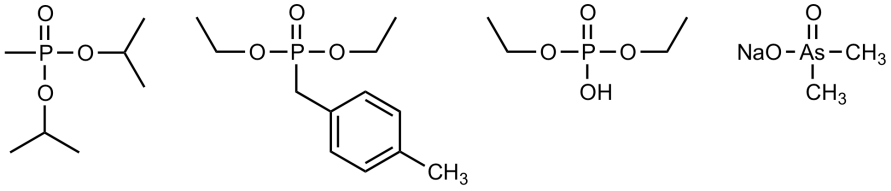

Figure 56: Structures of substrate analogues (DIMP, DE4MBP) and product analogues (DEP, CAC) used for co-crystallization.
DIMP: diisopropyl methylphosphonate. DE4MBP: diethyl 4-methylbenzylphosphonate. DEP: diethylphosphate. CAC: sodium cacodylate.
The ligands were assumed not to be very potent inhibitors and hence added in high concentrations. For co-crystallization set-ups the following amounts were used: 3% (v/v) DIMP, 1% (v/v) DE4MBP (limited solubility), 100 mM DEP, 100 mM CAC. DMSO and MeOH were added to increase the limited solubility of the substrate analogues, particularly for DE4MBP. For soaking studies, preformed crystals were soaked in reservoir solution supplemented with higher concentrations of ligand.
DIMP is a competitive inhibitor for GB *p*-NP (OP 2). Initial velocity of GB *p*-NP hydrolysis ([S]=$K_M^{GB\ p\text{-}NP}$=0.19mM) recorded in presence of various concentrations of DIMP yielded a competitive inhibition constant, K_i, for Dr0930_136 of 9.5 mM (see 7.6 for details).

Initially commercially available crystallization kits (see 3.6.1 for details) were used to screen for suitable crystallization conditions, as published crystallization conditions for wild-type Dr0930 and Dr0930 variants (Xiang *et al.*, 2009; Hawwa *et al.*, 2009b) gave no hits. Attempts to obtain complexed Dr0930 structures by co-crystallization or soaking of ligands into preformed crystals were performed. Streak- and macro-seeding experiments with product analogues gave no suitable crystals. Promising crystallization conditions obtained were manually refined in a grid screen, modifying precipitant concentration, additives, pH and protein concentration.

Efforts to obtain crystals for Dr0930_81, Dr0930_106, and Dr0930_134 were successful. The crystallization conditions are summarized in Table 30.

Table 30: Crystallization conditions for Dr0930 variants.

Dr0930 variant	crystallization conditons
Dr0930_81	10% (w/v) PEG-8000, 0.1 M imidazole pH 8.0, 0.2 M $Ca(OAc)_2$, 3% (v/v) DIMP; 14% ethylene glycol
Dr0930_106	0.01 M $NiCl_2$, 0.1 M Tris pH 8.5, 8% PEG MME 2000, 3% (v/v) DIMP, 3% (v/v) MeOH; 25% ethylene glycol
Dr0930_134	0.1 M MES pH 6.5, 1.3 M $MgSO_4$, 1% (v/v) DE4MBP; 25% ethylene glycol

The crystals were obtained by sitting- (Dr0930_81) and hanging-drop vapor (Dr0930_106, Dr0930_134) diffusion methods. For some crystal set-ups, MeOH and DMSO were added to the protein ligand mix in order to increase the solubility of DIMP and DE4MBP compounds. Dr0930_81: Dr0930-Y28L+D71N+E101G+E179D+V235L+L270M. Dr0930_106: Dr0930-Y28L+D71N+Y97F+E101G+E179D+V235L+L270M. Dr0930_134: Dr0930-Y28L+D71N+Y97F+E101G+E179D+V235L+P274L.

The crystals were flash-frozen in reservoir solution supplemented with ethylene glycol as a cryo-protectant (see Figure 57).

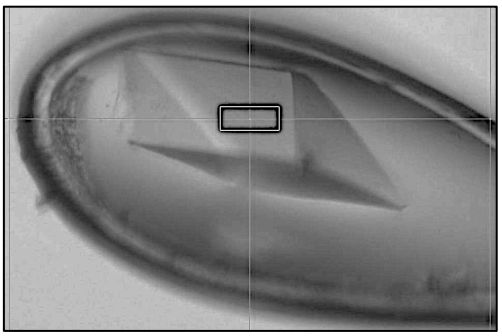

Figure 57: Crystal of a Dr0930 variant frozen in ethylene glycol.
Ethylen glycol was used as a cryo-protectant. In ethylene glycol frozen crystals showed no ice on the crystals and no ice rings in the diffraction pattern.

The diffraction data was collected at the Stanford Synchrotron Radiation Lightsource (SSRL BL7-1, Stanford, USA; Dr0930_81) and the Swiss Light source (SLS PXII, Villigen, Switzerland; Dr0930_106 and Dr0930_134). Data processing and structure determination was performed as described in 3.6.3 together with Nicholas Fox (group of Prof. Dr. David Barondeau, Texas A&M University, College Station, USA) or by Dr. Chitra Rajendran (group of Prof. Dr. Christine Ziegler, University of Regensburg).

The data sets had a resolution of 1.78-2.05 Å, and cell dimensions were as follows: a = 62 Å, b = 62 Å, c = 204 Å, $\alpha = \beta = 90°$, $\gamma = 120°$. The primitive trigonal space group was $P3_121$. The crystals contained one molecule in the asymmetric unit yielding a V_M of approximately 3.24 A^3/Da. Final R_{cryst} and R_{free} values for all structures were below 23.5% and 26.1%, respectively. The data collection and refinement statistics are summarized in Table 31.

Table 31: Data collection and refinement statistics for Dr0930_81, Dr0930_106 and Dr0930_134.

	Dr0930_81	**Dr0930_106**	**Dr0930_134**
	native, pH 8.0	native, pH 8.5	native, pH 6.5
Data collection			
beamline	SSRL BL 7-1	SLS PXII	SLS PXII
wavelength (Å)	0.9794	1.0	1.0
space group	P 31 21	P 31 21	P 31 21
unit cell dimensions	a=61.655Å	a=61.78Å	a=61.853Å
	b=61.655Å	b=61.78Å	b=61.853Å
	c=203.670Å	c=203.71Å	c=204.786Å
	α=β=90°, γ=120°	α=β=90°, γ=120°	α=β=90°, γ=120°
resolution range (Å)	50.0-2.05 (2.09-2.05)	47.37-1.79 (1.88-1.79)	47.46-1.78 (1.88-1.78)
no. of observed reflections	540199	233864	231779
no. of unique reflections	29424	43548	44209
redundancy	18.4 (19.1)	5.4 (5.2)	5.3
mosaicity	0.351	0.249	0.110
I (%)	100 (100)	99.1 (97.7)	99.44
I/σI	36.5 (7.8)	13.60	9.83
R_{merge} (%)[†]	-	0.050 (0.492)	0.075 (0.505)
R_{sym} (%)	13.7 (55.8)	-	-
Refinement			
residues in molecule	T2-G323	T2-G323	T2-G323
R_{cryst} (%)[‡]	23.5	21.9	20.13
R_{free} (%)[‡]	26.1	25.05	22.61
no. of protein non-hydrogen atoms		2702	2592
no. of water molecules	209	273	173
average B factor (Å^2)	18.9	38	46.7
rmsd bond length (Å)	0.012	0.012	0.015
rmsd angles (deg)	1.60	1.337	1.477
Ramachandran plot (%)			
favored regions	92.5	97.20	98.12
allowed regions	7.5	2.18	1.88
disallowed regions	0.00	0.62	0.00

rmsd: root mean square deviation.
Values in parenthesis indicate statistics for the highest resolution shell.
[†]$R_{merge} = \sum\sum_j |I_j (hkl) - \langle I (hkl)\rangle| / \sum\sum_j |\langle I (hkl)\rangle|$, where Ij is the intensity measurement for reflection j and $\langle I\rangle$ is the mean intensity over j reflections.
[‡]R_{cryst} or $R_{free} = \sum ||F_o (hkl)| - |F_c (hkl)|| / \sum |F_o (hkl)|$, where F_o and F_c are the observed and calculated structure factors, respectively. 5% of the reflections were excluded from the refinement and used to calculate R_{free}.
*In the structure of Dr0930_106 an additional density distant from the active site was identified that could not be assigned. The additional density had no influence on crystal packing or dimerization.

4.4.4.2 Analysis of beneficial mutations in engineered variants

Structural analysis showed that the 6-7 mutations located in the βα-loops 1-3, 5, 7 and 8 of Dr0930_81, Dr0930_106, and Dr0930_134 did not lead to a change of the overall backbone conformation (average backbone r.m.s.d = 0.43 Å) compared to wild-type Dr0930 (PDB IDs: 3FDK and 2ZC1). A structural superposition of the wild-type Dr0930 and Dr0930_134 backbones is shown in Figure 58A.

The two cobalt-binding sites and the metal-coordinating residues (bridging carboxylated lysine; α-metal coordinating: His21, His23, Asp264, His176, β-metal coordinating: His176, His204) were retained in the designed proteins and maintained their wild-type conformation. A density was observed that indicated the bridging hydroxide. The side chain of the active site residue Arg228, potentially involved in proton shuttling, was found to be flexible and adopts an alternate conformation relative to wild-type Dr0930 (see Figure 58B).

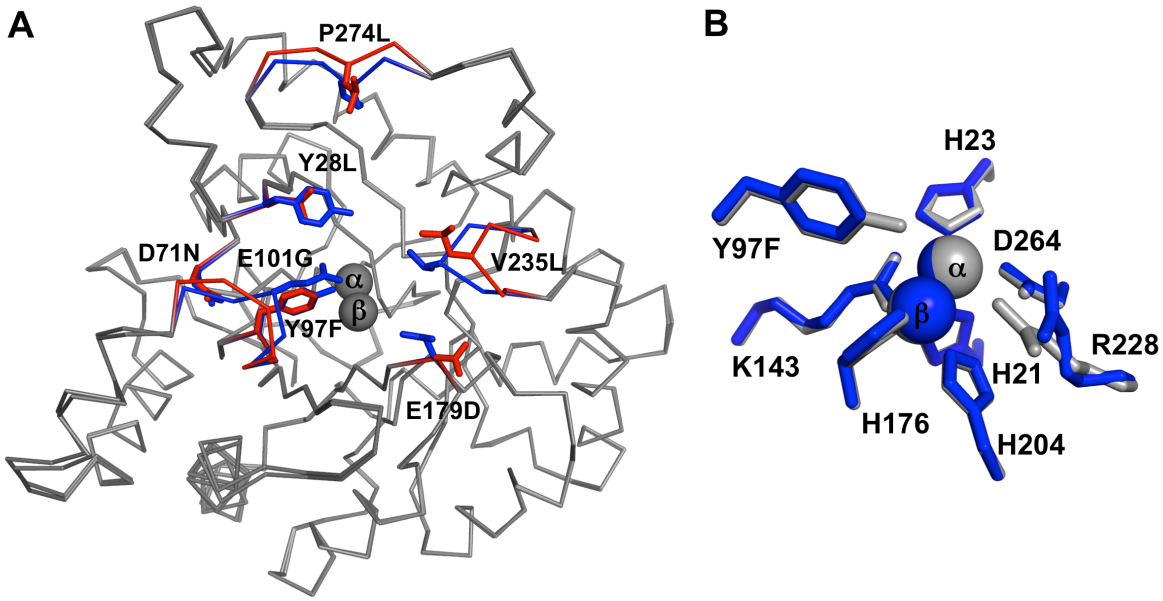

Figure 58: Structural superpositions of the engineered Dr0930_134 variant and wild-type Dr0930 (PDB ID 3FDK).
A: Overal structural superposition of Dr0930_134 and wild-type Dr0930. The ribbon backbones of Dr0930_134 and wild-type Dr0930 (both depicted in grey) superimpose with an r.m.s.d deviation of only 0.43 Å. The 7 mutations are indicated (blue sticks: wild-type Dr0930 residues; red sticks: Dr0930_134 residues). The largest backbone differences are observed in βα-loops 3 (comprises the mutations Y97F and E101G) and 8 (comprises the mutation P274L). Some variation can also be seen in βα-loop 7 (comprises the mutation V235L).
B: Active site superposition of wild-type Dr0930 (depicted in grey) and Dr0930_134 (depicted in blue). The metal coordinating His and Asp residues maintain their wild-type conformation. The active site residue R228 adopts an alternate conformation. The Y97F mutation does not alter the side chain conformation.

Except for residues W269 (βα-loop 8) and M234 (βα-loop 7), all invariable residues in the substrate binding pocket of Dr0930, align well with the residues in the wild-type enzyme (data not shown).

The structural changes around the mutated positions are illustrated in Figure 59.

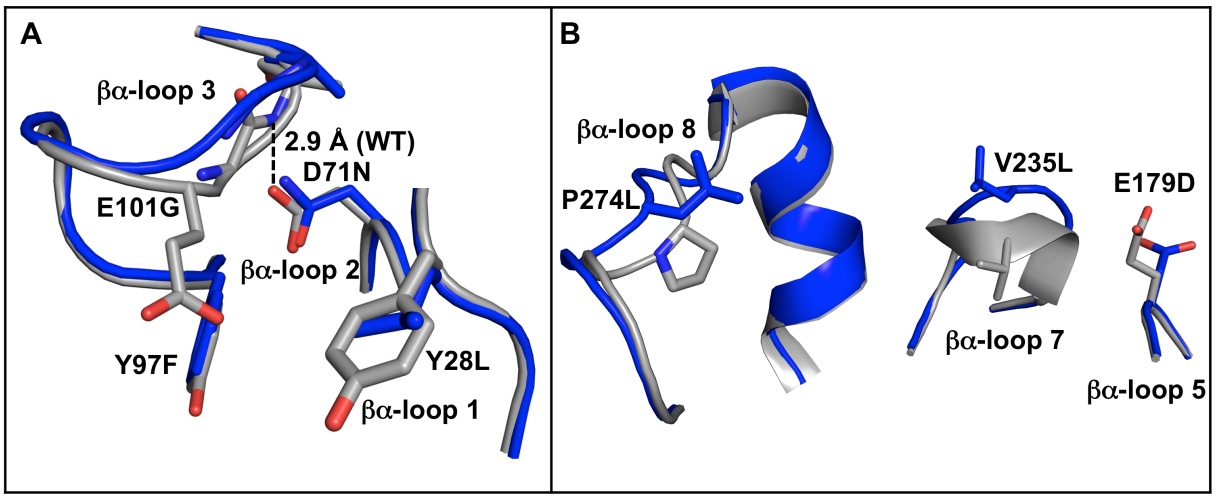

Figure 59: Structural superpositions of Dr0930_134 and wild-type Dr0930.
Wild-type Dr0930 (PDB ID 3FDK) and Dr0930_134 are depicted in grey and blue, respectively.
A: Excerpts of structural superpositions of βα-loops 1, 2 and 3. The βα-loop 3, comprising the mutations Y97F and E101G, is shifted by 3 Å at positions A99-A103, due to the elimination of a hydrogen bond between D71 and the backbone nitrogen of A103 (dashed line). The loop has a high *B*-factor, suggesting that it may be flexible. The mutations Y28L in βα-loop 1 and Y97F and E101G in βα-loop 3, caused an enlargement of the substrate binding pocket.
B: Excerpts of structural superpositions of βα-loops 5, 7 and 8 of wild-type Dr0930 and Dr0930_134. The βα-loop 7, harboring the V235L mutation, is flexible. D179 (βα-loop 5) adopts an alternate conformation. The βα-loop 8, harboring the mutation P274L, is shifted by 1.7 Å.

The βα-loop 1 comprises the mutation Y28L; by introducing a smaller, hydrophobic amino acid the size of the active site is increased, providing more space for the accommodation of the OP substrates. The βα-loop 3, composed of residues F96-E117, is more flexible in the engineered variants and was displaced by approximately 3 Å at positions A99-A103, due to the elimination of a hydrogen bond between the side chain of D71 (βα-loop 2) and the backbone nitrogen of A103. The E101G mutation enlarges the OP substrate binding pocket. The side chain of F97, present in Dr0930_106 and Dr0930_134, overall resembles the Y97 side chain in the wild-type enzyme (Figure 59A).

The D179 amino acid in βα-loop 5 is found in alternate conformations within the engineered variants. In Dr0930_134 the residue D179 forms no hydrogen bond to the neighboring R148 in βα-loop 4 (not shown), probably resulting in more flexibility. The

βα-loop 7 is composed of residues R228-T239. This loop is flexible but in a similar conformation as in the wild-type structure (PDB ID 2ZC1), hence providing no obvious explanation for the considerable increase in activity caused by the V235L mutation. The mutation L270M (βα-loop 8), present in Dr0930_81 and Dr0930_106, is found in a location remote from the active site (data not shown). It has not been demonstrated that this distant mutation has a beneficial effect by itself. The P274L mutation, present only in Dr0930_134, causes a shift of the backbone by 1.7 Å (Figure 59B).

The X-ray structures of the engineered variants helped to explain the partial trade-off between the native lactonase and the engineered OPH activities. Elimination of a crucial electrostatic interaction by the Y97F mutation and an enlargement of the active site lead to less effective binding and positioning of the lactone substate relative to the catalytic machinery; at the same time the latter only then allowed for improved binding of OPs.

4.4.5 Ligand docking studies with engineered Dr0930 variants

Attempts to obtain complexed structures of engineered Dr0930 variants by co-crystallization with substrate and product analogues or soaking of preformed crystals failed. Therefore, we docked the substrate EPXN into the active site of Dr0930_134 to assess its configurational and spatial orientation.

Docking of ligands into the active site of wild-type PTE and Dr0930_134 was performed by Christoph Malisi (group of Dr. Birte Höcker, MPI Tübingen) using the RosettaLigand program (Davis & Baker, 2009). RosettaLigand docking and the analysis of docking results were performed as described in 3.7. The RosettaLigand program allows for ligand and receptor backbone flexibility and has been used previously for several successful computational designs and ligand docking experiments, including the docking of OPs and lactones (Khare *et al.*, 2012; Ben-David *et al.*, 2012).

4.4.5.1 Retroperspective ligand docking

To test the validity of the docking models, the output of the RosettaLigand docking was evaluated using the DIMP-complexed crystal structure of wild-type PTE (PDB ID 1EZ2) from which the inhibitor was removed. DIMP (Figure 56) and EPXN

(OP 7; Figure 22) were docked into the active site of PTE, and the 10 top-scoring ligand poses each were analyzed. The poses obtained for the docked DIMP are essentially identical to the one obtained by X-ray crystallography. For the best two scoring poses, DIMP is positioned within 0.5-0.8 Å r.m.s.d., when compared to the DIMP pose in the crystal structure (Figure 60A). Furthermore, docking of EPXN into the active site of PTE yielded essentially identical binding modes. The phosphoryl oxygen of the DIMP ligand is coordinated by the β-metal, and the substituents at the P-center fit the assigned substrate binding pockets: the O-ethyl substituents fit the small and large subsites, and the *p*-NP ring fits the leaving group subsite in PTE (Figure 60B). The best two poses for DIMP and EPXN, superimposed with the native DIMP pose, are shown in the insets. Although, RosettaLigand allows for backbone flexibility, the side chains in the substrate binding pocket experienced neglectable conformational changes.

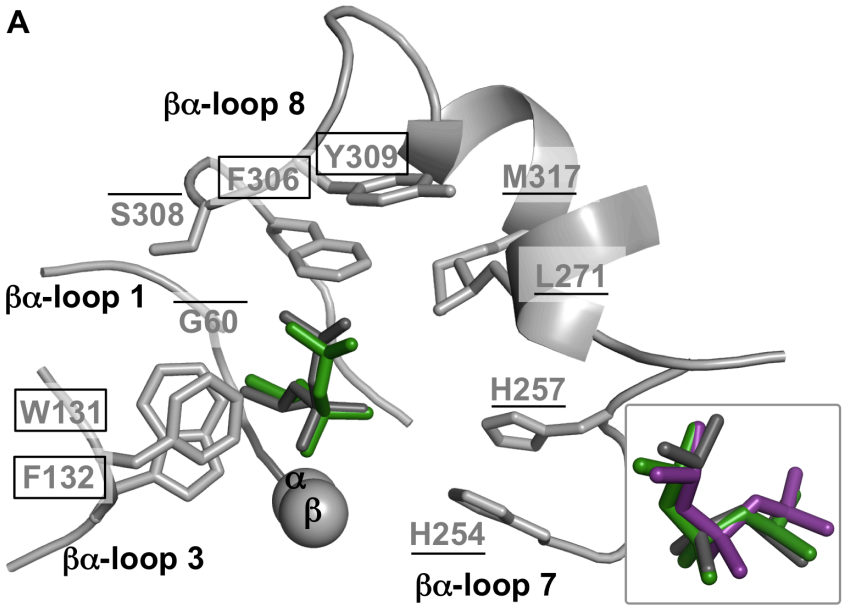

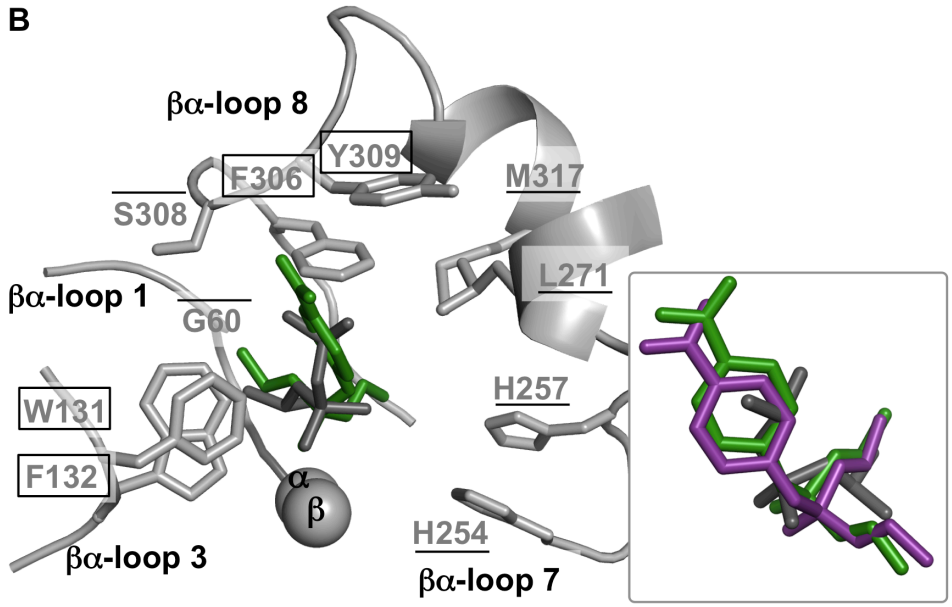

Figure 60: Docking poses of DIMP (A) and EPXN (B) in the crystal structure of wild-type PTE, obtained using the RosettaLigand program.
PTE (PDB ID 1EZ2) and the co-crystallized DIMP ligand are depicted in grey and dark grey, respectively. The docking poses are depicted in green and purple.
A: Active site and substrate binding pocket of PTE. One top-scoring docking pose of DIMP is superimposed with the native DIMP pose observed in the crystal structure. The two best docking poses of DIMP, superimposed with the native DIMP ligand, are shown in the inset in a different view. The docked DIMP ligands superimpose with an r.m.s.d of 0.5-0.8 Å with the native DIMP pose.
B: Active site and substrate binding pocket of PTE. One top-scoring docking pose of EPXN is superimposed with the native DIMP pose observed in the crystal structure. The phosphoryl oxygen of EPXN is coordinated by the β-metal. The O-ethyl substituents at the phosphorous center of EPXN fit the small (G60, S308, I106 and L303; I106 and L303 are not shown; overlined) and large (H254, H257, L271, M317; underlined) substrate binding pockets. The *p*-NP moiety occupies the leaving group pocket (W131, F132, F306, Y309; boxed) of PTE. The residues of the small, large and leaving group subsite are marked the same as in Figure 19B. The two best docking poses of EPXN, superimposed with the native DIMP ligand, are shown in the inset in a different view.

4.4.5.2 Docking of EPXN in the active site of Dr0930_134

Subsequently, EPXN was docked into the active site of Dr0930_134. In all poses obtained the phosphoryl oxygen of EPXN is hydrogen bonded to the R228 side chain (see Figure 61).

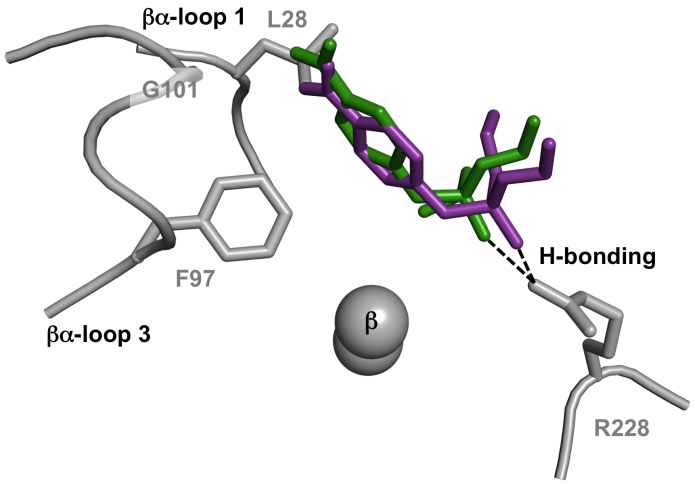

Figure 61: Docking poses of EPXN in the crystal structure of Dr0930_134, obtained by docking using the RosettaLigand program.
The EPXN docking poses are depicted in green and purple. The phosphoryl oxygen of EPXN is hydrogen bonded to the R228 side chain (dashed lines) instead of coordinating the β-metal as observed in the modelled PTE-EPXN complex (Figure 60B). The *p*-NP ring in the EPXN docking poses is orientated towards βα-loops 1 and 3. The residue R228 in the docked structure is shifted compared to the conformation obtained by crystallization.

The results indicate that R228 might be important for electrostatic coordination or activation of the substrate and/or stabilization of the intermediate (see also 4.3.3). However, as the RosettaLigand docking program allows only for small backbone flexibility, the electrostatic interaction between R228 and the phosphoryl oxygen of the EPXN ligand might be overestimated in the docking (personal communication C. Malisi).

Therefore, in an additional series of docking studies, the complexation of EPXN by the β-metal was enforced by introducing geometric constraints. The phosphoryl oxygen of the ligand was restricted to stay within 2.5 ± 0.4 Å to the β-metal. Moreover, the β-metal - O=P angle was set to 140° ± 30°. The docking poses obtained using these constraints were reasonable. The 20 top-scoring docking poses were analyzed and yielded essentially two clusters of poses. In the highest scoring and most frequently occupied poses the *p*-NP ring is oriented towards the βα-loop 3 (equivalent to leaving group subsite in PTE), the O-ethyl substituents both fit the large pocket generated by βα-loop 7 and 8 in Dr0930_134. In the second pose obtained, the *p*-NP moiety and one O-ethyl substituent fit the large pocket; the second O-ethyl substituent is oriented towards the βα-loop 3. The orientation of the EPXN docking poses in the substrate binding pocket of Dr0930_134 in cartoon and stick representation is shown in Figure 62A, the surface representation is shown in

Figure 62B. For each of the two clusters one representative docking pose is shown in green and purple, respectively. The insets illustrate the variation within the two clusters of docking poses.

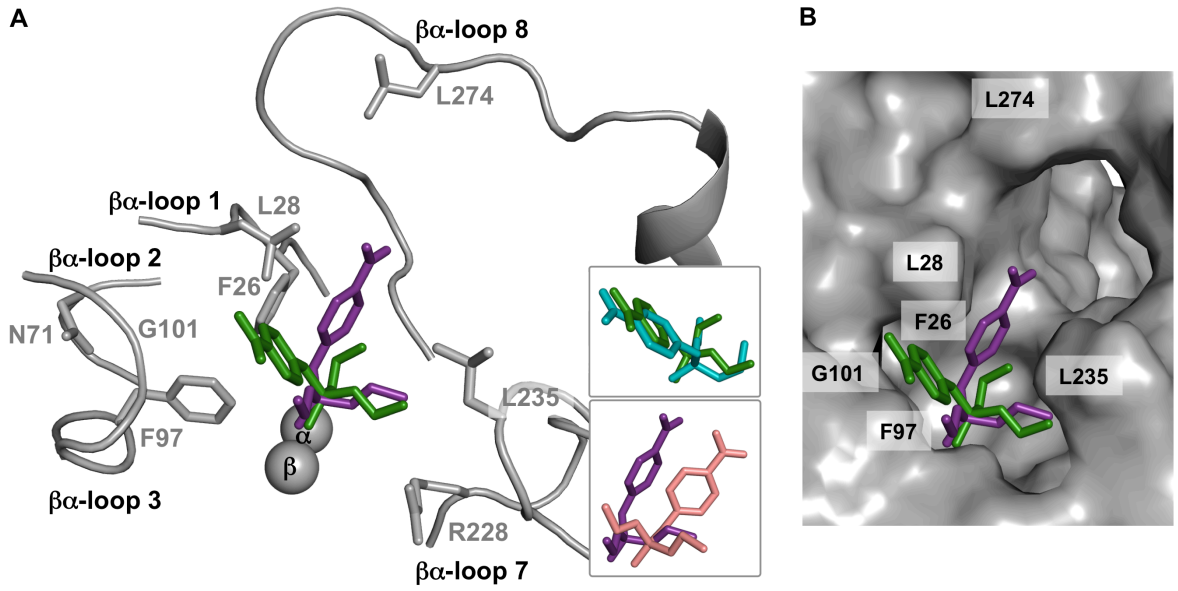

Figure 62: Docking poses of EPXN in the crystal structure of Dr0930_134, obtained by docking using the RosettaLigand program applying distance and angle constraints.
A: Active site and substrate binding pocket of Dr0930_134 in cartoon and stick representation. One representative of each cluster of docking poses of EPXN is shown in green and purple. The docking pose depicted in green belongs to the group of highest scoring and most frequently occupied cluster of docking poses, the docking pose in purple belongs to the second cluster of docking poses obtained. The variation within each cluster of docking poses is indicated in the insets. Docking poses for the first cluster are illustrated in green and cyan; the second cluster of docking poses is depicted in purple and light pink. Residue R228 is shifted compared to the conformation obtained by crystallization in order to accommodate the ligand (only one R228 side chain conformation is shown).
B: Active site and substrate binding pocket of Dr0930_134 in surface representation. Important active site residues are labeled.

In order to compare the configurational and spatial orientation of EPXN in Dr0930_134 and PTE, and in order to identify residues involved in substrate positioning for Dr0930_134, one top scoring EPXN-docking pose for Dr0930_134 was superimposed with the EPXN-docking pose obtained for PTE (Figure 63).

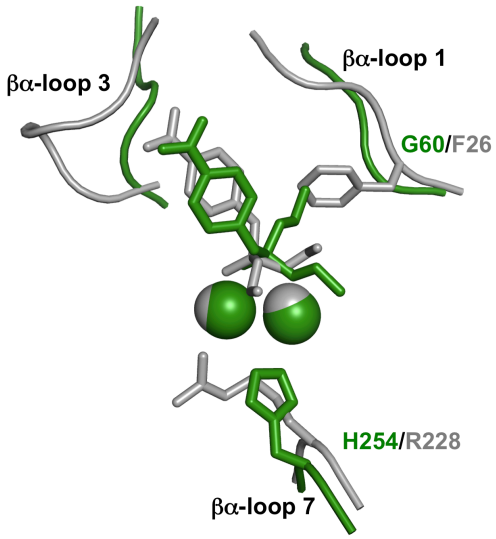

Figure 63: Structural superposition of the active sites of Dr0930_134 and PTE with the top scoring docking poses for EPXN each.
Dr0930_134 and wild-type PTE are depicted in grey and green, respectively. One top scoring EPXN docking pose is shown each. The docking poses for EPXN are identical with respect to the *p*-NP moiety, but differ in orientation of O-ethyl substituents. The O-ethyl substituents of the docked EPXN in Dr0930_134 are shifted to avoid a steric clash with the F26 side chain. The residue R228 in the docked structure of Dr0930_134 is shifted relative to the conformation obtained by crystallization (not shown).

Docking of EPXN yields similar binding modes in Dr0930_134 and PTE with respect to the orientation of the *p*-NP ring. The results of the stereopreference studies also indicated that the relative orientation of the substrates in Dr0930 and PTE are identical (4.4.3). However, the orientation of the O-ethyl substituents differs. The O-ethyl substituents cannot accommodate the same orientation as in PTE due to a steric clash of one O-ethyl substituent with F26 (βα-loop1). Hence, F26 seems to be important for substrate positioning (Figure 63). Site-saturation mutagenesis studies (see 4.3.4.4.1) also confirmed that this residue is important for the activity. The equivalent residue in PTE (G60) is also a crucial residue for the OPH activity (Chen-Goodspeed *et al.*, 2001a/b).

In all docked structures R228 is shifted compared to the conformation obtained by crystallization in order to accommodate the ligand. R228 is an essential residue for the OPH activity (see also 4.3.3), potentially being part of proton shuttling and coordination or activation of the substrate and/or stabilization of the intermediate. In order to entirely characterize the amino acid R228, the position might be analyzed by site-saturation mutagenesis.

5 FINAL DISCUSSION

5.1 Divergent and convergent evolution of enzymes

Enzymes are characterized by a remarkable adaptability and evolvability (Khersonsky *et al.*, 2006). Prominent examples are atrazine chlorhydrolases (AtzA, AtzB, AtzC) and the OP hydrolases, which degrade man-made chemicals such as the xenobiotic organohalogen herbicide atrazine and organophosphate compounds. These enzymes are thought to have evolved rapidly as they provide a novel nitrogen and phosphate source for the affected organisms (Aharoni *et al.*, 2005a; Khersonsky *et al.*, 2006; Janssen *et al.*, 2005; Wackett, 2004; de Souza *et al.*, 1998). In any case, the adaptility and evolvability depends on two criteria: (i) a high tolerance against destabilizing mutations (robustness) and (ii) the introduction of new phenotypic traits by a relatively low number of mutations (plasticity) (Glansdorff *et al.*, 2008; Kirschner & Gerhart, 1998).

Two mechanisms for the generation of diversity of protein folds and functions can be distinguished: convergent and divergent evolution. Enzymes that share the same function and have similar active sites but differ in overall structure and exhibit unrelated sequences have emerged independently from different precursors by convergent evolution (Hegyi & Gerstein, 1999). Prominent examples for convergent evolution are the mammalian chymotrypsin and the bacterial subtilisin. These enzymes share no sequence or fold similarity but function as serine proteases and use the same active site triad for catalysis (Neurath, 1984). In divergent evolution, proteins have evolved from a common ancestor by gene duplication and diversification (Aharoni *et al.*, 2005a). Divergent evolution can be traced through sequence and fold similarity, and conserved motifs such as key active site residues. Noteworthy, sequence diverges far more rapidly than structure (Elias & Tawfik, 2012), which is clearly illustrated for example by chymotrypsin and trypsin, prominent examples for divergent evolution (Neurath, 1967). Most noteworty, promiscuous activities (weak secondary or side activities) often serve as evolutionary starting points for the divergence of new functions (Khersonsky *et al.*, 2006). This notion is important to understand the divergent evolution of enzyme superfamilies in which catalytic chemistry is conserved while substrate specificity varies (Gerlt & Raushel, 2003; O'Brien & Herschlag, 1999).

5.2 *D. radiodurans* Dr0930: a promiscuous OP hydrolyzing enzyme

The bacterial phosphotriesterase (PTE) from *P. diminuta* PTE is by far the most efficient and best characterized OP hydrolyzing enzyme. A close homologue of PTE is the phosphotriesterase-like-lactonase Dr0930 from *D. radiodurans*. Both enzymes share the same TIM-barrel fold, approximately 31% sequence identity, and key active site features (Xiang *et al.*, 2009). PTE is thought to have evolved rapidly from a PLL precursor by gene duplication and diversification (Raushel & Holden, 2000; Afriat *et al.*, 2006).

Dr0930 efficiently hydrolyzes γ- and δ-lactones, and promiscuous activity for the hydrolysis of the phosphotriesters methyl- and ethyl-paraoxon has been reported (Xiang *et al.*, 2009; Hawwa *et al.*, 2009b). The promiscuous OPH activity of Dr0930 is thought to be due to physical similarities between the intermediate for the native lactonase reaction and the ground/intermediate state for the promiscuous OPH reaction (Elias *et al.*, 2008; Ben-David *et al.*, 2012). As a C-O bond within lactones versus a P-O bond within organophosphates is cleaved and the reactions proceed via a tetrahedral versus a pentavalent oxyanionic intermediate (Figure 23), Dr0930 exhibits both catalytic and substrate promiscuity.

In the framework of this thesis, the cobalt-substituted wild-type Dr0930 was characterized for its promiscuous OPH activity using a broad spectrum of OPs that vary in the size of the substituent at the P-center. Mutually, wild-type PTE was assayed for its hydrolysis activity against δ-nonanoic lactone (Figure 22; 4.2.3). It was found, that wild-type Dr0930 exhibits overall low promiscuous activities for the hydrolysis of phosphotriesters and methylphosphonates, with best activities for methylphosphonates comprising small substituents at the P-center (VX *p*-NP and MPXN). The catalytic efficiency of wild-type Dr0930 is in the range of 2.1 $M^{-1}s^{-1}$ to 6.1×10^{2} $M^{-1}s^{-1}$ and hence four to seven orders of magnitude lower when compared to wild-type Co/Co-PTE. Wild-type PTE hydrolyzes – in addition to a broad range of OPs – δ-nonanoic lactone with a catalytic efficiency of 6.8×10^{1} $M^{-1}s^{-1}$, which is five orders of magnitude lower compared to the lactonase activity of wild-type Dr0930. In summary, the efficiencies of the promiscuous and native activities differ, for both Dr0930 and PTE, by several orders of magnitude (Table 5; Table 6). Moreover, both enzymes exhibit high K_M and low k_{cat} values for the promiscuous substrates. This may result from improper substrate binding interaction and positioning relative to the catalytic machinery (Khersonsky & Tawfik, 2010). However, the mutually identified

enzymatic activities in wild-type Dr0930 and wild-type PTE in concert with the observed similarities of their sequences, structures and active site features support a common evolutionary relationship and reinforce that PTE evolved from a PLL precursor by gene duplication and diversification.

5.3 Laboratory evolution of Dr0930 for OP hydrolysis

The molecular evolution of organophosphate hydrolysis by the bacterial PTE was reconstructed in the laboratory by engineering Dr0930 for enhanced OPH activity, thereby changing its substrate specificity. Dr0930 is an ideal target for laboratory evolution as it is a robust and thermostable $(\beta\alpha)_8$-barrel protein (Hawwa *et al.*, 2009b). High protein stability enables a large number of destabilizing mutations to be accommodated while protein fitness is retained (Tokuriki & Tawfik, 2009). Moreover, thermostable $(\beta\alpha)_8$-barrels have been used earlier for the design of the non-natural retro-aldol (indole-3-glycerol phosphate synthase scaffold) and Kemp-elimination reactions (phosphoribosyl anthranilate isomerase scaffold) (Jiang *et al.*, 2008; Röthlisberger *et al.*, 2008).

5.3.1 Design of an efficient and multi-functional OP hydrolyzing Dr0930 variant

Using random mutagenesis, site-directed and site-saturation mutagenesis in combination with *in vitro* activity screening of *E. coli* crude extracts, Dr0930 variants were identified showing significantly enhanced catalytic efficiencies for the hydrolysis of OPs. In each round of mutagenesis the most active variants were purified and characterized by steady-state kinetics using a broad-spectrum of racemic *p*-NP analogues of G- and V-type nerve agents (VX, GB, VR, GD, GF) and phosphotriesters (MPXN, EPXN). An overview of the experimental workflow is given in Figure 64.

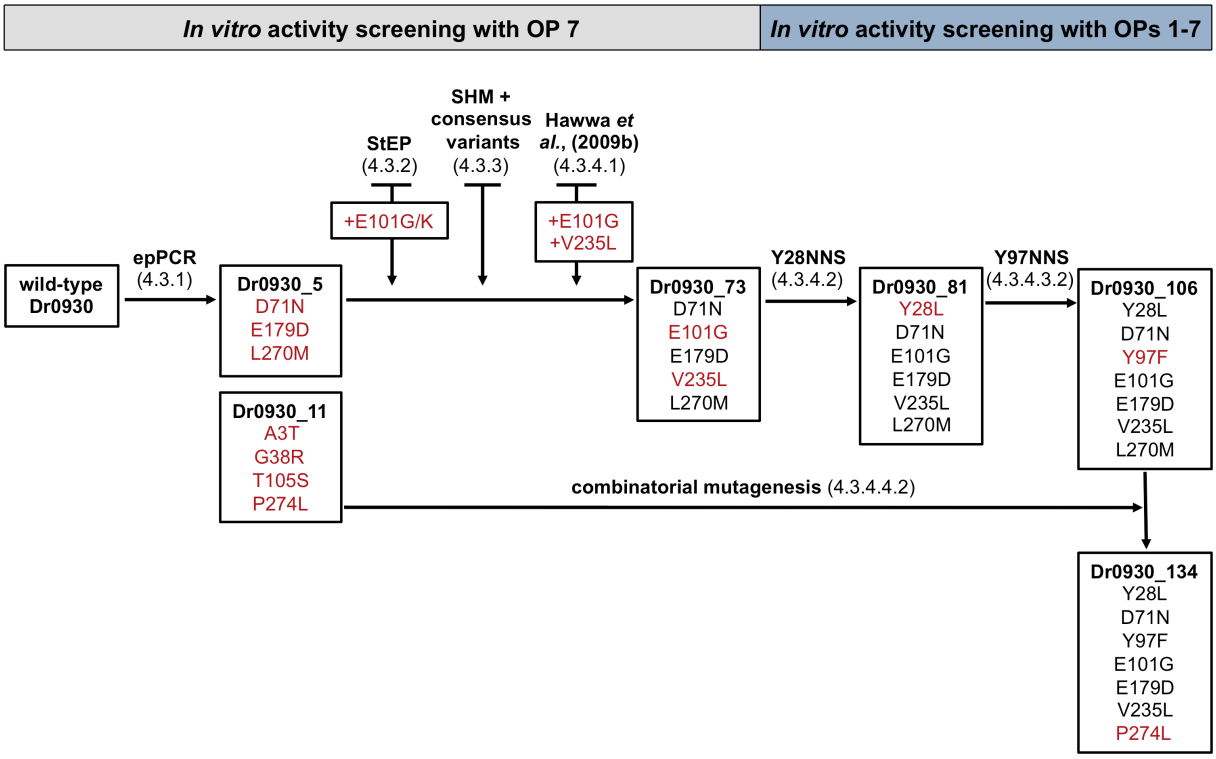

Figure 64: Overview of the experimental workflow.
The boxes illustrate the engineered Dr0930 variants. Amino acid exchanges in red are mutations that were newly identified in the individual steps. The applied mutagenesis technique is stated above the arrow; the corresponding chapters of this thesis are given in brackets. Three independent techniques are mentioned for the generation of the Dr0930_73 variant. The StEP technique identified the new mutations E101G/K. The SHM and consensus approach resulted in no variants that positively influenced the design. The mutations E101G and V235L identified by Hawwa *et al.*, (2009b) highlighted the importance of the previously identified E101G mutation in the StEP design and the V235M mutation identified by epPCR and screening. *Bona fide* beneficial exchanges were combined. The Dr0930_5 variant contains the additional mutation T2Q, which is thought to have no influence on the activity.

Initially, a random based error-prone PCR approach was performed on the starting template wild-type Dr0930 and screened for improved catalytic activity with EPXN (4.3.1). The best isolated Dr0930 variant, Co/Co-Dr0930_5 (D71N+E179D+L270M), exhibited a 25-fold increased catalytic efficiency of $7.2 \times 10^2\ M^{-1}s^{-1}$. Although the library was not screened for MPXN and the methylphosphonates VX *p*-NP, GB *p*-NP, VR *p*-NP, GD *p*-NP, and GD *p*-NP, the evolved variants also efficiently hydrolyzed these compounds. The highest catalytic efficiency of $1.4 \times 10^3\ M^{-1}s^{-1}$ observed for GB *p*-NP corresponds to a fold improvement of two orders of magnitude when compared to wild-type Dr0930. The best first generation variant not only showed the highest improvement in catalytic efficiency obtained in any single step of the total design, but – together with other variants isolated from the error-prone PCR library – also identified many positions (Y28, D71, E179, V235, L270, P274) essential for OPH activity (Table 7). This result

demonstrates the power of random mutagenesis although only a small fraction of the library was screened (7.4×10^{-3}%).

The four best isolated variants with elevated activity for the target substrate EPXN were recombined *in vitro* with wild-type Dr0930 and a previously designed variant (Dr0930-F26G+C72I; Xiang *et al.*, 2009) using the StEP protocol (4.3.2). The second-generation gene library was subsequently screened with EPXN and two new residues (G, K) were identified at position E101. However, no substantial increase in activity for EPXN was obtained for the variants isolated from the StEP approach. Steady-state enzyme kinetic characterization of purified variants that appeared to have higher activity in the crude extract screen were presumably isolated due to a higher expression level rather than improved enzymatic activity.

Subsequently, a SHM-library was generated by simultaneous targeted mutagenesis of ten defined residues, introducing a selected set of amino acids at each position (4.3.3). A newly developed DEAE filter paper screen enabled the pre-screen of 100,000 colonies. As the *in vitro* screen of the SHM library was only performed with the EPXN, the improvements were limited to increased hydrolytic activity for the phosphotriesters MPXN and EPXN (see Table 15) when compared to Dr0930_5. Moreover, all isolated variants contained the wild-type amino acid at position R228 (see Table 14), indicating that this residue is critical for the OPH activity. As the ten sites were mutagenized simultaneously, one single deleterious mutation leading to residues other than Arg at position 228, lead to a high number of inactive variants in the library. Moreover, variants contained mutations at position F26, while site-saturation mutagenesis confirmed that F26 residue is essential for activity (4.3.4.4.1). This disadvantage could not be compensated by increasing the screening throughput. Thus, also the consensus approach resulted in no variants that positively influenced the design (4.3.3.4).

The mutations E101G and V235L identified by Hawwa *et al.* (2009b) highlighted the importance of the previous identified E101G mutation in the StEP design (Table 11) and the V235M mutation identified in the epPCR (Table 7). The *bona fide* beneficial exchanges were combined on the Dr0930_5 template yielding Dr0930_73. The catalytic efficiencies for MPXN and EPXN improved by 4-5 fold, while the catalytic parameters for OPs 1-5 remained unchanged.

As the StEP and SHM approaches did not yield further improved variants, in the following based on Dr0930_73 smaller and more focused libraries were generated. In

general, focused, high quality libraries are advantageous as they require less screening effort (Reetz *et al.*, 2010; Lutz & Patrick, 2004). Single hot spots were consecutively mutagenized by site-directed or site-saturation mutagenesis with the goal to re-optimize previously identified key active-site residues located in βα-loops: Y28, D71, Y97, E101, M234, V235 (for Dr0930: Hawwa *et al.*, 2009b; for SsoPox: Elias *et al.*, 2008).

To ensure, that the design resulted in a simultaneous increase of the catalytic efficiencies towards all substrates, the smaller and more focused libraries were screened with all 7 OP compounds, while gradually reducing the substrate concentrations to screen specifically for improvements in k_{cat}/K_M. The more advanced rounds need to be performed at higher stringency to ensure the enrichment of significantly enhanced variants (Aharoni *et al.*, 2005b).

Site saturation mutagenesis at positions Y28 (4.3.4.2) and Y97 (4.3.4.3.2) and combinatorial mutagenesis with mutations obtained by epPCR hits (4.3.4.4.2) was performed. The individual variants contained only a single or a few exchanges, and gave fold improvements at a maximum of one order of magnitude. The beneficial mutations were then combined in an iterative design process.

Following several rounds of mutagenesis the variant Dr0930_134 was obtained which showed 1.7×10^2 (MPXN) to 6.9×10^4 (VR *p*-NP) fold higher catalytic efficiencies relative to wild-type Dr0930 for the hydrolysis of *p*-NP analogues of G- and V-type nerve agents and phosphotriesters (Figure 50A). The catalytic efficiencies of Dr0930_134 ranged from 10^4-10^5 $M^{-1}s^{-1}$ and attributed to a slight decrease in the K_M value for OP compounds and a substantial increase in k_{cat} (Table 6; Table 25). The k_{cat}/K_M values for the hydrolysis of methylphosphonates VX *p*-NP, GB *p*-NP and VR *p*-NP are particularly high (>2×10^5 $M^{-1}s^{-1}$), and the catalytic efficiencies with phosphotriesters and methylphosphonates containing a bulky substituent (GD *p*-NP and GF *p*-NP) are only lower by one order of magnitude. Moreover, Dr0930_134 approaches wild-type catalytic efficiencies for the GD *p*-NP substrate (approximately 10^4 $M^{-1}s^{-1}$; Figure 50B). The result proves that the Dr0930 enzyme exhibits great plasticity and evolvability.

5.3.2 Detailed characterization of engineered Dr0930 variants

The engineered variants were characterized for their residual native lactonase activity (4.4.1), their ability to hydrolyze P-S in addition to P-O bonds (4.4.2), and the stereoselectivity of the OP hydrolysis (4.4.3).

The results showed that the substantial increase in promiscuous OPH activity is accompanied by an equally strong decrease of the native lactonase activity (4.4.1). Dr0930_134 retains a k_{cat}/K_M for the hydrolysis of δ-nonanoic lactone of 2.8×10^3 $M^{-1}s^{-1}$, which corresponds to a fold decrease of 2.8×10^3 (Table 26; Figure 53), while the catalytic efficiencies for the hydrolysis of OPs increased by up to 6.9×10^4-fold, achieving absolute values of 10^5 $M^{-1}s^{-1}$ (Table 25; Figure 50A). Despite the partial trade-off, Dr0930_134 is a truly bifunctional enzyme exhibiting broad substrate specificity. Protein designs with both, weak and strong, trade-off have been reported (Aharoni *et al.*, 2005a and references therein; Seebeck & Hilvert, 2003; Claren *at al.*, 2009). Noteworthy, the conservation of the native function was not a constraint of the screen, which only searched for improved OPH activity. Most likely, in the case reported here the structural flexibility of the βα-loops and the conservation of most residues important for positioning for the native substrate (R228, D264, F26, L231, V235, W287) allowed for the conservation of the native function (Figure 19A); however, the elimination of a crucial electrostatic interaction by the Y97F mutation and an enlargement of the active site lead to reduced catalytic efficiencies relative to the wild-type enzyme as binding and positioning of the lactone substate relative to the catalytic machinery might be less effective; at the same time the latter only then allowed for improved binding of OPs (4.4.4.2).

The dramatic improvement of the promiscuous OPH activity for a broad range of OPs prompted us to further investigate the substrate specificity of the engineered Dr0930 variants. They were tested for their ability to degrade the phosphorothiolate DEVX (Diethyl-VX), a close analogue of the real nerve agent VX (4.4.2). In spite of their high catalytic efficiencies for the hydrolysis of P-O bonds within the *p*-nitrophenol analogues of VX, the k_{cat}/K_M values for the hydrolysis of the P-S bond of DEVX was only 1 $M^{-1}s^{-1}$. Noteworthy, the hydrolytic activity for DEVX did not increase in the course of the design. Although, phosphorothiolates are also hydrolyzed by PTE at significantly lower rates than methylphosphonates and phosphotriesters, the results also demonstrate, that *p*-nitrophenol analogues of VX and presumably also VR (P-O bond) are no faithful analgoues for the V-type nerve agents VX and VR (P-S

bond). In contrast, it has been demonstrated earlier, that activities with *p*-acetylphenyl substituted analogues of GB and GD nerve agents (containing P-O bonds) and the original GB and GD nerve agents (containing P-F bonds) are comparable, confirming the analogues of G-type nerve agents to be faithful substrates (Tsai *et al.*, 2010a).

Investigating the stereoselectivity of enzymes is particularly interesting, and several studies have been performed to enhance and inverse the inherent stereoselectivities of PTE (Tsai *et al.*, 2010a/b; Nowlan *et al.*, 2006; Hill *et al.*, 2003; Chen-Goodspeed *et al.*, 2001a/b; Li *et al.*, 2001) and PON1 (Goldsmith *et al.*, 2012). Hence, the stereoselectivities of wild-type Dr0930 and Dr0930_134 were monitored and compared with the stereoselectivity of PTE (4.4.3). The results showed that the Dr0930 variants exhibit the same stereopreference for the less toxic R_P isomers of OPs 1-5 as wild-type PTE (Table 28), indicating that the relative orientation of the OP substrates in the substrate binding pocket is identical. Remarkably, the evolution of higher detoxification rates for the *p*-NP analogues of G- and V-type nerve agents was accompanied by an enhancement in Dr0930's stereoselectivity (Table 29; Figure 55). The shift in enantiomeric preference [ratio k_{cat}/K_M (R_P) / k_{cat}/K_M (S_P)] between the wild-type enzyme and Dr0930_134 was high as 4.3×10^2-fold in the case of VR *p*-NP. The highest enantiomeric preference of 1.5×10^4-fold was observed for GB *p*-NP. Since the OP compounds were synthesized as racemates, their S_P isomers were also present during screening. However, we observed no inhibition by the S_P isomers.

Structural and computational analysis was performed to identify the structural basis for the enhanced OPH activity of the engineered Dr0930 variants.

Three variants including Dr0930_134 were successfully crystallized and their X-ray structures were solved to a resolution of 1.78-2.05 Å (4.4.4.1). However, ligand complexed structures were not obtained. The variants exhibited only minor structural differences relative to wild-type Dr0930 (Figure 58). By the introduction of 6-7 mutations the active site was enlarged and its hydrophobic character was increased, providing more suitable space to accommodate the OP substrates (Figure 59). Moreover, additional flexibility was gained due to the elimination of a hydrogen bond between residues of the $\beta\alpha$-loops 2 and 3. Mesecar and co-workers described similar effects with their OPH enhanced Dr0930 variants (Hawwa *et al.*, 2009b). From all PLL enzymes, only wild-type Dr0930 has been crystallized in the complexed

structure with an OP analogue. However, the complexed structure contained the small product analogue cacodylate, and hence allowed only to make a limited statement about the configurational and spatial orientation of OP substrates in the active site of Dr0930 (Hawwa *et al.*, 2009b). A strong shift in substrate specificity accompanied by only minor structural modifications in the active site has also been reported by Poelarends and co-workers. In their recent study they re-designed the substrate specificity of methylaspartate ammonia lyase from *Clostridium tetanomorphum* to accept a varity of amines and fumarates and to catalyze the asymmetric synthesis of aspartic acid derivatives. Using single amino acid substitutions that enlarged the substrate binding pocket they widened the substrate scope of the enzyme for both amine and fumarate derivatives, achieving an up to 70,000-fold shift in specificity (Raj *et al.*, 2012).

In order to identify the orientation of EPXN in the active site of Dr0930_134, the substrate was docked using the RosettaLigand program (Davis & Baker, 2009). The docking program has been successfully applied in earlier designs for the docking of OPs and lactones in the metallo-enzymes adenosine deaminase and PON1 (Khare *et al.*, 2012; Ben-David *et al.*, 2012). Initially, retroperspective docking experiments with wild-type PTE using DIMP and EPXN were performed yielding docking poses that were essentially identical to poses observed by crystallization, and hence confirmed the validity of the docking models (4.4.5.1). Then, EPXN was docked into the active site of Dr0930_134. When no constraints were set, the phosphoryl oxygen of EPXN hydrogen bonded to the side chain of R228, indicating a potential electrostatic interaction to the substrate/intermediate. Constraints were set to enforce a metal-complexed pose as observed in the PTE crystal structures. The best poses obtained were similar to the pose of EPXN when docked into the active site of PTE (Figure 63) and confirmed site-directed mutagenesis experiments that have indicated an important role of residues F26 and R228 for OPH activity (4.3.4.4.1 and 4.3.3). F26 might be important for substrate positioning and R228, potentially being part of proton shuttling, might be important for the coordination and/or activation of the substrate and/or stabilization of the intermediate.

5.3.3 Comparison of design achievemens to state-of-the-art designs for OPH activity

The catalytic efficiency of OP hydrolysis by Dr0930_134 is substantial in terms of absolute numbers and significantly better when compared to previous designs with PLL enyzmes (Hawwa *et al.*, 2009b; Elias *et al.*, 2008; Merone *et al.*, 2010) and the *de novo* design for OPH activity (Khare *et al.*, 2012). Moreover, the presented achievements are comparable to the designs made with a more efficient OP-hydrolyzing enzyme such as the lactonase PON1 (see also 1.2.2; Gupta *et al.*, 2011; Goldsmith *et al.*, 2012).

Mesecar and co-workers and Chabriere and co-workers made only modest achievements with the design of the PLL enzymes, Dr0930 and SsoPox, for the hydrolysis of MPXN and EPXN (Hawwa *et al.*, 2009b; Elias *et al.*, 2008; Merone *et al.*, 2010). The best published design for Dr0930 achieves a fold-improvement of only 1.8×10^2 and 5.6×10^2 for MPXN and EPXN and absolute values of k_{cat}/K_M are 1.1×10^2 $M^{-1}s^{-1}$ and 7.7×10^2 $M^{-1}s^{-1}$, respectively (Hawwa *et al.*, 2009b; our data confirmed a fold-improvement of only 65-fold for EPXN for their best variant – see 4.3.4.1). The highest fold improvement in k_{cat}/K_M published for SsoPox is 6.5-fold for EPXN (Elias *et al.*, 2008; Merone *et al.*, 2010).

The achievements made by Tawfik and Baker for the design of OPH activity of PON1 are more significant. Tawfik and co-workers optimized PON1 for hydrolysis of fluorogenic coumarinyl analogue of S_P-GF and *in-situ* generated S_P-GF. Excessive mutagenesis and a FACS-based high-throughput screen yielded a variant with a 8.6×10^4-fold improvement in catalytic efficiency (k_{cat}/K_M increased from 3.3 $M^{-1}s^{-1}$ to 2.9×10^5 $M^{-1}s^{-1}$) for the S_P-isomer of the GF analogue. The fold improvement for S_P-GF was significantly lower with only 1.4×10^2 compared to wild-type-like PON1 (Gupta *et al.*, 2011). In their latest design, Tawfik and co-workers enhanced the activity of a PON1 variant by re-optimizing earlier identified active-site residues for the hydrolysis of *in-situ* generated GD isomers by up to 3.4×10^2 fold in k_{cat}/K_M compared to the starting variant and 3.4×10^3 fold compared to wild-type-like PON1. However, improvements for other G-type agents isomers, GA, GB, and GF were significantly smaller, achieving only one order of magnitude fold-improvement compared to the starting variant (Goldsmith *et al.*, 2012).

Baker and co-workers computationally redesigned a mononuclear zinc metallo-enzyme, the mouse adenine deaminase, for organophosphate hydrolysis. After

optimization by subsequent directed evolution they achieved a catalytic efficiency of 9.8×10^3 $M^{-1}s^{-1}$ for one single substrate, the R_P-isomer of the coumarinyl analogue of GF. However, the authors noticed that their designed variant hydrolyzes only substrates with coumarinyl leaving group but not *p*-NP substituted substrates (Khare *et al.*, 2012).

In this work an extremely efficient OPH was designed, which hydrolyzes not only a broad spectrum of methylphosphonates (G and V-type nerve agent analogues), but also phosphotriesters. The catalytic efficiency for the hydrolysis of OPs by Dr0930 has been improved by 1.7×10^2 to 6.9×10^4 -fold thereby reaching k_{cat}/K_M values of 3.6×10^5 $M^{-1}s^{-1}$. The absolute values in k_{cat}/K_M approach the level of natural enzymes (Bar-Even *et al.*, 2011) and wild-type PTE (Figure 50B). To the best of our knowledge, designs yielding comparable high fold improvements and catalytic efficiencies for multiple substrates have not been described previously.

5.4 Implications for protein design and evolution

Taken together, the results of this thesis show that laboratory evolution can readily establish high OPH activity on the scaffold of Dr0930, providing strong evidence for the postulated natural evolution of PTE from members of the PLL family. Most noteworthy, only three mutations were sufficient to substantially alter the substrate specificity of Dr0930 and to achieve catalytic efficiencies as high as 1.4×10^3 $M^{-1}s^{-1}$ (Dr0930_5; Table 10). Hence, the results underline the catalytic versatility of the ubiquitous $(\beta\alpha)_8$-barrel fold (Sterner & Höcker, 2005). However, the results here (4.3.4.3.1.1; 4.3.4.3.1.2; 4.3.4.4.1) and in Xiang *et al.* (2009) demonstrate that the efficient OPH activity cannot be increased by simply structurally miminking the active site and substrate binding pocket of PTE.

Analogously to the rapid molecular evolution of PTE from a PLL precursor, the methyl-parathion hydrolase (MPH) from *Pseudomonas sp.* WBC-3 (1.2.2; an OPH enzyme with a β-lactamase fold) is speculated to have evolved by divergent evolution from *Bacillus thuringiensis* AiiA, a metallo-β-lactamase-like lactonase. However, the postulated evolutionary origin of the MPH is as yet based soley on sequence similarity, and detailed kinetic studies for this case of divergent evolution remain to be done (Elias & Tawfik, 2012).

5.5 Outlook

Testing the engineered Dr0930 variants for a broader substrate scope using another class of OPs, such as thiophosphotriesters (e.g. diazinon, parathion and chlorpyrifos), would be interesting. Also, characterization of the most proficient Dr0930 variants for the true nerve agents using an assay developed by Tawfik and co-workers where nerve agents are generated *in situ* in dilute aqueous solutions (Gupta *et al*., 2011) or analysis by an accredited laboratory might be scientifically interesting. Moreover, reversing the stereoselectivity of the designed variants for the more toxic S_P-isomers as described for PTE (Tsai *et al.*, 2010a/b; Nowlan *et al.*, 2006; Hill *et al.*, 2003; Chen-Goodspeed *et al.*, 2001a/b; Li *et al.*, 2001) and PON1 (Gupta *et al*., 2011; Goldsmith *et al.*, 2012) would be attractive.

6 REFERENCES

Adams, P. D., Grosse-Kunstleve, R. W., Hung, L. W., Ioerger, T. R., McCoy, A. J., Moriarty, N. W., Read, R. J., Sacchettini, J. C., Sauter, N. K. and Terwilliger, T. C. (2002). PHENIX: building new software for automated crystallographic structure determination. *Acta Crystallogr D Biol Crystallogr* 58(Pt 11): 1948-1954.

Afriat, L., Roodveldt, C., Manco, G. and Tawfik, D. S. (2006). The latent promiscuity of newly identified microbial lactonases is linked to a recently diverged phosphotriesterase. *Biochemistry* 45(46): 13677-13686.

Aharoni, A., Gaidukov, L., Khersonsky, O., Mc, Q. G. S., Roodveldt, C. and Tawfik, D. S. (2005). The 'evolvability' of promiscuous protein functions. *Nat Genet* 37(1): 73-76.

Aharoni, A., Griffiths, A. D. and Tawfik, D. S. (2005). High-throughput screens and selections of enzyme-encoding genes. *Curr Opin Chem Biol* 9(2): 210-216.

Armougom, F., Moretti, S., Poirot, O., Audic, S., Dumas, P., Schaeli, B., Keduas, V. and Notredame, C. (2006). Expresso: automatic incorporation of structural information in multiple sequence alignments using 3D-Coffee. *Nucleic Acids Res* 34(Web Server issue): W604-608.

Arnold, F. H. (2001). Combinatorial and computational challenges for biocatalyst design. *Nature* 409(6817): 253-257.

Aubert, S. D., Li, Y. and Raushel, F. M. (2004). Mechanism for the hydrolysis of organophosphates by the bacterial phosphotriesterase. *Biochemistry* 43(19): 5707-5715.

Austin, M. B., O'Maille, P. E. and Noel, J. P. (2008). Evolving biosynthetic tangos negotiate mechanistic landscapes. *Nat Chem Biol* 4(4): 217-222.

Banner, D. W., Bloomer, A. C., Petsko, G. A., Phillips, D. C., Pogson, C. I., Wilson, I. A., Corran, P. H., Furth, A. J., Milman, J. D., Offord, R. E., Priddle, J. D. and Waley, S. G. (1975). Structure of chicken muscle triose phosphate isomerase determined crystallographically at 2.5 angstrom resolution using amino acid sequence data. *Nature* 255(5510): 609-614.

Bar-Even, A., Noor, E., Savir, Y., Liebermeister, W., Davidi, D., Tawfik, D. S. and Milo, R. (2011). The moderately efficient enzyme: evolutionary and physicochemical trends shaping enzyme parameters. *Biochemistry* 50(21): 4402-4410.

Ben-David, M., Elias, M., Filippi, J. J., Dunach, E., Silman, I., Sussman, J. L. and Tawfik, D. S. (2012). Catalytic versatility and backups in enzyme active sites: the case of serum paraoxonase 1. *J Mol Biol* 418(3-4): 181-196.

Benning, M. M., Hong, S. B., Raushel, F. M. and Holden, H. M. (2000). The binding of substrate analogs to phosphotriesterase. *J Biol Chem* 275(39): 30556-30560.

Benning, M. M., Kuo, J. M., Raushel, F. M. and Holden, H. M. (1994). Three-dimensional structure of phosphotriesterase: an enzyme capable of detoxifying organophosphate nerve agents. *Biochemistry* 33(50): 15001-15007.

Benning, M. M., Kuo, J. M., Raushel, F. M. and Holden, H. M. (1995). Three-dimensional structure of the binuclear metal center of phosphotriesterase. *Biochemistry* 34(25): 7973-7978.

Benning, M. M., Shim, H., Raushel, F. M. and Holden, H. M. (2001). High resolution X-ray structures of different metal-substituted forms of phosphotriesterase from Pseudomonas diminuta. *Biochemistry* 40(9): 2712-2722.

Benschop, H. P. and Dejong, L. P. A. (1988). Nerve agent stereoisomers - analysis, isolation, and toxicology. *Acc Chem Res* 21: 368-374.

Bigley, A. N. and Raushel, F. M. (2010). Phosphotriesterase. *Handbook of Metalloproteins*, *John Wiley & Sons, Inc.*, *New York*.

Bigley, A. N. and Raushel, F. M. (2012). Catalytic mechanisms for phosphotriesterases. *Biochim Biophys Acta*, *published ahead of print.*

Bloom, J. D., Meyer, M. M., Meinhold, P., Otey, C. R., MacMillan, D. and Arnold, F. H. (2005). Evolving strategies for enzyme engineering. *Curr Opin Struct Biol* 15(4): 447-452.

Blum, M. M., Lohr, F., Richardt, A., Ruterjans, H. and Chen, J. C. (2006). Binding of a designed substrate analogue to diisopropyl fluorophosphatase: implications for the phosphotriesterase mechanism. *J Am Chem Soc* 128(39): 12750-12757.

Bolon, D. N. and Mayo, S. L. (2001). Enzyme-like proteins by computational design. *Proc Natl Acad Sci U S A* 98(25): 14274-14279.

Bornscheuer, U. T. and Pohl, M. (2001). Improved biocatalysts by directed evolution and rational protein design. *Curr Opin Chem Biol* 5(2): 137-143.

Brunger, A. T., Adams, P. D., Clore, G. M., DeLano, W. L., Gros, P., Grosse-Kunstleve, R. W., Jiang, J. S., Kuszewski, J., Nilges, M., Pannu, N. S., Read, R. J., Rice, L. M., Simonson, T. and Warren, G. L. (1998). Crystallography & NMR system: A new software suite for macromolecular structure determination. *Acta Crystallogr D Biol Crystallogr* 54(Pt 5): 905-921.

Bruns, C. M., Hubatsch, I., Ridderstrom, M., Mannervik, B. and Tainer, J. A. (1999). Human glutathione transferase A4-4 crystal structures and mutagenesis reveal the basis of high catalytic efficiency with toxic lipid peroxidation products. *J Mol Biol* 288(3): 427-439.

Buchbinder, J. L., Stephenson, R. C., Dresser, M. J., Pitera, J. W., Scanlan, T. S. and Fletterick, R. J. (1998). Biochemical Characterization and Crystallographic Structure of an Escherichia coli Protein from the Phosphotriesterase Gene Family. *Biochemistry* 37(30): 10860.

Bujard, H., Gentz, R., Lanzer, M., Stueber, D., Mueller, M., Ibrahimi, I., Haeuptle, M. T. and Dobberstein, B. (1987). A T5 promoter-based transcription-translation system for the analysis of proteins in vitro and in vivo. *Methods Enzymol* 155: 416-433.

Cadwell, R. C. and Joyce, G. F. (1994). Mutagenic PCR. *PCR Methods Appl* 3(6): S136-140.

Caetano-Anolles, G., Kim, H. S. and Mittenthal, J. E. (2007). The origin of modern metabolic networks inferred from phylogenomic analysis of protein architecture. *Proc Natl Acad Sci U S A* 104(22): 9358-9363.

Camilli, A. and Bassler, B. L. (2006). Bacterial small-molecule signaling pathways. *Science* 311(5764): 1113-1116.

Camps, J., Marsillach, J. and Joven, J. (2009). The paraoxonases: role in human diseases and methodological difficulties in measurement. *Crit Rev Clin Lab Sci* 46(2): 83-106.

Chapman, E. and Wong, C. H. (2002). A pH sensitive colorometric assay for the high-throughput screening of enzyme inhibitors and substrates: a case study using kinases. *Bioorg Med Chem* 10(3): 551-555.

Chen, R. (2001). Enzyme engineering: rational redesign versus directed evolution. *Trends Biotechnol* 19(1): 13-14.

Chen, S. L., Fang, W. H. and Himo, F. (2007). Theoretical study of the phosphotriesterase reaction mechanism. *J Phys Chem B* 111(6): 1253-1255.

Chen-Goodspeed, M., Sogorb, M. A., Wu, F., Hong, S. B. and Raushel, F. M. (2001). Structural determinants of the substrate and stereochemical specificity of phosphotriesterase. *Biochemistry* 40(5): 1325-1331.

Chen-Goodspeed, M., Sogorb, M. A., Wu, F. and Raushel, F. M. (2001). Enhancement, relaxation, and reversal of the stereoselectivity for phosphotriesterase by rational evolution of active site residues. *Biochemistry* 40(5): 1332-1339.

Cheng, T., Liu, L., Wang, B., Wu, J., DeFrank, J. J., Anderson, D. M., Rastogi, V. K. and Hamilton, A. B. (1997). Nucleotide sequence of a gene encoding an organophosphorus nerve agent degrading enzyme from Alteromonas haloplanktis. *J Ind Microbiol Biotechnol* 18(1): 49-55.

Chester, N. and Marshak, D. R. (1993). Dimethyl sulfoxide-mediated primer Tm reduction: a method for analyzing the role of renaturation temperature in the polymerase chain reaction. *Anal Biochem* 209(2): 284-290.

Chothia, C., Gough, J., Vogel, C. and Teichmann, S. A. (2003). Evolution of the protein repertoire. *Science* 300(5626): 1701-1703.

Chow, J. Y., Wu, L. and Yew, W. S. (2009). Directed evolution of a quorum-quenching lactonase from Mycobacterium avium subsp. paratuberculosis K-10 in the amidohydrolase superfamily. *Biochemistry* 48(20): 4344-4353.

Chow, J. Y., Xue, B., Lee, K. H., Tung, A., Wu, L., Robinson, R. C. and Yew, W. S. (2010). Directed evolution of a thermostable quorum-quenching lactonase from the amidohydrolase superfamily. *J Biol Chem* 285(52): 40911-40920.

Claren, J. (2008). Design stabiler und katalytisch aktiver $(\beta\alpha)_8$-Barrel Enzyme durch Rekombination von $(\beta\alpha)_4$-Halbbarrel Domänen. *Dissertation, Universität Regensburg.*

Claren, J., Malisi, C., Höcker, B. and Sterner, R. (2009). Establishing wild-type levels of catalytic activity on natural and artificial (beta alpha)8-barrel protein scaffolds. *Proc Natl Acad Sci U S A 106(10): 3704-3709.*

Cleland, W. W. (1970). In: The Enzymes (Boyer, P. D., ed.), *Academic Press, New York,* Vol. 2, pp. 1-65.

Collaborative Computational Project, Number 4 (1994). The CCP4 suite: programs for protein crystallography. *Acta Crystallogr D Biol Crystallogr* 50(Pt 5): 760-763.

Cooper, G. M. (2000). The Cell - A Molecular Approach; Chapter 10: The Chloroplast Genome *published by Sinauer Associates, Inc.*

Copley, S. D. (2009). Evolution of efficient pathways for degradation of anthropogenic chemicals. *Nat Chem Biol* 5(8): 559-566.

Datsenko, K. A. and Wanner, B. L. (2000). One-step inactivation of chromosomal genes in Escherichia coli K-12 using PCR products. *Proc Natl Acad Sci U S A* 97(12): 6640-6645.

Davis, I. W. and Baker, D. (2009). RosettaLigand docking with full ligand and receptor flexibility. *J Mol Biol* 385(2): 381-392.

Davis, I. W., Leaver-Fay, A., Chen, V. B., Block, J. N., Kapral, G. J., Wang, X., Murray, L. W., Arendall, W. B., 3rd, Snoeyink, J., Richardson, J. S. and Richardson, D. C. (2007). MolProbity: all-atom contacts and structure validation for proteins and nucleic acids. *Nucleic Acids Res* 35(Web Server issue): W375-383.

de Souza, M. L., Seffernick, J., Martinez, B., Sadowsky, M. J. and Wackett, L. P. (1998). The atrazine catabolism genes atzABC are widespread and highly conserved. *J Bacteriol* 180(7): 1951-1954.

DeFrank, J. J. and Cheng, T. C. (1991). Purification and properties of an organophosphorus acid anhydrase from a halophilic bacterial isolate. *J Bacteriol* 173(6): 1938-1943.

Dong, Y. J., Bartlam, M., Sun, L., Zhou, Y. F., Zhang, Z. P., Zhang, C. G., Rao, Z. and Zhang, X. E. (2005). Crystal structure of methyl parathion hydrolase from Pseudomonas sp. WBC-3. *J Mol Biol* 353(3): 655-663.

Dower, W. J., Miller, J. F. and Ragsdale, C. W. (1988). High efficiency transformation of E. coli by high voltage electroporation. *Nucleic Acids Res* 16(13): 6127-6145.

Dumas, D. P., Caldwell, S. R., Wild, J. R. and Raushel, F. M. (1989). Purification and properties of the phosphotriesterase from Pseudomonas diminuta. *J Biol Chem* 264(33): 19659-19665.

Elias, M., Dupuy, J., Merone, L., Mandrich, L., Porzio, E., Moniot, S., Rochu, D., Lecomte, C., Rossi, M., Masson, P., Manco, G. and Chabriere, E. (2008). Structural basis for natural lactonase and promiscuous phosphotriesterase activities. *J Mol Biol* 379(5): 1017-1028.

Elias, M. and Tawfik, D. S. (2012). Divergence and convergence in enzyme evolution: parallel evolution of paraoxonases from quorum-quenching lactonases. *J Biol Chem* 287(1): 11-20.

Emsley, P. and Cowtan, K. (2004). Coot: model-building tools for molecular graphics. *Acta Crystallogr D Biol Crystallogr* 60(Pt 12 Pt 1): 2126-2132.

Emsley, P., Lohkamp, B., Scott, W. G. and Cowtan, K. (2010). Features and development of Coot. *Acta Crystallogr D Biol Crystallogr* 66(Pt 4): 486-501.

Fersht, A. (1985). Measurement and magnitude of enzymatic rate constants. *Enzyme Structure and Mechanism, W. H. Freeman & Co., New York*, 2nd edition: 121-154.

Field, B. and Osbourn, A. E. (2008). Metabolic diversification - independent assembly of operon-like gene clusters in different plants. *Science* 320(5875): 543-547.

Gerlt, J. A. and Babbitt, P. C. (1998). Mechanistically diverse enzyme superfamilies: the importance of chemistry in the evolution of catalysis. *Curr Opin Chem Biol* 2(5): 607-612.

Gerlt, J. A. and Babbitt, P. C. (2001). Divergent evolution of enzymatic function: mechanistically diverse superfamilies and functionally distinct suprafamilies. *Annu Rev Biochem* 70: 209-246.

Gerlt, J. A. and Raushel, F. M. (2003). Evolution of function in (beta/alpha)8-barrel enzymes. *Curr Opin Chem Biol* 7(2): 252-264.

Glansdorff, N., Xu, Y. and Labedan, B. (2008). The Last Universal Common Ancestor: emergence, constitution and genetic legacy of an elusive forerunner. *Biol Direct* 3: 29.

Goldsmith, M., Ashani, Y., Simo, Y., Ben-David, M., Leader, H., Silman, I., Sussman, J. L. and Tawfik, D. S. (2012). Evolved stereoselective hydrolases for broad-spectrum G-type nerve agent detoxification. *Chem Biol* 19(4): 456-466.

Goldsmith, M. and Tawfik, D. S. (2012). Directed enzyme evolution: beyond the low-hanging fruit. *Curr Opin Struct Biol, published ahead of print.*

Gupta, R. D., Goldsmith, M., Ashani, Y., Simo, Y., Mullokandov, G., Bar, H., Ben-David, M., Leader, H., Margalit, R., Silman, I., Sussman, J. L. and Tawfik, D. S. (2011). Directed evolution of hydrolases for prevention of G-type nerve agent intoxication. *Nat Chem Biol* 7(2): 120-125.

Hall, B. G. (2004). Predicting the evolution of antibiotic resistance genes. *Nat Rev Microbiol* 2(5): 430-435.

Hartleib, J. and Ruterjans, H. (2001). High-yield expression, purification, and characterization of the recombinant diisopropylfluorophosphatase from Loligo vulgaris. *Protein Expr Purif* 21(1): 210-219.

Hawkins, P. C., Skillman, A. G., Warren, G. L., Ellingson, B. A. and Stahl, M. T. (2010). Conformer generation with OMEGA: algorithm and validation using high quality structures from the Protein Databank and Cambridge Structural Database. *J Chem Inf Model* 50(4): 572-584.

Hawwa, R., Aikens, J., Turner, R. J., Santarsiero, B. D. and Mesecar, A. D. (2009). Structural basis for thermostability revealed through the identification and characterization of a highly thermostable phosphotriesterase-like lactonase from Geobacillus stearothermophilus. *Arch Biochem Biophys* 488(2): 109-120.

Hawwa, R., Larsen, S. D., Ratia, K. and Mesecar, A. D. (2009). Structure-based and random mutagenesis approaches increase the organophosphate-degrading activity of a phosphotriesterase homologue from Deinococcus radiodurans. *J Mol Biol* 393(1): 36-57.

Hegyi, H. and Gerstein, M. (1999). The relationship between protein structure and function: a comprehensive survey with application to the yeast genome. *J Mol Biol* 288(1): 147-164.

Hennig, M., Jansonius, J. N., Terwisscha van Scheltinga, A. C., Dijkstra, B. W. and Schlesier, B. (1995). Crystal structure of concanavalin B at 1.65 A resolution. An "inactivated" chitinase from seeds of Canavalia ensiformis. *J Mol Biol* 254(2): 237-246.

Hennig, M., Pfeffer-Hennig, S., Dauter, Z., Wilson, K. S., Schlesier, B. and Nong, V. H. (1995). Crystal structure of narbonin at 1.8 A resolution. *Acta Crystallogr D Biol Crystallogr* 51(Pt 2): 177-189.

Hennig, M., Schlesier, B., Dauter, Z., Pfeffer, S., Betzel, C., Hohne, W. E. and Wilson, K. S. (1992). A TIM barrel protein without enzymatic activity? Crystal-structure of narbonin at 1.8 A resolution. *FEBS Lett* 306(1): 80-84.

Hill, C. M., Li, W. S., Thoden, J. B., Holden, H. M. and Raushel, F. M. (2003). Enhanced degradation of chemical warfare agents through molecular engineering of the phosphotriesterase active site. *J Am Chem Soc* 125(30): 8990-8991.

Ho, S. N., Hunt, H. D., Horton, R. M., Pullen, J. K. and Pease, L. R. (1989). Site-directed mutagenesis by overlap extension using the polymerase chain reaction. *Gene* 77(1): 51-59.

Hobbs, M. E., Malashkevich, V., Williams, H. J., Xu, C., Sauder, J. M., Burley, S. K., Almo, S. C. and Raushel, F. M. (2012). Structure and Catalytic Mechanism of LigI: Insight into the Amidohydrolase Enzymes of cog3618 and Lignin Degradation. *Biochemistry*, *published ahead of print.*

Höcker, B. (2005). Directed evolution of (betaalpha)(8)-barrel enzymes. *Biomol Eng* 22(1-3): 31-38.

Höcker, B., Jurgens, C., Wilmanns, M. and Sterner, R. (2001). Stability, catalytic versatility and evolution of the (beta alpha)(8)-barrel fold. *Curr Opin Biotechnol* 12(4): 376-381.

Holm, L. and Sander, C. (1997). An evolutionary treasure: unification of a broad set of amidohydrolases related to urease. *Proteins* 28(1): 72-82.

Hong, S. B. and Raushel, F. M. (1996). Metal-substrate interactions facilitate the catalytic activity of the bacterial phosphotriesterase. *Biochemistry* 35(33): 10904-10912.

Hong, S. B. and Raushel, F. M. (1999). Stereochemical constraints on the substrate specificity of phosphotriesterase. *Biochemistry* 38(4): 1159-1165.

Horne, I., Qiu, X., Russell, R. J. and Oakeshott, J. G. (2003). The phosphotriesterase gene opdA in Agrobacterium radiobacter P230 is transposable. *FEMS Microbiol Lett* 222(1): 1-8.

Inoue, H., Nojima, H. and Okayama, H. (1990). High efficiency transformation of Escherichia coli with plasmids. *Gene* 96(1): 23-28.

Jabri, E., Carr, M. B., Hausinger, R. P. and Karplus, P. A. (1995). The crystal structure of urease from Klebsiella aerogenes. *Science* 268(5213): 998-1004.

Jackson, C. J., Foo, J. L., Kim, H. K., Carr, P. D., Liu, J. W., Salem, G. and Ollis, D. L. (2008). In crystallo capture of a Michaelis complex and product-binding modes of a bacterial phosphotriesterase. *J Mol Biol* 375(5): 1189-1196.

Jain, R., Rivera, M. C., Moore, J. E. and Lake, J. A. (2003). Horizontal gene transfer accelerates genome innovation and evolution. *Mol Biol Evol* 20(10): 1598-1602.

Janssen, D. B., Dinkla, I. J., Poelarends, G. J. and Terpstra, P. (2005). Bacterial degradation of xenobiotic compounds: evolution and distribution of novel enzyme activities. *Environ Microbiol* 7(12): 1868-1882.

Jensen, R. A. (1976). Enzyme recruitment in evolution of new function. *Annu Rev Microbiol* 30: 409-425.

Jiang, L., Althoff, E. A., Clemente, F. R., Doyle, L., Rothlisberger, D., Zanghellini, A., Gallaher, J. L., Betker, J. L., Tanaka, F., Barbas, C. F., 3rd, Hilvert, D., Houk, K. N., Stoddard, B. L. and Baker, D. (2008). De novo computational design of retro-aldol enzymes. *Science* 319(5868): 1387-1391.

Kabsch, W. (1993). Automatic processing of rotation diffraction data from crystals of initially unknown symmetry and cell constants. *J Appl Cryst* 26: 795-800.

Kabsch, W. (2010). Xds. *Acta Crystallogr D Biol Crystallogr* 66(Pt 2): 125-132.

Khare, S. D., Kipnis, Y., Greisen, P., Jr., Takeuchi, R., Ashani, Y., Goldsmith, M., Song, Y., Gallaher, J. L., Silman, I., Leader, H., Sussman, J. L., Stoddard, B. L., Tawfik, D. S. and Baker, D. (2012). Computational redesign of a mononuclear zinc metalloenzyme for organophosphate hydrolysis. *Nat Chem Biol* 8(3): 294-300.

Khersonsky, O., Kiss, G., Röthlisberger, D., Dym, O., Albeck, S., Houk, K. N., Baker, D. and Tawfik, D. S. (2012). Bridging the gaps in design methodologies by evolutionary optimization of the stability and proficiency of designed Kemp eliminase KE59. *Proc Natl Acad Sci U S A*, *published ahead of print.*

Khersonsky, O., Malitsky, S., Rogachev, I. and Tawfik, D. S. (2011). Role of chemistry versus substrate binding in recruiting promiscuous enzyme functions. *Biochemistry* 50(13): 2683-2690.

Khersonsky, O., Roodveldt, C. and Tawfik, D. S. (2006). Enzyme promiscuity: evolutionary and mechanistic aspects. *Curr Opin Chem Biol* 10(5): 498-508.

Khersonsky, O., Röthlisberger, D., Dym, O., Albeck, S., Jackson, C. J., Baker, D. and Tawfik, D. S. (2010). Evolutionary optimization of computationally designed enzymes: Kemp eliminases of the KE07 series. *J Mol Biol* 396(4): 1025-1042.

Khersonsky, O. and Tawfik, D. S. (2005). Structure-reactivity studies of serum paraoxonase PON1 suggest that its native activity is lactonase. *Biochemistry* 44(16): 6371-6382.

Khersonsky, O. and Tawfik, D. S. (2010). Enzyme promiscuity: a mechanistic and evolutionary perspective. *Annu Rev Biochem* 79: 471-505.

Kim, J., Tsai, P. C., Chen, S. L., Himo, F., Almo, S. C. and Raushel, F. M. (2008). Structure of diethyl phosphate bound to the binuclear metal center of phosphotriesterase. *Biochemistry* 47(36): 9497-9504.

Kirschner, M. and Gerhart, J. (1998). Evolvability. *Proc Natl Acad Sci U S A* 95(15): 8420-8427.

Knowles, J. R. (1991). To build an enzyme. *Philos Trans R Soc Lond B Biol Sci* 332(1263): 115-121.

Kuhlman, B. and Baker, D. (2000). Native protein sequences are close to optimal for their structures. *Proc Natl Acad Sci U S A* 97(19): 10383-10388.

Laemmli, U. K. (1970). Cleavage of structural proteins during the assembly of the head of bacteriophage T4. *Nature* 227(5259): 680-685.

Le Gouill, C., Parent, J. L., Rola-Pleszczynski, M. and Stankova, J. (1994). Analysis of recombinant plasmids by a modified alkaline lysis method. *Anal Biochem* 219(1): 164.

Lewis, V. E., Donarski, W. J., Wild, J. R. and Raushel, F. M. (1988). Mechanism and stereochemical course at phosphorus of the reaction catalyzed by a bacterial phosphotriesterase. *Biochemistry* 27(5): 1591-1597.

Li, W. S., Lum, K. T., Chen-Goodspeed, M., Sogorb, M. A. and Raushel, F. M. (2001). Stereoselective detoxification of chiral sarin and soman analogues by phosphotriesterase. *Bioorg Med Chem* 9(8): 2083-2091.

Lutz, S. and Patrick, W. M. (2004). Novel methods for directed evolution of enzymes: quality, not quantity. *Curr Opin Biotechnol* 15(4): 291-297.

McCoy, A. J., Grosse-Kunstleve, R. W., Adams, P. D., Winn, M. D., Storoni, L. C. and Read, R. J. (2007). Phaser crystallographic software. *J Appl Crystallogr* 40(Pt 4): 658-674.

McPherson, A. (1982). The Preparation and Analysis of Protein Crystals. *John Wiley & Sons, Inc., New York.*

McRee, D. E. (1999). XtalView/Xfit - A versatile program for manipulating atomic coordinates and electron density. *J Struct Biol* 125(2-3): 156-165.

Meier, M. M. (2008). Interconversion of substrate specificity within the amidohydrolase superfamily of enzymes. *Diplomarbeit, Universität Regensburg.*

Merone, L., Mandrich, L., Porzio, E., Rossi, M., Muller, S., Reiter, G., Worek, F. and Manco, G. (2010). Improving the promiscuous nerve agent hydrolase activity of a thermostable archaeal lactonase. *Bioresour Technol* 101(23): 9204-9212.

Merone, L., Mandrich, L., Rossi, M. and Manco, G. (2005). A thermostable phosphotriesterase from the archaeon Sulfolobus solfataricus: cloning, overexpression and properties. *Extremophiles* 9(4): 297-305.

Merone, L., Mandrich, L., Rossi, M. and Manco, G. (2008). Enzymes with phosphotriesterase and lactonase activities in archaea. *Curr Chem Biol* 2(3): 237-248.

Merz, A., Yee, M. C., Szadkowski, H., Pappenberger, G., Crameri, A., Stemmer, W. P., Yanofsky, C. and Kirschner, K. (2000). Improving the catalytic activity of a thermophilic enzyme at low temperatures. *Biochemistry* 39(5): 880-889.

Mulbry, W. W. and Karns, J. S. (1989). Parathion hydrolase specified by the Flavobacterium opd gene: relationship between the gene and protein. *J Bacteriol* 171(12): 6740-6746.

Mullis, K. B. and Faloona, F. A. (1987). Specific synthesis of DNA in vitro via a polymerase-catalyzed chain reaction. *Methods Enzymol* 155: 335-350.

Munnecke, D. M. (1976). Enzymatic hydrolysis of organophosphate insecticides, a possible pesticide disposal method. *Appl Environ Microbiol* 32(1): 7-13.

Munro, N. (1994). Toxicity of the organophosphate chemical warfare agents GA, GB, and VX: implications for public protection. *Environ Health Perspect* 102(1): 18-38.

Murshudov, G. N., Vagin, A. A. and Dodson, E. J. (1997). Refinement of macromolecular structures by the maximum-likelihood method. *Acta Crystallogr D Biol Crystallogr* 53(Pt 3): 240-255.

Murzin, A. G., Brenner, S. E., Hubbard, T. and Chothia, C. (1995). SCOP: a structural classification of proteins database for the investigation of sequences and structures. *J Mol Biol* 247(4): 536-540.

Nagano, N., Orengo, C. A. and Thornton, J. M. (2002). One fold with many functions: the evolutionary relationships between TIM barrel families based on their sequences, structures and functions. *J Mol Biol* 321(5): 741-765.

Neurath, H. (1984). "Evolution of proteolytic enzymes." *Science* **224**(4647): 350-7.

Neurath, H., Walsh, K. A. and Winter, W. P. (1967). "Evolution of structure and function of proteases." *Science* **158**(809): 1638-44.

Nguyen, T. T., Brown, S., Fedorov, A. A., Fedorov, E. V., Babbitt, P. C., Almo, S. C. and Raushel, F. M. (2008). At the periphery of the amidohydrolase superfamily: Bh0493 from Bacillus halodurans catalyzes the isomerization of D-galacturonate to D-tagaturonate. *Biochemistry* 47(4): 1194-1206.

Notredame, C., Higgins, D. G. and Heringa, J. (2000). T-Coffee: A novel method for fast and accurate multiple sequence alignment. *J Mol Biol* 302(1): 205-217.

Nowlan, C., Li, Y., Hermann, J. C., Evans, T., Carpenter, J., Ghanem, E., Shoichet, B. K. and Raushel, F. M. (2006). Resolution of chiral phosphate, phosphonate, and phosphinate esters by an enantioselective enzyme library. *J Am Chem Soc* 128(49): 15892-15902.

O'Brien, P. J. and Herschlag, D. (1999). Catalytic promiscuity and the evolution of new enzymatic activities. *Chem Biol* 6(4): R91-R105.

O'Maille, P. E., Malone, A., Dellas, N., Andes Hess, B., Jr., Smentek, L., Sheehan, I., Greenhagen, B. T., Chappell, J., Manning, G. and Noel, J. P. (2008). Quantitative exploration of the catalytic landscape separating divergent plant sesquiterpene synthases. *Nat Chem Biol* 4(10): 617-623.

Ochman, H., Lawrence, J. G. and Groisman, E. A. (2000). Lateral gene transfer and the nature of bacterial innovation. *Nature* 405(6784): 299-304.

Omburo, G. A., Kuo, J. M., Mullins, L. S. and Raushel, F. M. (1992). Characterization of the zinc binding site of bacterial phosphotriesterase. *J Biol Chem* 267(19): 13278-13283.

Ostermeier, M., Shim, J. H. and Benkovic, S. J. (1999). A combinatorial approach to hybrid enzymes independent of DNA homology. *Nat Biotechnol* 17(12): 1205-1209.

Otwinowski, Z. and Minor, W. (1997). Processing of X-ray Diffraction Data Collected in Oscillation Mode. *Methods in Enzymology*, Volume 276: Macromolecular Crystallography, part A: 307-326.

Pace, C. N., Vajdos, F., Fee, L., Grimsley, G. and Gray, T. (1995). How to measure and predict the molar absorption coefficient of a protein. *Protein Sci* 4(11): 2411-2423.

Park, H. S., Nam, S. H., Lee, J. K., Yoon, C. N., Mannervik, B., Benkovic, S. J. and Kim, H. S. (2006). Design and evolution of new catalytic activity with an existing protein scaffold. *Science* 311(5760): 535-538.

Patrick, W. M. and Matsumura, I. (2008). A study in molecular contingency: glutamine phosphoribosylpyrophosphate amidotransferase is a promiscuous and evolvable phosphoribosylanthranilate isomerase. *J Mol Biol* 377(2): 323-336.

Pettersen, E. F., Goddard, T. D., Huang, C. C., Couch, G. S., Greenblatt, D. M., Meng, E. C. and Ferrin, T. E. (2004). UCSF Chimera - a visualization system for exploratory research and analysis. *J Comput Chem* 25(13): 1605-1612.

Porzio, E., Merone, L., Mandrich, L., Rossi, M. and Manco, G. (2007). A new phosphotriesterase from Sulfolobus acidocaldarius and its comparison with the homologue from Sulfolobus solfataricus. *Biochimie* 89(5): 625-636.

Potterton, L., McNicholas, S., Krissinel, E., Gruber, J., Cowtan, K., Emsley, P., Murshudov, G. N., Cohen, S., Perrakis, A. and Noble, M. (2004). Developments in the CCP4 molecular-graphics project. *Acta Crystallogr D Biol Crystallogr* 60(Pt 12 Pt 1): 2288-2294.

Radzicka, A. and Wolfenden, R. (1995). A proficient enzyme. *Science* 267(5194): 90-93.

Raj, H., Szymanski, W., de Villiers, J., Rozeboom, H. J., Veetil, V. P., Reis, C. R., de Villiers, M., Dekker, F. J., de Wildeman, S., Quax, W. J., Thunnissen, A. M., Feringa, B. L., Janssen, D. B. and Poelarends, G. J. (2012). Engineering methylaspartate ammonia lyase for the asymmetric synthesis of unnatural amino acids. *Nat Chem* 4(6): 478-484.

Raushel, F. M. (2002). Bacterial detoxification of organophosphate nerve agents. *Curr Opin Microbiol* 5(3): 288-295.

Raushel, F. M. (2011). Chemical biology: Catalytic detoxification. *Nature* 469(7330): 310-311.

Raushel, F. M. and Holden, H. M. (2000). Phosphotriesterase: an enzyme in search of its natural substrate. *Adv Enzymol Relat Areas Mol Biol* 74: 51-93.

Reetz, M. T., Prasad, S., Carballeira, J. D., Gumulya, Y. and Bocola, M. (2010). Iterative saturation mutagenesis accelerates laboratory evolution of enzyme stereoselectivity: rigorous comparison with traditional methods. *J Am Chem Soc* 132(26): 9144-9152.

Roodveldt, C. and Tawfik, D. S. (2005). Shared promiscuous activities and evolutionary features in various members of the amidohydrolase superfamily. *Biochemistry* 44(38): 12728-12736.

Roodveldt, C. and Tawfik, D. S. (2005). Directed evolution of phosphotriesterase from Pseudomonas diminuta for heterologous expression in Escherichia coli results in stabilization of the metal-free state. *Protein Eng Des Sel* 18(1): 51-58.

Röthlisberger, D., Khersonsky, O., Wollacott, A. M., Jiang, L., DeChancie, J., Betker, J., Gallaher, J. L., Althoff, E. A., Zanghellini, A., Dym, O., Albeck, S., Houk, K. N., Tawfik, D. S. and Baker, D. (2008). Kemp elimination catalysts by computational enzyme design. *Nature* 453(7192): 190-195.

Saiki, R. K., Gelfand, D. H., Stoffel, S., Scharf, S. J., Higuchi, R., Horn, G. T., Mullis, K. B. and Erlich, H. A. (1988). Primer-directed enzymatic amplification of DNA with a thermostable DNA polymerase. *Science* 239(4839): 487-491.

Sambrook, J., Fritsch, E. E. and Maniatis, T. (1989). Molecular cloning: a laboratory manual. *New York, Cold Spring Harbour.*

Samples, C. R., Raushel, F. M. and DeRose, V. J. (2007). Activation of the binuclear metal center through formation of phosphotriesterase-inhibitor complexes. *Biochemistry* 46(11): 3435-3442.

Sanger, F., Nicklen, S. and Coulson, A. R. (1977). DNA sequencing with chain-terminating inhibitors. *Proc Natl Acad Sci U S A* 74(12): 5463-5467.

Sarkar, G. and Sommer, S. S. (1990). The "megaprimer" method of site-directed mutagenesis. *Biotechniques* 8(4): 404-407.

Savile, C. K., Janey, J. M., Mundorff, E. C., Moore, J. C., Tam, S., Jarvis, W. R., Colbeck, J. C., Krebber, A., Fleitz, F. J., Brands, J., Devine, P. N., Huisman, G. W. and Hughes, G. J. (2010). Biocatalytic asymmetric synthesis of chiral amines from ketones applied to sitagliptin manufacture. *Science* 329(5989): 305-309.

Schrader, G. (1950). Organische Phosphorverbindungen als neuartige Insektizide. *Angew. Chemie* 62: 471-473.

Sears, L. E., Moran, L. S., Kissinger, C., Creasey, T., Perry-O'Keefe, H., Roskey, M., Sutherland, E. and Slatko, B. E. (1992). CircumVent thermal cycle sequencing and alternative manual and automated DNA sequencing protocols using the highly thermostable VentR (exo-) DNA polymerase. *Biotechniques* 13(4): 626-633.

Seebeck, F. P. and Hilvert, D. (2003). Conversion of a PLP-dependent racemase into an aldolase by a single active site mutation. *J Am Chem Soc* 125(34): 10158-10159.

Seelig, B. and Szostak, J. W. (2007). Selection and evolution of enzymes from a partially randomized non-catalytic scaffold. *Nature* 448(7155): 828-831.

Segel, I. H. (1993). Enzyme kinetics. Behaviour and analysis of rapid equilibrium and steady-state enzyme systems. *John Wiley & Sohns, Inc., New York.*

Seibert, C. M. and Raushel, F. M. (2005). Structural and catalytic diversity within the amidohydrolase superfamily. *Biochemistry* 44(17): 6383-6391.

Sethunathan, N. and Yoshida, T. (1973). A Flavobacterium sp. that degrades diazinon and parathion. *Can J Microbiol* 19(7): 873-875.

Shapir, N., Mongodin, E. F., Sadowsky, M. J., Daugherty, S. C., Nelson, K. E. and Wackett, L. P. (2007). Evolution of catabolic pathways: Genomic insights into microbial s-triazine metabolism. *J Bacteriol* 189(3): 674-682.

Sharp, P. A., Sugden, B. and Sambrook, J. (1973). Detection of two restriction endonuclease activities in Haemophilus parainfluenzae using analytical agarose - ethidium bromide electrophoresis. *Biochemistry* 12(16): 3055-3063.

Siddavattam, D., Khajamohiddin, S., Manavathi, B., Pakala, S. B. and Merrick, M. (2003). Transposon-like organization of the plasmid-borne organophosphate degradation (opd) gene cluster found in Flavobacterium sp. *Appl Environ Microbiol* 69(5): 2533-2539.

Siegel, J. B., Zanghellini, A., Lovick, H. M., Kiss, G., Lambert, A. R., St Clair, J. L., Gallaher, J. L., Hilvert, D., Gelb, M. H., Stoddard, B. L., Houk, K. N., Michael, F. E. and Baker, D. (2010). Computational design of an enzyme catalyst for a stereoselective bimolecular Diels-Alder reaction. *Science* 329(5989): 309-313.

Slatko, B. E. (1994). Thermal cycle dideoxy DNA sequencing. *Methods Mol Biol* 31: 35-45.

Stemmer, W. P. (1994). Rapid evolution of a protein in vitro by DNA shuffling. *Nature* 370(6488): 389-391.

Sterner, R. and Höcker, B. (2005). Catalytic versatility, stability, and evolution of the (betaalpha)8-barrel enzyme fold. *Chem Rev* 105(11): 4038-4055.

Sterner, R., Merkl, R. and Raushel, F. M. (2008). Computational design of enzymes. *Chem Biol* 15(5): 421-423.

Stüber, D., Matile, H. and Garotta, G. (1990). System for high level production in E. coli and rapid purification of recombinant proteins: application to epitope mapping, preparation of antibodies and structure-function analysis. *In: I. Lefkovits and B. Bernis, editors. Immunological Methods, 4th ed. Academic Press, New York.* 121-215.

Studier, F. W. and Moffatt, B. A. (1986). Use of bacteriophage T7 RNA polymerase to direct selective high-level expression of cloned genes. *J Mol Biol* 189(1): 113-130.

Studier, F. W., Rosenberg, A. H., Dunn, J. J. and Dubendorff, J. W. (1990). Use of T7 RNA polymerase to direct expression of cloned genes. *Methods Enzymol* 185: 60-89.

Thoden, J. B., Phillips, G. N., Jr., Neal, T. M., Raushel, F. M. and Holden, H. M. (2001). Molecular structure of dihydroorotase: a paradigm for catalysis through the use of a binuclear metal center. *Biochemistry* 40(24): 6989-6997.

Todd, A. E., Orengo, C. A. and Thornton, J. M. (2001). Evolution of function in protein superfamilies, from a structural perspective. *J Mol Biol* 307(4): 1113-1143.

Tokuriki, N. and Tawfik, D. S. (2009). Stability effects of mutations and protein evolvability. Curr Opin Struct Biol 19(5): 596-604.

Toscano, M. D., Woycechowsky, K. J. and Hilvert, D. (2007). Minimalist active-site redesign: teaching old enzymes new tricks. *Angew Chem Int Ed Engl* 46(18): 3212-3236.

Tsai, P. C., Bigley, A., Li, Y., Ghanem, E., Cadieux, C. L., Kasten, S. A., Reeves, T. E., Cerasoli, D. M. and Raushel, F. M. (2010). Stereoselective hydrolysis of organophosphate nerve agents by the bacterial phosphotriesterase. *Biochemistry* 49(37): 7978-7987.

Tsai, P. C., Fan, Y., Kim, J., Yang, L., Almo, S. C., Gao, Y. Q. and Raushel, F. M. (2010). Structural determinants for the stereoselective hydrolysis of chiral substrates by phosphotriesterase. *Biochemistry* 49(37): 7988-7997.

Vanhooke, J. L., Benning, M. M., Raushel, F. M. and Holden, H. M. (1996). Three-dimensional structure of the zinc-containing phosphotriesterase with the bound substrate analog diethyl 4-methylbenzylphosphonate. *Biochemistry* 35(19): 6020-6025.

Vyas, N. K., Nickitenko, A., Rastogi, V. K., Shah, S. S. and Quiocho, F. A. (2010). Structural insights into the dual activities of the nerve agent degrading organophosphate anhydrolase/prolidase. *Biochemistry* 49(3): 547-559.

Wackett, L. P. (2004). Evolution of enzymes for the metabolism of new chemical inputs into the environment. *J Biol Chem* 279(40): 41259-41262.

Wang, L., Althoff, E. A., Bolduc, J., Jiang, L., Moody, J., Lassila, J. K., Giger, L., Hilvert, D., Stoddard, B. and Baker, D. (2012). Structural analyses of covalent enzyme-substrate analog complexes reveal strengths and limitations of de novo enzyme design. *J Mol Biol* 415(3): 615-625.

Wang, W. and Malcolm, B. A. (1999). Two-stage PCR protocol allowing introduction of multiple mutations, deletions and insertions using QuikChange Site-directed Mutagenesis. *Biotechniques* 26(4): 680-682.

Wang, X., Minasov, G. and Shoichet, B. K. (2002). Evolution of an antibiotic resistance enzyme constrained by stability and activity trade-offs. *J Mol Biol* 320(1): 85-95.

Ward, T. R. (2008). Artificial enzymes made to order: combination of computational design and directed evolution. *Angew Chem Int Ed Engl* 47(41): 7802-7803.

Waterhouse, A. M., Procter, J. B., Martin, D. M., Clamp, M. and Barton, G. J. (2009). Jalview Version 2 - a multiple sequence alignment editor and analysis workbench. *Bioinformatics* 25(9): 1189-1191.

Weinreich, D. M., Delaney, N. F., Depristo, M. A. and Hartl, D. L. (2006). Darwinian evolution can follow only very few mutational paths to fitter proteins. *Science* 312(5770): 111-114.

Williams, L., Nguyen, T., Li, Y., Porter, T. N. and Raushel, F. M. (2006). Uronate isomerase: a nonhydrolytic member of the amidohydrolase superfamily with an ambivalent requirement for a divalent metal ion. *Biochemistry* 45(24): 7453-7462.

Wilson, G. G. and Murray, N. E. (1991). Restriction and modification systems. *Annu Rev Genet* 25: 585-627.

Wong, K. Y. and Gao, J. (2007). The reaction mechanism of paraoxon hydrolysis by phosphotriesterase from combined QM/MM simulations. *Biochemistry* 46(46): 13352-13369.

Woycechowsky, K. J., Vamvaca, K. and Hilvert, D. (2007). Novel enzymes through design and evolution. *Adv Enzymol Relat Areas Mol Biol* 75: 241-294, xiii.

Xiang, D. F., Kolb, P., Fedorov, A. A., Meier, M. M., Fedorov, L. V., Nguyen, T. T., Sterner, R., Almo, S. C., Shoichet, B. K. and Raushel, F. M. (2009). Functional annotation and three-dimensional structure of Dr0930 from Deinococcus radiodurans, a close relative of phosphotriesterase in the amidohydrolase superfamily. *Biochemistry* 48(10): 2237-2247.

Xiang, D. F., Patskovsky, Y., Xu, C., Fedorov, A. A., Fedorov, E. V., Sisco, A. A., Sauder, J. M., Burley, S. K., Almo, S. C. and Raushel, F. M. (2010). Functional identification and structure determination of two novel prolidases from cog1228 in the amidohydrolase superfamily. *Biochemistry* 49(31): 6791-6803.

Yang, H., Carr, P. D., McLoughlin, S. Y., Liu, J. W., Horne, I., Qiu, X., Jeffries, C. M., Russell, R. J., Oakeshott, J. G. and Ollis, D. L. (2003). Evolution of an organophosphate-degrading enzyme: a comparison of natural and directed evolution. *Protein Eng* 16(2): 135-145.

Zanghellini, A., Jiang, L., Wollacott, A. M., Cheng, G., Meiler, J., Althoff, E. A., Rothlisberger, D. and Baker, D. (2006). New algorithms and an in silico benchmark for computational enzyme design. *Protein Sci* 15(12): 2785-2794.

Zhang, X., Wu, R., Song, L., Lin, Y., Lin, M., Cao, Z., Wu, W. and Mo, Y. (2009). Molecular dynamics simulations of the detoxification of paraoxon catalyzed by phosphotriesterase. *J Comput Chem* 30(15): 2388-2401.

Zhao, H., Giver, L., Shao, Z., Affholter, J. A. and Arnold, F. H. (1998). Molecular evolution by staggered extension process (StEP) in vitro recombination. *Nat Biotechnol* 16(3): 258-261.

7 APPENDIX

7.1 DNA and protein sequences of wild-type Dr0930 and wild-type PTE

7.1.1 DNA and protein sequences of *Deinococcus radiodurans R1* Dr0930

***dr0930* DNA sequence:**

```
  1 ATGACGGCAC AGACGGTGAC GGGCGCAGTC GCGGCGGCTC AACTCGGAGC
 51 GACGCTGCCC CACGAACACG TGATTTTCGG CTACCCCGGC TACGCGGGCG
101 ACGTGACGCT CGGGCCATTC GACCACGCGG CAGCGCTCGC AAGCTGCACC
151 GAAACGGCGC GGGCGCTGCT GGCGCGCGGT ATTCAGACGG TGGTGGACGC
201 CACCCCCAAC GACTGCGGAC GCAACCCGGC CTTCCTGCGC GAGGTGAGCG
251 AGGCAACCGG CCTCCAGATT CTGTGCGCGA CCGGCTTTTA TTACGAGGGC
301 GAGGGCGCCA CGACCTACTT CAAGTTCCGC GCTTCTCTGG GTGACGCCGA
351 AAGCGAAATC TACGAGATGA TGCGGACCGA GGTGACCGAG GGCATCGCCG
401 GCACCGGCAT CCGCGCCGGG GTCATCAAGC TGGCGAGCAG CCGCGACGCC
451 ATCACCCCCT ACGAGCAACT GTTTTTCCGG GCGGCGGCGC GGGTGCAGCG
501 CGAAACCGGC GTGCCGATCA TCACCCACAC TCAGGAAGGC CAGCAGGGAC
551 CGCAGCAAGC CGAGCTGCTG ACCTCGCTCG GCGCGGACCC GGCGCGCATC
601 ATGATCGGGC ACATGGACGG CAACACCGAC CCGGCCTACC ACCGCGAGAC
651 GCTGCGCCAC GGCGTGAGCA TCGCCTTTGA CCGCATCGGC TTGCAGGGCA
701 TGGTGGGCAC CCCCACCGAC GCCGAGCGGC TAAGCGTGCT GACCACGCTG
751 CTCGGCGAGG GCTACGCCGA CCGGCTGCTG CTCTCGCACG ACAGCATCTG
801 GCACTGGCTG GGACGCCCGC CGGCCATCCC CGAAGCCGCC TTGCCCGCCG
851 TCAAGGACTG GCACCCTCTC CACATCTCCG ACGACATCTT GCCTGATCTG
901 CGGCGCCGGG GCATCACCGA GGAGCAGGTG GGGCAGATGA CGGTGGGCAA
951 CCCGGCCCGG CTGTTCGGGT AA
```

Dr0930 protein sequence:

```
  1 MTAQTVTGAV AAAQLGATLP HEHVIFGYPG YAGDVTLGPF DHAAALASCT
 51 ETARALLARG IQTVVDATPN DCGRNPAFLR EVSEATGLQI LCATGFYYEG
101 EGATTYFKFR ASLGDAESEI YEMMRTEVTE GIAGTGIRAG VIKLASSRDA
151 ITPYEQLFFR AAARVQRETG VPIITHTQEG QQGPQQAELL TSLGADPARI
201 MIGHMDGNTD PAYHRETLRH GVSIAFDRIG LQGMVGTPTD AERLSVLTTL
251 LGEGYADRLL LSHDSIWHWL GRPPAIPEAA LPAVKDWHPL HISDDILPDL
301 RRRGITEEQV GQMTVGNPAR LFG*
```

7.1.2 DNA and protein sequences of *Pseudomonas diminuta* PTE

***pte* DNA sequence:**

```
   1 ATGTCCATCG GGACCGGTGA CCGTATCAAC ACCGTTCGTG GGCCCATCAC
  51 CATCTCCGAA GCTGGTTTCA CCCTGACCCA CGAACACATC TGCGGTTCCT
 101 CCGCGGGTTT CCTGCGTGCT TGGCCGGAGT TTTTCGGTTC CCGTAAAGCT
 151 CTGGCTGAAA AAGCTGTTCG TGGTCTGCGT CGTGCTCGTG CTGCAGGTGT
 201 TCGTACCATC GTTGACGTTT CCACCTTCGA CATCGGCCGT GACGTTTCCC
 251 TGCTGGCTGA AGTTTCCCGT GCTGCTGATG TACACATCGT TGCTGCTACC
 301 GGTCTGTGGT TCGACCCGCC GCTGAGCATG CGTCTGCGTT CCGTTGAAGA
 351 ACTGACCCAG TTCTTCCTGC GTGAAATCCA GTACGGTATC GAAGACACCG
 401 GGATCCGTGC TGGTATCATC AAAGTTGCTA CCACCGGTAA AGCTACCCCG
 451 TTCCAGGAGC TCGTTCTGAA AGCTGCTGCT CGTGCTTCCC TGGCTACCGG
 501 GGTCCCGGTT ACCACCCACA CCGCTGCTAG CCAGCGTGAC GGTGAACAGC
 551 AGGCTGCTAT CTTCGAATCC GAAGGTCTGT CCCCGTCACG CGTTTGCATC
 601 GGTCACTCCG ACGACACCGA CGACTTAAGC TACCTGACCG CTCTGGCTGC
 651 TCGTGGGTAC CTGATCGGTC TGGACCACAT CCCGCACTCC GCTATCGGTC
 701 TGGAAGACAA TGCATCCGCT TCCGCTCTGC TGGGTATCCG TTCCTGGCAG
 751 ACCCGTGCTC TGCTGATCAA AGCTCTGATC GACCAGGGTT ACATGAAACA
 801 GATCTTGGTT TCCAACGACT GGCTGTTCGG TTTCTCGAGC TACGTTACCA
 851 ACATCATGGA CGTTATGGAC CGTGTTAACC CGGACGGTAT GGCTTTCATC
 901 CCGCTGCGTG TTATCCCGTT CCTGCGTGAA AAAGGTGTTC CGCAGGAAAC
 951 CCTGGCTGGT ATCACCGTTA CCAACCCGGC TCGTTTCCTG TCCCCGACCC
1001 TGCGTGCTTC CTGA
```

PTE protein sequence:

```
   1 MSIGTGDRIN TVRGPITISE AGFTLTHEHI CGSSAGFLRA WPEFFGSRKA
  51 LAEKAVRGLR RARAAGVRTI VDVSTFDIGR DVSLLAEVSR AADVHIVAAT
 101 GLWFDPPLSM RLRSVEELTQ FFLREIQYGI EDTGIRAGII KVATTGKATP
 151 FQELVLKAAA RASLATGVPV TTHTAASQRD GEQQAAIFES EGLSPSRVCI
 201 GHSDDTDDLS YLTALAARGY LIGLDHIPHS AIGLEDNASA SALLGIRSWQ
 251 TRALLIKALI DQGYMKQILV SNDWLFGFSS YVTNIMDVMD RVNPDGMAFI
 301 PLRVIPFLRE KGVPQETLAG ITVTNPARFL SPTLRAS*
```

7.2 Structure of various substrates for PLL enzymes and PTE

The structures of substrates for PLL enzymes and PTE listed in Table 4 are shown in Figure 65.

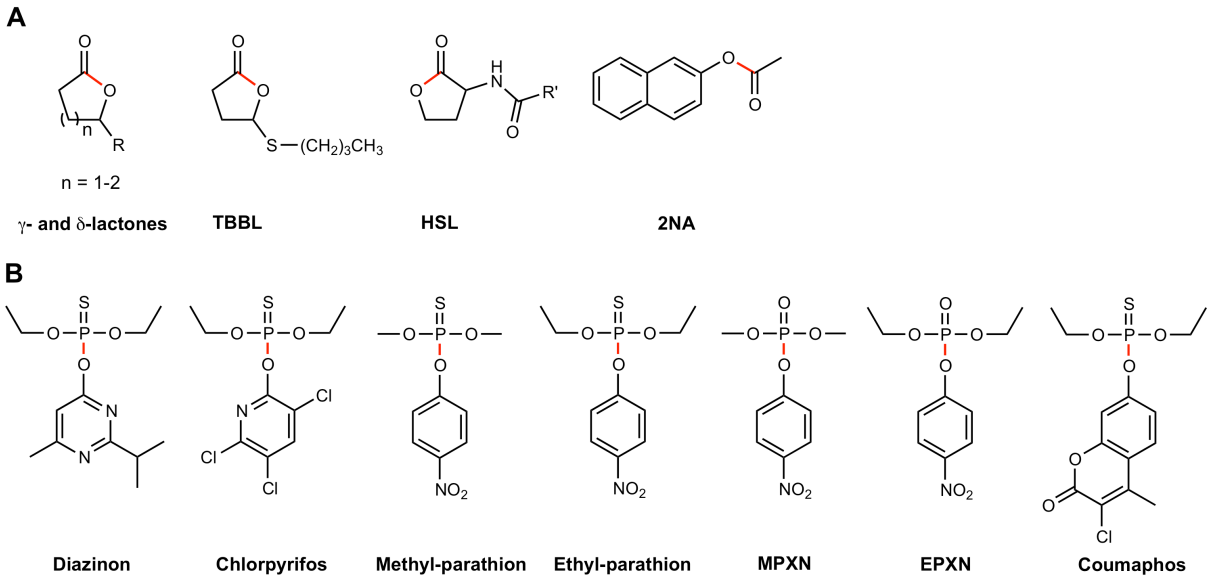

Figure 65: Structures of substrates of PLL enzymes and PTE: lactones and esters (A) and OPs (B).
A: Structures of lactones and esters: γ-/δ-lactone (R: alkyl side chain), TBBL (5-thiobutyl-γ-butyrolactone), HSL (homoserine lactone; R': alkyl side chain with or without 3-oxo group), and 2NA (2-naphthyl acetate). The cleaved C-O bond is highlighted in red.
B: Structures of OP compounds: diazinon, chlorpyrifos, methyl- and ethyl-parathion, methyl- and ethyl-paraoxon (MPXN and EPXN), and coumaphos. The cleaved P-O bond is highlighted in red.

7.3 Determination of the conversion factor ε_{577} for the pH-dependent colorimetric assay

The conversion factor ε_{577} (change of absorbance A_{577} per change in proton concentration, $\varepsilon_{577} = 1.17 \times 10^3\ M^{-1}cm^{-1}$) was determined by *in-situ* calibration with acetic acid (see Figure 66).

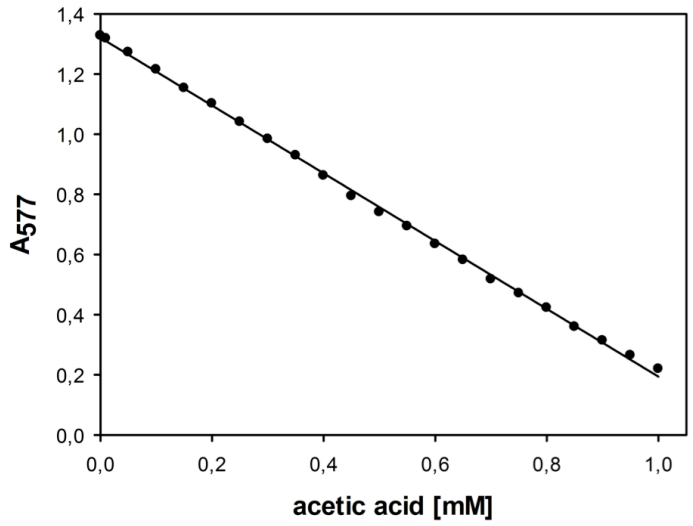

Figure 66: Determination of the conversion factor ε_{577} for the pH-dependent colorimetric assay. *In-situ* calibration with acetic acid gave a conversion factor ε_{577} of $1.17 \times 10^3\ M^{-1}cm^{-1}$ (linear fit). The reactions were performed in 2.5 mM BICINE (initial pH: 8.3), 0.1 mM $CoCl_2$, 1.4% DMSO, 0.1 mM *m*-cresol purple, 0.2 M NaCl and variable concentration of acetic acid (0-1 mM).

7.4 Determination of the enzyme metal content by ICP-MS

The metal content determined by ICP-MS for the Dr0930 and PTE enzyme preparations are listed in Table 32.

Table 32: Metal content determined by ICP-MS.

variant	metal content determined by ICP-MS
wild-type Co/Co-PTE	1.2 eq. Co, 0.1 eq. Zn
wild-type Co/Co-Dr0930	0.6-1.2 eq. Co, 0-0.12 eq. Zn, up to 0.23 eq. Fe
wild-type Zn/Zn-Dr0930	0.71 eq. Zn, 0.52 eq. Fe
wild-type Mn/Mn-Dr0930	2.15 eq. Mn, 0.14 eq. Zn, 0.28 eq. Fe
Co/Co-Dr0930_5	0.85 eq. Co, 0.44 eq. Zn, 0.02 eq. Fe
Co/Co-Dr0930_16	1.41 eq. Co, 0.28 eq. Zn, 0.02 eq. Fe
Co/Co-Dr0930_22	1.1 eq. Co, 0.13 eq. Zn, 0.03 eq. Fe
Co/Co-Dr0930_30	1.21 eq. Co
Co/Co-Dr0930_31	1.22 eq. Co, 0.09 eq. Zn
Co/Co-Dr0930_32	1.4 eq. Co, 0.06 eq Zn
Co/Co-Dr0930_70	1.24 eq. Co, 0.1 eq. Zn
Co/Co-Dr0930_73	1.33 eq. Co, 0.08 eq. Zn, 0.02 eq Fe
Co/Co-Dr0930_81	1.07 eq. Co
Co/Co-Dr0930_83	1.28 eq.Co
Co/Co-Dr0930_93	1.39 eq. Co
Co/Co-Dr0930_106	1.33-1.58 eq. Co
Co/Co-Dr0930_134	1.05-1.44 eq. Co

Abbreviation: eq.: equivalents of metal ion per enzyme subunit. An interval is given for multiple enzyme preparations.
Dr0930_5: Dr0930-T2Q+D71N+E179D+L270M. **Dr0930_16:** Dr0930-A3T+G38R+T105S. **Dr0930_22:** Dr0930-E101K+T105S. **Dr0930_30:** Dr0930-F26V+Y28I+D71G+C72I+E101M+Q178S+V235L+L270I. **Dr0930_31:** Dr0930-F26C+Y28I+D71A+E101N+Q178S+E179D+V235I. **Dr0930_32:** Dr0930-F26C+Y28I+D71G+E101D+Q178S+V235L+L270V. **Dr0930_70:** Dr0930-D71G+E101G+V235L. **Dr0930_73:** Dr0930-D71N+E101G+E179D+V235L+L270M. **Dr0930_81:** Dr0930-Y28L+D71N+E101G+E179D+V235L+L270M. **Dr0930_83:** Dr0930-Y28L+D71N+E101G+E179D+M235I+L270M. **Dr0930_93:** Dr0930-Y28L+D71N+Y97I+E101G+E179D+V235L+L270M. **Dr0930_106:** Dr0930-Y28L+D71N+Y97F+E101G+E179D+V235L+ L270M. **Dr0930_134:** Dr0930-Y28L+D71N+Y97F+E101G+E179D+V235L+P274L.

7.5 Sequence of most active Dr0930 variants isolated from the pTNA-*dr0930*-SHM library

The Dr0930 variants isolated from the SHM library are listed in Table 33.

Table 33: Most active variants isolated from pTNA-*dr0930*-SHM library.

Dr0930_#: mutations
30: F26V+Y28I+D71G+C72I+E101M+Q178S+V235L+L270I
31: F26C+Y28I+D71A+E101N+Q178S+E179D+V235I
32: F26C+Y28I+D71G+E101D+Q178S+V235L+L270V
33: F26I+Y28I+D71G+C72I+E101N+Q178S+E179D+V235I+L270V
34: F26V+Y28I+D71G+C72I+E101G+Q178S+E179D+V235M
35: F26I+Y28I+D71N+ E101G+Q178T+E179D+V235I+L270R
36: F26V+Y28A+D71L+E101G+Q178S+E179D+V235I+L270V
37: F26C+Y28V+D71G+E101C+Q178S+V235I+L270V
38: F26I+Y28T+D71N+C72I+E101N+V235L+L270V
39: F26C+Y28T+D71G+C72I+E101S+E179D+V235L
40: F26V+Y28I+D71G+C72I+E101V+Q178S+V235I+L270V
41: F26C+Y28I+D71L+E101M+Q178S+E179D+V235I+L270V
42: F26C+Y28V+D71N+C72I+E101N+E179D+V235I+L270V
43: F26C+Y28I+D71M+C72I+E101S+E179D+V235L+L270I
44: F26C+Y28T+D71N+E101S+E179D+V235L+L270V
45: F26C+Y28I+D71V+E101A+V235L
46: F26C+Y28T+D71N+E101K+Q178S+V235I
47: F26I+Y28I+D71G+E101S+Q178S+V235I+L270V
48: F26I+Y28I+D71N+E101G+Q178S+V235I+L270A
49: F26C+Y28I+D71M+E101D+Q178S+E179D+V235M+L270V
50: F26C+Y28I+D71V+E101C+Q178S+E179D+V235I
51: F26C+Y28I+D71A+E101L+Q178S+E179D+V235L+L270A
52: F26C+Y28I+D71L+E101V+Q178S+V235M+L270V
53: Y28I+D71L+C72I+E101V+V235L+L270I
54: F26V+Y28I+D71G+E101L+Q178S+V235I+L270I
55: F26C+Y28I+D71M+E101N+Q178S+V235I+L270I
56: F26C+Y28I+D71L+E101S+Q178S+E179D+V235L
57: F26C+Y28I+D71M+E101M+Q178S+V235I

Dr0930 variants contain the T2Q mutation.

7.6 Dixon Plot for determination of K_i

The Dixon plot is used to determine the dissociation constant (K_i) for an enzyme-inhibitor complex. The substrate analogue DIMP is a competitive inhibitor for GB *p*-NP (OP 2). The initial velocity of GB *p*-NP hydrolysis ([S] = $K_M^{GB\ p\text{-}NP}$ = 0.19 mM) recorded in presence of various concentrations of DIMP (0-500 mM) yielded a competitive inhibition constant, K_i, for Dr0930_134 of 9.5 mM (Figure 67).

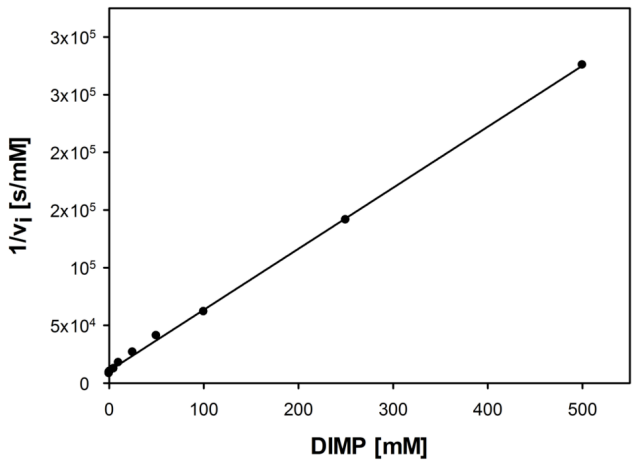

Figure 67: Dixon plot to determine K_i for DIMP and Dr0930_134.
The reactions were performed in 50 mM CHES, pH 9.0, 100 µM $CoCl_2$, 0.19 mM GB *p*-NP and various concentrations of DIMP (0-500 mM). The reaction was monitored at 400 nm (ε_{400} = 1.7 × 10^4 $M^{-1}cm^{-1}$) and 30 °C. Dr0930_134 was diluted in 20 mM HEPES pH 7.5, 100 µM $CoCl_2$ buffer supplemented with 1 mg/ml BSA in order to stabilze the protein at high dilutions. BSA has no influence on activity (data not shown). Reactions were performed with 3 nM enzyme concentration.
The solid line shows the result of a linear fit of the data points (SigmaPlot). The K_i value is determined using Equation 12, giving a value of 9.5 mM. The slope intersects at y=0 at a concentration of -15.6 mM DIMP (~K_i), confirming that DIMP is a competitive inhibitior for GB *p*-NP. Dr0930_134: Dr0930-Y28L+D71N+Y97F+E101G+E179D+V235L+P274L.

8 ACKNOWLEDGEMENTS

First and foremost, I would like to thank my PhD advisors Prof. Dr. Reinhard Sterner and Prof. Dr. Frank M. Raushel for their guidance and constant support throughout the course of this research. Thanks for your confidence in me. I deeply appreciate your support for grant and fellowship applications and I gratefully acknowledge that you enabled my research stay in Texas.

Financial support by the German Academic Exchange Foundation (DAAD), the University of Regensburg, and the *Fonds der Chemischen Industrie* is gratefully acknowledged.

I cordially thank all members of the 'Raushel Superfamily' for their support, useful discussions and a fantastic time in the Raushel lab. Special thanks go to my bench colleague Dr. Andrew Bigley for his advice, support and enthusiasm. Many thanks also go to Dr. Chengfu Xu for the synthesis of various OP substrates. I cordially thank Swapnil Ghodge and Dr. Siddhesh Kamat for ICP-MS measurements. Many thanks also go to Alissa Goble, Daniel Hitchcock, Eric Hobbs, Dr. Tamari Narindoshvili, Argentina Ornelas, Dr. Ping-Chuan Tsai, Anna Vladimirova and Dr. Dao Feng Xiang for a great time in the lab and in College Station.

I would like to thank my collaboration partners for their valuable contributions to this work: I cordially thank Prof. Dr. David Barondeau and in particular Nicholas Fox (Texas A&M University, College Station, USA), as well as Dr. Chitra Rajendran (University of Regensburg) for their introduction to protein crystallography and their work on X-ray structure determination. I gratefully thank Dr. Birte Höcker and Christoph Malisi (MPI Tübingen) for ligand docking studies and helpful discussions.

Many thanks go to PD Dr. Rainer Merkl and Dietmar Birzer for bioinformatics support. I gratefully thank Dr. Sandra Schlee for support in the evaluation of stereopreference data and valuable discussion.

Special thanks go to Florian Busch and David Peterhoff for valuable discussions, a precious time in the lab and proofreading of this work. Florian's irrepressible optimism and David's patient manner have been of great value.

I express my deepest gratitude to Christiane Endres and Sonja Fuchs for invaluable technical assistance and constant support. Technical assistance by Barbara Kellerer, Hermine Reisner and Jeannette Ueckert is also gratefully acknowledged. Thanks to Claudia Pauer for administrative support.

Many thanks go to my rotation students David Pöllmann, Veronika Schmid and Abby Sisco for their interest and their contribution to this work.

I would also like to thank all current and former members of the Sterner research group for their support, their fascination for this project and valuable discussions: Dr. Patrick Babinger, Barbara Beer, Linn Carstensen, Dr. Susanne Dietrich, Dr. Helmut Durchschlag, Dr. Alexander Ehrmann, Dr. Serap Evran, Bastian Groitl, Dr. Harald Guldan, Jan-Oliver Janda, Wolfgang Kaiser, Dr. Felix List, Bernd Reisinger, Dr. Bettina Rohweder, Dr. Daniel Schneider, Dr. Thomas Schwab, Dr. Tobias Seitz, Josef Sperl, Dr. Heike Stüer, Klaus-Jürgen Tiefenbach, Dr. Herman Zellner.

I cordially thank my parents, my family and friends for their encouragement and unlimited support.

Special thanks go to Jörg for his critical input, helpful discussions, patient and empathetic encouragement and support that aided to this thesis in innumerable ways.

9 EIDESSTATTLICHE ERKLÄRUNG

Ich versichere, dass ich die von mir vorgelegte Dissertation selbständig angefertigt, die benutzten Quellen und Hilfsmittel vollständig angegeben und die Stellen der Arbeit – einschliesslich Tabellen, Karten und Abbildungen –, die anderen Werken in Worlaut oder dem Sinn nach entnommen sind, in jedem Fall als Entlehnung kenntlich gemacht habe; dass diese Dissertation noch keiner anderen Fakultät oder Universität zur Prüfung vorgelegen hat; dass sie – abgesehen von der unten angegebenen Teilpublikation und den Tagungsbeiträgen – noch nicht veröffentlicht worden ist sowie, dass ich eine solche Veröffentlichung vor Abschluss des Promotionsverfahrens nicht vornehmen werde. Die Bestimmungen dieser Promotionsordnung sind mir bekannt. Die von mir vorgelegt Dissertation ist von Prof. Dr. R. Sterner und Prof. Dr. Frank M. Raushel betreut worden.

Regensburg, Juni 2012

_____

Monika M. Meier

Teilpublikation

Xiang, D. F., Kolb, P., Fedorov, A. A., Meier, M. M., Fedorov, L. V., Nguyen, T. T., Sterner, R., Almo, S. C., Shoichet, B. K. and Raushel, F. M. (2009). Functional annotation and three-dimensional structure of Dr0930 from Deinococcus radiodurans, a close relative of phosphotriesterase in the amidohydrolase superfamily. *Biochemistry* 48(10): 2237-2247.

Tagungsbeiträge

Poster

Meier, M. M., Xu, C., Fox, N., Barondeau, D., Sterner, R., and Raushel, F. M. Efficient Degradation of an Organophosphate Insecticide and Various Nerve Agent Analogues through Molecular Engineering of a Phosphotriesterase-like-lactonase. *7th Symposium of BZR Regensburg*, Kostenz, 26-27/09/2011

Meier, M. M., Xu, C., Fox, N., Barondeau, D., Sterner, R., and Raushel, F. M. Enhanced Degradation of an Organophosphate Insecticide and Various Nerve Agent Analogues through Molecular Engineering of the Dr0930 Active Site. *5th International Symposium on Experimental Standard Conditions of Enzyme Characterization (ESCEC) – Protein Structure Meets Enzyme Kinetics*, Rüdesheim, 12-16/09/2011

Meier, M. M., Xu, C., Fox, N., Barondeau, D., Sterner, R., and Raushel, F. M. Enhanced Degradation of an Organophosphate Insecticide and Various Nerve Agent Analogues through Molecular Engineering of the Dr0930 Active Site. *63th Gordon Research Conference – Enzymes, Coenzymes & Metabolic Pathways*, Waterville Vallely, USA, 10-15/07/2011

Meier, M. M., Xu, C., Sterner, R., and Raushel, F. M. Enhanced Degradation of Organophosphate Insecticides and Nerve Agent Analogues through Molecular Engineering of the Dr0930 Active Site. *Texas Enzyme Mechanism Conference*, Austin, USA, 08-09/01/2010

Vorträge

Protein Engineering of a Lactonase for Organophosphate Hydrolysis.
7th Symposium of BZR Regensburg, Kostenz, 27/09/2011

Protein Engineering of a Lactonase for Organophosphate Hydrolysis.
5th International Symposium on Experimental Standard Conditions of Enzyme Characterization (ESCEC) – Protein Structure Meets Enzyme Kinetics, Rüdesheim, 15/09/2011.

Molecular Engineering of the Dr0930 Active Site for Organophophate Hydrolysis.
29. Rabensteiner Kolleg, Pottenstein, 23/06/2011

Studying Molecular Evolution by Changing Substrate Specificities within the Amidohydrolase Superfamily of Enzymes.
27. Rabensteiner Kolleg, Pottenstein, 12/06/2009